QUANTUM LIQUIDS AND QUANTUM CRYSTALS

Convective instability of ^{3}He–^{4}He superfluid mixtures heated from below

A. A. Zadorozhko, T. V. Kalko, É. Ya. Rudavskiĭ,* V. K. Chagovets, and G. A. Sheshin

B. Verkin Institute for Low Temperature Physics and Engineering, National Academy of Sciences of Ukraine, pr. Lenina 47, 61103 Kharkov, Ukraine

(Submitted February 7, 2003)
Fiz. Nizk. Temp. **29**, 829–834 (August 2003)

The convective thermal instability of ^{3}He–^{4}He superfluid mixtures on heating from below is studied in the temperature interval 100–500 mK in mixtures with an initial concentration of 9.8% ^{3}He. It is found that at certain critical values of the power of the heat flux in the mixture there is a change in character of the heat transfer, indicating the onset of convective heat transfer. The critical temperature gradients associated with the onset of convection correspond to Rayleigh numbers many orders of magnitude greater than the Rayleigh numbers in the heating of the mixtures from above. The results are analyzed in the framework of the theory of the convective instability of binary mixtures. © *2003 American Institute of Physics.*
[DOI: 10.1063/1.1596788]

1. INTRODUCTION

In ordinary fluids, heat transfer with the aid of matter flow (convection) in a gravity field usually arises in heating the substance from below. In that case the heated fluid, being less dense, is pushed out in the direction counter to the force of gravity, and the temperature of the fluid tends to equalize. Most often the convective instability is studied in a layer of liquid confined between two horizontal planes (a Bénard cell) and heated from below; this situation was first considered theoretically by Rayleigh. Rayleigh–Bénard convection does not occur in superfluid ^{4}He because of the super thermal conductivity of He II, which makes it impossible to create temperature gradients in the liquid.

When ^{3}He impurities are added to He II, the thermal conductivity of the resulting ^{3}He–^{4}He superfluid mixtures becomes finite, making it possible to observe free convection. Experimental studies of convection processes in ^{3}He–^{4}He superfluid mixtures have been carried out in the Rayleigh–Bénard geometry at temperatures above 0.6 K.[1–5] This system has the peculiar property that the presence of a heat flux will give rise to both temperature and concentration gradients in the absence of a pressure gradient. At sufficiently low temperatures the normal component of the superfluid mixture consists practically only of ^{3}He quasiparticles, and therefore when the counterflow of normal and superfluid components arises, the ^{3}He atoms tend to move to the colder part of the cell. To cause a convective instability of the system in the experiments of Refs. 1–5, the cell was heated from below, so that the liquid with the lower density would be found in the lower part of the cell. Only in Ref. 7, where the special case of convection of a ^{3}He–^{4}He mixture near the λ point was studied, were measurements made for heating both from above and from below, and different results were obtained in the two cases. The question of convective instability of superfluid helium mixtures arises often in working with dilution refrigerators, where instability due to convection can arise in the diluted part.[6]

A key parameter used to describe convective processes is a dimensionless quantity proportional to the ratio of the repulsive force arising in the liquid in the heating region and the viscous force associated with dissipation. This parameter, called the Rayleigh number, is expressed as

$$R=\frac{g\beta\nabla T h^4}{\nu\chi}, \tag{1}$$

where g is the acceleration of gravity, β is the coefficient of thermal expansion, ∇T is the temperature gradient in the liquid, h is the vertical dimension, $\nu=\eta/\rho$ is the kinematic viscosity, $\chi=\kappa/\rho C_p$ is the thermal diffusivity, η is the coefficient of viscosity, κ is the thermal conductivity, C_p is the heat capacity, and ρ is the density of the liquid.

As was shown by Rayleigh, for $\beta>0$ steady convection arises in a horizontal layer of thickness h with a temperature gradient directed downward for $R>R_{cr}=1708$, which usually holds for classical liquids. In the case of superfluid ^{3}He–^{4}He mixtures heated from above, values of R_{cr} different from this criterion have been obtained, though they are of the same order of magnitude.[3] There the temperature gradients were directed upward, and the parameter β in formula (1) was treated as an effective coefficient of expansion β_{eff} which takes into account the change in density of the liquid due not only to temperature but also to concentration, and $\beta_{eff}<0$.

Theoretical studies of convection processes in superfluid ^{3}He–^{4}He mixtures[8–15] have also been done for the case of Rayleigh–Bénard convection. In those studies nonlinear equations were obtained which describe convection with allowance for two-fluid effects, and the influence of temperature and concentration on the convective instability of ^{3}He–^{4}He mixtures was analyzed.

In the present study, unlike the experiments of Refs. 1–5, instability processes in superfluid ^{3}He–^{4}He mixtures were studied with the liquid heated from below. The measurement cell was of a substantially different geometry from the Rayleigh–Bénard cell used previously to study the steady-state temperature and concentration gradients.[16] In addition, the first experiments at very low temperatures (below $\sim$0.5 K) are done, including at temperatures where the mixture studied undergoes phase separation.

2. FEATURES OF THE EXPERIMENTAL TECHNIQUE

The measurement cell used in this study was described in detail in Ref. 16. The liquid to be studied filled a cylinder 2.38 cm in diameter and 4.7 cm in height. The upper flange of the cell was in constant thermal contact with the mixing chamber of the dilution refrigerator. To reduce the Kapitsa thermal boundary resistance between the liquid under study and the flange, a heat exchanger made of ultradisperse silver powder, with a heat-transfer surface of 1.5 m^2, was used. The side walls of the cell were made of thin-walled stainless steel (0.1 mm thick), so that the thermal conductivity of the walls was much less than the effective thermal conductivity of the liquid.

The heat flux was produced by a plane heater placed directly in the liquid in the lower part of the cell. The temperature of the liquid was measured by two identical RuO_2 resistance thermometers. The lower thermometer was placed a distance of 20 mm from the lower flange of the cell, and the upper thermometer a distance of 10 mm from the lower flange. The resistance of the thermometers was measured by a Cryobridge 441 ac bridge, with a measurement error that is equal to ± 0.2 mK at a temperature of 250 mK and decreases with decreasing temperature.

Simultaneously with the temperature measurements the concentration of the mixture at the same places in the cell was determined by measuring the dielectric constant. Capacitive concentration sensors in the form cylindrical capacitors 0.5 cm in height were used, having electrodes in the form coils of brass foil and a gap between plates of 0.1 and 0.2 mm for the upper and lower sensors, respectively. The nominal capacitance of the sensors was 750 and 300 pF, which made it possible to determine the relative concentration of ^{3}He to an accuracy of 0.05% and 0.1%.

The temperature of the mixing chamber was determined by a ^{3}He melting-curve thermometer. This thermometer was placed on the mixing chamber plate and was used to calibrate the resistance thermometers. We investigated a ^{3}He–^{4}He mixture with a molar concentration $x_0 = 9.8\%$ ^{3}He, which was prepared by mixing pure components. The measurements were made in the temperature range 100–500 mK at the saturated vapor pressure.

3. CRITICAL TEMPERATURE GRADIENT AND THE ONSET OF CONVECTION

We measured the steady-state temperature and concentration gradients in the mixture at several constant values of the heat flux radiated by the heater at the bottom of the cell. The temperature of the liquid was changed from one value to another by changing the temperature of the upper flange. Figure 1 shows the typical dependence of the temperature gradient ∇T on the heat flux power $\dot{Q}$ at various average temperatures between sensors. All of the plots have kinks at certain critical values of the power $\dot{Q}_{cr}$, indicating an increase in the effective thermal conductivity of the liquid, $\kappa_{eff} = \dot{Q}_{cr}/\Delta T$, which is naturally attributed to the onset of convective heat transport.

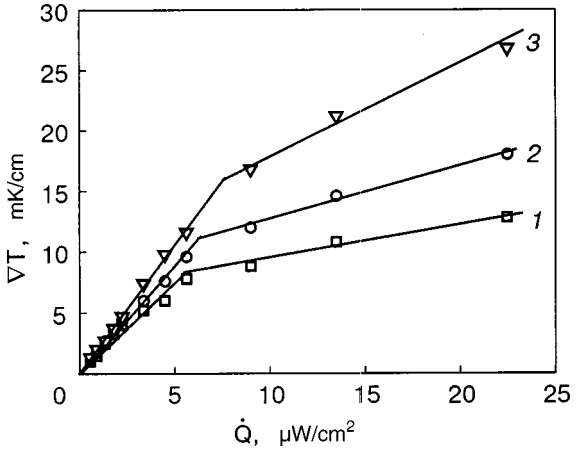

FIG. 1. Steady temperature gradient versus the heat flux power density at a constant mean temperature of the liquid, T [mK]: 150 (*1*), 200 (*2*), 300 (*3*).

The critical values of the temperature gradient ∇T_{cr} at the respective critical values of the heat flux $\dot{Q}_{cr}$ are plotted as a function of the average temperature of the liquid in Fig. 2. In the presence of a heat flux the maximum on this curve practically coincides with the phase separation temperature T_s of the mixture studied. The values of T_s for various heat flux powers were measured in Ref. 16 from the kink on the temperature dependence of the concentration of the mixture registered by the capacitive concentration sensors. Here, because of the presence of temperature and concentration gradients along the height of the cell, phase separation of the mixture begins near the upper flange of the cell, where the temperature is lowest and the concentration highest. For this reason the temperature indicated in Fig. 2, corresponding to the average temperature of the liquid in the region between the two thermometers, can be substantially higher than the temperature of the mixture in the upper part of the cell.

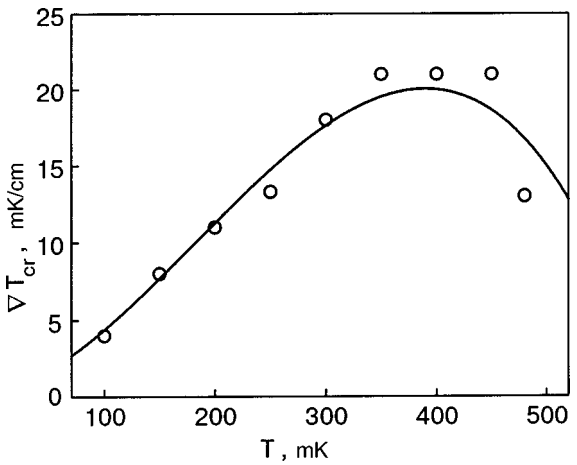

FIG. 2. Temperature dependence of the critical temperature gradients associated with the onset of convection.

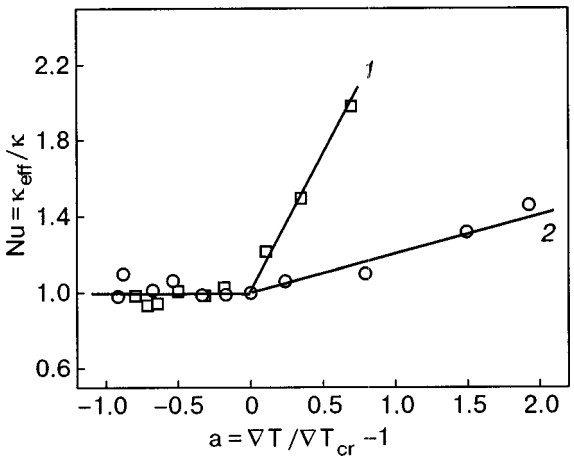

FIG. 3. Dependence of the Nusselt number on the parameter a for two mean temperatures of the cell, T [mK]: 250 (*1*), 400 (*2*).

The values of $\nabla T_{\rm cr}$ to the right of the maximum in Fig. 2 pertain to the initial homogeneous mixture. To the left of the maximum the critical temperature gradients pertain to the lower separated phase, the concentration of which is determined by the phase diagram and the heat flux power. Apparently it is also important here that as the temperature of the separated mixture is varied, a certain amount of the substance will undergo a transition from one phase to the other, in accordance with the phase diagram.

The change in the character of the heat transfer upon the onset of convection is clearly manifested in the dependence of the Nusselt number $\mathrm{Nu}=\kappa_{\rm eff}(\dot{Q})/\kappa$ on the the dimensionless parameter $a=(\nabla T(\dot{Q})/\nabla T_{\rm cr}-1)$, where κ is the value of the thermal conductivity prior to the onset of convection. This dependence is shown in Fig. 3 for two temperatures. A Nusselt number $\mathrm{Nu}=1$ for $a<0$ corresponds to a diffusive mechanism for the the spreading of heat, while for $a>0$ a convective mechanism of heat transport is realized. The point of intersection of these curves at $a=0$ determines the thermal conductivity and the critical temperature gradient at the instant that convection begins. As can be seen in Fig. 3, the slope of the $\mathrm{Nu}(a)$ curves in the convective region increases with decreasing temperature.

The values obtained for the temperature gradients for different values of the heat flux allow one to determine the corresponding Rayleigh numbers. In the case of mixtures the formula for R differs from expression (1), which is valid for the pure components, since convection can arise in a mixture on account of nonuniformities of both the temperature and concentration. For superfluid ^{3}He–^{4}He mixtures formula (1) takes the form[3,11,12]

$$R=\frac{|\beta_{\mu_4,P}|g\nabla T h^4}{\nu_n\chi_{\rm eff}}, \tag{2}$$

where $\nu_n=\eta_n/\rho_n$ is the kinematic viscosity of the normal component of the mixture, with density ρ_n, and $\chi_{\rm eff}=\kappa_{\rm eff}/\rho C_P$ is the effective thermal diffusivity. The thermal expansion coefficient $\beta_{\mu_4,P}$ at a constant ^{4}He chemical potential μ_4 in the mixture is expressed as[9,10]

$$\beta_{\mu_4,P}=\beta_T-\frac{\gamma c}{T}\beta_c, \tag{3}$$

where $\beta_T=-1/\rho\,(\partial\rho/\partial T)_{P,c}$ is the ordinary thermal expansion coefficient of a liquid, c is the mass concentration of the mixture, which is related to the molar concentration x as

$$c=\frac{m_3 x}{m_3 x+m_4(1-x)}$$

(m_3 and m_4 are the masses of the ^{3}He and ^{4}He atoms):

$$\beta_c=-\frac{1}{\rho}\left(\frac{\partial\rho}{\partial c}\right)_{\mu_4 P};$$

$$\gamma=\left(\frac{\partial\ln c}{\partial\ln T}\right)_{\mu_4 P}=\frac{T}{c}\frac{(\partial\mu_4/\partial T)}{(\partial\mu_4/\partial c)_{T,P}}.$$

Estimates show that the ordinary thermal expansion coefficient of the mixture under the conditions of this experiment is very small ($|\beta_T|\sim 10^{-3}$ K^{-1}), and the main contribution in formula (3) comes from the second term, which is due to the change of the density of the mixture as a result of the change in concentration, which is almost two order of magnitude larger than the first. Ultimately the critical Rayleigh number $R_{\rm cr}$ calculated according to Eq. (2) for this experiment has a value $R_{\rm cr}\sim 10^7-10^9$, which is many orders of magnitude lower than $R_{\rm cr}$ for the Rayleigh–Bénard case, when one is considering steady-state convection on heating from above.[3]

4. CRITICAL CONCENTRATION GRADIENT. CONCENTRATION RAYLEIGH NUMBER

As we have said, in the analysis of the convective instability of binary mixtures a substantial role is played by nonuniformity of the concentration, which is determined by the value of the concentration gradient created by the heat flux. The system of hydrodynamic equations for a mixture in which both heat flow and a diffusive flow of matter are present contains two dimensionless Rayleigh numbers:[17] the usual (temperature) Rayleigh number R_T, which relates to the temperature gradient and corresponds to expression (1), and the concentration Rayleigh number R_c,

$$R_c=\frac{g\beta_c\nabla c h^4}{\nu D}, \tag{4}$$

where D is the diffusion coefficient. The concentration gradient ∇c arising in the presence of heat flux in a superfluid mixture has been measured[16] as a function of the heat flux power $\dot{Q}$ under the conditions of the given experiment. The $\nabla c(\dot{Q})$ curves show a distinct kink corresponding to the onset of convection (see Fig. 5 of Ref. 16). The measured values of the critical concentration gradients $\nabla c_{\rm cr}$ can be used in Eq. (4) to calculate the number $(R_c)_{\rm cr}$. The resulting temperature dependence of $(R_c)_{\rm cr}$ is shown in Fig. 4, which also shows for comparison the critical values of the usual temperature Rayleigh number $(R_T)_{\rm cr}$ calculated according to Eq. (1) and the critical Rayleigh number calculated for the case of steady convection in superfluid ^{3}He–^{4}He mixtures in ac-

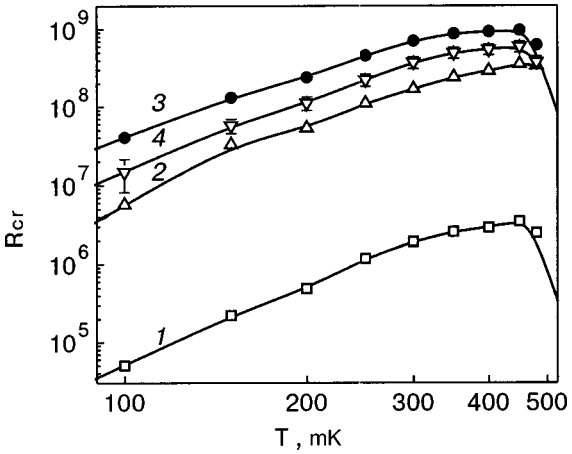

FIG. 4. Dependence of the critical Rayleigh number on the mean temperature of the mixture: *1*—temperature Rayleigh number; *2*—concentration Rayleigh number; *3*—calculation according to Eq. (2); *4*—calculation according to Eq. (5).

cordance with Eq. (2). As is seen from Fig. 4, the concentration Rayleigh number is two orders of magnitude higher than the temperature Rayleigh number.

To describe the convective instability of mixtures some superposition of the numbers R_T and R_c is usually used. For the conditions of the given experiment the most adequate model is apparently that of a cavity with impermeable boundaries,[17] for which the equilibrium flux of matter is equal to zero and the diffusion and thermodiffusion fluxes compensate each other. In this case the parameter that determines the stability boundary of the mixture is the modified Rayleigh number

$$\tilde{R}=R_T(1+\alpha^2 N)(1+\varepsilon)-R_C, \tag{5}$$

which agrees with the expression for the total Rayleigh number determined in Ref. 7, where

$$\alpha=-\frac{k_T}{T}, \quad N=\frac{T}{C_P}\left(\frac{\partial\mu}{\partial c}\right)_{T,P},$$

μ is the chemical potential of the mixture, $k_T=-(\nabla c/\nabla T)T$ is the thermodiffusion ratio, and the parameter ε describes the relation between the gradients of the temperature and concentration:

$$\varepsilon=-\frac{\beta_c}{\beta_T}\frac{\nabla c}{\nabla T}. \tag{6}$$

The critical value of the modified Rayleigh number $\tilde{R}$ is also shown in Fig. 4. The fact that it almost agrees in order of magnitude with the critical Rayleigh number calculated according to relation (2) attests to the closeness of the approaches used for describing the convective instability of the mixtures in Refs. 3, 11, 12, and 17.

However, the nature and mechanism of convection in superfluid ^{3}He–^{4}He mixtures heated from below remain open questions. Ordinarily steady convection is realized on heating from above,[1–5] on account of the anomalous thermodiffusion effect (a decrease in the ^{3}He concentration in the heated part of the cell), wherein the value of k_T is positive. In Ref. 10 it was predicted to be possible in principle to have unsteady oscillatory convection on heating from below. An important circumstance here is that the relaxation of the temperature in the mixture occurs much faster (at the speed of second sound) than the relaxation of the concentration (at the rate of diffusion processes). Consider an element of the liquid found at height z and having temperature T_1 and concentration c_1; if it is adiabatically shifted to a height $z+\delta$, it will be surrounded by liquid at a temperature T_2 and concentration c_2, where $T_1>T_2$ and $c_1<c_2$. After the rapid temperature relaxation the element will acquire a temperature T_2, while at the same time its concentration will still be much less than c_2. For this reason it is heavier than the surrounding liquid and will move downward under the influence of gravity. The time of downward motion is determined by dissipative processes, and in the course of this motion the ^{3}He concentration in the element will increase because of relaxation of the concentration, which leads to a decrease in the density of the liquid. As a result, at a certain height this element will become lighter than the surrounding liquid and will be pushed upward. This up-and-down oscillatory motion signifies the onset of oscillatory convection.

Oscillatory convection in superfluid ^{3}He–^{4}He mixtures has been observed previously in experiments on heating from above,[1–3] and in that case the critical Rayleigh number corresponding to oscillatory convection was several times greater than the value of R_{cr} for steady convection. In the present experiments the temperature oscillations characteristic of oscillatory convection were not detected within the aforementioned error limits of the temperature measurements. According to a theoretical analysis of oscillatory convection in superfluid ^{3}He–^{4}He mixtures in Ref. 10, its observation at low temperatures (below $\sim$0.8 K) is estimated to require too large a value of the critical temperature gradient, making its realization unlikely under the conditions of the present experiment.

5. CONCLUSION

These experiments on the convective instability of superfluid ^{3}He–^{4}He mixtures at temperatures below 0.5 K on heating from below have shown that in this case thermal convection arises at large temperature gradients, corresponding to Rayleigh numbers many order of magnitude greater than the corresponding values for the case of heating from above. Apparently the destabilizing factor that initiates convection is phase separation of the superfluid mixtures in the presence of a heat flux. The convective instability arising in a system in which ther is an interface between two phases with the light liquid found on top and there is seemingly no reason for instability to arise is sometimes called "anticonvection."[18] However, anticonvection has not been observed experimentally in the studies known to us, and it has been studied theoretically in the linear approximation only for layers unbounded in the horizontal direction.[18] In the present study we have obtained results that might argue in favor of the existence of the anticonvection effect.

Yet another factor promoting the development of instability in a liquid can be vortex formation in the superfluid helium and the resulting onset of turbulent flows at large temperature gradients in the liquid. Identification of the mechanism and type of convection in the superfluid

^{3}He–^{4}He mixture on heating from below will require additional experimental and theoretical research.

The authors thank V. N. Grigor'ev, L. Kh. Ingel', K. É. Nemchenko, Zh. A. Suprunova, V. I. Polezhaev, K. V. Rusanov, and E. B. Soboleva for helpful discussions.

This study was supported by the NATO Science Program, Grant PST.CLG 978495.

*E-mail: rudavskii@ilt.kharkov.ua

[1] P. Warkeutin, H. Haucke, and J. Wheatley, Phys. Rev. Lett. **45**, 918 (1980).
[2] H. Haucke, Y. Maeno, P. Warkeutin, and J. Wheatley, J. Low Temp. Phys. **44**, 505 (1981).
[3] Y. Maeno, H. Haucke, R. E. Ecke, and J. Wheatley, Phys. Rev. Lett. **54**, 340 (1985); J. Low Temp. Phys. **59**, 305 (1985).
[4] G. P. Metcalfe and R. P. Behringer, Phys. Rev. A **41**, 5735 (1990).
[5] T. S. Sullivan, V. Steinberg, and R. E. Ecke, J. Low Temp. Phys. **90**, 343 (1993).
[6] J. C. Wheatley, R. E. Rappy, and R. T. Jonhson, J. Low Temp. Phys. **4**, 1 (1971).
[7] G. Lee, P. Lucas, and A. Tyler, Phys. Lett. **75A**, 81 (1979).
[8] V. Steinberg, Phys. Rev. Lett. **45**, 2050 (1980).
[9] V. Steinberg, Phys. Rev. A **24**, 975 (1981).
[10] V. Steinberg, Phys. Rev. A **24**, 2584 (1981).
[11] A. Fetter, Phys. Rev. B **26**, 1164 (1982); Phys. Rev. B **26**, 1174 (1982).
[12] R. P. Behringer, Rev. Mod. Phys. **57**, 657 (1985).
[13] A. P. Gridin, Zh. Éksp. Teor. Fiz. **97**, 1852 (1990) [Sov. Phys. JETP **70**, 1045 (1990)].
[14] G. Metcalfe and R. P. Behringer, J. Low Temp. Phys. **78**, 231 (1993).
[15] A. Ya. Parshin, JETP Lett. **10**, 362 (1969).
[16] A. A. Zadorozhko, T. V. Kalko, É. Ya. Rudavskii, V. K. Chagovets, and G. A. Sheshin, Fiz. Nizk. Temp. **29**, 367 (2003) [Low Temp. Phys. **29**, 275 (2003)].
[17] G. Z. Gershuni and E. M. Zhukhovitskiĭ, *Convective Stability of an Incompressible Fluid* [in Russian], Nauka, Moscow (1972).
[18] L. Kh. Ingel', Usp. Fiz. Nauk **167**, 779 (1997).

Translated by Steve Torstveit

Simulation of a stochastic vortex tangle*

L. P. Kondaurova, S. K. Nemirovskii, and M. V. Nedoboiko

*Kutateladze Institute of Thermophysics SB RAS, Novosibirsk 630090, Russia***

(Submitted December 19, 2002)
Fiz. Nizk. Temp. **29**, 835–839 (August 2003)

We present the results of a simulation of the chaotic dynamics of quantized vortices in the bulk of superfluid He II. The evolution of vortex lines is calculated on the basis of the Biot—Savart law. The dissipative effects arising from the interaction with the normal component or/and from relaxation of the order parameter are taken into account. Chaotic dynamics appears in the system via a random forcing, i.e., we use the Langevin approach to the problem. In the present paper we require the correlator of the random force to satisfy the fluctuation-dissipation relation, which implies that thermodynamic equilibrium should be reached. We describe numerical methods for integration of the stochastic differential equation (including a new algorithm for reconnection processes), and we present the results of a calculation of some characteristics of a vortex tangle such as the total length, the length distribution of the loops, and the energy spectrum. © *2003 American Institute of Physics.* [DOI: 10.1063/1.1596789]

1. INTRODUCTION

Quantized vortices appearing in quantum fluids influence many properties of the systems. In general, the set of these vortices represents a chaotic vortex tangle (VT) consisting of separated vortex loops (closed vortex lines). To describe the influence of a VT, it is necessary to know the statistical description of the VT at various moments of the time evolution because quantized vortices exhibit different properties different in processes: thermodynamic equilibrium and nonequilibrium (turbulent). For example, quasi-equilibrium features are essential in the process of fast quenching. In contrast, in experiments with thermal flows and/or counterflows in He II the set of vortices shows very nonequilibrium (turbulent type) properties. The statistical descriptions of these two cases are strongly different. Thus the distribution of vortex loops over their lengths $n(l)=dN(l)/dl$ is governed by the formula[1] $n(l)\propto l^{-5/2}$ in the thermal equilibrium case, while in turbulent helium we have[2] $n(l)\propto l^{-4/3}$. There exist many works devoted to numerical investigations of vortex tangles and to the turbulent state of helium, e.g., Refs. 3–10. We note that the aforementioned calculations have been done in the local approximation. Originally simple vortex structures (VS) with time turn into a very strongly tangled system. If a self-crossing of the filaments happens in this system, the reconnection of vortex line occurs and thus the vortex loops divide or merge. Reconnections change the topology of the vortex structures and affect the evolution of a VT. In the papers mentioned above, reconnection was simulated from the condition of equality between the local and nonlocal contributions to the velocity of a vortex filament point, i.e., $v_{nl}\approx\kappa/2\pi\Delta\approx v_l\approx c\kappa\ln(R/a_0)/4\pi R$, where $\Delta=2R/[c\ln(R/a_0)]$ is the minimal distance between the pair of vortices, κ is the quantum of circulation, R is the radius of curvature at the given point, c is a constant ($\simeq 1$), and a_0 is the cutoff parameter concerning the radius of the vortex core. Thus, in those works only the distance between the points of a vortex line was chosen as the criterion for reconnection. In our opinion, this is a slightly incorrect approach, because the elements of the filaments can go away from each other and the crossing may not occur. In contrast to the above-mentioned papers, we consider the entire Biot—Savart equation. Moreover, we take into account possible random disturbances in the system of vortices. The disturbances are simulated by the addition of a new term to the Biot—Savart equation. The details are found below. This statement is conventional for the description of dynamical systems with stochastic perturbations. Moreover, in this work the following condition of reconnections is proposed: if the elements of a VT have intersected during the temporal step of the calculation, the reconnection occurs.

2. STATEMENT OF THE PROBLEM AND THE DYNAMICAL EQUATIONS

We consider the dynamics of vortex loops in three-dimensional infinite space. The induced velocity of helium at a point r is given by the Biot—Savart law:

$$\mathbf{v}(\mathbf{r})=\frac{\kappa}{4\pi}\int\frac{(\mathbf{S}-\mathbf{r})\times d\mathbf{s}}{|\mathbf{S}-\mathbf{r}|^3}.$$

The formulas for the velocity of vortex line points in the absence of dissipation takes the form:[3]

$$\frac{d\mathbf{s}}{dt}=\dot{\mathbf{S}}_0=\frac{\kappa}{4\pi}\int\frac{(\mathbf{S}_1-\mathbf{S})\times d\mathbf{S}_1}{|\mathbf{S}_1-\mathbf{S}|^3}+\frac{\kappa}{4\pi}\ln\left(\frac{2\sqrt{S_+S_-}}{e^{1/4}\cdot a_0}\right)\mathbf{S}'\times\mathbf{S}'', \tag{1}$$

where $\mathbf{S}(\xi,t)$ is the radius vector of the vortex line points, ξ is a parameter, in this case the arc length, $\mathbf{S}'$ is the arc length derivative, S_+ and S_- are the lengths of two adjacent line elements that hold the point $\mathbf{s}$ between, and the prime denotes differentiation with respect to the arc length ξ. The second term of Eq. (1) is the local part of the velocity, and the first term is the nonlocal part obtained by integration over

the rest of the vortex line and over all of the other loops. Taking into account the frictional force of vortices, the normal component of helium, and the rapidly fluctuating random term (Langevin force), we obtain the equation for the dynamics of a point of the vortex line:

$$\dot{\mathbf{S}}=\dot{\mathbf{S}}_0+\alpha[\mathbf{S}'\times(\mathbf{v_n}-\dot{\mathbf{S}}_0)]-\alpha'\mathbf{S}'\times[\mathbf{S}'\times(\mathbf{v_n}-\dot{\mathbf{S}}_0)]+A(t,\xi), \quad (2)$$

where

$$\langle A(t,\xi)\rangle=0, \quad \langle A_i(t_1,\xi_1)A_j(t_2,\xi_2)\rangle = D\delta_{ij}\delta(t_1-t_2)\delta(\xi_1-\xi_2)=D\delta_{ij}\delta(\xi_1-\xi_2)\times\langle n(t)n(t')\rangle,$$

i, j are the spatial components; t_1, t_2 are arbitrary points in time; ξ_1, ξ_2 define any points on the vortex line; D is the intensity of the Langevin force; α, α' are the friction coefficients; $n(t)$ is Gaussian white noise with $\langle n(t)\rangle=0$, $\langle n(t)n(t')\rangle=\delta(t-t')$. Let's assume further that the difference between the normal and the superfluid velocities of helium equals zero, $\mathbf{v}_n=0$, and neglect the term with α'. This statement corresponds to the absence of heat flow. Thus we finally obtain the dynamical equation for a vortex line:

$$\dot{\mathbf{S}}=\dot{\mathbf{S}}_0-\alpha\mathbf{S}'\times\dot{\mathbf{S}}_0+\sigma(\xi)n(t). \quad (3)$$

In integral form Eq. (3) is as follows:

$$\mathbf{S}(t,\xi)=\mathbf{S}(t_0,\xi)+\int_{t_0}^{t}\mathbf{B}(\xi,t)dt+\sigma(\xi)\int_{t_0}^{t}dW, \quad (4)$$

where $\mathbf{B}(\xi,t)=\dot{\mathbf{S}}_0-\alpha\mathbf{S}'\times\dot{\mathbf{S}}_0$, and $W(t)=\int_{t_0}^{t}n(t')dt$ is the standard Wiener process. In our model the initial condition is six completely symmetrical rings with an orientation making the total momentum of the system equal to zero.

3. THE NUMERICAL ALGORITHM AND THE DESCRIPTION OF RECONNECTIONS

Equation (4) was solved by the Euler method:

$$S_{n+1}=S_n+hB(\xi,t_n)+\sqrt{h}\sigma(\xi)\eta_n,$$

where S_n is the approximate solution of the equation at a mesh point at time t_n; h is the integration step in time at a mesh point t_n; $\{\eta_n\}$ is a set of mutually independent normal random vectors with mutually independent components in the aggregate $\eta_{n,j}$ $(j=1,2,3)$, having zero expectation value and a variance of 1. The component of vector η_n was calculated by the formula $\eta_{n,j}=\sqrt{-2\ln\alpha_1}\cos(2\pi\alpha_2)$, where α_1 and α_2 are random numbers from the interval (0,1) obtained by a pseudorandom-number generator. The Euler method is the first order on the mean-square approximation in the time step. The functions $\mathbf{S}'$, $\mathbf{S}''$, $\dot{\mathbf{S}}_0$ were calculated as in Ref. 3. To keep the calculation procedure coherent, points on the vortex line were added and removed as in Ref. 10.

The first step in the modeling of a reconnection process is the selection of point pairs that are the candidates for reconnection. After the pairs were defined, it was assumed that the line segments between each of the pairs were moving with a constant velocity (V_i, V_j) during the time step, as illustrated in Fig. 1.

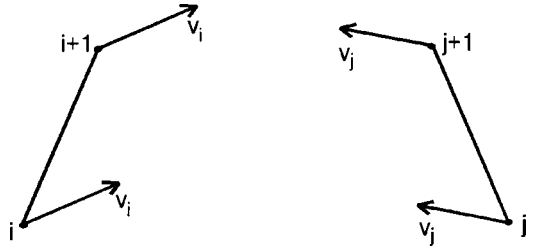

FIG. 1. The elements of vortex lines to reconnect.

From compatibility of the equations

$$x_i+V_{x,i}h+(x_{i+1}-x_i)s1=x_j+V_{x,j}h+(x_{j+1}-x_j)s;$$
$$y_i+V_{y,i}h+(y_{i+1}-y_i)s1=y_j+V_{y,j}h+(y_{j+1}-y_j)s;$$
$$z_i+V_{z,i}h+(z_{i+1}-z_i)s1=z_j+V_{z,j}h+(z_{j+1}-z_j)s;$$
$$0\leqslant s1\leqslant 1; \quad 0\leqslant s\leqslant 1$$

the meeting of these line segments during the time step was determined. Here $(x_i,y_i,z_i,x_{i+1},y_{i+1},z_{i+1})$; $(x_j,y_j,z_j,x_{j+1},y_{j+1},z_{j+1})$ are the coordinates of the first and the second pairs of points, respectively, and $V_{x,i}$, $V_{y,i}$, $V_{z,i}$; $V_{x,j}$, $V_{y,j}$, $V_{z,j}$ are the projections of the velocities of the points and the line segments on the coordinate axis. If the line segments have met, the reconnection occurs. Thus, if the points originally belonged to the same loop, a pair of new loops was generated. Otherwise a confluence of the loops occurs.

4. THE RESULTS

The initial radii of the rings were $R=2\cdot10^{-5}$ m. The initial condition was chosen in such a way that the total momentum of the system was equal to zero. The rings were situated symmetrically at equal distance in pairs around the coordinate origin. The distance between them was $d=10^{-5}$ m. The parameters in Eq. (2) are $\alpha=0.0098$, $D=4\cdot10^{-5}$ m/s.

Simulation was performed with a constant temporal step $h=5\cdot10^{-8}$ s and initial steps along the vortex line of $\Delta l_0=2\pi\cdot10^{-7}$ m. The steps Δl along the vortex line were controlled later by the procedure of inserting and removing of points, so that $\Delta l_0/2\leqslant\Delta l\leqslant2\Delta l_0$. It follows from Eq. (4) that small (or those with a high curvature) loops move very rapidly, and their dissipation (decrease in size) is very high due to the friction. Therefore, small loops were removed during our calculations. Kinks appearing on vortex lines were removed also. For our case, the loops were canceled if there were less than 5 points.

Vortex configurations at various times are presented in Fig. 2. One can see a vortex structure with drastic evolution in time. After numerous time steps the system evolved into separated vortex tangles. It was noted that during the evolution, the vortex tangles arose and then vanished in different places. It is reminiscent of the intermittency phenomenon in classical turbulence.

From the simulation, several quantities were calculated and plotted as functions of time (see Fig. 3). One can see the phases of evolution for vortex structures. At the beginning, the total length, averaged curvature, and the density of vortex lines increase at a steady volume. After a certain value of the density has been achieved, many small loops developed and the VT begin to decay. Later, one can observe a tendency to

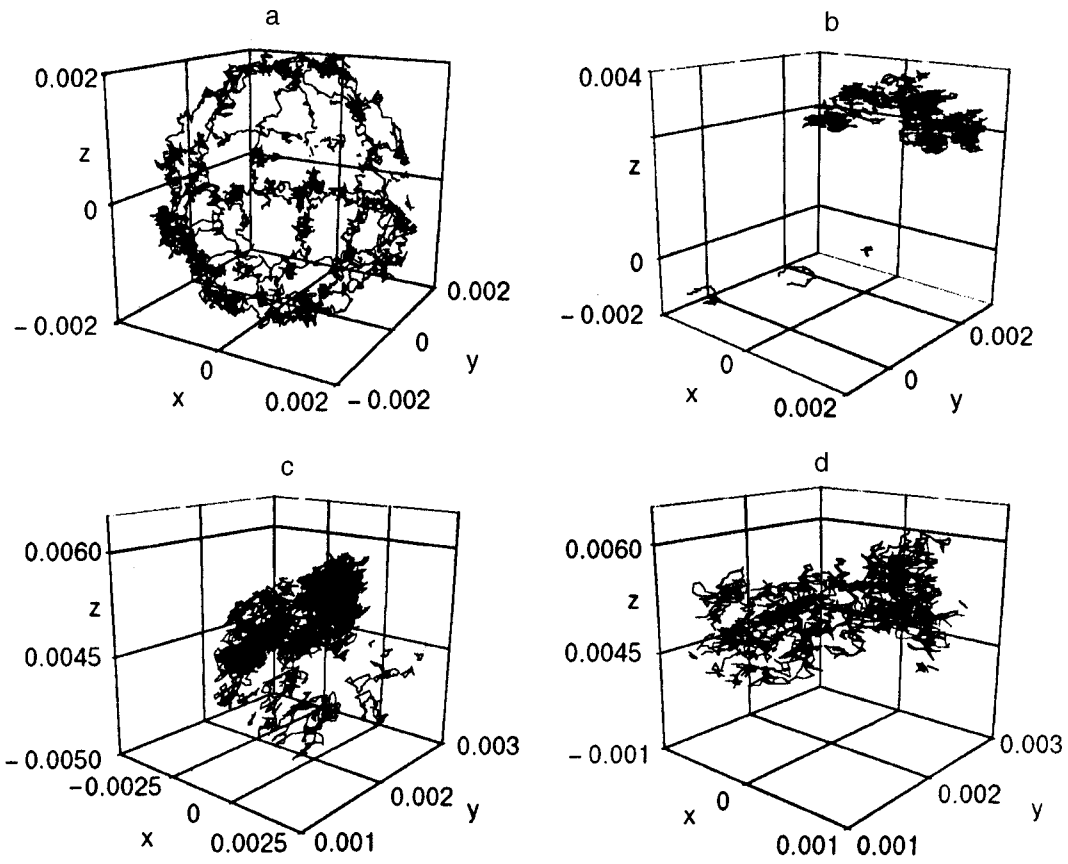

FIG. 2. The vortices at different times *t*, s: $4.30\cdot10^{-5}$ (a), $9.792\cdot10^{-4}$ (b), $1.0892\cdot10^{-3}$ (c), $1.1444\cdot10^{-3}$ (d). The configurations are plotted in a three-dimensional view.

a fluctuating steady state. However, after a time $t=9.792\cdot10^{-4}$ s, the volume suddenly begin to decrease. It is consistent with the disappearance of detached loops (see Fig. 2c and 2d). Then the fluctuating steady state is again reached.

We also did calculations for some statistical characteristics of the vortex structure. The distribution of the loop number vs. its length and the VT energy spectrum were calculated. Figure 4 shows the length distribution of the vortex loops in the time region $t\approx1.1443$ s. The decreasing of the number of loops is described by the following function: $n(l)dl\sim l^{-0.93}$. The same dependence was observed both for different times and for each vortex tangle within the vortex structure. It is difficult to extract physically meaningful results from these data. On the one hand, equilibrium has been reached. On the other hand, the distribution of vortex loops disagrees with the results obtained for thermal equilibrium and the turbulent stationary state.

The average kinetic energy of flow induced by a vortex loop can be evaluated as follows:[11]

$$E=\left\langle \int \frac{\rho_s V_s^2}{2} d^3r \right\rangle$$

$$=\int_k \frac{d^3k}{4\pi k^2}\left\langle 2\pi\rho_s\kappa^2 \int_0^{L'}\int_0^{L} \mathbf{S}(\xi_1)\dot{\mathbf{S}}(\xi_2) \times\exp\{-ik[\mathbf{S}(\xi_1)-\mathbf{S}(\xi_2)]\}d\xi_1 d\xi_2 \right\rangle$$

$$=\int_0^\infty E(k)dk,$$

$$E(k)=\frac{\rho_s\kappa^2}{2(2\pi)^3}\int \frac{d\Omega_k}{k^2}\int_0^{L}\int_0^{L'} \dot{\mathbf{S}}(\xi_1)\dot{\mathbf{S}}(\xi_2) \times\exp\{-i\mathbf{k}[\mathbf{S}(\xi_1)-\mathbf{S}(\xi_2)]\}d\xi_1 d\xi_2,$$

where $d\Omega_k=k^2\sin\theta_k d\theta_k d\Phi_k$ is the volume element, $\mathbf{k}$ is the

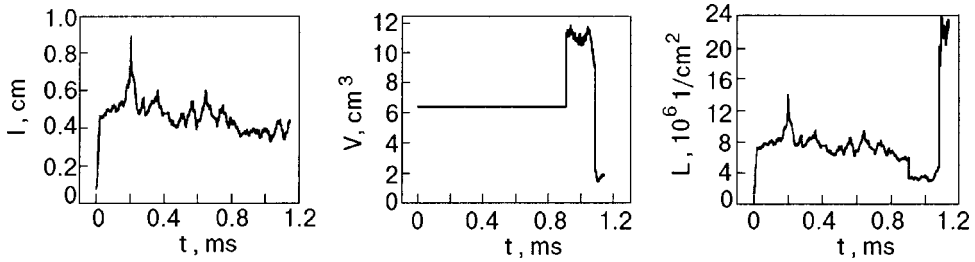

FIG. 3. Plots of the total lines *l*, the volume *V* filled with vortices, and the density of vortex lines *L* as functions of time.

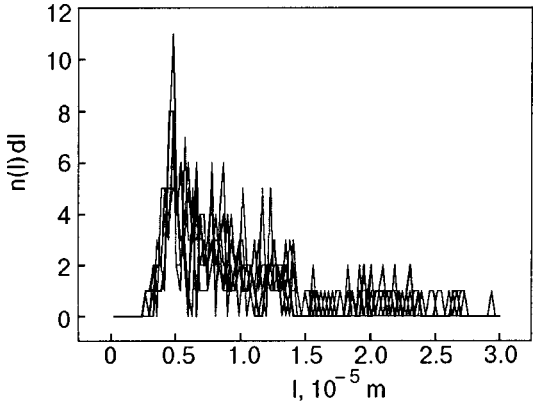

FIG. 4. The length distribution of the vortex loops in the time region near $t \approx 1.1443$ s.

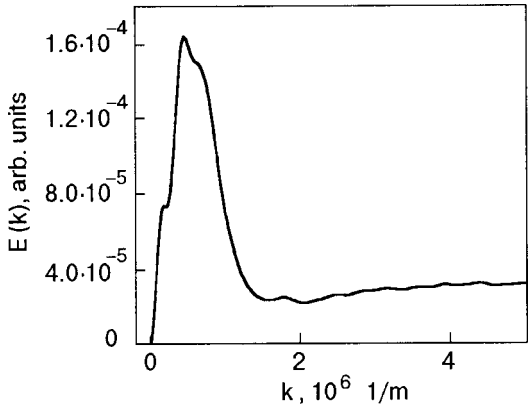

FIG. 5. The energy spectrum of the vortex tangle at $t = 1.1445 \cdot 10^{-3}$ s.

wave vector, and ρ_s is the superfluid density. For the isotropic case, the spectral density is expressed as follows:

$$E(k) = \frac{\rho_s \kappa^2}{(2\pi)^2} \int_0^L \int_0^{L'} \frac{\sin(k|\mathbf{S}(\xi_1) - \mathbf{S}(\xi_2)|)}{k|\mathbf{S}(\xi_1) - \mathbf{S}(\xi_2)|} [d\mathbf{S}(\xi_1) \times d\mathbf{S}(\xi_2)],$$

where k is the wave number. It is seen that there exist different regions of wave number k: small with respect to $(V)^{1/3}$, high with respect to $1/\sqrt{L}$, and intermediate values. In the region of small wave numbers one has $E(k) \propto k^2$, and for high numbers, $E(k) \propto k^{-1}$.

Figure 5 shows our numerical results of the VT spectral density for the time $t = 1.1445 \times 10^{-3}$ s. In the region of small wave numbers. The simulation data fit the approximation $E(k) \propto k^2$. In the region of high wave numbers, it is difficult to discern a regularity from these data, since the spectral density and the numerical error are of the same scale. In the intermediate region the energy decreases according to the formula $E(k) \propto k^{-2.9}$.

5. CONCLUSION

The numerical results obtained demonstrate that initially smooth vortex rings transform into a highly chaotic vortex tangle. In spite of the fact that the total length fluctuates about a constant value, we think that the thermal equilibrium state has not yet been reached. For instance, the spectral density of the energy agrees with the equipartition law only for a small k-zone. The vortex loop distribution over their lengths also differs from the one expected for thermal equilibrium. This state is closer to the turbulent case observed by other authors. During evolution the vortex tangles arise and disappear in different places. It resembles the favor intermittency phenomenon in classical turbulence. Our preliminary simulation demonstrates that the Langevin approach applied in this paper is a very promising method for the study of chaotic vortex structures.

This work is supported by INTAS grant 2001-0618.

*This report was submitted at the 3rd International Workshop on Low Temperature in Microgravity Environment Physics (CWS-2002).
**E-mail: theory@itp.nsc.ru

[1] N. D. Antunes and L. M. A. Bettencourt, Phys. Rev. Lett. **82**, 2824 (1999).
[2] T. Araki, M. Tsubota, and S. K. Nemirovskii (to be published).
[3] K. W. Schwarz, Phys. Rev. B **31**, 5782 (1985).
[4] P. G. Saffman, Stud. Appl. Math. **49**, 371 (1970).
[5] M. E. Agishtein and A. A. Migdal, Mod. Phys. Lett. A **1**, 221 (1986).
[6] K. W. Schwarz, Phys. Rev. B **38**, 2398 (1988).
[7] T. F. Buttke, J. Comp. Physiol. **76**, 301 (1988).
[8] D. C. Samuelse, Phys. Rev. B **46**, 11714 (1992).
[9] M. Tsubota and S. Mackawa, J. Low Temp. Phys. **89**, 4411 (1992).
[10] R. G. M. Aarts, *A Numerical Study of Quantized Vortices in He II*, Tech. Univer. Eindhoven (1993).
[11] S. K. Nemirovskii, Phys. Rev. B **57**, 5792 (1997).

This article was published in English in the original Russian journal. Reproduced here with stylistic changes by AIP.

Unstable states of a superfluid confined between rotating spheres*

A. Gongadze, L. Kiknadze, Yu. Mamaladze,** and S. Tsakadze

E.A. Andronikashvili Institute of Physics of the Georgian Academy of Sciences, 6 Tamarashvili Str., Tbilisi 380077, Georgia

(Submitted December 19, 2002)
Fiz. Nizk. Temp. **29**, 840–841 (August 2003)

The unstable states (including those related to self-accelerations of pulsars) in which the mutual friction causes an irreversible motion of vortices are considered. © *2003 American Institute of Physics.* [DOI: 10.1063/1.1596790]

INTRODUCTION

Concentric spheres with radii R_1 and R_2 rotating with a constant or variable angular velocity ω are considered. Both equilibrium and metastable states of this system are solutions of the equations of vortex dynamics with a given velocity and zero mutual friction between the vortices and the normal component. This force brings about transitions from one equilibrium or metastable state to another upon a change of angular velocity. But there also exist such configurations of vortices which cannot stay stable even if the variation of the velocity of rotation is interrupted.

In this publication of our report at CWS-2002 the part devoted to equilibrium and metastable rotation (see Ref. 1) is omitted. This paper is dedicated to the mechanism of the unstable processes and to the difference between double-cylinder and double-sphere devices.

BREAKING AND CONNECTION OF VORTICES

A clear example of the difference between coaxial cylinders and spheres is the generation of the first vortices. Fetter[2] showed that vortex generation begins at the outer cylinder at $\omega > \hbar \ln(2C)/2mRd$ $(d \equiv R_2 - R_1, \quad R \equiv (R_1 + R_2)/2, \, C \approx 1)$, but the generated vortex has no equilibrium position in the space between the cylinders until ω exceeds the value $\hbar \ln(d/a)/md^2$. Therefore, the vortices move to the inner cylinder, annihilate on it, and deposit the circulation there. In contrast to this, in the case of spheres a part of the axis of rotation lies in the liquid, and a vortex has an equilibrium position there if $\omega > \hbar \ln(2R/a)/2mR^2$ (Ref. 1). That value is less than the critical velocity of vortex generation at the equator of the outer sphere: $\hbar \ln(2C)/2mR_2 d$. In this situation is all of the vortices generated have equilibrium positions in the vicinity of the axis of rotation and move to them, being broken in two parts.

The same processes of vortex breaking and the opposite processes of two-vortex connection happen when vortices displace to their equilibrium positions or when a metastable vortex cluster[3] expands or compresses according to variations of the angular velocity.

The mechanism of these processes is shown in Fig. 1. The left part shows what happens when a vortex approaches the inner sphere from the area $r > R_1$. At first the interaction of the vortex with the sphere (''with its own image'') manifests itself in the nearest part of the vortex to the equator, which begins to distort. The prominent part of the vortex line and its image make the ''leading pair.'' The sequence of the following events is represented by Fig. 1 (left): the above-mentioned part of the vortex interacting with its image stretches along the equator, moves faster and faster, approaches the wall nearer and nearer, and annihilates at it. So the vortex breaks in two parts, and the edges of two remaining vortices find their equilibrium positions, not shown in Fig. 1.

The second picture of Fig. 1 (right) shows what happens when a vortex approaches the equator of the inner sphere from the area $r < R_1$. Then a vortex approaches the equator simultaneously with its continuation situated on the other side of the equator. Here, being perpendicular to the surface, the ends of the vortices form the leading pair. They move along the equator, approach each other, and annihilate. The remaining parts of the vortices join and form one vortex outside the inner sphere.

Thus, the opposite processes of vortex breaking and connection at the equator of the inner sphere do not represent a sequence of similar events observed in reverse order. The leading pairs, their orientation, and the directions of their gathering are different.

ANNIHILATION OF OUTGOING VORTICES

The position near the equator of the outer sphere is also where the equilibrium rotation of a vortex with the vessel and the normal component is impossible. The vortex may appear here, e.g., as a result of deceleration of an almost freely rotating double sphere. Then the interaction with its own image becomes decisive, and a vortex leaves the vessel moving along and to the equator. It is known that the mutual friction results in a time dependence $(t_{an} - t)^{1/2}$ for compress-

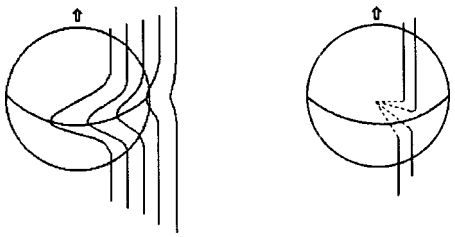

FIG. 1. The sequence of events during the breaking of a vortex moving to the axis of rotation (left), and the beginning of the connection of two vortices outgoing from the inner sphere (right).

ing linear dimensions: the distance from the vortex to the wall of the cylinder[4] and the radius of the ring[5] (t_{an} is the instant of annihilation). A freely rotating vessel responds to the changes of liquid angular momentum (which is proportional to the area outlined by the vortex and the wall) by a change of rotation velocity. The result is self-accelerations superimposed on the general deceleration of the vessel. In the case of a cylinder $d\omega/dt \propto (t_{an}-t)^{-1/2}$ (Ref. 4), in accordance with Packard's idea that the annihilation of vortices may be the cause of pulsar self-accelerations (starquakes).[6] But a pulsar is a sphere, and in this case it is possible to represent the annihilating vortex as something like a small compressing ring. Then the self-acceleration also would happen, but the derivative $d\omega/dt$ would be finite. However, this statement requires more-detailed consideration.

CONCLUSIONS

More-detailed observations of pulsar self-accelerations, modeling experiments (like Ref. 7), and more-detailed theoretical studies are desirable to compare the data, to discuss the similarities and differences between the cylindrical and spherical models and pulsars, and to distinguish between the processes taking place in the pulsar solid crust and the neutron liquid pierced by vortices.

This work was supported in part by INTAS (Network OPEN 97-1643) and by Grant 2.17.02 of the Georgian Academy of Sciences. We thank the Organizing Committee of CWS-2002 for support of the attendance of one of us (Yu.M.) at the workshop, Prof. W. Glaberson for discussions about experimental possibilities connected with the creation of a freely rotating device, and Prof. G. Kharadze for his interest and attention.

*This report was submitted at the 3rd International Workshop on Low Temperature Physics in Microgravity Environment (CWS-2002).
**E-mail: yum@iph.hepi.edu.ge; yum270629@yahoo.com

[1] L. Kiknadze and Yu. Mamaladze, J. Low Temp. Phys. **127**, 271 (2002).
[2] A. L. Fetter, Phys. Rev. **153**, 285 (1967).
[3] Y. Kondo, J. Korhonen, and M. Krusius, *Proceedings of LT-19, PG.G10* (1991); Y. Kondo, A. Gongadze, Y. Pattz, Y. Korhonen, M. Krusius, and O. Lounasmaa, Physica B **178**, 90 (1992); A. D. Gongadze and G. E. Vachnadze, Zh. Eksp. Teor. Fiz. **109**, 471 (1996) [sic].
[4] L. V. Kiknadze and Yu. G. Mamaladze, Zh. Eksp. Teor. Fiz. **75**, 607 (1978). [Sov. Phys. JETP **48**, 305 (1978)].
[5] C. F. Barenghi, R. J. Donnelly, and W. F. Vinen, J. Low Temp. Phys. **52**, 189 (1983).
[6] B. E. Packard, Phys. Rev. Lett. **28**, 1080 (1972).
[7] J. S. Tsakadze and S. J. Tsakadze, Usp. Fiz. Nauk **115**, 503 (1975) [Sov. Phys. Usp. **18**, 242 (1975)]; J. Low Temp. Phys. **39**, 649 (1980); S. J. Tsakadze, Fiz. Nizk. Temp. **6**, 674 (1980) [Sov. J. Low Temp. Phys. **6**, 325 (1980)].

This article was published in English in the original Russian journal. Reproduced here with stylistic changes by AIP.

SUPERCONDUCTIVITY, INCLUDING HIGH-TEMPERATURE SUPERCONDUCTIVITY

Features of the angular dependence of the critical current in thin epitaxial films of HTSC $YBa_2Cu_3O_{7-\delta}$ in a magnetic field

Yu. V. Fedotov,† É. A. Pashitskiĭ, and S. M. Ryabchenko*

Institute of Physics of the National Academy of Sciences of Ukraine, pr. Nauki 46, 03028 Kiev, Ukraine

V. A. Komashko, V. M. Pan, V. S. Flis, and Yu. V. Cherpak

Institute of Metal Physics of the National Academy of Sciences of Ukraine, bul'var Vernadskogo 36, 03142 Kiev, Ukraine

(Submitted January 8, 2003)
Fiz. Nizk. Temp. **29**, 842–857 (August 2003)

The dependence of the critical current density j_c on the magnitude and direction of the magnetic field **H** is investigated in thin epitaxial films of $YBa_2Cu_3O_{7-\delta}$ having a high value of j_c in the absence of field ($\sim 10^6$ A/cm^2 at 77 K) and a thickness d less than twice the magnetic field penetration depth λ. It is found that the $j_c(H)$ curves have a low-field plateau both for fields perpendicular and parallel to the film. In a magnetic field perpendicular to the film, the ''effective pinning'' plateau extends to a field corresponding to a density of Abrikosov vortices threading the film at which it is no longer favorable for them all to be pinned at edge dislocations in the interblock walls, and a fraction of them become unpinned. In contrast, in a field parallel to the film the end of the plateau is unrelated to depinning of threading vortices parallel to the film; instead, $j_c(H)$ decreases after the plateau region because the magnetic field parallel to the film weakens the pinning of vortices perpendicular to the film. The low-field plateau on $j_c(H)$ for an in-plane is wider than that for the case of normal magnetization. Therefore, the dependence of j_c on the angle between **H** and the normal to the film has a single maximum at which the field is lying in the film plane. In films obtained by laser or electron-beam evaporation of $YBa_2Cu_3O_{7-\delta}$ or its constituents, the measurements of j_c on which were made by an inductive method, the decrease of j_c with increasing field in the film plane begins at fields lower than the first critical field for penetration of the vortices into the film plane. For the magnetron-deposited film, where j_c was measured by a transport method, this decrease of j_c begins in a field much higher than that critical field. The possible relationships between the parameters of the $j_c(H)$ curves and the first critical field for penetration of the vortices into the film plane are discussed, including some which lead to different angular dependences of the critical current. © *2003 American Institute of Physics.*
[DOI: 10.1063/1.1596791]

1. INTRODUCTION

According to the experimental data (see, e.g., the reviews[1,2]), the critical current density j_c in thin c-oriented[1] epitaxial films of high-T_c superconductors (HTSCs) of the $YBa_2Cu_3O_{7-\delta}$ (YBCO) type reaches values 1–2 orders of magnitude greater than in the best single crystals, as high as $(1-3)\times 10^6$ A/cm^2 at 77 K in zero field, and it depends not only on the strength of the applied magnetic field H but also on its direction in relationship to the film plane and to the direction of the supercurrent passing through the film.

The $j_c(H,\theta,\varphi)$ curves in different films and under different conditions of measurement are not the same (θ is the angle between **H** and the normal to the film plane, and φ is the angle between the projection of **H** onto this plane and the current direction). For example, in Refs. 3–5 a single maximum of $j_c(H,\theta)$ was observed, at $\theta=90°$, at which j_c was several times higher than at $\theta=0$. The authors of those papers[3–5] attributed it to intrinsic pinning of the vortices due to the layered crystal structure of the HTSCs. However, it was subsequently established[6] that the pinning of the vortices on the atomic layers is extremely weak and can account for a value of j_c in YBCO of not more than 10^3 A/cm^2. In Ref. 7 a $j_c(\theta)$ curve with two maxima was observed: at $\theta=90°$ (**H**$\|ab$) and at $\theta=0$ (**H**$\|$**c**). The authors of Ref. 7 ascribed the peak at **H**$\|$**c** to vortex pinning on twins of the crystal structure. However, the pinning at coherent twin boundaries is also weak, since the region of elastic deformation of the crystal lattice of YBCO near twins (and, hence, the width of the potential well for vortex pinning) is limited to 1–2 interatomic distances.

In Ref. 8 the θ dependence was investigated both for fields perpendicular to the current ($\varphi=90°$) and for fields lying in the plane defined by the normal to the film and the current direction ($\varphi=0$). In both cases the $j_c(\theta)$ curve had a single maximum, at $\theta=90°$, and in every case that maximum was somewhat higher for $\varphi=90°$ than for $\varphi=0$.

In Refs. 9–12 the angular dependence of $j_c(H,\theta)$ mainly had two maxima, corresponding to the transverse ($\theta=0$) and longitudinal ($\theta=90°$) orientations of the field relative to the film plane (i.e., the ab plane). In some measurements only one maximum of $j_c(H,\theta)$ was observed, at $\theta=90°$, and in one of the films,[12] deposited by off-axis dc magnetron sputtering on the R cut of sapphire with a CeO_2 buffer layer, a single maximum of $j_c(H,\theta)$ was observed but at $\theta=0$. It was also shown that the character of the $j_c(\theta)$ curves at fixed values of the field varies as a function of temperature T and applied magnetic field strength H and is different for different films.

The features of the angular dependence of $j_c(\theta)$ were explained in Refs. 1, 2, 11, and 12 as being due to the presence of corresponding systems of extended linear defects in the different films: edge dislocations (EDs) and screw dislocations (SDs), causing anisotropy of the pinning of Abrikosov vortices for different directions of the magnetic flux trapped by them. In particular, enhancement of the pinning would occur when the magnetic field direction coincides with the predominant direction of the extended defects. The effectiveness of the pinning on EDs in YBCO is due to the fact that the radius r_c of the nonsuperconducting cores of the EDs are comparable in size to the radius of the normal core of an Abrikosov vortex. This also pertains to SDs, the cores of which have a radius which, though larger than that of the EDs, is nevertheless comparable to the radius of a vortex core. However, while the density of EDs can reach 10^{11} cm^{-2}, the average density of SDs is generally not more than 10^8–10^9 lines/cm^2, and so their contribution to the total pinning of the vortices is small.

For c-oriented epitaxial films of YBCO there are two characteristic systems of EDs. The first is due to the fact that in the ab plane, parallel to the substrate, these films are not ideally monocrystalline but have a mosaic structure of ''weakly'' (if the a and b axes are not distinguished) misoriented single-crystal regions (blocks).

The formation of a mosaic with alternating a and b axes in adjacent single-crystal blocks (they are sometimes called domains in the literature) leads to matching ''on average'' of the orthorhombic crystalline structure of the film with the tetragonal structure in the heteroplane of the substrate. According to the data of high-resolution electron microscopy,[13] the misorientation angles θ_b of the a and/or b axes of adjacent regions in high-quality films amounts to a few degrees or even a fraction of a degree. Of course, if the a and b axes of adjacent blocks are distinguished, then the actual misorientation angles are equal to $90° \pm \theta_b$. The transverse dimensions of the blocks are 20–500 nm. Their boundaries are dislocation walls consisting of linear chains of EDs with dislocation lines directed along the c axis. The density of these ''threading'' dislocations (on average over the area of the film) is usually very large, up to 10^{11} lines/cm^2.

It was shown in Refs. 14–16 that the dislocation walls are rather transparent to supercurrent up to a current density of 10^6–10^7 A/cm^2. Under certain conditions it is their transparency that determines j_c in the film. Here the cores of the EDs of the dislocation walls are extremely efficient pinning centers for vortices trapping magnetic flux normal to the film plane.[16,17] In particular, the characteristic magnetic-field dependence of $j_c(H,\theta=0)$ found in Refs. 16 and 18–20 is explained in Ref. 16 on the basis of a statistical model for the pinning of an ensemble of mutually interacting vortices on threading EDs at ''low-angle'' interblock boundaries.

In addition, epitaxial films characteristically have misfit dislocations which relieve the stresses caused by a slight difference in the lattice parameters of the film and substrate. The lines of misfit dislocations form a network in the plane of the film near its interface with the substrate. The density of these dislocations varies depending on the difference of the lattice parameters of the substrate and film in the heteroplane and on the thickness of the film and its deposition technology. These in-plane dislocations can be efficient pinning centers for vortices trapping magnetic flux in the film plane, provided that it is favorable for in-plane vortices to enter the film.

These arguments permitted the authors of Refs. 1, 2, 11, and 12 to interpret the situation with two maxima or one maximum of $j_c(H,\theta)$ as resulting from the different development of the systems of threading and in-plane EDs in the films, depending on their growth technology. In Ref. 17 a model of single-particle core pinning of vortices on the cores of EDs in a magnetic field directed at an arbitrary angle to the dislocation line was considered. This analysis qualitatively confirmed the soundness of the ideas developed in Refs. 1, 2, 11, and 12 as to the possible nature of the anisotropy of $j_c(H,\theta)$. However, both the argumentation in Refs. 1, 2, 11, and 12 and the analysis in Ref. 17 pertain to conditions corresponding to film thicknesses $d \gg \lambda(T)$ and do not take into account the specifics of the entry of in-plane vortices into thin films. Here and below $\lambda(T)=\lambda_0(1-T/T_c)^{-1/2}$ is the temperature-dependent penetration depth of the magnetic field into the superconductor, and T_c is the critical temperature of the superconducting transition.

For a consistent treatment of the angular dependence of $j_c(H,\theta)$ in thin HTSC films with $d \leqslant 2\lambda$ it is necessary to take into account the difference of the conditions of penetration of Abrikosov vortices into films for the transverse ($\theta=0$) and longitudinal ($\theta=90°$) directions of the field **H** (henceforth referred to as ''transverse'' and ''longitudinal'' fields). In this paper we shall show that it is just this circumstance, together with the specifics of the field dependence $j_c(H,\theta=0)$ in YBCO epitaxial films,[16,18–20] that makes it possible to understand the nature of the various anomalies in the angular dependence of $j_c(H,\theta)$.

It should also be noted that the discussion of the $j_c(H=\text{const},\theta)$ curves at different magnetic field strengths in the reviews[1,2] was based on measurements of j_c starting at comparatively high fields. In turn, the magnetic-field curves $j_c(H,\theta=\text{const})$ in YBCO epitaxial films with high values of $j_c(H=0)$ have been studied only for $\theta=0$,[16,18–20] revealing peculiar low-field behavior. There have been practically no published reports on the $j_c(H,\theta=\text{const},\varphi=\text{const})$ curves for different θ and φ starting at extremely low fields.

2. EXPERIMENT

In the present study we have investigated the field dependence and angular dependence of j_c in thin c-oriented epitaxial films of HTSC $YBa_2Cu_3O_{7-\delta}$ that we obtained by three different methods: pulsed laser deposition (PLD), joint

electron-beam evaporation of Y, BaF_2, and Cu followed by annealing in an O_2 atmosphere (JEBE), and off-axis magnetron sputtering (OAMS). The films obtained by PLD and JEBE were studied by measuring the complex magnetic susceptibility by a contact-free inductive method, and the OAMS films were studied by a four-probe transport method. The nominal thicknesses of the films (determined by the growth technologies according to the growth time and conditions) and by measurements on a MII-4 interferometer) were around 300 nm for the PLD and OAMS films and 90 nm for the JEBE film.

2.1. Film samples and their growth

The measurements were made on two laser-deposited films (PP8 with $T_c = 87.9$ K and P532 with $T_c = 89.6$ K) with nominal thicknesses $d \approx 300$ and 360 nm, respectively, grown in several different deposition regimes on single-crystal substrates of $LaAlO_3$ oriented along the (100) plane and mechanically polished to optical quality, and one film (TN2, with $d \approx 90$ nm and $T_c = 89.2$ K) grown by the joint electron-beam deposition of copper, yttrium, and BaF_2 on a single-crystal (100) substrate of $LaAlO_3$ with a subsequent annealing in an oxygen atmosphere. The dimensions of these films in the plane were 0.5×0.5 cm. In addition, we studied a film (K6300, with T_c near 90 K, $d \approx 300$ nm, and in-plane dimensions of 10×10 mm) grown by the dc OAMS method on a single-crystal sapphire substrate (R-cut) coated with a buffer layer of CeO_2 (see Ref. 11 for a description of the technique).

Film PP8 was deposited by evaporation of $YBa_2Cu_3O_{7-\delta}$ from two rotating stoichiometric targets by a double-beam solid-state Nd-YAG laser with a specially shaped profile of the laser beam (see Ref. 21 for details). The substrate temperature was 740–750 °C, and the oxygen pressure in the chamber was around 0.2 mbar. Under these conditions the average transverse size of the single-crystal blocks, according to an electron microscopic analysis,[13] is 40–150 nm and increases with the substrate temperature. The misorientation of adjacent blocks did not exceed 1–2°. Films grown under these conditions have a narrow transition in temperature to the superconducting state and a high critical current density (up to 3×10^6 A/cm^2 at 77 K). The film P532 was obtained on the same apparatus but under conditions corresponding to a wider transition to the superconducting state and a lower value of j_c.

The substrate temperature during the OAMS was varied from 720 to 750 °C. At temperatures below 720 °C, an x-ray analysis revealed a 5–10% content of the *a*-oriented phase. The pressure of the 3:1 argon:oxygen mixture in the chamber was 10^{-1} torr.

The deposition of the film by the OAMS method occurs at a rate of 0.02–0.03 nm/s and is close to a two-dimensional, monolayer-by-monolayer growth, while for the PLD the rate of deposition is 0.1–0.2 nm/s and occurs by an island (three-dimensional) growth mechanism. For this reason OAMS films usually contain substantially fewer stacking faults and the accompanying dislocation loops (a rough estimate based on the HREM data gives 10^9 lines/cm^2) than for the PLD film. The block domains in the OAMS films are usually larger in size—up to 250 nm, the interblock boundaries are more ordered and equidistant, and the azimuthal misorientation angles are less than a degree.[22] The average density of threading EDs in the OAMS films is somewhat lower than in the PLD films, around 10^{10} lines/cm^2. One should expect similar characteristics for the K6300 film, even though $j_c(H=0, T=77\ \text{K})$ for this particular film is only 1×10^6 A/cm^2, which is smaller than that for the OAMS films by a factor of 2.5–3.

2.2. Methods of measurement of the critical current

The measurements of $j_c(T, H, \theta)$ for all the films were made at temperatures $T \geqslant 77$ K. Low static magnetic fields were used in the measurements: 0.5 T or less for the inductive measurements, and 1 T or less for the transport measurements.

Measurements of j_c in the PP8, P532, and TN2 films were made by the contact-free low-frequency magnetic susceptibility method at a frequency of 937 Hz. This method is based on analysis of the dependence of the imaginary part χ'' of the magnetic susceptibility of a thin film on the amplitude of an alternating magnetic field h_{ac} perpendicular to the film plane. It has been shown[23] that $\chi''(h_{ac})$ has a maximum at a certain value $h_{ac} = h_m$. For a film in the form a disk the relation between j_c and h_m is described by the expression $j_c = 1.030 h_m / d$, where d is the film thickness. This same expression also gives a good description of the results of experiments on films of other isometric shapes, including square films.[24] The amplitude h_{ac} was varied over the range 0.001–5 mT. The detection system included an SR-830 lock-in amplifier connected to a computer. The maximum of $\chi''(h_{ac})$ was determined by approximating $\chi''(h_{ac})$ near the maximum by a second-order polynomial. A static magnetic field **H** (up to 0.5 T) oriented in the horizontal plane was produced either by a system of Helmholtz coils with a vertical axis of rotation (field of 0.0001–0.05 T) or by a resistive electromagnet with an iron yoke (field of 0.002–0.5 T). In the first case the axes of the launching and receiving coils of the detection system and the orientation of the film sample were fixed, and in the second case the launching and receiving coils were rotated together with the sample mounted in them. Thus in both versions only the angle between the static magnetic field and the normal to the film plane were measured (to an accuracy of $\pm 3°$). The alternating magnetic field inducing the supercurrent, on the other hand, always coincided with the normal to the film. Consequently, the induced currents were circular and always remained in the film plane. They had components both perpendicular and parallel to the plane in which the applied magnetic field was rotated. Thus, unlike the transport measurements of $j_c(H, \theta, \varphi)$, in these measurements the angle φ is undetermined. However, since according to the data of Ref. 8 the $j_c(H, \theta)$ curves for $\varphi = 0$ and 90° are qualitatively similar and only slightly different quantitatively, one would expect that the $j_c(H, \theta)$ curves obtained by the contact-free inductive method will reflect the features of the θ dependence of $j_c(H, \theta, \varphi)$ and, in particular, those which are due to the specifics of the penetration of in-plane vortices into a thin film. Meanwhile, it would be helpful to do a more detailed theoretical analysis of the inductive method of measuring j_c in a static magnetic field inclined to the plane. That will not be done in this paper.

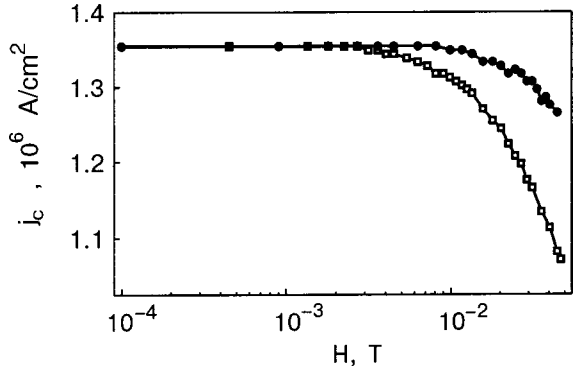

FIG. 1. Magnetic-field dependence of the critical current density at $T=77$ K in the film PP8 for magnetic field directions perpendicular ($\theta=0$) (□) and parallel ($\theta=90°$) (●) to the film plane.

The value of $j_c(H,\theta)$ in the OAMS film K6300 was determined by measuring the current–voltage characteristics during passage of a transport current (four-probe configuration). For making the transport measurements, narrow (250 μm wide) bridges with eight contact pads were prepared from the film by a photolithographic technique. The current passed only perpendicular to the plane in which the applied magnetic field rotated upon variation of the angle θ (i.e., $\varphi=90°$). A serious shortcoming of the apparatus used for the transport measurements of $j_c(\theta,H)$ was the impossibility of working with fields below 0.03–0.04 T.

2.3. Results of the measurements

The magnetic-field dependence of j_c for the film PP8 at a temperature of 77 K is shown in Fig. 1 for parallel and perpendicular field directions. The analogous curves for the films P532 and TN2, only in a wider interval of static magnetic fields and for the field orientations $\theta=0$, 45, 70, 80, and 90°, are shown in Figs. 2 and 3, respectively. It is seen that the $j_c(H,\theta=\text{const})$ curves are superficially similar to each other for all of these films and all orientations of the field and are also similar to that which was observed in Refs. 16 and 18–20 at $\theta=0$. There is also a relatively wide ''plateau'' at $0\leqslant H\leqslant H_m$ where j_c is independent of H. After that there is a certain transition region, followed by a rather steep drop of $j_c(H)$. For $\theta=0$ the fall of $j_c(H)$ on the ''steep'' part is close to linear in a semilogarithmic plot (linear in j_c and logarithmic in H).

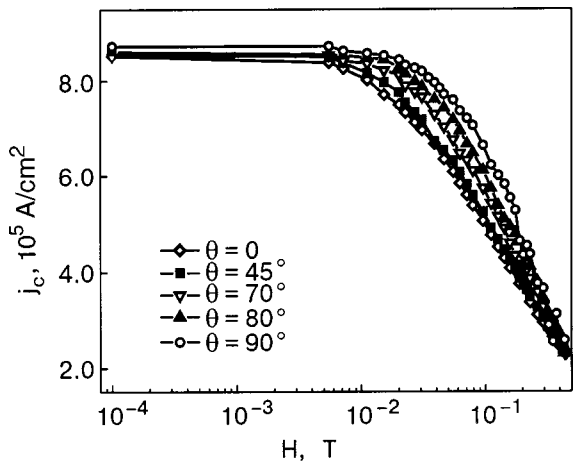

FIG. 2. Magnetic-field dependence of the critical current density at 77 K in the film P532 for magnetic field directions at angles $\theta=0$, 45, 70, 80, and 90° to the normal to the film. The scatter of the curves for different θ at low fields reflects the error of measurement.

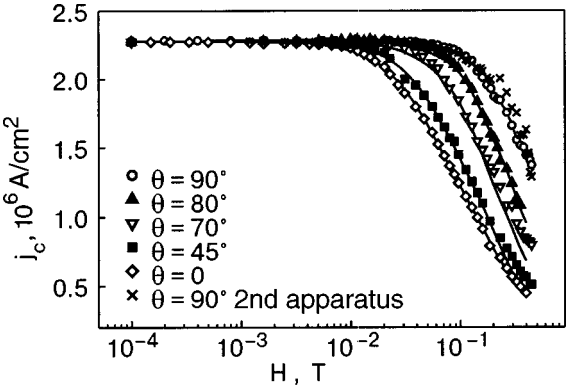

FIG. 3. Magnetic-field dependence of the critical current density at $T=77$ K in the film TN2 for different angles θ between the magnetic field direction and the normal to the film. The key to the symbols for $\theta=0$, 45, 70, 80, and 90° is given in the figure. For $\theta=90°\pm3°$ the results of two different measurements using two different apparatus for measuring the angles are shown by the circlets and crosses. The curves for $\theta=0$ and 90° are drawn through the experimental points, while those for $\theta=45$, 70, and 80° are constructed according to formula (5) with the use of interpolated experimental curves for $j_c(H,\theta=0)$ and $j_c(H,\theta=90°)$.

As was mentioned in Ref. 16, there are two types of c-oriented YBCO epitaxial films. In the higher-current type (with $j_c(H=0,T=77\text{ K})\approx(1.5–3)\times10^6$ A/cm^2) the transition from the plateau to the logarithmic part is of the nature of a sharp kink. This kink has been attributed[16] to a change of the mechanism limiting j_c from one imposed by the transparency to supercurrent of the interblock boundaries to one imposed by the depinning of the ensemble of mutually interacting vortices pinned on threading edge dislocations at low-angle interblock boundaries. For films with a somewhat lower (although still extremely high) critical current density this transition is smoother and is described in terms of only the second of the j_c-limiting mechanisms mentioned above. For films of this latter kind it is convenient to characterize the width of the low-field plateau H_m by the value of the field at the point of intersection of the asymptote to the plateau with the extension of the linearly falling (in the semilog plot) part of $j_c(H,\theta)$.

As is seen in Figs. 1–3, the films PP8, P532, and TN2 at $\theta=0$ have moderately large values of $j_c(H=0,\ T=77\text{ K})=1.35\times10^6$, 8.6×10^5, and 2.28×10^6 A/cm^2, respectively, and the transition to the logarithmic part of the curve is quite smooth. The curves for the different field directions $0<\theta<90°$ differ in that the plateau becomes progressively wider with increasing θ, and in the case when the field lies in the film plane ($\theta=90°\pm3°$) the plateau is 2.5–3 times wider than for $\theta=0$. With increasing θ the $j_c(H,\theta)$ curves for all the films are shifted almost parallel to one another on a semilog plot, to higher fields relative to $j_c(H,\theta=0)$. A more careful examination reveals that the slope of the curves increases somewhat (see, e.g., Fig. 2). This behavior of the curves means that they can be obtained from each other only approximately by a scaling of the magnetic field, i.e., by

multiplying the fields at which they attain the same value of j_c by a certain factor which increases with increasing θ. For all the curves with $\theta \neq 0$ this factor varies, albeit weakly, as a function of $j_c/j_c(H=0)$. The deviation of the curves from a "parallel shift" on a semilog plot is especially noticeable for $\theta=90°$ at $j_c/j_c(H=0) \leqslant 0.9$. For example, in the film PP8 (Fig. 1) the curve for $\theta=90°$ can be obtained to a fair approximation from the curves for $\theta=0$ by multiplying the fields at which they attain some value of j_c by a factor of 2.75 ± 0.15. It can be obtained more precisely by multiplying by a factor that varies from 2.9 for $j_c/j_c(H=0) \to 1$ to 2.6 for $j_c/j_c(H=0)=0.93$. For the film P532 the "scaling factors" for the field are 2.75, 2.63, 2.24, and 1.51 for $j_c/j_c(H=0)=0.95$, 0.9, 0.75, and 0.5, respectively. Thus, strictly speaking, there is no logarithmic segment on the falling part of the $j_c(H,\theta=90°)$ curve, and its absence is increasingly obvious the larger the level of fall one is analyzing.

Let us discuss the differences between the $j_c(H,\theta)$ curves obtained for films of substantially different thickness. The results for the film TN2 (Fig. 3) are essentially similar in type on a qualitative level to those shown for film PP8 in Fig. 1 or film P532 in Fig. 2. Granted, the value of $j_c(H=0, T=77\ \text{K})$ is noticeably higher for TN2 than for PP8 or P532, and the transition from the plateau to the logarithmic part of $j_c(H)$ for $\theta=0$ is somewhat sharper for TN2 than for the other two films. But the intersection of the linear asymptote to the logarithmic part of the curve with the continuation of the plateau (the line $j_c=j_c(H=0)$) gives practically the same value of H_m for all three films: $H_m(T=77\ \text{K}) \approx 0.01$ T. And here the width of the plateau in a "parallel" field ($\theta=90°$) is substantially wider for the film TN2 than for PP8 and P532. Deviations from $j_c(H=0)$ start to appear only for 0.08 T, and the analog of the intersection of the asymptotes takes place at 0.15–0.20 T, while for PP8 and P532 the corresponding values are 0.017–0.02 and 0.025–0.03 T, respectively.

It is of interest to discuss in more detail the behavior of $j_c(H,\theta=90°)$ on the falling part. This part of the curve was specially taken twice on two different apparatus for measuring the angles between the field direction and the normal to the film plane. Both sets of points are shown in Fig. 3. It is seen that one of them is somewhat closer to parallel transport (with a slightly increasing steepness) of the curve for $\theta=0$ in semilogarithmic coordinates. At the same time, the second set, which should differ from the first only in a possible difference of the orientation of the magnetic field within the error limits of its adjustment is actually noticeably different from it and has a sharp rise in steepness. A detailed discussion of the nature of $j_c(H,\theta=90°)$ will not be given in this paper. We note only that the correct investigation of the details of its behavior (specifically for the given field orientation) apparently requires more precise control of the alignment of the field orientation in the film plane than was realized in taking the data of Figs. 1–3.

Figure 4a shows the angular dependence of j_c for the films P532 and PP8 at 77 K in a field of 0.047 T. The analogous curves obtained at a temperature of 83 K are shown in Fig. 4b. We see that the $j_c(\theta)$ curves of both films at the two temperatures at which the measurements were made each

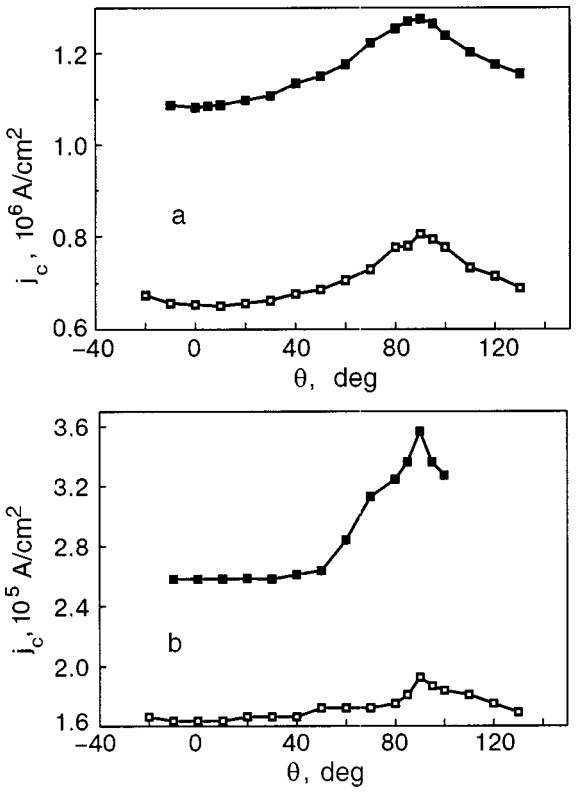

FIG. 4. Angular dependence of $j_c(H=0.047\ \text{T},\theta)$ in the films PP8 (■) and P532 (□) for $T=77$ K (a) and 83 K (b).

have a maximum at $\theta=90°$, with a value of j_c at the maximum which is somewhat less than $j_c(H=0)$. This character of the $j_c(H=\text{const},\theta)$ curves in a field exceeding the width of the plateau of the magnetic-field dependence both for $\theta=0$ and for $\theta=90°$ would be expected on the basis of the $j_c(H,\theta=\text{const})$ curves for different values of θ. For comparison of the character of the $j_c(\theta)$ curves obtained at different temperatures it is convenient to plot these curves normalized to their maximum value at each of the temperatures. The $j_c(\theta)$ curves at temperatures of 77 and 83 K are presented in such a form in Fig. 5a (film PP8) and Fig. 5b (film P532). It is seen that the normalized curves for these films behave differently with changing temperature. For the film PP8 the total variation of the normal angular dependence of j_c in a field of 0.047 T is noticeably stronger at 83 K than at 77 K, while for film P532 their relationship is just the opposite. This situation most likely reflects the fact that the widths of the plateaus and of the transition regions from the plateaus to the logarithmic magnetic-field dependence of $j_c(H,\theta=0)$ in the given samples have different ratios to the field 0.047 T at which the measurements of the angular dependence were made. Furthermore, these films apparently also have different coefficients in the temperature dependence of the of the plateau widths in terms of the reduced temperature. According to the data of Ref. 16, and in accordance with the model developed in that paper, the change of the plateau width is proportional to the change in temperature, $\tau=(1-T/T_c)$. We shall not analyze the temperature dependence of the total variation of $j_c(H,\theta)$ in more detail but shall discuss only the main aspects of the results.

Figure 6 gives the $j_c(H=\text{const},\theta)$ curves for the film TN2 at a temperature of 77 K for several different values of

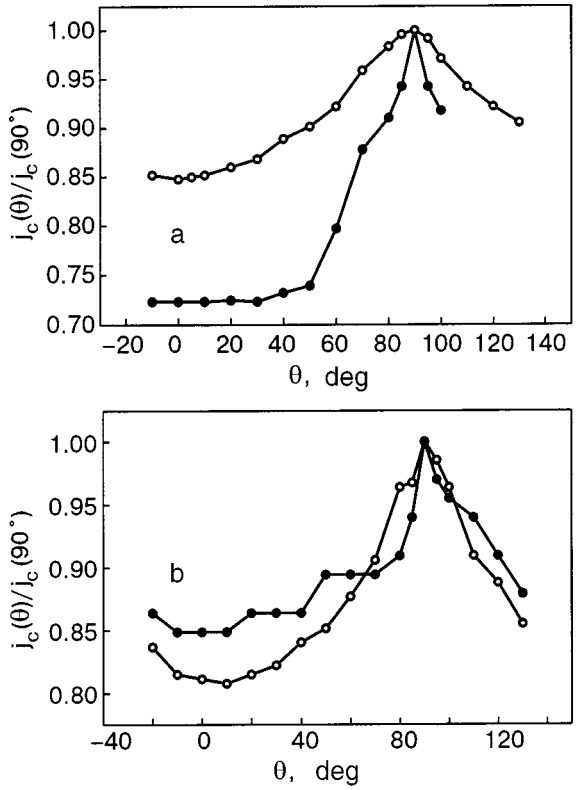

FIG. 5. Angular dependence of j_c normalized to the maximum value at $\theta = 90°$ in a magnetic field $H = 0.047$ T at temperatures of 77 K (○) and 83 K (●) for films PP8 (a) and P532 (b).

H. As for the other films investigated in the present study, these curves have a single maximum at $\theta = 90°$. It is seen that the peak at $\theta = 90°$ becomes sharper as the field at which the curves are measured is increased. These characteristics are in complete agreement with the $j_c(H, \theta = \text{const})$ curves shown in Fig. 3.

The curves of the field dependence and angular dependence of $j_c(H, \theta)$ for the OAMS film K6300, with the same nominal thickness as for PP8 and P532, were obtained from the data of transport measurements; they are of a provisional nature and were taken in order to show their qualitative difference from the curves obtained by the inductive method for the films PP8, P532, and TN2. The curves of $j_c(H, \theta$

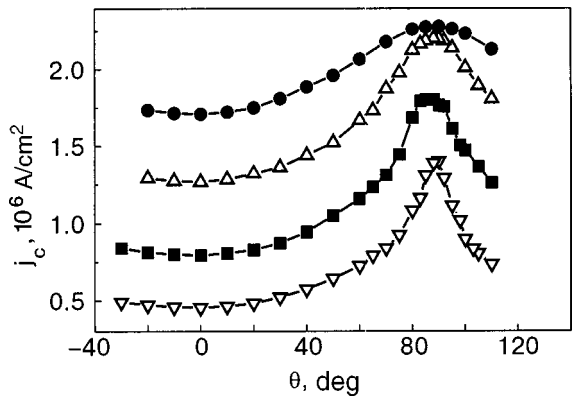

FIG. 6. Angular dependence of $j_c(H, \theta)$ in the film TN2 at 77 K for a series of fixed values of H [T]: 0.05 (●), 0.1 (△), 0.2 (■), 0.4 (▽). The curves are drawn through the points.

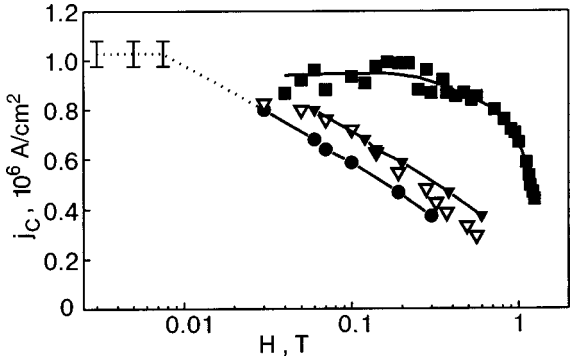

FIG. 7. Magnetic-field dependence of the critical current density of the magnetron-deposited film K6300 for $\theta = 0$ (●), 60° (▽), and 90° (■), obtained by transport measurements at 77 K. The dotted line shows a hypothetical continuation of the curve for $\theta = 0$ into the region $H \leqslant 0.03$ T. Lines have been drawn through to the points corresponding to $\theta = 0$ and 90° as a guide to the eye. For comparison with the curve obtained at $\theta = 60°$ the points calculated according to Eq. (4) have been plotted (▼) and a line drawn through them.

$= \text{const}$) for $\theta = 0$, 60, and 90° are shown in Fig. 7. They were obtained for $H > 0.03$ T, and therefore do not allow one to trace the presence and width of the low-field plateau for $\theta = 0$ and 60°. The measurements made by the inductive method on the other OAMS films show that the low-field plateau of $j_c(H, \theta = 0)$ in them is usually narrower than in the laser deposited films, apparently because of the larger sizes of the single-crystal blocks. The dotted line in Fig. 7 shows the hypothetical continuation of the $j_c(H, \theta = 0)$ curve to low fields under the assumption that $H_m = 0.005–0.01$ T. From this we can conclude that in the region where $j_c(H, \theta = 90°)$ varies slowly with field (against the background of the measurement error), i.e., $0.04 \text{ T} < H < 0.4$ T, the values of j_c are practically equal or at most 5–10% less than the value of $j_c(H = 0)$. Consequently, this region of constant (within the error limits) values of $j_c(H, \theta = 90°)$ is a plateau for this field orientation. The deviations from it become appreciable only in fields above 0.3–0.4 T, and one can speak of an ''intersection of the asymptotes'' in a field of 0.7–0.8 T. Thus the plateau on the $j_c(H, \theta = 90°)$ curve for the film K6300 is anomalously wide, an order of magnitude wider than for the laser-deposited films of the same thickness. Curves of the angle dependence $j_c(\theta)$ obtained on this film at 77 K in fields of 0.19 and 0.3 T are shown in Fig. 8. It is seen that the tops of the peaks of $j_c(\theta)$ at $\theta = 90°$ are not sharp: the change in j_c from $\theta = 90°$ to the nearest adjacent experimental points (80° and 100°) is too small for the peak at $\theta = 90°$ to be assumed to be narrow and sharp like the peak observed[25] for Nb–Ti films. Consequently, the anomalously wide low-field plateau on the $j_c(H, \theta = 90°)$ curve for the film K6300 is not due to an ''accidental'' coincidence with a narrow peak of $j_c(H = \text{const}, \theta)$ at an exact orientation $\theta = 90°$ during the measurements of $j_c(H, \theta = 90°)$.

At the present time we cannot say conclusively whether or not the observed anomaly of $j_c(H, \theta = 90°)$ is due to general properties of OAMS films or to features of our particular sample. It cannot be ruled out that it is a manifestation of differences in the inductive and transport methods of measuring the critical current in a static field lying in the film plane. Measurements of the angle dependence of the critical

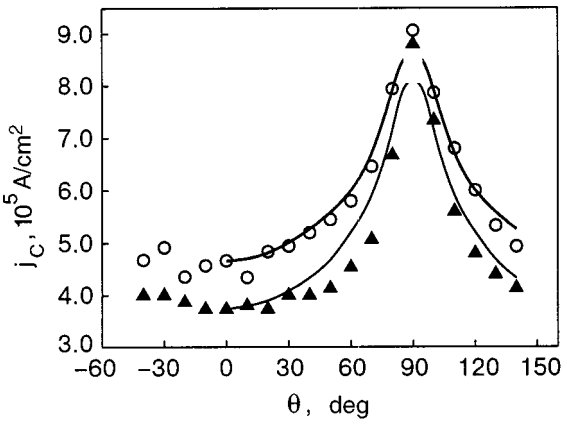

FIG. 8. Angular dependence of $j_c(\theta)$ obtained by a transport method on the film K6300 at 77 K in magnetic fields of 0.19 T (○) and 0.30 T (▲). The points are experimental. The lines have been drawn according to the equation $j_c(H,\theta)=j_c(H\cos\theta),\theta=0)$ with the use of the $j_c(H,\theta=0)$ dependence found experimentally.

current in OAMS films, including K6300, will be continued, and an experimental comparison of the two methods of measurement will be done on the same film. The results of these additional studies and their theoretical analysis will be published separately.

3. DISCUSSION OF THE EXPERIMENTAL DATA AND THEIR QUALITATIVE INTERPRETATION

As we know, the first critical field H_{c1}^{bulk} of a type-II superconductor corresponds to the start of penetration of Abrikosov vortices into a spindle-shaped sample magnetized along the axis or into a disk-shaped sample magnetized in the plane. Here the smaller of the dimensions of the sample should be much greater than λ. For anisotropic superconductors of the HTSC type, H_{c1}^{bulk} will furthermore take on the value $H_{c1,\perp}^{\text{bulk}}$ or the value $H_{c1,\parallel}^{\text{bulk}}$ in cases when the magnetizing field is directed perpendicular to or parallel to the axis of anisotropy of the superconducting properties of the substance (the c axis in the case of YBCO). For a transverse orientation of the external magnetic field **H** with respect to the plane of a thin c-oriented HTSC film of thickness $d\ll D$ (where D is the longitudinal dimension of the film), the external field necessary for the start of vortex penetration is much less than $H_{c1,\parallel}^{\text{bulk}}$ because of the demagnetizing effect (the demagnetizing factor is close to unity) and is approximately equal to

$$H_{c1}^{\text{film}}\approx\sqrt{\frac{d}{D}}H_{c1,\parallel}^{\text{bulk}}. \tag{1}$$

Here $H_{c1,\parallel}^{\text{bulk}}$ is the anisotropic analog for HTSCs of the quantity $H_{c1}^{\text{bulk}}=\phi_0\ln\kappa/4\pi\lambda^2$, where $\kappa=\lambda/\xi=\lambda_0/\xi_0$ is the Ginzburg–Landau parameter ($\kappa\gg1$ in cuprate HTSCs), $\xi=\xi_0\tau^{-1/2}$ is the coherence length, and $\phi_0=hc/2e$ is the magnetic flux quantum. For YBCO the parameter $\lambda_0\approx150$ nm and the parameter $\xi_0\approx1.5$ nm, so that $\kappa\approx100$. AT a temperature $T=77$ K for $T_c=92$ K, when $\tau\approx0.16$, $\lambda\approx380$ nm, and $\xi\approx3.8$ nm, the first critical field of a bulk sample $H_{c1}^{\text{bulk}}(T=77\text{ K})\approx5$ mT. According to Eq. (1), for the investigated films, with thicknesses $d\approx100-300$ nm and a longitudinal dimension $D\approx10$ mm, we obtain the estimate $H_{c1}^{\text{film}}(T=77\text{ K})\approx(0.5-1.0)\times10^{-4}$ T, which is comparable to the Earth's magnetic field and one to two orders of magnitude smaller than the width of the low-field plateau H_m on the $j_c(H,\theta=0)$ curve. It is important to note that, starting at low fields of 2–3 times H_{c1}^{film} (i.e., fields slightly larger than the Earth's magnetic field at 77 K or fields of 1–2 mT at 4.2 K), the magnetic induction B in a transversely magnetized film with $d\ll D$ is equal in magnitude to the applied external field. This corresponds to an appreciable density of Abrikosov vortices in the film, equal to H/ϕ_0, starting at extremely low fields. In addition, it must be taken into account that for $d\leqslant2\lambda(T)$ the magnetic field penetrates almost completely into the film, so that $B\approx H$ for any field direction, even when there are no vortices penetrating the film.

In the case of a longitudinal orientation of **H** the corresponding coefficient of the magnetization tensor is equal to zero, and the magnetic field flows around the film, penetrating into it from both sides to a depth of λ. The formation of vortices in the film becomes unfavorable. As was shown in Refs. 26 and 27, the external field necessary for the first chain of vortices to penetrate into a film of thickness $d<2\lambda$ will be much greater than $H_{c1,\perp}^{\text{bulk}}$, and for an isotropic superconductor it is given by the expression

$$H_{c1}^{(1)}(d)\approx\frac{2\phi_0}{\pi d^2}\ln\left(\frac{d}{\xi}\right)\equiv8\left(\frac{\lambda_0}{d}\right)^2H_{c1}^{\text{bulk}}(T\to0)\times\left(1+\frac{\ln(d/\lambda_0)+\ln(\tau)/2}{\ln\kappa}\right). \tag{2}$$

We see that $H_{c1}^{(1)}(d)\gg H_{c1}^{\text{bulk}}$. However, for cuprate HTSCs it is also necessary to take into account the strong anisotropy of the superconducting properties due to the layered structure of these compounds. As a consequence of this anisotropy, the magnetic field penetration depth along the c axis, λ_c, is much larger and the coherence length ξ_c much smaller than the corresponding parameters λ_{ab} and ξ_{ab} in the layer plane ab. As a result, the critical field for penetration of Abrikosov vortices into a HTSC film with $d<\lambda_{ab}$ in the case of a longitudinal field orientation will be

$$\tilde{H}_{c1}(d)\approx\frac{2\phi_0}{\pi d^2\Gamma}\ln\left(\frac{d}{\xi_c}\right), \tag{3}$$

where $\Gamma=\lambda_c/\lambda_{ab}$ is the anisotropy parameter, and $\xi_c(T)=\xi_0/(\Gamma\sqrt{\tau})$. For YBCO, according to published data, $\Gamma\approx5-7$. The value of $\tilde{H}_{c1}(d)$ depends weakly on temperature in the temperature interval corresponding to $\tau>0.1$. As an estimate we get $\tilde{H}_{c1}(d)\approx0.013-0.017$ T for films of thickness $d\approx300$ nm and $\tilde{H}_{c1}(d)\approx0.12-0.15$ for films with $d\approx100$ nm.

At low longitudinal fields $H<\tilde{H}_{c1}(d)$ the magnetic field lines envelop the superconducting film, penetrating into it from both sides to a depth λ, but the tangential component of the field does not enter the film in the form of vortices. In a field **H** inclined to the film plane the magnetic flux can pass all the way through the film (in the form of Abrikosov vortices perpendicular to the film and with a length $l\approx d$) on account of the transverse component of the magnetic field, $H_\perp=H\cos\theta$. Vortex penetration will be energetically favorable at places where there are linear edge dislocations thread-

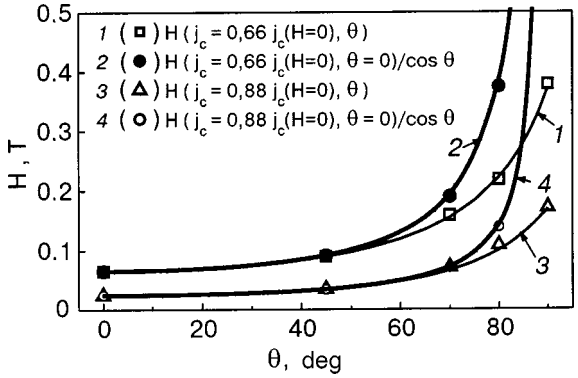

FIG. 9. Values of the fields at which $j_c(H,\theta)$ amounts to 66% (□) and 88% (△) of $j_c(H=0)$ for different θ. Curves *1* and *3* were drawn through the experimental points as a guide to the eye. Curves *2* and *4* correspond to fields for which the values of $j_c(H,\theta=0)$ amount to 66% and 88% of their zero-field value divided by cos θ; ●, ○ are the values of the angles at which the data in Fig. 3 were obtained.

ing completely through the film and having nonsuperconducting cores parallel to the *c* axis. Core pinning of vortices will take place at the cores of these edge dislocations, in accordance with the mechanism considered in Refs. 16 and 17 for pinning in a transverse magnetic field. The role of the transverse field in the present case will be played by the field component perpendicular to the film, $H_\perp$. The tangential component of the field near the surface of the film must, of course, vary continuously. Satisfaction of this requirement causes bending of the field lines of the magnetic flux trapped by a vortex near the surface of the film, and the length of that part of the the vortex along which its core coincides with the core of the edge dislocation is shortened somewhat in comparison with d. Because of this, the vortex pinning force on threading EDs should be weakened slightly with increasing θ.

If one ignores this weakening of the pinning force, then for $H<\tilde{H}_{c1}(d)$ the angular dependence of $j_c(H,\theta\neq 0)$ will be determined by the field dependence of $j_c(H,\theta=0)$ studied in Refs. 16, 18, and 19, but now as a function of $H_\perp$ instead of H, i.e.,

$$j_c(H,\theta)=j_c(H_\perp,\theta=0). \tag{4}$$

The estimates of $\tilde{H}_{c1}(d,T=77\ \mathrm{K})$ made above show that a large part of the field interval in which the data of Figs. 1–3 were obtained corresponds to the condition $H<\tilde{H}_{c1}(d)$. This allows one to check whether relation (4) holds. Such a check for the film TN2 is shown in Fig. 9, which shows plots of the θ dependence of the values of the magnetic fields at which $j_c(H,\theta)$ takes on certain values. As these values we have chosen 1.5×10^6 A/cm^2 and 2×10^6 A/cm^2, which correspond to 0.66 and 0.88, respectively, times the value of $j_c(H=0,\ T=77\ \mathrm{K})=2.27\times10^6$ A/cm^2. Curves *2* and *4* in this figure correspond to the functions $2\times10^6/\cos\theta$ and $1.5\times10^6/\cos\theta$, which reflect relation (4). We see that for $j_c(H,\theta)=0.88j_c(H=0)$ relation (4) holds well in the angular interval $0<\theta<70°$, while for $j_c(H,\theta)=0.66j_c(H=0)$ it holds in a somewhat narrower interval $0<\theta<50°$. The fields at which the deviations from relation (4) appear correspond to values which are lower than the above estimate of $\tilde{H}_{c1}(d=90\ \mathrm{nm})$ by a factor of 1.5–2. The probable reason for this is the decrease of the pinning force on a vortex perpendicular to the film because of the bending of the magnetic field lines of the flux trapped by the vortex and, accordingly, the bending of the core of the vortex in the subsurface region of the film.

In addition, one notices the circumstance that both for the films PP8 and P532 (see Figs. 1 and 2) and for TN2 (Fig. 3) the decrease of $j_c(H,\theta=90\pm3°)$ with increasing field begins at considerably lower values of the field (by a factor of about 1.5–3) than the values of $\tilde{H}_{c1}(d)$ corresponding to these films, where in-plane vortices begin to enter the film. Of course, the penetration of the film by in-plane vortices need not automatically lead to a decrease in $j_c(H,\theta=90°)$. They may be strongly pinned, and the plateau at $j_c(H,\theta=90°)$ may extend to even higher fields. But the falloff of $j_c(H,\theta=90°)$ in fields less than $\tilde{H}_{c1}$ requires explanation. The possible error in the above estimate of $\tilde{H}_{c1}$ may lessen the disagreement a little but cannot eliminate it.

The decrease in j_c in a magnetic field parallel to the film plane under conditions when the vortices due to that field cannot yet enter the film is probably due to the influence of the in-plane field on the pinning conditions for vortices perpendicular to the film which have been created by the magnetic field of the measuring current flowing through it. They will also be pinned by threading edge dislocations. Here, too, one should take into consideration the same near-surface bending of the magnetic field lines of the total (external and current-induced) flux trapped by a vortex normal to the film. This bending decreases the length along which the core of the ED is coincident with the core of the vortex. As a result, the pinning of these vortices will be weakened, leading to a decrease of j_c. In this paper we will not go into the details of the above-described mechanism for the weakening of the pinning of vortices threading the film by a longitudinal field. However, if such a mechanism is indeed realized, then the magnetic-field dependence of the critical current density for an arbitrary direction of the field θ should be described not by relation (4) but by a modification of it:

$$j_c(H,\theta)=j_c(H_\perp,\theta=0)\frac{j_c(H_\parallel,\theta=90°)}{j_c(H=0)}, \tag{5}$$

where $H_\parallel=H\sin\theta$.

A check of relation (5) for the film TN2 is shown in Fig. 3. The functions $j_c(H,\theta=0)$ and $j_c(H,\theta=90°)$ are found by interpolation from the lines drawn through the experimental points for $\theta=0$ and 90°. These were then used to construct curves corresponding to Eq. (5) for $\theta=45°$, 70°, and 80°. It is seen that within the error limits of the measurements the experimental points in Fig. 3 lie on the curves constructed for the corresponding angles. A slight disagreement can be observed in the highest-field part of the curve for $\theta=45°$. It is lessened considerably if the function for $j_c(H,\theta=90°)$ is constructed by interpolation of the points corresponding to the second angle-measuring apparatus, which are shown by the crosses in Fig. 3.

Thus the above comparison shows that the widening of the plateau on $j_c(H,\theta=\mathrm{const})$ when the field is inclined is due to the decrease of $H_\perp$ with increasing θ. Nevertheless, the widening of the plateau for $H\to90°$ is limited. Here, unlike the case of a magnetic field perpendicular to the film,

when the ''effective pinning'' plateau extends to fields at which a certain density of Abrikosov vortices threading the film is reached, the end of the low-field plateau in a field parallel to the film occurs under conditions such that the film is not penetrated by vortices parallel to it, or at least the end of the plateau is not caused by such vortices. It is brought about by the weakening of the pinning of vortices normal to the film, most likely created by the field of the measuring current, in an in-plane magnetic field.

A check of the applicability of expression (5) was done for the data of Fig. 2 and for the data of Fig. 3 and gave excellent results.

Let us now consider the possible consequences of relations (3)–(5) for the angular dependence of $j_c(H=\text{const},\theta)$ obtained in various fixed fields, as is most often done in measurements of this kind. As we have said, the $j_c(H,\theta=0)$ curves in thin epitaxial films of YBCO are characterized by the presence of a rather wide plateau in low fields $H<H_m(T)$. Over the extent of this plateau one has $j_c(H)=j_c(H=0)=j_c^{(0)}=\text{const}$. According to Ref. 16, the value of $H_m(T)$, which characterizes the width of the plateau, depends linearly on the reduced temperature τ, at least within the domain of applicability of the Ginzburg–Landau model. We note that for $H<H_m(T)$ the density of vortices is not yet very high, and all the vortices are pinned on edge dislocations at the interblock boundaries. A single-particle mechanism of core pinning of the vortices on the cores of EDs, which was examined in Ref. 17, is realized. In higher fields $H>H_m(T)$ a falloff of $j_c(H,\theta=0)$ occurs, which is approximated over a rather wide interval of fields by the relation $j_c(H,\theta=0)\approx\alpha\ln(H^*/H)$, where $H^*=H_m e^{1/\alpha}$, $\alpha\approx\text{const}$ (for different samples α has a value of 0.22 ± 0.02). Since $H_m(T)$ is always much greater than H_{c1}^{film}, the main part of the plateau and, especially, the region of the falloff of $j_c(H)$ correspond to a finite density of Abrikosov vortices perpendicular to the film plane. In the region $H>H_m(T)$ the interaction between vortices become important. The position of the vortices relative to one another is correlated, and eventually a vortex lattice forms. The relative number of vortices pinned on EDs begins to decrease.

According to the model developed in Ref. 16, in which Abrikosov vortices are accidentally trapped by pinning centers (the cores of EDs) in c-oriented epitaxial films with a random distribution of sizes of the single-crystal blocks, H_m depends on their average linear dimension $\langle L\rangle$. The value of H_m increases with decreasing $\langle L\rangle$ as $\langle L\rangle^{-2}$, so that the relationship between H_m and $\tilde{H}_{c1}(d)$ can be different in different films. Here the form of relation (4) or (5) will depend substantially on the relationship between the values of H_m and $\tilde{H}_{c1}(d)$ and also on the relationship between the Lorentz force $F_L=(\phi_0/c)j$ and the local force F_p of core pinning of a vortex on an ED.

Let us first consider the case $H_m(T)<\tilde{H}_{c1}(d)$, which is realized in the films studied here. It should generally be the case for thin epitaxial films of YBCO with relatively large single-crystal domains, $\langle L\rangle\geqslant 20-25$ nm in size, and at temperatures relatively close to T_c ($T\geqslant 77$ K), so as to satisfy the condition $d\leqslant 2\lambda(T)$. Under these conditions one should observe no angular dependence at low fields $H<H_m$, i.e., $j_c(\theta)=j_c^{(0)}=\text{const}$, in accordance with the single-particle mechanism of vortex pinning on EDs in the plateau region. Angular dependence should arise at higher fields, lying in the interval $H_m(T)<H<\tilde{H}_{c1}(d)$. In this interval the longitudinal component of the field, $H_\parallel=H\sin\theta$, penetrates into the film, since $d\leqslant 2\lambda(T)$, but it does not create vortices parallel to the film. However, for values of the transverse component of the field $H_\perp>H_m$, which holds in an angular interval $0\leqslant\theta\leqslant\theta_m$, where θ_m is determined by the relation

$$\cos\theta_m=H_m(T)/H, \tag{6}$$

the field dependence $j_c(H_\perp,\theta=0)$ now corresponds to the falling part of the curve. With increasing θ (for $\theta\leqslant 90°$) the transverse component $H_\perp=H\cos\theta$ decreases and $j_c(\theta)$ increases to a maximum for $\theta>\theta_m$, where $H_\perp$ again becomes less than H_m and $j_c(\theta)\to j_c^{(0)}$. Consequently, in this field interval one should observe a minimum of $j_c(\theta)$ at $\theta=0$ and a maximum at $\theta=90°$. The value of $j_c(\theta>\theta_m)$ at the maximum of the angular dependence will be equal to or less than $j_c^{(0)}$ on account of the weakening of the flux pinning perpendicular to the film as a result of the bending of the vortices in the subsurface region of the film due to the presence of the tangential field component. As the field at which the measurements of $j_c(\theta)$ are made is increased, the maximum near $\theta=90°$ should become progressively narrower but lower. At low fields (or small angles θ), i.e., in the region where the flux pinning is not yet weakened substantially by the bending of the threading vortices due to the longitudinal component of the field and that effect can be neglected, the $j_c(\theta)$ curve can be obtained from $j_c(H,\theta=0)$ with the use of relation (4). At higher fields (at larger angles) one should use relation (5). These conclusions accord with the experimental data in Figs. 4–6 and agree qualitatively with the data in Fig. 8.

At the same time, the data presented in Fig. 8, unlike the data of Figs. 4–6, do not show any lowering of $j_c(\theta=90°)$ as the field is increased from 0.19 to 0.3 T and, judging from Fig. 7, $j_c(\theta=90°)\approx j_c^{(0)}$ in these fields, even though fields from 0.19 to 0.3 T correspond to the condition $H\geqslant\tilde{H}_{c1}(d)$ and one would expect an additional contribution to the lowering of $j_c(H,\theta=90°)$ as a result of the possible depinning of in-plane vortices which have penetrated the film. If those vortices are strongly pinned and do not give an additional contribution, the effect of the vortex bending should be preserved. However, no manifestations of it are seen in Figs. 7 and 8. The reason for this should be clarified in further studies.

At higher fields $H>\tilde{H}_{c1}(d)>H_m(T)$ in the angular region $0\leqslant\theta\leqslant\theta_m$ the minimum of $j_c(\theta)$ should be observed, as before, near $\theta=0$, and an increase of $j_c(\theta)$ should occur in the region $\theta\to\theta_m$. With further increase of θ up to 90° the trend of the curves will be determined by the relationship between $H_\parallel$ and $\tilde{H}_{c1}(d)$ and the concrete form of $j_c(H,\theta=90°)$, i.e., by the degree of weakening of the flux pinning force at threading EDs in an inclined field. The maximum of $j_c(\theta)$ near $\theta=90°$ can become quite broad and be almost smeared out. It can be acquire an additional (most likely shallow) dip at its center in the angular region where $H_\parallel>\tilde{H}_{c1}(d)$. This may occur because of depinning of the in-plane vortices that arise in this case and also because angles $\theta\geqslant\theta_m$ correspond to $H_\perp<H_m(T)$. Here $j_c(H_\perp,\theta=0)$ is independent of field, and the flux pinning force at threading

EDs, because of the bending of the vortices, tends toward a minimum value close to the pinning for a vortex perpendicular to the core of an ED.[17] The reason for the possible increase of $j_c(\theta \approx 90°)$ against the background of the lowering discussed above may be additional pinning of the curved parts of the vortices. It can occur on extended misfit EDs localized along the interface between the film and substrate and also on other extended stacking faults lying in the film plane.

We note that the pinning of in-plane vortices arising at $H_\parallel > \tilde{H}_{c1}(d)$ can be extremely strong, since these vortices should be trapped in the potential well between two Bean–Livingston barriers at the boundaries of the thin film. The depth of the potential well will depend on d/λ and, as was shown in Ref. 25, will be large for $d < \lambda$. As a result, electromagnetic pinning of longitudinal vortices arises in the film, similar to that studied in Ref. 25 in thin films of a superconducting niobium–titanium alloy. The value of $H_\perp$ will become comparable to H_{c1}^{film}, given by Eq. (1), in an extremely narrow interval of angles θ near 90°, and the transverse component of the field will no longer create threading vortices. In transport measurements with a narrow bridge the number of vortices threading the film which are excited by the transport current can become so small that their depinning will not control $j_c(\theta = 90°)$. In that case the field dependence $j_c(H, \theta = 90°)$ begins to be controlled by the electromagnetic pinning of of in-plane vortices and one should observe a narrow (fraction of a degree), high peak on the curve of $j_c(\theta)$ at $\theta = 90°$. In the inductive measurements of j_c it would seem that such a peak should be found at fields $H_\parallel$ for which the angular amplitude of the ''rocking'' of the total field, static plus induced, becomes less than the angular half-width of the $\theta = 90°$ peak (discussed above) on the $j_c(\theta)$ curve registered in transport measurements with a narrow bridge. This should correspond to fields $H_\parallel$ which are a hundred or more times higher than the amplitude of the current-inducing alternating field perpendicular to the film. Although this condition holds for the data obtained on the film TN2 (see Fig. 3) at the highest static field used, growth of $j_c(H, \theta = 90°)$ was not registered in that field region. One might try to explain the anomalous width of the plateau at $\theta = 90°$ in the transport-method data for the film K6300 (Fig. 7) by the electromagnetic pinning of in-plane vortices. However, the character of the angular curves for this film in Fig. 8 rule out the possibility of a narrow (from a fraction of a degree to a few degrees), sharp peak at $\theta = 90°$, since at angles differing from 90° by $\pm 10°$ the values of $j_c(\theta)$ in Fig. 8 are close to $j_c(90°)$. Thus, if the difference in the techniques of the transport measurements of the critical current did play a role in the radical difference of the curve of $j_c(H, \theta = 90°)$ for the films PP8, P532, and TN2 from the film K6300, they do not reduce to a matter of taking into account the ''rocking'' of the total field due to the alternating induced field, nor can the anomalous width of the plateau on $j_c(H, \theta = 90°)$ for the film K6300 be explained as a manifestation of electromagnetic pinning of in-plane vortices.

In addition, we note the following circumstance. It is known[26] that the surface barrier to the entry of in-plane vortices in fields much greater than $\tilde{H}_{c1}(d)$ may be practically absent while at the same time the barrier to their exit is high. The vortices will be held in the film by electromagnetic forces and will not leave it until the field has decreased below a certain limit. In the experiment we paid attention to the possibility of hysteresis due to this circumstance, but it was not manifested outside the error limits.

Thus the plateau on the $j_c(H, \theta = 90°)$ curve has a completely different nature than the plateau on $j_c(H, \theta = 0)$, which is due to the pinning of numerous vortices by a network of edge dislocations in low-angle boundaries between single-crystal blocks (domains). They are due to the absence of depinning of in-plane vortices because in-plane vortices do not enter the film for $H < \tilde{H}_{c1}(d)$ and such vortices are strongly pinned at higher fields and to the absence (or negligibility) of a decrease in the pinning force of vortices perpendicular to the film under the influence of an in-plane field less than a certain value. If the pinning of vortices normal to the film were not weakened because of bending of the magnetic field lines and, accordingly, of the vortex cores, then this plateau could extend to the depinning fields for in-plane vortices, which exceed the field $\tilde{H}_{c1}(d)$. Consequently, as a minimum, we can say that in the films PP8, P532, and TN2 the pinning of in-plane vortices does not determine the mechanism that limits the critical current flowing in the film plane.

The situation with the film K6300 is not yet completely clear. The above discussion shows that the decrease of $j_c(H, \theta = 90°)$ in this case also does not correspond to what would be expected if it were due to depinning of in-plane vortices. However, manifestations of a weakening of the pinning of vortices normal to the film by a field parallel to the film are absent in K6300 up to fields of 0.3–0.4 T, substantially exceeding $\tilde{H}_{c1}(d)$ and an order of magnitude greater than the fields at which these manifestations become noticeable in the films PP8 and P532, which have the same thickness as K6300. This apparently occurs for reasons related to the film growth and/or preparation for the critical current measurements and will require additional studies for clarification.

The experimental data presented in Figs. 4–6 and 8 pertain to fields in the interval $H \geqslant \tilde{H}_{c1}(d) > \tilde{H}_m(T)$. However, for all the films represented in these figures the fall of $j_c(H, \theta = 90°)$ at the fields used in the measurements is small compared to $j_c^{(0)}$, and the maxima of the $j_c(\theta)$ curves near $\theta = 90°$ are quite broad. Apparently this maximum is not two-humped. At the same time, the marked broadening of this peak to its utter disappearance can be demonstrated if the $j_c(\theta)$ curves are plotted using the data for the film P532 in fields near 0.5 T (see Fig. 2).

Let us now consider the hypothetical case when the opposite relationship holds, $H_m(T) > \tilde{H}_{c1}(d)$. It can be realized in thicker epitaxial films at temperatures for which $T \ll T_c$ and $2\lambda(T) \leqslant d$, and the average size of the domains is small, e.g., $\langle L \rangle \leqslant 10$ nm, and $H_m(T)$ is relatively large. Then in the low-field region $H < \tilde{H}_{c1}(d)$ one should observe a maximum of $j_c(H = \text{const}, \theta)$ at $\theta = 0$. It will arise because of a decrease of the pinning force for vortices normal to the film under the influence of a field component parallel to the film $H_\parallel = H \sin\theta$ that increases with increasing θ. In the lowest fields it will be so broad that there is no angular dependence

$j_c(\theta)$. It can remain so wide as to be unobservable in the whole field interval $H<\tilde{H}_{c1}(d)$. In the field interval

$$\tilde{H}_{c1}(d)\leqslant H\leqslant H_m(T), \tag{7}$$

starting with angles $\theta\geqslant\theta_1$, where θ_1 is determined from the condition

$$\sin\theta_1=\tilde{H}_{c1}(d)/H, \tag{8}$$

one has $H_{\|}>H_{c1}^{(1)}(d)$, and in-plane vortices can penetrate into the film. The flat maximum of $j_c(\theta)$ near $\theta=0$ will persist for $\theta<\theta_1$, and part of the $j_c(\theta)$ curve for $\theta\geqslant\theta_1$ will depend on the pinning conditions for these vortices. In the case of their weak pinning the fall of $j_c(\theta)$ in this region is enhanced, and the maximum at $\theta=0$ becomes more pronounced. In the case of strong pinning the entry of in-plane vortices into the film has no effect on $j_c(\theta)$, which will be governed by the depinning of vortices perpendicular to the film. In an extremely narrow angular region around $\theta=90°$ there can be a sharp peak of $j_c(\theta)$ due to electromagnetic pinning of in-plane vortices. It can be manifested under conditions such that the vortices normal to the film (including those created by the measuring current) will be absent or for some other reasons their pinning will not govern j_c.

At still higher fields and for $\theta\geqslant\theta_1$ the division into vortices perpendicular to the film that are bent near the surface and vortices lying in the plane of the film loses meaning. The bending stiffness of the vortices is enhanced, and the critical current will be governed by the depinning of inclined vortices having projections normal to and parallel to the film. Because of the presence of in-plane linear defects in epitaxial films (in particular, misfit dislocations near the interface), the mechanism of single-particle core pinning of inclined vortices on these dislocations can be turned on as the angle of inclination of the field approaches $\theta=90°$. Of course, it will be efficient if the lines of these dislocations lie in the interior of the film in the region where the vortices under discussion are situated, i.e., at distances from the interface that are at least a little less than λ and/or d. In this case at a sufficient density of in-plane dislocations an additional (no longer extremely narrow) maximum of $j_c(\theta)$ can arise at $\theta=90°$. In fields less than H_m the value of $j_c(\theta=0)$ will be equal to $j_c^{(0)}$, which gives a maximum at $\theta=0$. In larger fields $j_c(\theta=0)$ will decrease, and this maximum will be lowered to disappearance, while for $\theta=90°$ a maximum will appear. Thus in the field region $\tilde{H}_{c1}(d)\leqslant H\leqslant H_m(T)$ for films with the corresponding parameters one can observe two maxima of $j_c(\theta)$, at $\theta=0$ and 90°, or even a single maximum at $\theta=0$. It is not ruled out that this corresponds to the conditions of observation of the $j_c(\theta)$ curves in Refs. 7 and 9–12.

Thus all of the experimentally observed angular curves of $j_c(\theta)$ find qualitative explanation in the framework of simple models of flux pinning in thin HTSC films.

4. CONCLUSION

We have obtained the magnetic-field curves $j_c(H,\theta=\text{const})$ in thin ($d<2\lambda$) c-oriented epitaxial films of YBCO prepared by different technologies for magnetic fields directed at different angles to the film. We have also found the angular dependence $j_c(H=\text{const},\theta)$. We have shown that, although the magnetic-field curves are outwardly similar, having a low-field plateau in both cases, the nature of the plateau is different. When the field is perpendicular to the film the plateau arises under conditions such that a rather large number of Abrikosov vortices are present, which are pinned on a network of threading edge dislocations at low-angle boundaries between single-crystal blocks in the film. The ''effective pinning'' plateau extends to a field corresponding to the attainment of a density of vortices threading the film such that it becomes energetically unfavorable for the ensemble of mutually interacting vortices to be pinned at EDs at interblock boundaries. In a field parallel to the film the low-field plateau can be realized under conditions such that the in-plane vortices do not penetrate into the film in fields below the first critical field for a film magnetized parallel to the plane and less than 2λ thick or if such vortices have no influence on the critical current at higher fields. The end of the low-field plateau does not correspond to depinning of in-plane vortices that have penetrated into the film. The decrease of $j_c(H)$ at the end of the plateau is due to the weakening of the pinning of vortices normal to the film in a magnetic field parallel to the film. This weakening is due to bending of the normal vortices in the subsurface region of the film in the presence of an in-plane field. Because of this, the part of the vortex that is spatially coincident with the core of an edge dislocation threading the film is shortened, weakening the pinning. The low-field plateau on the $j_c(H)$ curve for an in-plane field is wider than the ''effective pinning'' plateau in the case of normal magnetization. Under those conditions the dependence of j_c on the angle between **H** and the normal to the film at a fixed field strength has a single maximum that occurs when the field lies in the plane.

In the films deposited by laser evaporation of $YBa_2Cu_3O_{7-\delta}$ or electron-beam evaporation of the components of this compound, on which j_c was measured by the inductive method, the fall of j_c with increasing in-plane field begins before the first critical field for penetration of vortices into the film is reached. For the film deposited by magnetron sputtering, on which j_c was measured by a transport method, this falloff begins in fields much higher than that critical field. The reasons for this difference most likely lie in the particulars of the deposition of a given film or of the lithographic fabrication of the narrow bridge for the transport measurements and will require additional study in order to reach a definitive conclusion. Unfortunately, simultaneous measurements by two methods, inductive and transport, were not made on any of the films. Such a comparative study is planned for the future.

We have shown that the diversity of the shapes of the angular curves $j_c(H=\text{const},\theta)$ depends on the detailed parameters of the epitaxial films of the HTSC $YBa_2Cu_3O_{7-\delta}$ with a nanostructural network of low-angle interblock dislocation boundaries (the thickness, the density of threading and in-plane EDs, the dimensions of the mosaic blocks, their misorientation angles) and the experimental conditions (temperature, field strength). The various possible combinations of film parameters relevant to the magnetic-field dependence of the critical current and to the conditions for penetration of in-plane Abrikosov vortices into a film with $d<2\lambda(T)$ per-

mit a qualitative explanation of the main behavioral features of $j_c(H,\theta)$ reported in the literature.

This study was supported in part by INTAS (Grant 99-0585).

The authors are grateful to S. K. Tolpygo (SUNY, Stony Brook) for providing sample TN2 for study and to A. V. Semenov (Institute of Physics of the National Academy of Sciences of Ukraine, Kiev) for participating in a discussion of a number of questions in this study.

†Deceased.
*E-mail: ryabch@iop.kiev.ua

[1)]A *c*-oriented $YBa_2Cu_3O_{7-\delta}$ film is one in which the crystallographic *c* axis is oriented along the normal to the film plane. This orientation is ensured by the conditions during nucleation and growth of the film on a suitable substrate.

[1] V. M. Pan, *Physics and Materials Science of Vortex States, Flux Pinning and Dynamics*, Vol. 356 of NATO ASI Series, R. Kossowsky, S. Bose, V. Pan, and Z. Durusoy (Eds.), Kluwer Academic Publishers, Dordrecht, The Netherlands (1999), p. 1.
[2] V. M. Pan, Usp. Fiz. Met. **1**, 49 (2000).
[3] D. K. Christen, C. E. Klabunde, R. Feenstra, D. H. Lowndes, and D. M. Kroeger, Physica B **165–166**, 1415 (1990).
[4] Y. Kuwasawa, T. Yamaguchi, T. Tosaka, S. Aoki, and S. Nakano, Physica C **169**, 39 (1990).
[5] T. Nishizaki, T. Aomine, I. Fujii, K. Yamamoto, S. Yoshii, T. Terashima, and Y. Bando, Physica C **181**, 223 (1991); **185–189**, 2259 (1991).
[6] A. A. Zhukov, H. Küpfer, G. K. Perkins, A. D. Caplin, T. Wolf, K. I. Kugel, A. L. Rakhmanov, M. G. Mikheev, V. I. Voronkova, M. Kläser, and H. Wühl, *Physics and Materials Science of Vortex States, Flux Pinning and Dynamics*, Vol. 356 of NATO ASI Series, R. Kossowsky, S. Bose, V. Pan, and Z. Durusoy (Eds.), Kluwer Academic Publishers, Dordrecht, The Netherlands (1999), p. 521.
[7] B. Roas, L. Schultz, and G. Saemann-Ischenko, Phys. Rev. Lett. **64**, 479 (1990).
[8] T. Nishizaki, F. Ichikawa, T. Fukami, T. Aome, T. Terashima, and Y. Bando, Physica C **204**, 304 (1993).
[9] D. H. Lowndes, D. K. Christen, C. E. Klabunde, Z. L. Wang, D. M. Kroeger, J. D. Budai, Shen Zhu, and D. P. Norton, Phys. Rev. Lett. **74**, 2355 (1995).
[10] H. Safar, Y. Y. Coulter, M. P. Maley, S. Foltyn, P. Arendt, X. D. Wu, and J. O. Willis, Phys. Rev. B **52**, R9875 (1995).
[11] V. A. Komashko, A. G. Popov, V. L. Svetchnikov, A. V. Pronin, V. S. Melnikov, A. Yu. Galkin, V. M. Pan, C. L. Snead, and M. Suenaga, Solid State Commun. **13**, 209 (2000).
[12] V. M. Pan, A. L. Kasatkin, V. S. Flis, V. A. Komashko, V. L. Svetchnikov, A. V. Pronin, C. L. Snead, M. Suenaga, and H. W. Zandbergen, J. Low Temp. Phys. **117**, 1537 (1999).
[13] V. M. Pan, V. S. Flis, O. P. Karasevska, V. I. Matsui, I. I. Peshko, V. L. Svetchnikov, M. Lorenz, A. N. Ivanyuta, G. A. Melkov, E. A. Pashitskii, and H. W. Zandbergen, J. Supercond.: Novel Incorp. Magn. **14**, 105 (2001).
[14] A. Gurevich and E. A. Pashitskii, Physica B **57**, 13878 (1998).
[15] É. A. Pashitskiĭ, V. I. Vakaryuk, S. M. Ryabchenko, and Yu. V. Fedotov, Fiz. Nizk. Temp. **27**, 131 (2001) [Low Temp. Phys. **27**, 96 (2001)].
[16] Yu. V. Fedotov, S. M. Ryabchenko, E. A. Pashitskii, V. I. Vakaryuk, A. V. Semenov, V. M. Pan, and V. S. Flis, Fiz. Nizk. Temp. **28**, 245 (2002) [Low Temp. Phys. **28**, 172 (2002)].
[17] E. A. Pashitskii and V. I. Vakaryuk, Fiz. Nizk. Temp. **28**, 16 (2002) [Low Temp. Phys. **28**, 11 (2002)].
[18] B. Dam, J. M. Huijbregtse, F. C. Klaassen, R. C. F. van der Geest, G. Doornbos, J. H. Rector, A. M. Testa, S. Freisem, J. C. Martinez, B. Stäuble-Pumpin, and R. Griessen, Nature (London) **399**, 439 (1999).
[19] E. Mezzetti, R. Gerbaldo, G. Ghigo, L. Gozzelino, B. Minetti, C. Camerlingo, A. Monaco, G. Cuttone, and A. Rovelli, Phys. Rev. B **60**, 7623 (1999).
[20] V. M. Pan, E. A. Pashitskii, S. M. Ryabchenko, V. A. Komashko, A. V. Pan, S. X. Dou, A. V. Semenov, C. G. Tretiatchenko, and Yu. V. Fedotov, IEEE Trans. Appl. Supercond. **13**, June (2003), accepted.
[21] I. Peshko, V. Flis, and V. Matsui, J. Phys. D: Appl. Phys. **34**, 732 (2001).
[22] S. K. Streiffer, B. M. Lairson, C. B. Eom, B. M. Clemens, J. C. Bravman, and T. H. Geballe, Phys. Rev. B **43**, 13007 (1991).
[23] R. Clem and A. Sanchez, Phys. Rev. B **50**, 9355 (1994).
[24] M. Wurlitzer, M. Lorenz, K. Zimmer, and P. Esquinazi, Phys. Rev. B **55**, 11816 (1995).
[25] G. Stejic, A. Gurevich, E. Kadyrov, D. Christen, R. Joynt, and D. C. Larbalestier, Phys. Rev. B **49**, 1274 (1994).
[26] A. A. Abrikosov, Zh. Éksp. Teor. Fiz. **46**, 1464 (1964) [Sov. Phys. JETP **19**, 988 (1964)].
[27] A. A. Abrikosov, *Fundamentals of the Theory of Metals*, North-Holland, Amsterdam (1988), Mir, Moscow (1987)

Translated by Steve Torstveit

Critical current of asymmetric SFIFS tunnel structures

E. A. Koshina and V. N. Krivoruchko*

A. A. Galkin Donetsk Physicotechnical Institute, ul. R. Lyuksemburg 72, 83114 Donetsk, Ukraine
(Submitted January 15, 2003)
Fiz. Nizk. Temp. **29**, 858–867 (August 2003)

The physics of critical current inversion (π state of the junction) and enhancement in SFIFS tunnel junctions (S and F are superconducting and ferromagnetic metals, and I is an insulator) is discussed on the basis of a microscopic theory of the proximity effect. The ground state and the critical current of an asymmetric $(SF)_L I(FS)_R$ junction with a strong ferromagnetic field on one of its ''banks'' are investigated. It is shown that SFINS junctions with strong magnetism of the F layer are found in a ground state with a $\pm\pi/2$ difference of the superconducting phases on the banks (N is a normal nonmagnetic metal). The dependence of the dc Josephson effect on temperature and on the angle between the magnetic moments of the F layers in SFIFS junctions is investigated. © *2003 American Institute of Physics.* [DOI: 10.1063/1.1596792]

1. INTRODUCTION

In this paper we examine the features of the steady-state properties of asymmetric SFIFS tunnel junctions due to the mutual influence of the magnetism and superconductivity in proximity SF structures (S is a superconducting metal, F is a ferromagnetic metal, and I is an insulator). In the most general case the ''proximity effects'' can include phenomena due to the ''penetration'' of the order parameter (some state) of one material into another material in contact with it which initially did not have that type of ordering. In SN structures (N is a normal nonmagnetic metal) proximity effects of superconductivity are well known and have been intensively studied (see, e.g., Ch. 5 of Ref. 1). Those structure have a single type of ordering: superconductivity. In the case of SF structures there are two competing types of ordering: ferromagnetism and superconductivity. On the one hand, upon adiabatically penetrating into the ferromagnet layer a Cooper pair interacts with the local exchange field h_F, in which case the electrons with spin ''up'' acquire an energy $H_{\rm exc}=\mu_B h_F$ (μ_B is the Bohr magneton) and electrons with spin ''down'' lose an energy $H_{\rm exc}=\mu_B h_F$; this effect determines the features of the proximity superconductivity of the F layer. On the other hand, in tunneling from the F metal into S an electron loses an excess energy $\delta E\sim H_{\rm exc}$ over a time $\tau\sim\hbar/H_{\rm exc}$ and a distance $\lambda_F\sim\hbar v_F/H_{\rm exc}$ from the SF boundary ($\hbar$ is Planck's constant, and v_F is the velocity of electrons on the Fermi surface). For $v_F\sim10^5-10^6$ m/s and $H_{\rm exc}\sim10^2$ K$\sim10^{-14}$ erg, the parameter λ_F reaches values $\lambda_F\sim10^{-8}-10^{-7}$ m. It is this quantity ($\lambda_F\sim10^2$ Å for ''dirty'' metals) that characterizes the scale of the magnetic correlations in the S layer. As a result of this ''magnetic'' part of the proximity effect the superconducting metal will exhibit spin splitting of the quasiparticle states, spin-polarized localized states will form inside the energy gap, and a nonuniform magnetic ordering will be induced.[2] On the whole, an SF structure must be treated as a highly correlated system having magnetic and superconducting properties.

A review of current papers on the thermodynamics of SF systems and, in particular, phase diagrams of SF junctions and superlattices can be found in Ref. 3. As to the transport properties, studies of the Josephson effect for SFS junctions with a rather thick F layer have made it possible to observe directly the so-called π-phase superconductivity. This superconducting state is characterized by a spontaneous shift by π of the macroscopic phase difference of the wave functions of the condensate on the ''banks'' of the junction and by the opposite sign of the critical current I_c. This was predicted theoretically back in Refs. 4 and 5 but was only recently observed experimentally.[6–9] The more complex SFIFS junctions, which are made up of bilayers of thin magnetic and bulk superconducting metals separated by an insulating layer, were first investigated by the present authors in Refs. 10 and 11. In subsequent studies[12–14] the Josephson effect was studied in systems of this kind in relation to the mutual orientation of the magnetic moments of the F layers. The theory predicted that at certain values of the exchange field and parameters of the SF interface an SFIFS junction with a parallel orientation of the magnetizations of the F layers can undergo a transition to the π state, while in the case of an antiparallel orientation the Josephson critical current can even increase with increasing exchange field, and the tunnel junction itself remains in the 0 state. These results conflicted with the conventional ideas about the suppression of the superconducting properties of a system by the exchange field and, naturally, stimulated further research on SFIFS tunnel junctions. For example, the dependence of the critical current on the thickness of the F layer and the transparency of the SF and FI boundaries was investigated on the basis of a self-consistent numerical solution of the system of Usadel equations in Ref. 14, and the influence of spin–orbit scattering on the inversion and enhancement of the tunneling supercurrent was studied in Ref. 15.

In the studies mentioned, the discussion of the transport characteristics, as a rule, was limited to consideration of symmetric SFIFS junctions, i.e., junctions with identical parameters of the bilayers. The assumption that the ''banks'' of SFIFS junctions are absolutely identical may be something of an idealization of the real experimental situation. For designing experiments and interpreting the results it is advisable to discuss the ''stability'' of the transport properties of

SFIFS tunnel junctions against deviations from identical parameters of the bilayers.

The goal of the present study is to investigate the properties of asymmetric $(SF)_L I(FS)_R$ junctions. In Sec. 2 we formulate a junction model and present the main results of a microscopic theory of the proximity effect for a bilayer consisting of a thin layer of a magnetic metal and a bulk superconducting metal. The physics of the phenomena of inversion of the sign and enhancement of the amplitude of the critical current in SFIFS tunnel junctions is discussed in Sec. 3. The cases of some extremely asymmetric junctions are considered in Sec. 4, and their properties are studied by analytical and numerical methods. Contacts with an arbitrary orientation of the exchange fields of the ferromagnets on the banks are discussed in Sec. 5, and the case of arbitrary temperatures $T<T_c$ in Sec. 6. The main results are summarized in the Conclusion.

2. JUNCTION MODEL AND THE PROXIMITY EFFECT IN AN SF BILAYER

We consider an $(SF)_L I(FS)_R$ tunnel junction with SF bilayers as the two ''banks'' and an insulating layer I having such low transparency that the influence of the currents on the state of the electrodes can be neglected. Let all quantities depend only on the coordinate x along the normal to the interfacial surface, i.e., the transverse dimensions of the junction are much less than the Josephson penetration depth λ_J. We consider the case when the ''dirty'' limit holds for both the S and F metals, i.e., $l_{S,F}<\xi_{S,F}$, and the thickness of the metals satisfies the conditions

$$d_S \gg \xi_S, \quad d_F \ll \min(\xi_F, \xi). \tag{1}$$

Here $l_{S,F}$ are the mean free paths of electrons in the S and F layers, $\xi_S \sim (D_S/2\pi T_c)^{1/2}$, $\xi_F \sim (D_F/2H_{\rm exc})^{1/2}$, $\xi \sim (D_F/2\pi T_c)^{1/2}$ are the effective coherence lengths of the metals (for the F metal the choice of coherence length depends on the relationship of the parameters T_c (the critical temperature of the S metal) and $H_{\rm exc}$ (exchange field of the F metal), and $D_{S,F}$ are the diffusion coefficients of the S and F metals. The condition $d_S \gg \xi_S$ allows us to neglect the decrease of the critical temperature of the SF bilayer in comparison with the critical temperature of the bulk S metal; the critical temperature of the superconducting transition for the F metal is assumed equal to zero. It is also assumed everywhere below that the F metal is found in a single-domain state, and the magnetization is parallel to the SF boundary, i.e., there is no spontaneous magnetic flux penetrating into the S layer. Under these conditions the mutual influence of the magnetism and superconductivity is due to just the proximity effects. (In Eq. (1) and below we use a system of units in which $\hbar=\mu_B=k_B=1$.)

As we know, the problem of the tunneling properties of junctions whose banks are proximity bilayers is solved in two steps: one must first determine the superconducting characteristics of the bilayers and then find the electronic parameters of the junction. The proximity superconducting effect for layered SF systems with a bulk S layer and thin F layer and an arbitrary transparency of the SF boundary has been discussed in detail in our previous papers.[11,16] In the case when the spin–orbit scattering can be neglected, i.e., the subbands of electrons with spins ''up'' and ''down'' do not mix with each other, the SF bilayer is described by the following system of Usadel equations for one spin subband (e.g., electrons with spin ''up''):

For the S metal

$$\Phi_S = \Delta_S + \xi_S^2 \frac{\pi T_c}{\omega G_S} [G_S^2 \Phi_S']', \qquad G_S = \frac{\omega}{(\omega^2 + \Phi_S \tilde{\Phi}_S)^{1/2}}, \tag{2}$$

$$\Delta_S \ln(T/T_c) + 2\pi T \sum_{\omega>0} [(\Delta_S - \Phi_S G_S)/\omega] = 0; \tag{3}$$

for the F metal

$$\Phi_F = \xi^2 \frac{\pi T_c}{\tilde{\omega} G_F} [G_F^2 \Phi_F']', \quad G_F = \frac{\tilde{\omega}}{(\tilde{\omega}^2 + \Phi_F \tilde{\Phi}_F)^{1/2}}. \tag{4}$$

Here Δ_S is the superconducting order parameter of the S metal, $\tilde{\omega} = \omega + i(\pm H_{\rm exc})$, where the sign of the exchange field depends on the relative orientation of the exchange fields of the ferromagnets on the banks of the contact; $\omega = \pi T(2n+1)$, $n=0,\pm 1,\pm 2,\ldots$ are the Matsubara frequencies; the summation over frequencies in Eq. (3) is cut off at the Debye frequency ω_D; $\tilde{\Phi}(\omega, H_{\rm exc}) = \Phi^*(\omega, -H_{\rm exc})$; a prime denotes differentiation with respect to the coordinate x. In Eq. (4) we have used the effective coherence length ξ of the normal nonmagnetic metal with a diffusion coefficient D_F; it is convenient to introduce this in place of ξ_F in order to consider both the limit $H_{\rm exc} \to 0$ (an SN bilayer with $d_N \ll \xi$) and the limit $H_{\rm exc} \gg \pi T_c$. We note that for $H_{\rm exc} \neq 0$ the functions $\Phi_{S,F}(\omega)$ lose symmetry with respect to a change of sign of the energy variable ω. This is one of the differences between SF and SN bilayers. We have taken into account the normalization of the usual Usadel functions $F_{S,F}$ and $G_{S,F}$ for the S and F layers explicitly and have introduced modified Usadel functions $\Phi_{S,F}$ in analogy with Ref. 17; these are defined by the relations $F_S = G_S \Phi_S/\omega$ and $F_F = G_F \Phi_F/\tilde{\omega}$.

Equations (2)–(4) must be supplemented by boundary conditions for the functions Φ_S and Φ_F. In the interior of the S layer we have $\Phi_S(\infty) = \Delta_S(\infty) = \Delta_0(T)$, where $\Delta_0(T)$ is the order parameter of the spatially uniform superconductor at a temperature T in the BCS theory; at the outer boundary of the ferromagnet we have $\Phi_F'(-d_F)=0$ (we assume that the S metal occupies the region $x>0$ and the F metal the region $x<0$). The boundary conditions at the SF boundary have the form[16]

$$\frac{1}{\tilde{\omega}} \gamma \xi G_F^2 \Phi_F' \Big|_{x=0} = \frac{1}{\omega} \xi_S G_S^2 \Phi_S' \Big|_{x=0}, \tag{5}$$

$$\xi \gamma_{BF} G_F \Phi_F|_{x=0} = \tilde{\omega} G_S \left(\frac{\Phi_S}{\omega} - \frac{\Phi_F}{\tilde{\omega}} \right) \Big|_{x=0}. \tag{6}$$

Here $\gamma=\rho_S\xi_S/\rho_F\xi$ is the proximity effect parameter, which characterizes the intensity of the superconducting correlations induced in the F layer on account of the proximity of the S layer, $\gamma_{BF}=R_B/\rho_F\xi$ is a parameter taking into account the effects of finite transparency of the boundary, $\rho_{S,F}$ is the resistance of the S and F metals in the normal state, and R_B is the product of the resistance of the SF boundary times its area. We note that an additional physical condition for the validity of relations (5) and (6), which we are assuming is met here, is that the difference in the boundary parameters γ and γ_{BF} for electrons with opposite spin orientations is negligible.

The condition $d_F \ll \min(\xi_F,\xi)$ allows us to neglect the spatial dependence of the variables in the F layer. As a result, the problem of the proximity effect for a bilayer can be reduced to a boundary-value problem for the S layer and an additional expression describing the superconductivity in the F layer. The degree of interaction of the S and F layers depends on three parameters: $\gamma_M=\gamma d_F/\xi$, $\gamma_B=\gamma_{BF}d_F/\xi$, and the value of the exchange interaction $H_{\rm exc}$ of the ferromagnetic metal. The parameter γ_M contains processes that destroy Cooper pairs at the SF boundary and is determined by the degree of difference of the densities of states for electrons in the S and F metals. Large values of γ_M correspond to larger densities of quasiparticle states on the F side as compared to the S side in the SF bilayer. In that case the diffusion of quasiparticles into the S layer will lead to suppression of the superconducting state in it at a distance of the order of ξ_S from the boundary. In the opposite limit ($\gamma_M \ll 1$) the penetration of quasiparticles from the F layer is small, and the superconducting properties of the S layer near the boundary are little changed. The parameter γ_B directly describes the electrical quality of the SF boundary. As can be seen from its definition, good electrical contact of the S and F metals corresponds to small values of γ_B ($\gamma_B \ll 1$); if $\gamma_B \gg 1$, then there is an appreciable potential barrier between the S and F metals.

For arbitrary values of the parameters the system of equations (2)–(6) requires a self-consistent numerical solution (Ref. 14 can serve as an example of such an approach). However, for a weak ($\gamma_M \ll 1$) or strong ($\gamma_M \gg 1$) proximity effect one can obtain general analytical solutions for arbitrary values of the transparency of the SF boundary and arbitrary values of the exchange field.[16] We shall examine these cases below.

For a weak proximity effect we have the following expression for the function $\Phi_S(\omega)\equiv\Phi_S(\omega,0)$:

$$\Phi_S(\omega)=\Delta_0\left\{1-\frac{\gamma_M\beta\tilde{\omega}}{\gamma_M\beta\tilde{\omega}+\omega A}\right\}, \tag{7}$$

where

$$\beta=\left[\frac{(\omega^2+\Delta_0^2)^{1/2}}{\pi T_c}\right]^{1/2},$$

$$A\equiv A(\omega)=\left[1+\frac{\gamma_B\tilde{\omega}}{(\pi T_c)^2}\left(\frac{2\omega}{\beta^2}+\gamma_B\tilde{\omega}\right)\right]^{1/2}.$$

Using the boundary conditions, we obtain the following expression for the modified Usadel function of the F metal in the leading approximation in γ_M (see Ref. 16 for details):

$$\Phi_F(0)\approx\frac{G_S\Phi_S}{[\omega(\gamma_B/\pi T_c+G_S/\tilde{\omega})]|_{x=0}}. \tag{8}$$

For the case of a strong proximity effect we obtain the expression

$$\Phi_S(\omega)=B(T)\frac{\pi T_c+\gamma_B\tilde{\omega}}{\gamma_M\tilde{\omega}}. \tag{9}$$

At all temperatures $T<T_c$ the function $B(T)$ can be approximated to an accuracy of $\sim 1\%$ (Ref. 18) by the expression $B(T)=2T_c[1-(T/T_c)^2][7\zeta(3)]^{-1/2}$, where $\zeta(3)$ is the Riemann zeta function. In the limiting case $\gamma_M \gg 1$ we obtain for the function $\Phi_F(\omega)$ describing the superconductivity in the F layer an approximate expression that is independent of the transparency of the boundary:

$$\Phi_F(\omega)=\frac{B_M(T)}{\omega},\quad \text{where}\quad B_M(T)=B(T)\frac{\pi T_c}{\gamma_M}. \tag{10}$$

It follows from Eqs. (7) and (9) that because of its proximity to the F metal, ferromagnetic correlations will be induced in the S metal, and the Green's functions of the S layer will now depend on $H_{\rm exc}$. Thus one can speak of an exchange-induced magnetic interaction in the S layer and characterize the SF bilayer as a single system with strong superconducting and magnetic correlations. It is because of this "magnetic proximity effect" that an SFIFS junction can undergo a transition to the π state even in the case when the thickness of the ferromagnetic layer is much less than the correlation length. This mechanism differs from the mechanisms for the transition of a junction to the π state due to the presence of magnetic impurities[19,20] or to the direct access to a microscopic current-carrying electronic state inside a weak link.[22–24] The case considered here also differs from the situation in SF structures with a bulk F layer, where because of the difference in the Fermi momenta of electrons with opposite spin $k_\uparrow$ ($k_\downarrow$) the superconducting wave function in the F layer oscillates with a characteristic spatial scale $\sim 1/(k_\uparrow - k_\downarrow)\sim v_F/H_{\rm exc}$. It is the spatial variation of the phase of the superconducting order parameter in the ferromagnetic layer that causes the oscillatory dependence of the critical current on the exchange field in SFS tunnel junctions.[4,5,25]

3. PHYSICS OF THE PHENOMENON OF INVERSION OF THE SIGN AND ENHANCEMENT OF THE AMPLITUDE OF THE CRITICAL CURRENT

Let us illustrate what we have said about the unity of the superconducting and magnetic properties of an SF bilayer for the example of a symmetric SFIFS junction.

Parallel orientation of the magnetizations

Suppose that the proximity effect is so weak ($\gamma_M \to 0$) that the change of the superconducting properties of the S layer can be neglected. For $\gamma_M=0$ we have $\Phi_S(\omega,x)=\Phi_S(\infty)=\Delta_0$, and for the amplitude of the critical current we can obtain the expression (see relation (17) below in the case $\tilde{\omega}_L=\tilde{\omega}_R$)

$$j_c^p=\frac{eR_N}{2\pi T_c}I_c\approx\frac{T}{T_c}\Delta_0^2\sum_{\omega>0}\frac{1+\gamma_{BT}\omega^2(2\beta^{-2}+\gamma_{BT})-\gamma_{BT}^2H_{\rm exc}^2}{\beta^2[(1+\gamma_{BT}\omega^2(2\beta^{-2}+\gamma_{BT})-\gamma_{BT}^2H_{\rm exc}^2)^2+4\gamma_{BT}^2\omega^2H_{\rm exc}^2(\beta^{-2}+\gamma_{BT})]},\tag{11}$$

where $\gamma_{BT}=\gamma_B/\pi T_c$, and R_N is the resistance of the junction in the normal state. For $H_{\rm exc}\to 0$ expression (11) reproduces the result obtained for SNINS junctions.[26] We see that when the value of the exchange field becomes large enough, i.e., $(\gamma_{BT}H_{\rm exc})^2>[1+\gamma_{BT}\omega^2(2\beta^{-2}+\gamma_{BT})]$, the critical current changes sign. This means that the phase difference between the order parameters in the banks of the contact changes by π. We stress that for $\gamma_M=0$ a change of state of the S layer does not occur, but here the wave function of the condensate in the F layer acquires a phase of $\sim\pi/2$ practically in a jump (because of the condition $d_F\ll\xi_F$). Indeed, as follows from the boundary conditions (8), for $\gamma_BH_{\rm exc}\gg\pi T_c$ we have $F_F(0)\sim -i(\Delta_0/\gamma_BH_{\rm exc})\mathrm{sgn}(H_{\rm exc})$.

In the opposite case of a strong proximity effect ($\gamma_M\gg 1$) and an arbitrary transparency, the amplitude of the critical current can be written as

$$j_c^p\approx\frac{T}{T_c}B_M^2\sum_{\omega>0}\frac{\omega^2-H_{\rm exc}^2}{\omega^2(\omega^2+H_{\rm exc}^2)^2}.\tag{12}$$

As in the case of a weak proximity effect, for $H_{\rm exc}\to 0$ Eq. (12) goes over to the expression for the critical current of an SNINS junction. At a sufficiently strong exchange field ($H_{\rm exc}>\pi T_c$) the critical current again changes sign, i.e., the junction goes into the π state. Let us illustrate the phase shift in the limit $\gamma_B=0$. It follows from Eq. (9) that $\Phi_S(\omega)$ is given by the expression

$$\Phi_S(\omega)\approx B(T)\frac{\pi T_c}{\gamma_M}\frac{\omega-iH_{\rm exc}}{\omega^2+H_{\rm exc}^2},\tag{13}$$

and the anomalous Green's function $F_F(\omega,H_{\rm exc})$ obeys the relation $F_F(\omega,H_{\rm exc})=\Phi_S/(\omega^2+\Phi_S^2)^{1/2}$. Since a typical value is $\omega\sim\pi T_c$, it follows from Eq. (13) and the expression for $F_F(\omega,H_{\rm exc})$ that if $H_{\rm exc}\gg\pi T_c$, then the phase of the anomalous Green's function changes by $\pi/2$ in comparison with the limit $H_{\rm exc}\to 0$.

Thus for SFIFS systems with sufficiently strong magnetism the phase shift of the order parameter on both banks will be equal to $\pi/2$, and so the π state of the junction will be preferred.

Antiparallel orientation of the magnetizations

For the sake of definiteness, let us assume that $\tilde\omega_L=\omega+iH_{\rm exc}$ and $\tilde\omega_R=\omega-iH_{\rm exc}$. For an extremely weak proximity effect ($\gamma_M=0$) and arbitrary transparency we have

$$j_c^a=\frac{T}{T_c}\Delta_0^2\sum_{\omega>0}\beta^{-2}\{[1+\gamma_{BT}\omega^2(2\beta^{-2}+\gamma_{BT})-\gamma_{BT}^2H_{\rm exc}^2]^2+4\gamma_{BT}^2\omega^2H_{\rm exc}^2(\beta^{-2}+\gamma_{BT})\}^{-1/2}.\tag{14}$$

The main contribution to the sum is given by $\omega\ll\pi T_c$. For small ω the summand is proportional to $1/[1-(\gamma_{BT}H_{\rm exc})^2]$, i.e., $j_c^a(H_{\rm exc})>j_c^a(0)$, if $0<H_{\rm exc}<\gamma_{\rm BT}^{-1}$. Thus for an antiparallel orientation of the magnetizations of the banks there exists an interval of values of the exchange field in which the critical current of the junction increases.

In the case of a strong proximity effect ($\gamma_M\gg 1$) and arbitrary transparency we obtain

$$j_c^a=\frac{eR_N}{2\pi T_c}I_c=\frac{T}{T_c}B_M^2\sum_{\omega>0}\omega^{-2}[(\omega^2+H_{\rm exc}^2)^2+2(\omega^{-2}B_M^2-H_{\rm exc}^2)]^{-1/2}.\tag{15}$$

The summand increases for $0<H_{\rm exc}<(B_M^2/\omega^2-\omega^2)^{1/2}$, and in this interval of exchange fields $j_c^a(H_{\rm exc})>j_c^a(0)$. Thus in the case of a strong proximity effect there also exists an interval of values of $H_{\rm exc}$ in which the amplitude of the critical current increases with increasing value of the exchange field.

In this case the physics of the phenomenon is somewhat different from the previous case. It does not have to do with the total phase shift across the junction (the phase shifts on the banks of the junction compensate each other) but is due to the influence of the exchange field on the spin of the electron. It is convenient to pass to the limit $T\to 0$ and to continue the function $F_{F\uparrow\downarrow}(\omega,H_{\rm exc})$ onto the complex plane by means of the substitution $\omega\to -i\varepsilon$. For the density of states in the F layer for one spin band we obtain the expression (the case $\gamma_M=0$)[14]

$$N_{F\uparrow}(\varepsilon,H_{\rm exc})=\mathrm{Re}\frac{\Delta_0}{\{[\varepsilon+\tilde\gamma_B(\varepsilon-H_{\rm exc})]^2-\Delta_0^2\}^{1/2}},\tag{16}$$

where $\tilde\gamma_B=\dfrac{\gamma_B\beta^2}{\pi T_c}$.

It follows from (16) that on the Fermi surface ($\varepsilon=0$)

$$N_{F\uparrow}(0,H_{\rm exc})=\mathrm{Re}\frac{H_{\rm exc}\gamma_B}{\pi T_c[(\gamma_BH_{\rm exc}/\pi T_c)^2-1]^{1/2}},$$

i.e., for $H_{\rm exc}/\pi T_c=1/\gamma_B$, the feature of the density of states of the Cooper pairs in the F layer coincides with the Fermi level. The overlap of the features $\sim\varepsilon^{1/2}$ in the density of states of the banks (for opposite spin bands) leads to enhancement of the amplitude of the critical current of the junction.

4. ASYMMETRIC $(SF)_LI(FS)_R$ JUNCTIONS

The behavior of the critical current of asymmetric $(SF)_LI(FS)_R$ junctions with strong ferromagnetism on one of the banks has some interesting features that have not been discussed before. We now turn to a discussion of these. Using expressions (7)–(10), we investigate the dependence of the steady-state properties of an asymmetric $(SF)_LI(FS)_R$ tunnel junction on the parameters of the bilayer (the proximity effect, the degree of transparency of the SF boundary, the value of the exchange field of the ferromagnetic metal) and the relative orientation of the magnetization of the banks. In

the general case the expression for the critical current I_c of an $(SF)_L I(FS)_R$ junction can be written in the form[11]

$$(eR_N/2\pi T_c)I_c = j_c = (T/T_c)\mathrm{Re}\sum_{\omega>0} G_{FL}(\omega)\Phi_{FL}(\omega) \times G_{FR}(\omega)\Phi_{FR}(\omega)/\tilde{\omega}_L\tilde{\omega}_R$$
$$= \mathrm{Re}\sum_{\omega>0} G_{SL}(\omega)\Phi_{SL}(\omega)G_{SR}(\omega)\Phi_{SR}(\omega)/ \omega^2[1+2\tilde{\omega}_L G_{SL}(\omega)(\gamma_B\pi T_c) + \tilde{\omega}_L^2(\gamma_B\pi T_c)^2]^{-1/2}[1+2\tilde{\omega}_R G_{SR}(\omega) \times(\gamma_B\pi T_c)+\tilde{\omega}_R^2(\gamma_B\pi T_c)^2]^{-1/2}. \quad (17)$$

Let us first give some analytical results for a junction with $H_{\mathrm{exc}L} \gg \pi T_c$ in the case of a strong proximity effect ($\gamma_M \gg 1$) and complete transparency ($\gamma_B = 0$) of both SF boundaries.

Parallel orientation of the exchange fields

As we have said, owing to the unified magnetic and superconducting properties of the S and F layers, the superconducting wave functions on the banks of the junction have, on top of the phase of the wave function of a spatially uniform superconductor, an additional phase which depends on the value of the exchange field. Using Eq. (9), we obtain for the anomalous Green's function (since $\Phi_S \sim 1/\gamma_M$ and is small, we assume that $G_S \approx 1$)

$$F_{SL}(\omega, H_{\mathrm{exc}L}) \approx B_M \frac{\exp(i\pi/2)}{\omega H_{\mathrm{exc}L}}, \quad (18)$$

i.e., as we have mentioned, the wave function of a bilayer with a strong exchange field acquires a phase $\varphi_L = \pi/2$. If the exchange field on both banks is large enough, $H_{\mathrm{exc}L(R)} \gg \pi T_c$, then $F_{SL}F_{SR} = B_m^2 \exp(i\pi)/(\omega^2 H_{\mathrm{exc}L}H_{\mathrm{exc}R})$, and the amplitude of the critical current is small:

$$j_c^p \sim -\frac{B_M^2}{H_{\mathrm{exc}L}H_{\mathrm{exc}R}}\sum_{\omega>0}\omega^{-2}. \quad (19)$$

At a finite value of the field on the right bank, $H_{\mathrm{exc}R} > 0$, the total phase change $\varphi_L + \varphi_R$ due to the proximity effect is equal to $\tan^{-1}(H_{\mathrm{exc}R}/\omega) + \pi/2$, and the expression for the amplitude of the critical current becomes finite:

$$j_c^p \sim -\frac{B_M^2 H_{\mathrm{exc}R}}{H_{\mathrm{exc}L}}\sum_{\omega>0}\omega^{-2}(\omega^2 + H_{\mathrm{exc}R}^2)^{-1}. \quad (20)$$

Antiparallel orientation of the exchange fields

Let us consider the change of the phases of the superconducting wave functions for an antiparallel orientation of the magnetizations on the banks of the junction. For the sake of definiteness let $\tilde{\omega}_{L,R} = \omega \mp i H_{\mathrm{exc}L,R}$ (the minus sign corresponds to the left bank and the plus sign to the right). The anomalous Green's functions are

$$F_{SL,R}(\omega, H_{\mathrm{exc}L,R}) = B_M \frac{\exp[\pm i\tan^{-1}(H_{\mathrm{exc}L,R}/\omega)]}{\omega(\omega^2 + H_{\mathrm{exc}L,R}^2)^{1/2}}. \quad (21)$$

If the exchange field on both banks is strong, $H_{\mathrm{exc}L} \gg \pi T_c$ and $H_{\mathrm{exc}R} \gg \pi T_c$, then the change in phase of the pair amplitude owing to the proximity to the ferromagnet is equal to $\pi/2$ on the right bank and $-\pi/2$ on the left; the total phase change is equal to zero. The asymptotic value of the amplitude of the critical current of such a junction differs from (19) only in the sign.

In the general case when $H_{\mathrm{exc}L} \gg \pi T_c$ and $H_{\mathrm{exc}R} > 0$, the total phase change $\varphi_L + \varphi_R$ due to the proximity effect is equal to $\pi/2 - \tan^{-1}(H_{\mathrm{exc}R}/\omega)$, and the transition of the junction to the π state with increasing $H_{\mathrm{exc}R}$ will not occur. The asymptotic value of the critical current amplitude of this contact differs from expression (20) only in the sign. At a fixed strong exchange field on the left bank of the junction there is an interval of values of the exchange field on the right bank within which an increase in the critical current amplitude is observed with increasing $H_{\mathrm{exc}R}$.

SFINS $\pi/2$ junctions

SFINS junctions with strong ferromagnetism of the F layer have some curious properties. Repeating the arguments made above, we find that if $H_{\mathrm{exc}L} \gg \pi T_c$ and $H_{\mathrm{exc}R} \to 0$, the total phase change due to the proximity effect is equal to $\pi/2$ (a $\pi/2$ junction). The amplitude of the critical current here tends toward the value

$$j_c^p \sim \frac{B_M^2}{H_{\mathrm{exc}R}}\mathrm{Re}\sum\frac{1}{\omega^3}\exp(i\pi/2) = 0.$$

Thus SFINS junctions with strong ferromagnetism of the F layer are found in a ground state with a phase difference of $\pm\pi/2$ on their banks. We stress that this mechanism of realizing the $\pi/2$ state of a tunnel junction is essentially different from the mechanism previously discussed for SFS junctions with a thick F layer,[27] where the possibility of a transition to the $\pi/2$ state is due to fluctuations of the critical current in the plane of the SFS junction.

Numerical analysis

Let us flesh out the analytical results obtained for limiting values of the parameters with the more general numerical treatment. Using Eq. (17) and the analytical solutions of the Usadel equations (7) and (9), we can calculate the critical current amplitude for $(SF)_L I(FS)_R$ junctions in which the parameters of the SF bilayers are different. Previously[11] we have considered asymmetric $(SF)_L I(FS)_R$ junctions in which the parameters of the S and F metals are the same but the SF boundaries differ in transparency and resistance, i.e., the right and left electrodes have different values of γ_M and γ_B. Let us discuss the opposite situation, when the parameters γ_M and γ_B of the banks are the same but the values of the exchange fields $H_{\mathrm{exc}R}$ and $H_{\mathrm{exc}L}$ are different.

Figure 1a shows the results of a numerical calculation of the amplitude of the critical current of an asymmetric $(SF)_L I(FS)_R$ junction for the case of a weak proximity effect and a finite transparency of the SF boundary ($\gamma_M = 0.1$, $\gamma_B = 0$). It is seen that for a fixed value of $H_{\mathrm{exc}L}$ and an antiparallel orientation of the magnetizations (dashed curves in the figure) of the bands of the junction there is a certain interval $H_{\mathrm{exc}R} > 0$ within which enhancement of the current

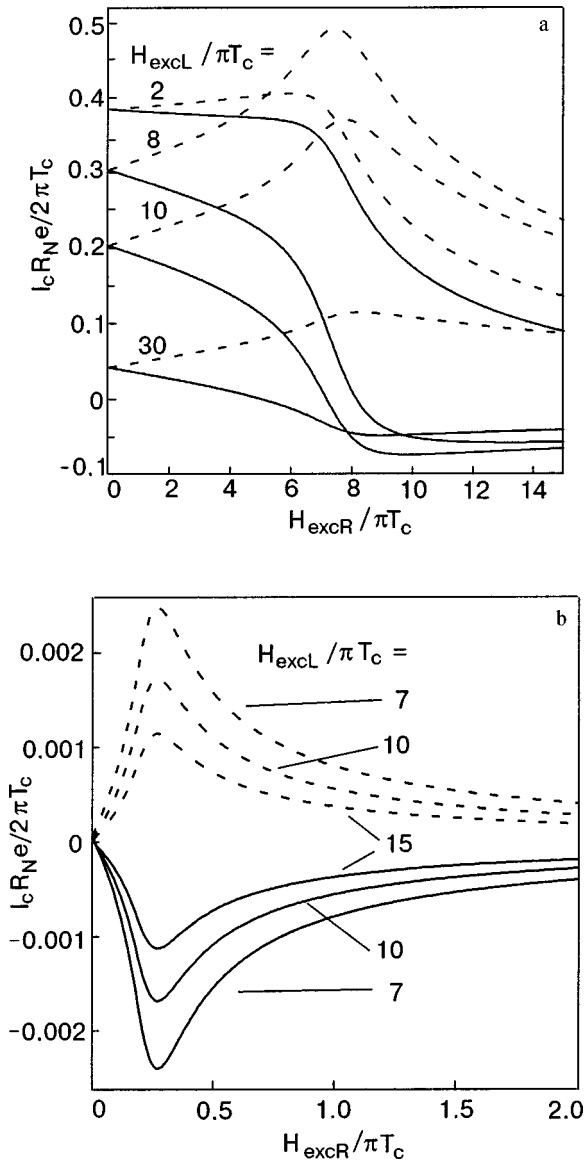

FIG. 1. Dependence of the critical current amplitude of an asymmetric $(SF)_L I(FS)_R$ junction on the energy of the exchange field of the right bank for $T \ll T_c$, $\gamma_{BL} = \gamma_{BR} = 0$ and specified values of the exchange interaction on the left bank, $H_{excL}/\pi T_c$: a—$\gamma_{ML} = \gamma_{MR} = 0.1$; b—$\gamma_{ML} = \gamma_{MR} = 10$. Here and in Figs. 2 and 3 the solid curves are for the mutually parallel and the dashed curves for the mutually antiparallel orientations of the magnetizations of the banks of the junction.

occurs with increasing H_{excR}. For a parallel orientation of the magnetizations (solid curves) there is a certain interval of values of H_{excR} within which a transition of the junction to a state with π-phase superconductivity occurs. For the case of a strong proximity effect by the behavior of the critical current amplitudes in $(SF)_L I(FS)_R$ junctions are analogous. The difference consists in the fact that for the same value of H_{excL} for a parallel orientation of the magnetizations the transition of the junction to the π state occurs at a lower value of H_{excR}, while in the case of an antiparallel orientation the interval of H_{excR} within which enhancement of the critical current occurs is narrower than for the case of a weak proximity effect.

For a geometry with an antiparallel orientation of the magnetizations on the banks of the junction one notices nonmonotonic behavior of the critical current amplitude at the maximum as the values of the exchange field are varied. For example, for $H_{excL} = 2\pi T_c$ (see Fig. 1a) the maximum of the critical current amplitude is observed at $H_{excR} \approx 0.65\pi T_c$, and its value in reduced units is equal to $j_c = 0.4$. For $H_{excL} = 8\pi T_c$ the maximum current amplitude is observed at $H_{excR} = 7.5\pi T_c$ and is is considerably higher than in the former case: $j_c = 0.5$. Analysis of the numerical results showed that the largest values of the maximum amplitude of the critical current are reached in symmetric SFIFS junctions.

The behavior of the critical current amplitude in junctions with a strong exchange field on one of the banks ($H_{excL} \gg \pi T_c, H_{excR}$) is illustrated in Fig. 1b, which presents the results for the case $\gamma_M = 10$ and $\gamma_B = 0$ and fixed (large) values of H_{excL}. It is seen that for contacts of this kind one has $j_c(H_{excL}, H_{excR} = 0) \to 0$ ($\pi/2$ junctions). For an antiparallel orientation of the magnetizations of the banks of the junctions (the dashed curves in Fig. 1b) a substantial enhancement of the critical current takes place in the field interval $0 < H_{excR} < 0.3\pi T_c$. With increasing H_{excL} the value of the critical current amplitude at the maximum decreases, while the interval of H_{excR} values within which current enhancement occurs become narrower. In the geometry with a parallel orientation of the magnetizations of the banks (solid curves) an inversion of the sign of the current occurs already at low values of H_{excR}. It is impossible not to notice the mirror symmetry as a function of the supercurrent amplitude $j_c(H_{excL} \gg \pi T_c, H_{excR})$ of the junction on the geometry of the experiment. Consequently, by changing the magnetization direction on one of the banks of the junction, one can change the sign of the tunneling current while leaving its absolute value practically unchanged. Such junctions are undoubtedly of interest from the standpoint of experimental detection and study of the phenomena under discussion as well as for practical applications. Strictly speaking, this property of the junctions is achieved back by the choice of the parameters γ_M and γ_B of the boundaries. Apparently this requires additional experimental efforts. In the general case the curves of $j_c(H_{excL} \gg \pi T_c, H_{excR})$ are asymmetric with respect to the abscissa.

5. TEMPERATURE DEPENDENCE OF THE CRITICAL CURRENT

The temperature dependence of the critical current will be discussed for the example of symmetric SFIFS junctions. Figure 2 shows the results of a numerical calculation of the dependence of the critical current amplitude on the value of the exchange field at different temperatures. It is seen that for an antiparallel orientation of the magnetizations (the dashed curves) one observes enhancement of the critical current with increasing exchange field, with a pronounced feature at $T \to 0$, which is smoothed out with increasing temperature. That is, one should expect a substantial enhancement of the critical current at sufficiently low temperatures.[14] The interval of values of the exchange fields within which this enhancement exists becomes narrower with increasing temperature. For $T > 0.5T_c$ the enhancement of the critical current vanishes.

The transition to a state with a spontaneous π shift in the phases of the superconducting wave functions on the banks

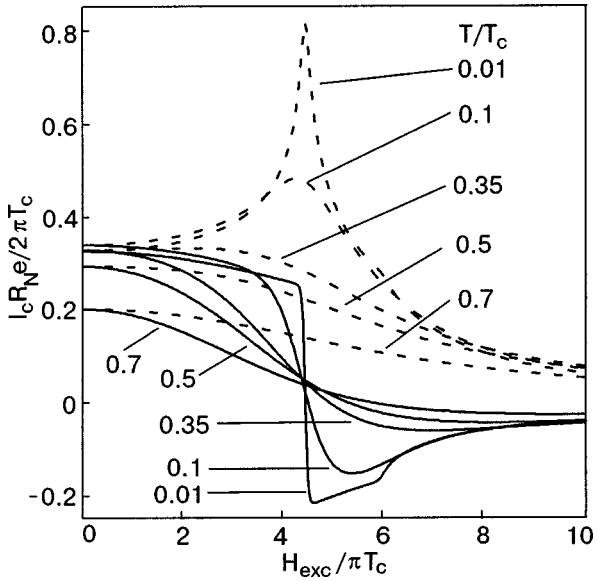

FIG. 2. Dependence of the critical current of a symmetric SFIFS junction with $\gamma_{ML}=\gamma_{MR}=0.1$ and $\gamma_{BL}=\gamma_{BR}=0.1$ on the exchange energy for various values of the temperature T/T_c.

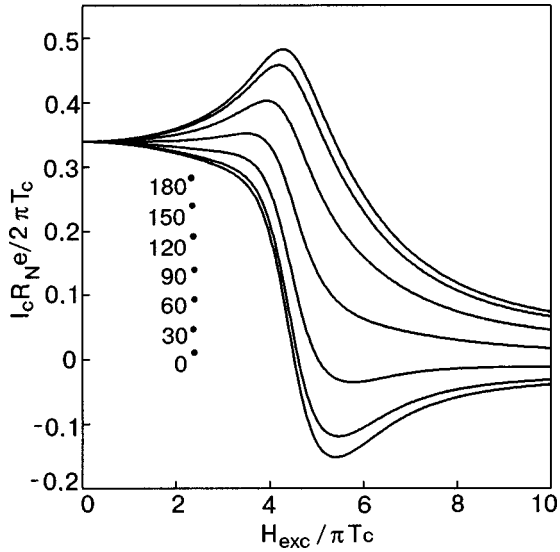

FIG. 3. Angular dependence of the critical current of a symmetric SFIFS junction on the exchange energy for various values of the angle between the magnetic moments of the ferromagnetic layers. $\gamma_{ML}=\gamma_{MR}=0.1$ and $\gamma_{BL}=\gamma_{BR}=0.1$, $T\ll T_c$.

of the junction is more stable against a change in temperature. The π state can occur in practically the entire temperature range in which the superconducting state exists.

In the case of a strong proximity effect ($\gamma_M\gg 1$) the enhancement vanishes at still lower temperatures, $T>0.15T_c$, and the point of transition of the junction to the π state is less sensitive to temperature than in the case of a weak proximity effect.

6. ANGULAR DEPENDENCE OF THE CRITICAL CURRENT

Let us consider the dependence of the critical current amplitude of an SFIFS junction on the angle between the directions of the magnetizations of its banks. (The magnetic moments in the layers are directed parallel to the plane of the junction but are misoriented with respect to each other by an angle θ.) With the use of the well-known relations of quantum mechanics (see, e.g., Ref. 28), the critical current amplitude of a junction in which the magnetizations of the banks are oriented at an angle θ can be written in the form

$$j_c(\theta)=j_c^p\cos^2(\theta/2)+j_c^a\sin^2(\theta/2), \tag{22}$$

where j_c^p and j_c^a are the critical current amplitudes for the parallel and antiparallel geometries, respectively.

Figure 3 illustrates the results of a numerical calculation of $j_c(\theta)$ according to formula (22) in the case of a weak proximity effect ($\gamma_M=0.1$) and a finite transparency of the boundaries ($\gamma_B=0.1$). The current amplitudes j_c^p and j_c^a were calculated with the use of relation (17). It is seen that the phenomena of enhancement and inversion of the current current are rather sensitive to noncollinearity of the magnetic moments of the F layers. Analogous results were obtained for contacts with a strong proximity effect.

Thus by varying the relative orientation of the magnetizations of the magnetic-field layers of an $(SF)_LI(FS)_R$ junction, one can switch from enhancement of the Josephson current to inversion of the current and π-phase superconductivity of the junction.

CONCLUSION

In the framework of a microscopic theory of the proximity effect for magnetic and superconducting metals we have studied the ground state and the critical current of asymmetric $(SF)_LI(FS)_R$ junctions. Attention was paid mainly to SFIFS systems with strong ferromagnetism of one of the banks and to the physics of the phenomena of inversion and enhancement of the critical current. It was shown that SFINS junctions with strong magnetism of the F layer are found in a state with a $\pi/2$ phase difference across its banks. We investigated the dependence of the dc Josephson effect in a SFIFS junction on the angle between the magnetic moments of its banks and on the temperature. We showed that by varying the magnetization direction on one of the banks of an asymmetric $(SF)_LI(FS)_R$ junction, one can change the sign of the tunneling current while leaving its absolute value practically unchanged.

The authors thank M. A. Belogolovskiĭ for a helpful discussion of this study.

*E-mail: krivoruc@krivoruc.fti.ac.donetsk.ua

[1] E. L. Wolf, *Principles of Electron Tunneling Spectroscopy*, Oxford University Press (1985).
[2] V. N. Krivoruchko and E. A. Koshina, Phys. Rev. B **66**, 014521 (2002).
[3] Yu. A. Izyumov, Yu. A. Proshin, and M. G. Khusainov, Usp. Fiz. Nauk **172**, 113 (2002).
[4] A. I. Buzdin, L. N. Bulaevskiĭ, and S. V. Panyukov, JETP Lett. **35**, 178 (1982).
[5] A. I. Buzdin and M. Yu. Kupriyanov, JETP Lett. **53**, 321 (1991).
[6] V. V. Ryazanov, V. A. Obozov, A. Yu. Rusanov, A. V. Veretennikov, A. A. Golubov, and J. Aarts, Phys. Rev. Lett. **86**, 2427 (2001).
[7] T. Kontos, M. Aprili, J. Lesuer, and X. Grison, Phys. Rev. Lett. **86**, 304 (2001).
[8] V. V. Ryazanov, V. A. Obozov, A. V. Veretennikov, and A. Yu. Rusanov, Phys. Rev. B **65**, 020501 (R) (2002).
[9] Y. Blum, A. Tsukernik, M. Karpovski, and A. Palevski, Phys. Rev. Lett. **89**, 187004 (2002).
[10] E. A. Koshina and V. N. Krivoruchko, JETP Lett. **71**, 123 (2000).
[11] E. A. Koshina and V. N. Krivoruchko, Phys. Rev. B **63**, 224515 (2001).

[12] F. S. Bergeret, A. F. Volkov, and K. E. Efetov, Phys. Rev. Lett. **86**, 3140 (2001).
[13] V. N. Krivoruchko and E. A. Koshina, Phys. Rev. B **64**, 172511 (2001).
[14] A. A. Golubov, M. Yu. Kupriyanov, and Ya. V. Fominov, JETP Lett. **75**, 223 (2002).
[15] V. N. Krivoruchko and R. V. Petryuk, Phys. Rev. B **66**, 134520 (2002).
[16] E. A. Koshina and V. N. Krivoruchko, Fiz. Nizk. Temp. **26**, 157 (2000) [Low Temp. Phys. **26**, 115 (2000)].
[17] A. A. Golubov and M. Yu. Kupriyanov, J. Low Temp. Phys. **70**, 83 (1988).
[18] M. Yu. Kupriyanov and V. F. Lukichev, Fiz. Nizk. Temp. **8**, 1045 (1982) [Low Temp. Phys. **8**, 526 (1982)].
[19] L. N. Bulaevskiĭ, V. V. Kuziĭ, and A. A. Sobyanin, JETP Lett. **25**, 290 (1977).
[20] A. V. Andreev, A. I. Buzdin, and R. M. Osgood, Phys. Rev. B **43**, 10124 (1991).
[21] M. Siegrist and T. M. Rice, J. Phys. Soc. Jpn. **61**, 4283 (1992).
[22] A. F. Volkov, Phys. Rev. Lett. **74**, 4730 (1995).
[23] J. J. A. Baselmans, A. F. Morpurgo, B. J. van Wees, and T. M. Klapwijk, Nature (London) **397**, 43 (1999).
[24] J. J. A. Baselmans, T. T. Heikkila, B. J. van Wees, and T. M. Klapwijk, Phys. Rev. Lett. **89**, 207002 (2002).
[25] E. A. Demler, G. B. Arnold, and M. R. Beasley, Phys. Rev. B **55**, 15174 (1997).
[26] A. A. Golubov and M. Yu. Kupriyanov, Zh. Éksp. Teor. Fiz. **96**, 1420 (1989) [Sov. Phys. JETP **69**, 805 (1989)].
[27] A. Zyuzin and B. Spivak, Phys. Rev. B **61**, 5902 (2000).
[28] L. D. Landau and E. M. Lifshitz, *Quantum Mechanics: Non-Relativistic Theory*, 3rd ed., Pergamon Press, Oxford (1977), Nauka, Moscow (1974).

Translated by Steve Torstveit

Electrical conductance of superconducting point contacts containing magnetic impurities

S. I. Beloborod'ko*

B. Verkin Institute for Low Temperature Physics and Engineering, National Academy of Sciences of Ukraine, pr. Lenina 47, 61103 Kharkov, Ukraine

(Submitted March 26, 2003)
Fiz. Nizk. Temp. **29**, 868–870 (August 2003)

The nonlinear electrical conductance of superconductor–constriction–normal-metal contacts containing magnetic impurities is investigated. The influence of the transparency of the potential barrier arising at the boundary of metals in contact on the behavior of the conductance and on the value of the excess current is analyzed. It is shown that in the case of a low transparency the differential conductance of such a contact is proportional to the electron density of states. © *2003 American Institute of Physics.* [DOI: 10.1063/1.1596793]

By studying the features of the nonlinear conductance $\sigma(V)=dI/dV$ and the temperature dependence of the excess current $I_{\rm exc}$ of superconductor–constriction–normal-metal (S–c–N) point contacts one can determine the value and temperature dependence of the energy gap $\Delta_0(T)$.[1,2] Thus for a clean contact ($l_i \gg a$, l_i is the elastic mean free path of the electrons, and a is the diameter of the contact)

$$I_{\rm exc}=\frac{4}{3}\frac{1}{R}\Delta_0(T), \tag{1}$$

where R is the contact resistance in the normal state.

As was shown in Ref. 3, the presence of magnetic impurities in the superconductor affects the current–voltage characteristic and excess current of an S–c–N contact. As the concentration of magnetic impurities increases, the feature on the nonlinear conductance of the contact due to the energy gap begins to smear out and shift to lower energies, and the excess current is no longer determined by the value of the energy gap but depends on the value of the order parameter $\Delta(T)$, which is related to $\Delta_0(T)$ by the expression[4]

$$\Delta_0(T)=\Delta(T)(1-g^{2/3})^{3/2} \tag{2}$$

($g=1/(\Delta(T)\tau_s)$, where τ_s is the mean free time for spin-flip scattering on the impurities).

For $g>1$ the gap in the spectrum of the superconductor is equal to zero, while the order parameter remains nonzero in a certain region of magnetic impurity concentrations (gapless region). In this region[3]

$$I_{\rm exc}=\frac{\pi}{8}\frac{1}{R}\Delta(T)^2\tau_s\tanh\left(\frac{eV}{2T}\right) \tag{3}$$

there occurs a change in the temperature dependence of the excess current, which near T_c is proportional to $(1-T/T_c)$, while for a superconductor without magnetic impurities Eq. (1) gives $I_{\rm exc}\sim(1-T/T_c)^{1/2}$.

In Ref. 3 the problem of S–c–N contacts containing magnetic impurities was considered for the case of a boundary transparency $d=1$. In an experiment, because of the difference of the parameters of the metals in contact, one actually has $d<1$. It is therefore of interest to study the influence of arbitrary transparency of the potential barrier arising at the boundary on the nonlinear conductance and excess current of S–c–N contacts containing magnetic impurities. Using the standard method of solving a system of equations for the Green's functions in an S–c–N contact[5] with the boundary conditions obtained in Ref. 2 for the interface between metals, we obtain for the current–voltage characteristic of the contact

$$\begin{aligned} I(V)=\frac{1}{R}\int_{-\infty}^{+\infty}d\varepsilon\left[\tanh\left(\frac{\varepsilon+eV}{2T}\right)+\tanh\left(\frac{\varepsilon+eV}{2T}\right)\right] \\ \times|(2d^{-1}-1)+G_\varepsilon|^{-2}\{|1+G_\varepsilon|^2+|F_\varepsilon|^2 \\ +4(d^{-1}-1)\mathrm{Re}(G_\varepsilon)\}, \end{aligned} \tag{4}$$

$$G_\varepsilon=u/(u^2-1)^{1/2};\quad F_\varepsilon=1/(u^2-1)^{1/2},$$

where $u=\varepsilon/\Delta_\varepsilon$ is determined from the equation (Δ_ε is a complex energy-dependent order parameter of the superconductor[4])

$$\frac{\varepsilon}{\Delta(T)}=u[1-g(1-u^2)^{-1/2}]. \tag{5}$$

In the absence of magnetic impurities τ_s goes to infinity, and formula (4) agrees with the expression for the current obtained in Ref. 2.

To explain the experimental results on the current–voltage characteristics of S–c–N contacts containing magnetic impurities[6,7] a modified Blonder–Tinkham–Klapwijk (BTK) theory[8] that takes into account the smearing of the density of quasiparticle states due to the finite damping time of the electrons is often used. Formally the results of the BTK theory in the framework of the model considered here are obtained in the strong depairing regime ($|u|\gg 1$). In this case we obtain from Eq. (5) the following expression for u:

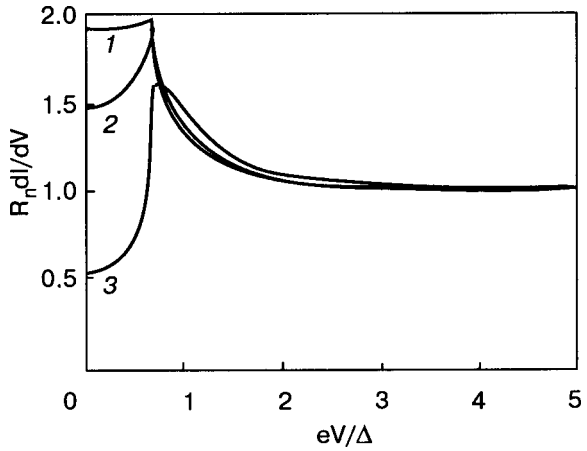

FIG. 1. Normalized conductance $R_n dI/dV$ for $g=1/(\Delta\tau_s)=0.1$ ($\Delta_0/\Delta=0.694$) versus eV/Δ for different d: 0.99 (*1*), 0.9 (*2*), 0.56 (*3*).

$$u=\frac{\varepsilon}{\Delta(T)}+ig \quad (i=(-1)^{1/2}). \tag{6}$$

For $eV\gg\max(\Delta(T),1/\tau_s)$, by writing Eq. (4) in the form $I=V/R+I_{\rm exc}$ we obtain for the excess current $I_{\rm exc}$

$$I_{\rm exc}=\frac{\pi}{8}\frac{1}{R_n}\Delta(T)^2 d\tau_s\tanh\left(\frac{eV}{2T}\right), \tag{7}$$

where R_n is the renormalized resistance of the contact in the normal state, $R_n=R(d=1)/d$. From a comparison of formulas (3) and (7) it follows that decreasing the transparency of the barrier will lead to a decrease of the excess current.

By differentiating expression (4) we get for the conductance $\sigma(V)$ at $T=0$

$$\sigma(V)=\frac{1}{R}|(2d^{-1}-1)+G_\varepsilon|^{-2}\{|1-G_\varepsilon|^2+|F_\varepsilon|^2 +4(d^{-1}-1)\mathrm{Re}(G_\varepsilon)\}_{\varepsilon=eV}. \tag{8}$$

The $\sigma(V)$ curves are shown in Fig. 1 for different values of d. In contrast to the results of Ref. 3, here the conductance has a minimum at zero voltage V (the ''zero'' anomaly that is often observed experimentally[6]).

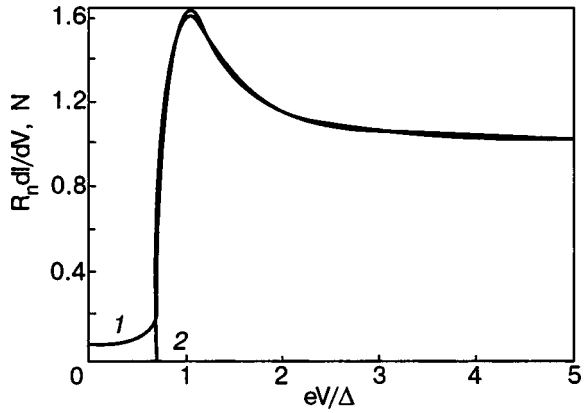

FIG. 2. Normalized conductance $R_n dI/dV$ for $g=1/(\Delta\tau_s)=0.1$ ($\Delta_0/\Delta=0.694$) versus eV/Δ for $d=0.1$ (*1*), and the electron density of states N (*2*).

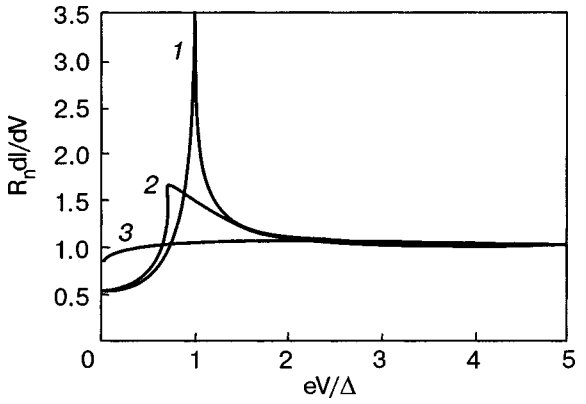

FIG. 3. Normalized conductance $R_n dI/dV$ for $d=0.56$ and different values of $g=1/(\Delta\tau_s)$: 0 (*1*), 0.1 (*2*), 1.1 (*3*).

With decreasing transparency of the barrier the character of the dependence of the conductance goes over from the regime of direct conduction of the contact to tunneling regimes for which $\sigma(V)$ is proportional to to the electron density of states. The normalized differential conductance (for $d=0.1$, $g=0.1$) and the density of states (for which we will not give the details of the calculation) are shown in Fig. 2. It is seen that the curves practically coincide.

The $\sigma(V)$ curve for $d=0.56$ is shown in Fig. 3 for different values of g. As in the case $d=1$, the maximum on the $\sigma(V)$ curve is shifted to lower energies with increasing g, and the relative value of this maximum decreases.

The results of this study show that in the case when the transparency of the barrier in an S–c–N contact containing magnetic impurities is less than unity, a minimum of the conductance appears at zero voltage. Decreasing the transparency causes a decrease of the excess current. In the limit of low transparency the differential conductance of the contact is proportional to the electron density of states.

In closing the author thanks A. N. Omel'yanchuk and I. K. Yanson for a helpful discussion.

*E-mail: biloborodko@ilt.kharkov.ua

[1] A. V. Zaĭtsev, Zh. Éksp. Teor. Fiz. **78**, 221 (1980) [Sov. Phys. JETP **51**, 1111 (1980)].
[2] A. V. Zaĭtsev, Zh. Éksp. Teor. Fiz. **86**, 1742 (1984) [Sov. Phys. JETP **59**, 1015 (1984)].
[3] S. I. Beloborod'ko and A. N. Omel'yanchuk, Fiz. Nizk. Temp. **17**, 994 (1991) [Sov. J. Low Temp. Phys. **17**, 518 (1991)].
[4] A. A. Abrikosov and V. P. Gor'kov, Zh. Éksp. Teor. Fiz. **39**, 1781 (1960) [Sov. Phys. JETP **12**, 1243 (1961)].
[5] V. A. Khlus and A. N. Omel'yanchuk, Fiz. Nizk. Temp. **11**, 543 (1985) [Sov. J. Low Temp. Phys. **11**, 298 (1985)].
[6] Yu. G. Naidyuk, A. V. Moskalenko, I. K. Yanson, and C. Geibel, Fiz. Nizk. Temp. **24**, 495 (1998) [Low Temp. Phys. **24**, 374 (1998)].
[7] A. V. Moskalenko, Yu. G. Naidyuk, I. K. Yanson, M. Hedo, Y. Inada, Y. Onuki, Y. Haga, and E. Yamamoto, Fiz. Nizk. Temp. **27**, 831 (2001) [Low Temp. Phys. **27**, 613 (2001)].
[8] A. Plecenik, M. Grajcar, S. Benacka, P. Seidel, and A. Pfuch, Phys. Rev. B **49**, 10016 (1994).

Translated by Steve Torstveit

LOW-TEMPERATURE MAGNETISM

Magnetoelastic surface waves in a semi-infinite ferromagnet in an external magnetic field

Yu. A. Fridman* and D. V. Spirin

V. I. Vernadskiĭ Tavricheskiĭ National University, ul. Yaltinskaya 4, 95007 Simferopol, Ukraine
(Submitted August 19, 2002; revised January 20, 2003)
Fiz. Nizk. Temp. **29**, 871–877 (August 2003)

The magnetoelastic wave spectra are found for a semi-infinite Heisenberg ferromagnet in an external magnetic field. Near the surface of the ferromagnet the interaction of Rayleigh waves with surface spin waves gives rise to an additional activation energy in the spin-wave spectrum and leads to a decrease in the sound velocity. The magnetoelastic coupling increases the difference between the velocity of surface acoustic waves and that of bulk sound waves. © *2003 American Institute of Physics.* [DOI: 10.1063/1.1596794]

INTRODUCTION

The great progress achieved in nanotechnology in recent years has made it possible to create ultrathin magnetic films.[1,2] In this connection the nature of the surface magnetism in such systems becomes a topical question. Although this problem has been the subject of a large number of papers,[3–15] interest in it continues unabated.

The theoretical model usually chosen to describe the surface properties of the system (the magnetic crystal or film) is that of a semi-infinite Heisenberg ferromagnet, i.e., a ferromagnet occupying a half space with one free surface.[3] For example, the thermodynamic properties of the semi-infinite Ising and Heisenberg models were studied in Ref. 5. The temperature dependence of the surface magnetization was investigated in Ref. 6. The contribution of surface spin waves to the thermodynamics of the system was the subject of Refs. 7 and 8. The influence of the anisotropy field on the thermodynamics of a magnet near the surface of the sample was studied in Refs. 9–13. In such systems a rotation of the magnetization vector with depth can occur as a result of the presence of a magnetic field or a dipole interaction.[14] The spectra of surface spin waves of isotropic (and anisotropic with respect to exchange) Heisenberg ferromagnets with different types of crystal lattices were studied in Ref. 15.

However, a model taking into account only the exchange and single-ion interactions is not completely adequate, since in addition to the magnetic there are also elastic degrees of freedom, which have a substantial influence on the behavior of the system.[16] This now is an active research topic. For example, in Ref. 17 the existence of a new type of surface excitations was predicted, due to the presence of a piezomagnetic effect in the system studied. The velocity of propagation of surface acoustic excitations in ferro- and antiferromagnets and the possibility of controlling this velocity were studied in Ref. 18.

As we have said, surface spin waves that decay into the interior of the sample can exist near the surface. It has been determined[3] that the frequency of these surface spin waves differs insignificantly from the frequency of bulk waves: the difference of their energies is a quantity of order $\mathbf{k}_{\|}^4$, where $\mathbf{k}$ is the wave vector. It was shown, in particular, that in this respect they are different from Rayleigh acoustic waves, the frequency of which differs from that of bulk phonons in the first order of $\mathbf{k}_{\|}$.

Since the properties of any real magnetic material depend in part on the coupling of its atomic magnetic moments with the elastic subsystem, it is of interest to take the coupling of the spins with the elastic strain field of the crystal lattice into account in the model we are considering. We will be interested primarily in the coupling of surface spin waves with Rayleigh acoustic waves.

As the method of study we have chosen the time Green's function technique, the details of which for systems of a similar type have been set forth in Ref. 10.

CALCULATION OF THE GREEN'S FUNCTIONS

We choose as our model a semi-infinite Heisenberg ferromagnet with the magnetoelastic coupling taken into account. The OY axis of the Cartesian coordinate system is directed perpendicular to the surface in such a way that the unoccupied half plane corresponds to positive values of y. The OX and OZ axes are parallel to the surface. In such a geometry the position of an atom is determined by the vector $\mathbf{l}=\mathbf{l}_{\|}+\mathbf{y}\ell$, where $\ell=0$ corresponds to the outer layer.

We assume that the exchange integral in the surface layer, J_S, is different from the exchange integral in the layers with $\ell>0$, which we denote by J, and that the exchange coupling between layers is $J_{\perp}$. The ferromagnet is found in an external magnetic field directed along the OZ axis. We shall assume that the magnetoelastic coupling and the elastic energy are isotropic. Then the Hamiltonian of the system can be written in the form

$$\mathcal{H}=-\frac{1}{2}\sum_{\mathbf{l}_\parallel}\sum_{\boldsymbol{\delta}_\parallel} J_S(\delta_\parallel)\mathbf{S}(\mathbf{l}_\parallel 0)\cdot\mathbf{S}(\mathbf{l}_\parallel+\boldsymbol{\delta}_\parallel,0)$$

$$-\frac{1}{2}\sum_{\mathbf{l}_\parallel}\sum_{\boldsymbol{\delta}_\parallel}\sum_{\ell=1}^{\infty} J(\boldsymbol{\delta}_\parallel)\mathbf{S}(\mathbf{l}_\parallel\ell)\cdot\mathbf{S}(\mathbf{l}_\parallel+\delta_\parallel,\ell)$$

$$-\sum_{\mathbf{l}_\parallel}\sum_{\Delta_\parallel}\sum_{\ell=1}^{\infty} J(\Delta_\parallel)\mathbf{S}(\mathbf{l}_\parallel\ell)\cdot\mathbf{S}(\mathbf{l}_\parallel+\boldsymbol{\Delta}_\parallel,\ell+1)$$

$$-H_0\sum_{\mathbf{l}_\parallel}\sum_{\ell=1}^{\infty} S_z(\mathbf{l}_\parallel\ell)+\mathcal{H}_{me}+\mathcal{H}_e. \tag{1}$$

Here $\mathbf{S}(\mathbf{l}_\parallel\ell)$ is the spin at site $\mathbf{l}$, $\boldsymbol{\delta}_\parallel$ is a vector between nearest neighbors in the layer, $\boldsymbol{\Delta}_\parallel$ is a vector between nearest neighbors in adjacent layers, H_0 is the external magnetic field, and $\mathcal{H}_{me}$ and $\mathcal{H}_e$ are the Hamiltonians of the magnetoelastic and elastic interactions.

The Hamiltonian of the magnetoelastic interaction in (1) can be written in the form

$$\mathcal{H}_{me}=\lambda\sum_{\mathbf{l}_\parallel}\sum_{\ell=0}^{\infty}\sum_{i,j=x,y,z} u_{ij}(\ell)S_i(\mathbf{l}_\parallel\ell)S_j(\mathbf{l}_\parallel\ell), \tag{2}$$

where u_{ij} are components of the strain tensor, which we shall assume are dependent on ℓ, and λ is the magnetoelastic coupling constant. The elastic energy of the system has the form

$$\mathcal{H}_e=\sum_{\ell=0}^{\infty}\int dxdz\,\frac{E}{2(1-\sigma^2)}(u_{xx}^2+u_{yy}^2+u_{zz}^2)$$

$$+\sum_{\ell=0}^{\infty}\int dxdz\,\frac{E}{2(1-\sigma^2)}\{2\sigma(u_{xx}u_{yy}+u_{xx}u_{zz}$$

$$+u_{yy}u_{zz})+2(1-\sigma)(u_{xy}^2+u_{xz}^2+u_{yz}^2)\}, \tag{3}$$

where E is Young's modulus, σ is Poisson's ratio, and for brevity of notation we have stopped indicating that the components of the strain tensor are functions of ℓ. In writing Hamiltonian (3) it is necessary to take into account the crystal structure of the system. For example, for a system with cubic symmetry the elastic energy will be determined by three elastic constants: C_{11}, C_{12}, and C_{44}. These elastic constants C_{ij} are related to the coefficients E and σ (Ref. 19). The approximation we have made will lead to a quantitative difference but will not alter the results qualitatively.

We use the Holstein–Primakoff transformation[20] for the spin operators:

$$S^+(\mathbf{l}_\parallel\ell)=\sqrt{2S}a(\mathbf{l}_\parallel\ell),\quad S^z(\mathbf{l}_\parallel\ell)=S-a^+(\mathbf{l}_\parallel\ell)a(\mathbf{l}_\parallel\ell),$$

where $a^+(\mathbf{l}_\parallel\ell)$ and $a(\mathbf{l}_\parallel\ell)$ are magnon creation and annihilation operators, and S is the spin of the magnetic ion. The Fourier transform of the operator $a(\mathbf{l}_\parallel\ell)$ has the form

$$a(\mathbf{l}_\parallel\ell)=\frac{1}{N}\sum_{\mathbf{k}_\parallel} a(\mathbf{k}_\parallel\ell)\exp(i\mathbf{k}_\parallel\cdot\mathbf{l}_\parallel),$$

and an analogous transformation can be done for $a^+(\mathbf{l}_\parallel\ell)$.

We write the strain vector $\mathbf{u}(\ell)$ in the form

$$\mathbf{u}(\mathbf{k}_\parallel\ell)=\mathbf{u}^{(0)}(\ell)+\mathbf{u}^{(1)}(\mathbf{k}_\parallel\ell),$$

where $\mathbf{u}^{(0)}(\ell)$ are the spontaneous strains and $\mathbf{u}^{(1)}(\mathbf{k}_\parallel\ell)$ is the dynamic part of the strain vector. Quantizing $\mathbf{u}^{(1)}(\mathbf{k}_\parallel\ell)$ in the standard way,[21] we obtain

$$\mathbf{u}^{(1)}(\mathbf{k}_\parallel\ell)=\sqrt{\frac{1}{2N}}\sum_{\mathbf{k}_\parallel}\frac{\mathbf{e}}{\sqrt{m\omega_0(\mathbf{k}_\parallel)}}[b^+(\mathbf{k}_\parallel\ell)\exp(i\mathbf{k}\cdot\mathbf{r})$$

$$+b(\mathbf{k}_\parallel\ell)\exp(-i\mathbf{k}\cdot\mathbf{r})]$$

(where $\mathbf{e}$ is the unit vector of the phonon polarization, m is the mass of the magnetic ion, $\omega_0(\mathbf{k}_\parallel)$ is the phonon frequency without allowance for the magnetoelastic coupling, and b^+ (b) is the phonon creation (annihilation) operator) and, using the Holstein–Primakoff transformation, we can write the Hamiltonian (1) in the form

$$\mathcal{H}_{SW}=\sum_{\ell}\sum_{\mathbf{k}_\parallel}\omega_0(\mathbf{k}_\parallel)b^+(\mathbf{k}_\parallel\ell)b(\mathbf{k}_\parallel\ell)$$

$$+\sum_{\mathbf{k}_\parallel} d_\parallel^S(\mathbf{k}_\parallel)a^+(\mathbf{k}_\parallel 0)a(\mathbf{k}_\parallel 0)$$

$$+\sum_{\ell}\sum_{\mathbf{k}_\parallel} d_\parallel(\mathbf{k}_\parallel)a^+(\mathbf{k}_\parallel\ell)a(\mathbf{k}_\parallel\ell)$$

$$-\sum_{\ell}\sum_{\mathbf{k}_\parallel} d_\perp(\mathbf{k}_\parallel)a^+(\mathbf{k}_\parallel\ell)a(\mathbf{k}_\parallel\ell+1)$$

$$-\sum_{\ell}\sum_{\mathbf{k}_\parallel} d_\perp(\mathbf{k}_\parallel)a^+(\mathbf{k}_\parallel\ell+1)a(\mathbf{k}_\parallel\ell)$$

$$+\frac{1}{2}\sum_{\ell}\sum_{\mathbf{k}_\parallel} N(\ell)[a^+(\mathbf{k}_\parallel\ell)a^+(\mathbf{k}_\parallel\ell)$$

$$+a(\mathbf{k}_\parallel\ell)a(\mathbf{k}_\parallel\ell)]+\sum_{\ell}\sum_{\mathbf{k}_\parallel}\Phi(\mathbf{k}_\parallel\ell)$$

$$\times[a(\mathbf{k}_\parallel\ell)b(\mathbf{k}_\parallel\ell)-a^+(\mathbf{k}_\parallel\ell)b(\mathbf{k}_\parallel\ell)]$$

$$+\sum_{\ell}\sum_{\mathbf{k}_\parallel}\Phi^*(\mathbf{k}_\parallel\ell)[a^+(\mathbf{k}_\parallel\ell)b^+(\mathbf{k}_\parallel\ell)$$

$$-a(\mathbf{k}_\parallel\ell)b^+(\mathbf{k}_\parallel\ell)]. \tag{4}$$

In Eq. (4) we have introduced the following notation:

$$d_\parallel^S(\mathbf{k}_\parallel)=H_0+I_S(0)-I_S(\mathbf{k}_\parallel)+I_\perp(0)+H_S,$$

$$d_\perp(\mathbf{k}_\parallel)=I_\perp(\mathbf{k}_\parallel),$$

$$d_\parallel(\mathbf{k}_\parallel)=H_0+I(0)-I(\mathbf{k}_\parallel)+2I_\perp(0)+H_B,$$

$$I_S(\mathbf{k}_\parallel)=S\sum_{\delta_\parallel} J_S(\boldsymbol{\delta}_\parallel)\exp(i\mathbf{k}_\parallel\cdot\boldsymbol{\delta}_\parallel),$$

$$I(\mathbf{k}_\parallel)=S\sum_{\boldsymbol{\delta}_\parallel} J(\boldsymbol{\delta}_\parallel)\exp(i\mathbf{k}_\parallel\cdot\boldsymbol{\delta}_\parallel),$$

$$I_\perp(\mathbf{k}_\parallel)=S\sum_{\Delta_\parallel} J_\perp(\boldsymbol{\Delta}_\parallel)\exp(i\mathbf{k}_\parallel\cdot\boldsymbol{\Delta}_\parallel),$$

$$\mathrm{N}(\ell)=\lambda S[u_{xx}^{(0)}(\ell)-u_{yy}^{(0)}(\ell)],$$

$$H_B=\lambda S[u_{xx}^{(0)}(\ell)+u_{yy}^{(0)}(\ell)-2u_{zz}^{(0)}(\ell)],$$

$$H_S=\lambda S[u_{xx}^{(0)}(0)+u_{yy}^{(0)}(0)-2u_{zz}^{(0)}(0)],$$

$$\Phi(\mathbf{k}_\parallel \ell) = \frac{\lambda S}{2}\sqrt{\frac{S}{m\omega_0}}[e_y k_z + e_z k_y + i(e_x k_z + e_z k_x)].$$

In the function $\Phi(\mathbf{k}_\parallel \ell)$ the dependence on ℓ is determined by the components of the polarization vector e_i.

We introduce the Green's functions

$$G_{-+}(\mathbf{k}_\parallel t;\ell\ell') = i\Theta(t)\langle[a(\mathbf{k}_\parallel \ell;t)a^+(\mathbf{k}_\parallel \ell';0)]\rangle,$$
$$G_{++}(\mathbf{k}_\parallel t;\ell\ell') = i\Theta(t)\langle[a^+(\mathbf{k}_\parallel \ell;t)a^+(\mathbf{k}_\parallel \ell';0)]\rangle,$$
$$D_{-+}(\mathbf{k}_\parallel t;\ell\ell') = i\Theta(t)\langle[b(\mathbf{k}_\parallel \ell;t)a^+(\mathbf{k}_\parallel \ell';0)]\rangle,$$
$$D_{++}(\mathbf{k}_\parallel t;\ell\ell') = i\Theta(t)\langle[b^+(\mathbf{k}_\parallel \ell;t)a^+(\mathbf{k}_\parallel \ell';0)]\rangle. \quad (5)$$

Fourier transformation of the Green's function $G_{-+}(\mathbf{k}_\parallel t;\ell\ell')$ with respect to time gives

$$G_{-+}(\mathbf{k}_\parallel t;\ell\ell')\int_{-\infty}^{\infty}\frac{d\Omega}{2\pi}\exp(i\Omega t)G_{-+}(\mathbf{k}_\parallel \Omega + i\eta;\ell\ell').$$

The Fourier transforms for the remaining Green's functions have an analogous form. We write an equation of motion for the Green's function $G_{-+}(\mathbf{k}_\parallel t;\ell\ell')$:

$$i\frac{\partial}{\partial t}G_{-+}(\mathbf{k}_\parallel t;\ell\ell') = -\delta(t)\delta_{\ell\ell'} + i\Theta(t) \times\langle\{[a(\mathbf{k}_\parallel \ell;t),\mathcal{H}_{SW}],a^+(\mathbf{k}_\parallel \ell';0)\}\rangle. \quad (6)$$

Doing the Fourier transformation with respect to time in (6), we obtain

$$\begin{aligned}\Omega G_{-+}(\mathbf{k}_\parallel \Omega;\ell\ell') = &-\delta_{\ell\ell'} + \delta_{\ell 0}d_\parallel^S(\mathbf{k}_\parallel)G_{-+}(\mathbf{k}_\parallel \Omega;\ell\ell')\\ &+(1-\delta_{\ell 0})d_\parallel(\mathbf{k}_\parallel)G_{-+}(\mathbf{k}_\parallel \Omega;\ell\ell')\\ &-d_\perp(\mathbf{k}_\parallel)G_{-+}(\mathbf{k}_\parallel \Omega;\ell+1,\ell')\\ &-(1-\delta_{\ell 0})d_\perp(\mathbf{k}_\parallel)G_{-+}(\mathbf{k}_\parallel \Omega;\ell\\ &-1,\ell')+\mathrm{N}(\ell)G_{++}(\mathbf{k}_\parallel \Omega;\ell\ell')\\ &-\Phi(\mathbf{k}_\parallel \ell)D_{-+}(\mathbf{k}_\parallel \Omega;\ell\ell')\\ &+\Phi^*(\mathbf{k}_\parallel \ell)D_{++}(\mathbf{k}_\parallel \Omega;\ell\ell').\end{aligned}$$

This equation can be transformed to

$$\begin{aligned}G_{-+}(\mathbf{k}_\parallel z;\ell\ell') = &G_0(z;\ell\ell') - \mathrm{N}(\ell)G_0(z;\ell\ell')\\ &\times G_{++}(\mathbf{k}_\parallel z;\ell\ell')\\ &+\Phi(\mathbf{k}_\parallel \ell)G_0(z;\ell\ell')\\ &\times D_{-+}(\mathbf{k}_\parallel \Omega;\ell\ell') - \Phi^*(\mathbf{k}_\parallel \ell)\\ &\times G_0(z;\ell\ell')D_{++}(\mathbf{k}_\parallel z;\ell\ell').\end{aligned}$$

Here we have gone over to the complex plane, $\Omega\to z$, and have introduced the resolvent

$$\begin{aligned}G_0(z;\ell\ell') = &[z\delta_{\ell\ell'} - \hat{\mathbf{K}}(\ell\ell')]^{-1},\ \hat{\mathbf{K}}(\ell\ell')\\ &= \delta_{\ell\ell'}[\delta_{\ell 0}d_\parallel^S + (1-\delta_{\ell 0})d_\parallel^S] - \delta_{\ell'\ell+1}d_\perp\\ &-\delta_{\ell'\ell-1}(1-\delta_{\ell 0})d_\perp.\end{aligned}$$

An analogous equation for the Green's function for a semi-infinite Heisenberg ferromagnet was obtained in Ref. 10. Besides the equation for $G_{-+}(\mathbf{k}_\parallel z;\ell\ell')$, we will need three more equations:

$$\begin{aligned}G_{++}(\mathbf{k}_\parallel z;\ell\ell') = &-\mathrm{N}(\ell)G_0(-z;\ell\ell')G_{-+}(\mathbf{k}_\parallel z;\ell\ell')\\ &-\Phi(\mathbf{k}_\parallel \ell)G_0(-z;\ell\ell')\\ &\times D_{-+}(\mathbf{k}_\parallel \Omega;\ell\ell') + \Phi^*(\mathbf{k}_\parallel \ell)\\ &\times G_0(-z;\ell\ell')D_{++}(\mathbf{k}_\parallel z;\ell\ell'),\\ zD_{-+}(\mathbf{k}_\parallel z;\ell\ell') = &-\Phi^*(\mathbf{k}_\parallel \ell)G_{-+}(\mathbf{k}_\parallel \Omega;\ell\ell')\\ &+\Phi^*(\mathbf{k}_\parallel \ell)G_{++}(\mathbf{k}_\parallel z;\ell\ell')\\ &+\omega_0(\mathbf{k}_\parallel)D_{-+}(\mathbf{k}_\parallel z;\ell\ell'),\\ zD_{++}(\mathbf{k}_\parallel z;\ell\ell') = &-\Phi(\mathbf{k}_\parallel \ell)G_{-+}(\mathbf{k}_\parallel \Omega;\ell\ell')\\ &+\Phi(\mathbf{k}_\parallel \ell)G_{++}(\mathbf{k}_\parallel z;\ell\ell')\\ &-\omega_0(\mathbf{k}_\parallel)D_{++}(\mathbf{k}_\parallel z;\ell\ell').\end{aligned}$$

The solution of this system has the form

$$G_{-+}(\mathbf{k}_\parallel z;\ell\ell') = \frac{G_0(z;\ell\ell')[1-\Lambda G_0(-z;\ell\ell')]}{1-\Lambda[G_0(-z;\ell\ell')+G_0(z;\ell\ell')]-G_0(z;\ell\ell')G_0(-z;\ell\ell')(2\mathrm{N}\Lambda+\mathrm{N}^2)}, \quad (7)$$

where for brevity of notation we have not indicated the dependence of Λ and N on $\mathbf{k}_\parallel$ and ℓ. The quantity

$$\Lambda(\mathbf{k}_\parallel \ell) = -\frac{2\omega_0}{z^2-\omega_0^2}|\Phi(\mathbf{k}_\parallel \ell)|^2$$

is proportional to the phonon Green's function.[22] The poles of the Green's function (7) determine the spectra of magnetoacoustic waves.

The zeroth magnon Green's function $G_0(z;\ell\ell')$, which was obtained in Ref. 10, can be written as

$$G_0(z;\ell\ell') = g_\infty(z)\left[\exp(i\kappa_\perp|\ell-\ell'|) - \exp[i\kappa_\perp(\ell+\ell')]\frac{g_s(z,\kappa_\perp)}{g_s(z,-\kappa_\perp)}\right], \quad (8)$$

where

$$g_\infty(z) = \frac{i}{2d_\perp(\mathbf{k}_\parallel)\sin[\kappa_\perp(z)]} \quad (9)$$

is the Green's function of the bulk sample,

$$g_s(z) = \frac{1}{d_\parallel^S(\mathbf{k}_\parallel) - d_\parallel(\mathbf{k}_\parallel) + d_\perp(\mathbf{k}_\parallel)\exp[-i\kappa_\perp(z)]} \quad (10)$$

is the Green's function of the surface in the absence of magnetoelastic coupling,

$$\cos[\kappa_\perp(z)]=\frac{d_\parallel - z}{2d_\perp}, \tag{11}$$

where $\kappa_\perp(z)$ is chosen so that one always has $\mathrm{Im}(\kappa_\perp)>0$. For fixed $\mathbf{k}_\parallel$ the frequencies of the surface spin waves are found in regions above $\Omega_m(\mathbf{k}_\parallel)$ and below $\Omega_M(\mathbf{k}_\parallel)$,[10] where

$$\Omega_m(\mathbf{k}_\parallel)=d_\parallel(\mathbf{k}_\parallel)-2d_\perp(\mathbf{k}_\parallel),$$

$$\Omega_M(\mathbf{k}_\parallel)=d_\parallel(\mathbf{k}_\parallel)+2d_\perp(\mathbf{k}_\parallel).$$

We shall further assume that the crystal has a simple cubic lattice and that the distance between layers and between nearest neighbors within a layer is equal to a_0. The exchange coupling between layers and in the plane will be assumed equal: $J=J_\perp=J_S/\varepsilon$. Then in the long-wavelength limit

$$d_\parallel(\mathbf{k}_\parallel)=H_0+2H_x+H_S+\frac{1}{8}H_x a_0^2 k_\parallel^2-\ldots,$$

$$d_\parallel^S(\mathbf{k}_\parallel)=H_0+H_x+H_B+\frac{1}{8}\varepsilon H_x a_0^2 k_\parallel^2-\ldots,$$

$$d_\perp(\mathbf{k}_\parallel)=H_x-\frac{1}{4}H_x a_0^2 k_\parallel^2-\ldots,\quad H_x=4SJ. \tag{12}$$

ANALYSIS OF THE SOLUTIONS

Waves for $\ell\to\infty$

In this case $\kappa_\perp$ is real and

$$G_0(z,\ell\ell')=\frac{i}{2d_\perp(\mathbf{k}_\parallel)\sin[\kappa_\perp(z)]}=\frac{i}{\sqrt{4d_\perp^2-(d_\parallel-\Omega_S)^2}}.$$

Here Ω_S is the spin-wave frequency and Ω_A is the frequency of acoustic vibrations.

As is easily shown, in the interior of the sample the spontaneous strains have the form

$$u_{xx}^{(0)}=u_{yy}^{(0)}=\frac{\lambda S^2}{E}\frac{\sigma(\sigma+1)}{1+2\sigma},$$

$$u_{zz}^{(0)}=-\frac{\lambda S^2}{E}\frac{(\sigma+1)^2}{1+2\sigma}. \tag{13}$$

It follows that $\mathrm{N}(\ell)=0$. Then the spin-wave dispersion relation is determined from the condition

$$\frac{1}{G_0(z;\ell\ell')}=0.$$

It follows from this last equation that

$$\sqrt{4d_\perp^2-(d_\parallel-\Omega_S)^2}=0,$$

from which we obtain the lower boundary of the continuous spectrum of spin-wave frequencies:

$$\Omega_{Sm}=H_0+H_B+\frac{5}{8}H_x a_0^2 k_\parallel^2,\quad H_B=2\lambda^2 S^2\frac{1+3\sigma}{E}. \tag{14}$$

The spectrum of acoustic waves is determined from the condition

$$1-\Lambda(\mathbf{k}_\parallel\ell)[G_0(-z;\ell\ell')+G_0(-z;\ell\ell')]=0,$$

the solution of which gives the spectrum of acoustic excitations:

$$\Omega_{A,i}=s_i\mathbf{k}_\parallel. \tag{15}$$

The index i takes values of t or ℓ and denotes the different polarizations of the acoustic wave; s_i is the sound velocity for the ith polarization:

$$s_t=s_{t0}\sqrt{1-\frac{S^3\lambda^3\cos^2\varphi_k}{m_0 s_{t0}^2 A}},$$

$$s_\ell=s_{\ell 0}\sqrt{1-\frac{S^3\lambda^2\sin^2\varphi_k}{m_0 s_{\ell 0}^2 A}}, \tag{16}$$

where φ_k is the angle between the wave vector and the OZ axis, and s_{i0} is the velocity of i-polarized sound in the crystal in neglect of the magnetoelastic coupling. The parameter A is introduced for brevity of notation and is defined as

$$A=\sqrt{(H_0+H_B)(H_0+4H_x+H_B)}.$$

Waves on the surface $\ell=0$

In the case of surface waves $\kappa_\perp$ is purely imaginary, and

$$G_0(z;00)=[d_\parallel^S-d_\parallel+d_\perp(\mathbf{k}_\parallel)\exp(-i\kappa_\perp(z))]^{-1}$$

$$\approx[(d_\parallel-\Omega_S)^2-4d_\perp^2]^{-1/2}.$$

The spin-wave dispersion relation on the surface has been found previously;[10] in the case considered here the gap in the spectrum increases on account of the magnetoelastic coupling:

$$\Omega_S=H_0+H_S+\frac{5}{8}H_x a_0^2 k_\parallel^2-\ldots. \tag{17}$$

In Eq. (17) we have dropped the term proportional to $k_\parallel^4$.

Assuming that $\Omega_A\ll d_\parallel$, which always holds, we have

$$\Omega_A=s\mathbf{k}_\parallel,$$

$$s=s_0\left(1-\frac{2S^3\lambda^2\gamma_e}{m_0 s_0^2\sqrt{(H_0+H_S)(H_0+4H_x+H_S)}}\right)^{1/2}, \tag{18}$$

$$\gamma_e=e_y^2\cos^2\varphi_k+(e_x\cos\varphi_k+e_z\sin\varphi_k)^2.$$

As expected, the frequency of surface phonons lies below the continuous spectrum of frequencies of bulk acoustic waves.

It is seen from Eq. (18) that the sound velocity renormalized by the magnetoelastic coupling is twice as large near the surface as in the volume of the crystal.

Furthermore, the equilibrium condition should hold on the surface:

$$\sigma_{ik}\mathbf{n}_k=0, \tag{19}$$

where σ_{ik} is the stress tensor and $\mathbf{n}_k$ is a unit vector normal to the surface. Boundary conditions (19) are valid in the case of sufficiently long wavelengths, when the influence of the inhomogeneous exchange can be neglected (as we are assuming). Equation (19) for $\ell=0$ leads to the following condition:

$$u_{yy}^{(0)}+\sigma u_{xx}^{(0)}+\sigma u_{zz}^{(0)}=0.$$

We assume that the magnetization vector on the surface is parallel to OZ (which holds even in the absence of magnetic field). Minimization of the free energy jointly with the last condition gives

$$u_{xx}^{(0)}=u_{yy}^{(0)}=\frac{\lambda S^2}{E}\,\frac{\sigma(\sigma+1)}{1+2\sigma},$$

$$u_{zz}^{(0)}=-\frac{\lambda S^2}{E}\,\frac{(\sigma+1)^2}{1+2\sigma}.$$

i.e., the spontaneous strains on the surface coincide with the strains in the bulk (see Eq. (13)). Then the energy of the magnetoelastic field on the surface of the crystal is equal to

$$H_S=2\lambda^2 S^2\frac{1+3\sigma}{E}. \tag{20}$$

The dependence of the direction of the polarization vector on the coordinate y is known.[22] It is obvious that γ_e will depend on the penetration depth of the Rayleigh wave into the crystal.

CONCLUSION

We have investigated the model of a semi-infinite Heisenberg ferromagnet with the magnetoelastic coupling taken into account and have determined the spectra of coupled magnetoelastic waves near the surface of the ferromagnet.

Magnetoelastic waves propagating in the bulk of a ferromagnet have an additional activation energy H_B given by expression (14). Comparing their spectrum with the dispersion relation of magnetoelastics surface waves, one can see these expressions agree to an accuracy up to the wave velocity, i.e., the coefficient in front of $k_\parallel^2$. It follows from (14) and (20) that $H_S=H_B$. This result was obtained in neglect of the magnetoelastic coupling in Ref. 10, where it was shown that the frequency of surface spin waves lies below the boundary Ω_m of the frequency band of bulk oscillations of the spin subsystem. The relation $\Omega_S<\Omega_m$ continues to hold when the magnetoelastic coupling is taken into account.

It should be noted that when the single-ion anisotropy perpendicular to the XOZ plane is taken into account in the surface layer, the magnetic moment of the surface layer will be directed at some angle to the OZ axis. Accordingly, the boundary conditions change. Simple calculations show that in this case $H_S<H_B$. Thus the gap between the spectrum of surface and bulk waves will be of zeroth order in $\mathbf{k}_\parallel$ not only on account of anisotropy[10] but also on account of magnetoelastic coupling.

The sound velocity changes near the surface in the same way as does the velocity of ''quasi-spin'' waves in a ferromagnet. From Eqs. (16) and (18) we get

$$s_b^2=s_{0b}^2(1-\Delta),\quad s_s^2=s_{0s}^2(1-2\Delta),$$

where s_{0b} and s_{0s} are the velocities of bulk and surface waves of some polarization in neglect of the magnetoelastic coupling, and the explicit form of Δ is obvious [see Eqs. (16) and (18)]. We note that if the wave vector is directed along the OZ axis, then it follows from (18) that only the normal (''transverse'') component of the Rayleigh wave interacts with the ''quasi-spin'' waves.

Localization of the oscillations is determined by the gap separating the surface wave frequency from the bulk wave frequency.[23] It is easy to see that decreasing the velocity of the Rayleigh waves will lead to a decrease of their penetration depth into the crystal. At the same time, the coupling of the magnetic moments with the elastic system does not alter the characteristic depth to which surface spin waves exist. As can be seen from Eq. (8), $\kappa_\perp$ does not depend on the magnetoelastic coupling parameter.

*E-mail: frid@tnu.crimea.ua

[1] J. J. Krebs, B. T. Jonker, and G. A. Prinz, J. Appl. Phys. **63**, 3467 (1988).
[2] D. P. Pappas, K.-P. Kamper, and H. Hopster, Phys. Rev. Lett. **64**, 3179 (1990).
[3] A. A. Maradudin and D. L. Mills, J. Phys. Chem. Solids **28**, 1855 (1967); **30**, 78E (1969).
[4] T. Kaneyoshi, J. Phys.: Condens. Matter **3**, 4497 (1991).
[5] S. Selzer and N. Majlis, Phys. Rev. B **26**, 404 (1982); **27**, 544 (1983).
[6] G. T. Rado, Bull. Am. Phys. Soc. II **2**, 127 (1957).
[7] R. F. Wallis, A. A. Maradudin, I. P. Ipatova, and A. A. Klochikhin, Solid State Commun. **5**, 89 (1967).
[8] D. L. Mills, Phys. Rev. B **1**, 264 (1970).
[9] G. T. Rado, Phys. Rev. B **40**, 407 (1989).
[10] D. L. Mills, Phys. Rev. B **40**, 11153 (1989).
[11] D. L. Mills, Phys. Rev. B **39**, 12306 (1989).
[12] R. C. O'Handley and J. P. Woods, Phys. Rev. B **42**, 6568 (1990).
[13] Y. Endo, Phys. Rev. B **46**, 11129 (1992).
[14] Yu. N. Mitsay, K. M. Skibinsky, M. B. Strugatsky, A. P. Korolyuk, V. V. Tarakanov, and V. I. Khizhnyi, J. Magn. Magn. Mater. **219**, 340 (2000).
[15] T. G. Petrova and E. S. Syrkin, Fiz. Nizk. Temp., **17**, 411 (1991) [Sov. J. Low Temp. Phys. **17**, 215 (1991)].
[16] E. A. Turov and V. G. Shavrov, Usp. Fiz. Nauk, **140**, 429 (1983) [Sov. Phys. Usp. **26**, 593 (1983)].
[17] Yu. V. Gulayaev, Yu. A. Kuzavko, I. N. Oleĭnik, and V. G. Shavrov, Zh. Eksp. Teor. Fiz., **84**, 674 (1987) [Sov. Phys. JETP **60**, 386 (1984)].
[18] S. V. Gerus and V. V. Tarasenko, Fiz. Tverd. Tela (Leningrad), **17**, 2247 (1975) [Sov. Phys. Solid State **17**, 1487 (1975)].
[19] L. D. Landau and E. M. Lifshitz, *Theory of Elasticity*, Pergamon Press, Oxford (1970), Nauka, Moscow (1965).
[20] T. Holstein and H. Primakoff, Phys. Rev. Ser. 2 **58**, 1098 (1940).
[21] L. D. Landau and E. M. Lifshitz, *Statistical Physics*, 3rd ed., Pergamon Press, Oxford (1980), Nauka, Moscow (1976).
[22] A. A. Abrikosov, L. P. Gor'kov, and I. E. Dzhaloshinskiĭ, *Methods of Quantum Field Theory in Statistical Physics*, Prentice-Hall, Englewood Cliffs, New Jersey (1963), Fizmatgiz, Moscow (1962).
[23] A. M. Kosevich, *Theory of the Crystal Lattice* [in Russian], Vishcha Shkola, Kharkov (1988).

Translated by Steve Torstveit

Dynamics of domain walls with lines in rare-earth orthoferrites in magnetic and electric fields with exchange relaxation processes taken into account

E. G. Ekomasov*

Bashkir State University, ul. Frunze 32, 450074 Ufa, Russia
(Submitted May 30, 2002; revised April 11, 2003)
Fiz. Nizk. Temp. **29**, 878–884 (August 2003)

The influence of exchange relaxation on the dynamics of domain walls with a ''fine structure'' in rare-earth orthoferrites in the presence of external magnetic and electric fields is investigated. A system of differential equations is obtained which describe the dynamics of a domain wall with a solitary line. The dependence of the steady-state velocity of the domain wall and line on the values of the relaxation parameters and on the components of the magnetic and electric fields is found. The results are compared with the known experimental results. © *2003 American Institute of Physics.* [DOI: 10.1063/1.1596795]

INTRODUCTION

Rare-earth orthoferrites (REOs) with the chemical formula $RFeO_3$ (R is an ion of the rare-earth elements) and crystal symmetry group D_{2h}^{16} are noncollinear antiferromagnets with weak ferromagnetism (WFM).[1] The study of this class of weak ferromagnets is of great interest because, in particular, the domain-wall (DW) velocities in them are high, having record values among the magnets that have been studied to date.[2,3] Three types of magnetic ordering are possible in REOs: G_xF_z, G_zF_x, and G_y. The first two have weak ferromagnetism, e.g., for G_xF_z the ferromagnetic vector **m** is directed along the crystallographic **c** axis, while the antiferromagnetic vector **l** is along **a**.[1,2] The third type of structure is purely antiferromagnetic. The structure of the DWs can be of two types: with and without a rotation of the vector **m**.[1,3] The first of these corresponds to a structure with a simultaneous rotation of the vectors **m** and **l**, while the second corresponds to a rotation of the vector **l** with only a change in modulus of the vector **m**. The realization of some particular type of DW and plane of rotation of the vectors **m** and **l** in it is determined by the signs and relationships among the anisotropy constants of the orthoferrite.[3] Under certain conditions a transition can occur from one type of DW to another, as is observed, e.g., in dysprosium orthoferrite $DyFeO_3$ at $T=150$ K.[4]

By now the dynamics of uniform DWs in REOs has been studied in detail experimentally and in the main has been explained theoretically.[5–9] However, usually only the relaxation terms that are of relativistic origin are taken into account in the equations of motion. Meanwhile, the terms in the equations of motion which describe relaxation processes due to the exchange interaction have been obtained in Refs. 10 and 11, for example. As was shown in Refs. 10–12, these terms can play a substantial role in the study of high-frequency and acoustic properties of REOs, the damping of spin waves, and the braking of DWs and solitons.

It has been predicted theoretically[3] that two types of ''fine structure'' of the DWs can exist in REOs: ''A''—wide segments with rotation of the ferromagnetic vector **m**, separated by lines without rotation of **m** (ZRLs) (the fine structure is illustrated in Fig. 1 and is mainly considered in Sec. 2); ''B''—wide segments of a DW with no rotation of **m**, separated by lines with rotation of **m** (this situation is briefly considered in Sec. 3); it is pointed out its formation is more probable near the phase transition in the DW itself or near the surface of the sample, where the relationship between the anisotropy constants can change. The lines separating parts of the DW with the same structure but with different orientations of the vectors **m** and **l** will simply be called ''lines'' here. To avoid misunderstandings, we emphasize that they are not the usual Bloch lines in DWs. The dynamic characteristics of these DWs[13,14] should differ substantially from the characteristics of DWs with lines in ferromagnets. For example, the gyrotropic term of the dynamic force acting on a line in a REO appears in an external field perpendicular to the plane of rotation of **l**, and in absolute value it can be comparable to the inertial and viscous terms. We have also shown that the mobility of the lines in a DW at rest in a REO is influenced substantially not only by the ordinary relaxation and external magnetic field but also by exchange relaxation and the external electric field.[15,16] Recently published experimental studies[17–19] have reported results that can be interpreted as the observation of dynamic lines on an isolated Néel DW moving at supersonic velocity in an REO. However, the conditions of those experiments were different from those that had previously been considered theoretically. It is therefore of interest to study the dynamics of an isolated Néel DW with a solitary line moving along it simultaneously

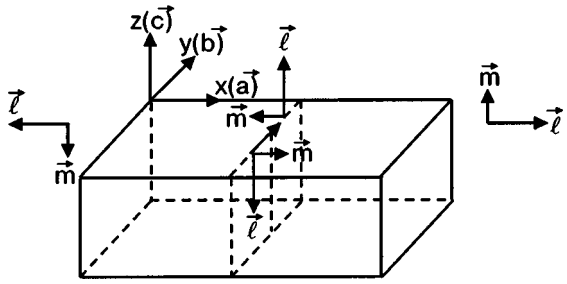

FIG. 1. Schematic view of the fine structure of a Néel domain wall with rotation of the ferromagnetic vector in the magnetic phase G_xF_z.

under the influence of external magnetic and electric fields with the damping of an exchange nature taken into account (because of the high velocities of the DW and line). In the present study we use a previously proposed variant of the collective variables method for the velocity of the center of a solitary line in an isolated Néel DW ($dx_0/dt, dy_0/dt$) to obtain effective nonlinear algebraic equations in the presence of magnetic and electric fields of arbitrary orientation and additional exchange relaxation. In some particular and limiting cases one can find solutions of these systems of equations which describe the dependence of the velocity of the line on the value of the fields and the exchange relaxation.

1. MODEL AND BASIC EQUATIONS

For simplicity we shall consider the REO in a two-sublattice model. Its state is conveniently described by normalized vectors **m** and **l**:

$$\mathbf{m}=\frac{1}{2M_0}(\mathbf{M}_1+\mathbf{M}_2),\quad \mathbf{l}=\frac{1}{2M_0}(\mathbf{M}_1-\mathbf{M}_2), \tag{1}$$

where $\mathbf{M}_1$ and $\mathbf{M}_2$ are the sublattice magnetization vectors and M_0 is the equilibrium magnetic moment of the sublattice. The energy density of the REO can be written as the sum of the energies of the magnetic and magnetoelectric subsystems:

$$w=w_m+w_e. \tag{2}$$

We shall proceed from the standard form of the energy density for the magnetic subsystem:[1,2]

$$w_m=\frac{1}{2}am^2+\frac{1}{2}A(\nabla\cdot\mathbf{l})^2+\mathbf{d}\cdot[\mathbf{m}\times\mathbf{l}]+w_a(\mathbf{l})-2M_0\mathbf{m}\cdot\mathbf{H}. \tag{3}$$

where a and A are the homogeneous and inhomogeneous exchange constants, $w_a(\mathbf{l})$ is the energy density of the magnetic anisotropy, and **H** is an external magnetic field. The axes of a Cartesian coordinate system x, y, z are assumed to be directed along the crystallographic axes **a**, **b**, **c** of the crystal (see Fig. 1), and then $\mathbf{d}=d\mathbf{e}_y$, where d is the exchange–relativistic Dzyaloshinskiĭ coupling constant. We note that a more general expression for w_m should contain two constants describing the Dzyaloshinskiĭ interaction, but the difference between them, Δd, is of a purely relativistic nature, and therefore it is much less than these constants themselves ($|\Delta d|\sim 10^{-2}d$).[6] Neglecting the fourth-order anisotropy, we write the energy density of the magnetic anisotropy in the form

$$w_a=\frac{a_1}{2}l_x^2+\frac{a_3}{2}l_z^2, \tag{4}$$

where a_1 and a_3 are the second-order anisotropy constants.

The energy density of the magnetoelectric subsystem is written in the form[15]

$$w_e=-(\mathbf{E}\cdot\mathbf{P})=E_x(\gamma_x^yJ_{xy}^y+\gamma_x^zJ_{xz}^z)+E_y(\gamma_y^xJ_{yx}^x+\gamma_y^zJ_{yz}^z)+E_z(\gamma_z^xJ_{zx}^x+\gamma_z^yJ_{zy}^y), \tag{5}$$

where $J_{ij}^k=l_i(\partial l_j/\partial x_k)-l_j(\partial l_i/\partial x_k)$, **E** is the external electric field, and γ_i^k are the magnetoelectric constants.

The equations of motion for the vectors **m** and **l** in the exchange approximation have the form[10]

$$\begin{aligned}\dot{\mathbf{m}}&=\frac{\gamma}{2M_0}\{[\mathbf{m}\times\mathbf{H}_m]+[\mathbf{l}\times\mathbf{H}_l]\}+\alpha\{[\mathbf{l}\times\dot{\mathbf{l}}]+[\mathbf{m}\times\dot{\mathbf{m}}]\}-\frac{\lambda_2\gamma}{2M_0^2}\Delta\mathbf{H}_m,\\ \dot{\mathbf{l}}&=\frac{\gamma}{2M_0}\{[\mathbf{l}\times\mathbf{H}_m]+[\mathbf{m}\times\mathbf{H}_l]\}+\alpha\{[\mathbf{m}\times\dot{\mathbf{l}}]+[\mathbf{l}\times\dot{\mathbf{m}}]\}+\frac{\lambda_1\gamma}{2M_0^2}\mathbf{H}_l,\end{aligned} \tag{6}$$

where $\mathbf{H}_m=\delta w/\delta\mathbf{m}$, $\mathbf{H}_l=\delta w/\delta\mathbf{l}$, γ is the gyromagnetic ratio, and α, λ_1, and λ_2 are the relativistic and exchange relaxation constants. For the case $m\ll l$, which is analogous to the case of pure antiferromagnets[10] [when the condition $\lambda_1 H/(2M_0H_E)\ll 1$ holds, where $H_E=a/(4M_0)$], the vector **m** is related to the vector **l** by the expression

$$\mathbf{m}=\frac{\chi_\perp}{2\gamma M_0}\left\{[\dot{\mathbf{l}}\times\mathbf{l}]+\frac{\lambda_1\chi_\perp}{2\gamma M_0^2}[\dot{\mathbf{l}}\times\mathbf{l}]\right\}+\frac{1}{a}\{[\mathbf{l}\times\mathbf{d}]-2M_0[\mathbf{l}(\mathbf{l}\cdot\mathbf{H})-\mathbf{H}]\}. \tag{7}$$

where $\chi_\perp=M_0/H_E$ is the transverse component of the magnetic susceptibility (transverse in respect to the equilibrium direction of **l**). By substituting (7) into the first of Eqs. (6) under the conditions $\lambda_1 H_d/2M_0H_E, 2\lambda_2 H/A\ll 1$, $H_d=d/2M_0$, it is easy to obtain

$$\begin{aligned}&[\ddot{\mathbf{l}}\times\mathbf{l}]-c^2[\Delta\mathbf{l}\times\mathbf{l}]+\frac{\gamma}{4M_0^2}[\mathbf{d}\times\mathbf{l}](\mathbf{d}\cdot\mathbf{l})+\frac{\gamma^2a}{4M_0^2}\left[\frac{\partial w_a}{\partial\mathbf{l}}\times\mathbf{l}\right]\\ &\quad=-\frac{c^2}{A}[\mathbf{H}_l^e\times\mathbf{l}]-\frac{2\gamma M_0}{\chi_\perp}\left(\alpha-\frac{\lambda_2}{M_0}\Delta\right)[\dot{\mathbf{l}}\times\mathbf{l}]\\ &\quad\quad-\frac{\lambda_1\chi_\perp}{2\gamma M_0^2}\{[\dddot{\mathbf{l}}\times\mathbf{l}]+[\ddot{\mathbf{l}}\times\dot{\mathbf{l}}]\}+\gamma\{2[[\mathbf{H}\times\dot{\mathbf{l}}]\times\mathbf{l}]\\ &\quad\quad+[[\dot{\mathbf{H}}\times\mathbf{l}]\times\mathbf{l}]\}-\frac{\gamma^2}{2M_0}[[\mathbf{H}\times\mathbf{d}]\times\mathbf{l}],\end{aligned} \tag{8}$$

$$\mathbf{H}_l^e=2E_i\gamma_i^k\left(\frac{\partial l_k}{\partial x_k}\mathbf{e}_i-\frac{\partial l_i}{\partial x_k}\mathbf{e}_k\right)_{i\neq k},\quad i,k=x,y,z,$$

$$c^2=\frac{\gamma^2Aa}{4M_0^2}.$$

For $\lambda_1=\lambda_2=E=H=0$ Eq. (8) agrees with the equation for **l** in Ref. 2. Equations (8) in the angle variables $\mathbf{l}=l(\cos\theta,\sin\theta\sin\varphi,\sin\theta\cos\varphi)$ usually used in the solution of dynamical problems have an awkward form and are presented in the Appendix.

2. APPROXIMATE DESCRIPTION OF THE DYNAMICS OF A DW WITH FINE STRUCTURE "A." LINES WITHOUT ROTATION OF m

In view of the complexity and awkwardness of the equations obtained, their analytical solution is a complicated mathematical problem even in the simplest case of an iso-

lated DW with one line. In what follows we shall therefore use a simplified description in the framework of the collective variables method. We first consider the magnetic phase G_xF_z (where within a domain $\mathbf{m}\|OZ$ and $\mathbf{l}\|OX$) and a Néel DW with rotation of $\mathbf{m}$ (the plane of rotation is parallel to the YZ axis) and containing a vertical line with zero rotation of $\mathbf{m}$ (Fig. 1) in the presence of a magnetic field $\mathbf{H}(H_x,H_y,H_x)$ and electric field $\mathbf{E}(0,0,E_z)$ and with allowance for exchange relaxation ($\lambda_1,\lambda_2\neq 0$). When the right-hand side is zero and $K_{ab}\gg K_{cb}>0$ (where $K_{ab}=(d^2/a)-a_1$ and $K_{cb}=(d^2/a)-a_3$ are the effective anisotropy constants in the ab and cb planes) Eqs. (8) written in angle variables (see Appendix) have the stationary solution $\theta(x-v_{dw}t)$ and $\varphi(y-v_Lt)$,[14] where x is the coordinate perpendicular to the plane of the DW, v_{dw} and v_L are the velocities of the DW and ZRLs, respectively. The boundary conditions in this case have the following form: $\theta(+\infty)=0$, $\theta(-\infty)=\pi$, $\theta_x'(\pm\infty)=0$, $\varphi(+\infty)=0$, $\varphi(-\infty)=\pi$, and $\varphi_y'(\pm\infty)=0$. Taking this solution into account and employing the method used in Refs. 14 and 20, one can obtain a system of equations of motion for the velocities of the center of the solitary line x_0,y_0:

$$\frac{m_x}{\tau}\dot{x}_0-\frac{\pi M_0H_y}{\gamma H_E}\dot{y}_0-m_c\lambda H_z=0, \tag{9}$$

$$\frac{m_y}{\tau}\dot{y}_0+\frac{\pi M_0H_y}{\gamma H_E}\dot{x}_0+\pi\delta H_xm_c+\pi E_z\gamma_z^x=0, \tag{10}$$

where

$$m_x=\left[m_{dw}+m_{Lx}\left(1-\frac{\dot{y}_0^2}{c^2}\right)^{1/2}\right]\left(1-\frac{\dot{x}_0^2}{c^2}\right)^{1/2},$$

$$m_y=m_L\left(1+\varepsilon_2\frac{\delta_0^2}{\Lambda^2}+\varepsilon_1\left(\frac{\dot{y}_0}{c}\right)^2\frac{\delta_0^2}{\Lambda^2}\right)\times\left[\left(1-\frac{\dot{x}_0^2}{c^2}\right)\Big/\left(1-\frac{\dot{y}_0^2}{c^2}\right)\right]^{1/2},$$

$$m_{dw}=m_0\left[1+\varepsilon_2\frac{\delta_0^2}{\delta^2}+\varepsilon_1\left(\frac{\dot{x}_0}{c}\right)^2\frac{\delta_0^2}{\delta^2}\right], \tag{11}$$

$$m_{Lx}=m_L\left[1+\varepsilon_2\frac{\delta_0^2}{\delta^2}+\varepsilon_2\frac{\delta_0^2}{\Lambda^2}Q+3\varepsilon_1\left(\frac{\dot{x}_0}{c}\right)^2\frac{\delta_0^2}{\delta^2}+\varepsilon_1\left(\frac{\dot{y}_0}{c}\right)^2\frac{\delta_0\Lambda_0}{\Lambda\delta}\right],$$

$$\varepsilon_1=\frac{1}{3}\frac{\lambda_1^*c^2}{\alpha\delta_0^2},\quad \varepsilon_2=\frac{1}{3}\frac{\lambda_2}{\alpha M_0\delta_0^2},\quad m_c=2M_0\frac{d}{a}.$$

$$m_0=\frac{M_0\lambda}{\gamma^2\delta_0H_E},\quad m_L=\frac{2M_0\delta_0}{\gamma^2\Lambda_0H_E},\quad Q=\frac{K_{ab}-K_{cb}}{K_{cb}}\gg 1,$$

$$\delta=\delta_0\left(1-\frac{\dot{x}_0^2}{c^2}\right)^{1/2},\quad \tau^{-1}=2\alpha\gamma H_E,$$

$$\delta_0=\left(\frac{A}{K_{ab}-K_{cb}}\right)^{1/2},$$

$$\Lambda=\Lambda_0\left(1-\frac{\dot{y}_0^2}{c^2}\right)^{1/2},\quad \Lambda_0=\left(\frac{A}{K_{cb}}\right)^{1/2},\quad \lambda_1^*=\frac{\lambda_1\chi_\perp^2}{2\gamma^2M_0^3},$$

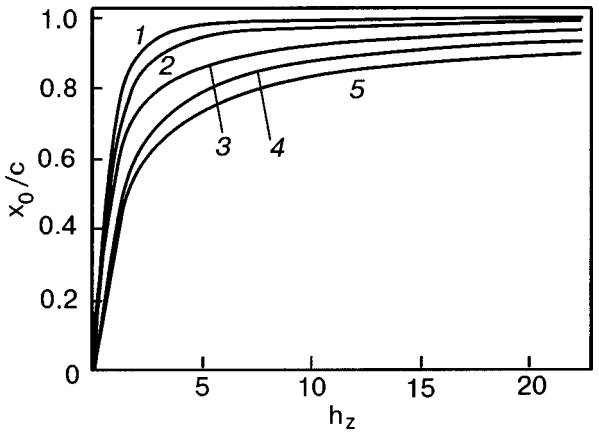

FIG. 2. Dependence of the DW velocity $\dot{x}_0$ on the value of the external magnetic field h_z for $Q_1=100$, $H_y=H_x=E_z=0$: $\varepsilon_1=\varepsilon_2=0$ (*1*); $\varepsilon_1=0$, $\varepsilon_2=0.5$ (*2*); $\varepsilon_1=\varepsilon_2=0.5$ (*3*); $\varepsilon_1=0$, $\varepsilon_2=1$ (*4*); $\varepsilon_1=\varepsilon_2=1$ (*5*).

and λ is the period of the fine structure of the DW. We note that the term proportional to $\dot{y}_0^3/(1-\dot{y}_0^2/c^2)^{3/2}$, which is connected to having $\lambda_1\neq 0$ in Eq. (10), was obtained in Ref. 21 for the case when a term due to the DW bending induced by the moving line is included in the force of friction. Using Eqs. (9) and (10), one can find the dependence of the steady DW velocity on the external magnetic and electric fields. Since an analytical solution of this system of equations cannot be found in the general case, let us consider a few particular cases.

2.1. $H_x=H_y=E_z=0$ (only the component H_z is nonzero)

In this case the line is at rest ($\dot{y}_0=0$), and the dependence of the DW velocity $\dot{x}_0=\dot{x}_0(H_z,\lambda_1,\lambda_2)$ has the form

$$\dot{x}_0=c\left(\xi-\frac{b_2}{3b_1}\right)^{1/2}, \tag{12}$$

where

$$\xi=\sqrt[3]{-q+\sqrt{D}}+\sqrt[3]{-q-\sqrt{D}},\quad D=q^2+p^2,$$

$$q=\frac{1}{54b_1^3}(2b_2^3-9b_1b_2b_3+27b_1^2b_4),\quad p=\frac{3b_1b_3-b_2^2}{9b_1^2}, \tag{13}$$

$$b_1=1+\left(\frac{f_2}{h_z}\right)^2,\quad b_2=2f_1f_2\left(\frac{1}{h_z}\right)^2-3,$$

$$b_3=\left(\frac{f_1}{h_z}\right)^2+3,\quad b_4=-1, \tag{14}$$

$$f_1=1+Q_1^{-1}+\varepsilon_2(1+6Q_1^{-1}),\quad \mu_{dw}^0=\frac{\gamma\delta_0d}{\alpha a},$$

$$h_z=\frac{\mu_{dw}^0H_z}{c}, \tag{15}$$

$$f_2=\varepsilon_1(1+3Q_1^{-1})-1-Q_1^{-1}(1+\varepsilon_2),\quad Q_1^{-1}=\frac{2\delta_0^2}{\Lambda_0\lambda}.$$

A plot of $\dot{x}_0(h_z)$ for different values of the damping parameters is shown in Fig. 2. It is seen that taking λ_1 and λ_2 into account has a substantial effect on the form of this function, although the presence of $\lambda_1 \neq 0$ begins to have a substantial effect only at large values of the DW velocity.

In the limiting case $\dot{x}_0 \to c$ we obtain the following expression for the DW velocity:

$$\dot{x}_0 = c\left\{1 - \left[\frac{(\varepsilon_1+\varepsilon_2)Q(1+3m_\Lambda/m_0)}{h_z}\right]^{2/3}\right\}. \tag{16}$$

We see from (16) that $(c-\dot{x}_0) \sim h_z^{-2/3}$ (as in Ref. 16, where it was assumed that $\lambda_1 = 0$), unlike the case when only the relativistic relaxation is taken into account, where $\Delta v_{dw} \sim H_z^{-2}$. The main contribution to the braking of the DW in this case comes from relaxation processes of exchange origin, which are determined in equal measure by both constants λ_2 and λ_1.

We note that in the case of low DW velocities as well (unlike Refs. 15 and 16, where $\lambda_1 = 0$), Eq. (9) still reduces to a cubic algebraic equation with the solution $\dot{x}_0 = \xi c$, but now the coefficients will be equal to

$$p = \frac{f_1}{\varepsilon_1(1+3Q_1^{-1})}, \quad q = -\frac{h_z}{\varepsilon_1(1+3Q_1^{-1})}. \tag{17}$$

2.2. $H_x, H_y, H_z, E_z \neq 0$

In this case the line moves together with the DW along the x axis and transversely to the DW along the y axis and the dependence $\dot{x}_0(H_x, H_y, E_z, \lambda_1, \lambda_2)$ cannot be obtained in explicit form. However, using Eq. (10), we calculate the dependence of the line velocity $\dot{y}_0$ on the parameters H_x, H_y, E_z, λ_1, and λ_2 and the DW velocity $\dot{x}_0$ (what is usually measured in experiments on the dynamics of DWs containing lines[19]), which will be determined by a law of the form (12)–(14), where now

$$h_z \to l, \quad f_1 \to f_1^* = 1+\varepsilon_2 Q^{-1}, \quad f_2 \to f_2^* = \varepsilon_1 Q^{-1} - 1, \tag{18}$$

$$l = \left[-\frac{a_0\dot{x}_0}{c}\left(1-\frac{\dot{x}_0^2}{c^2}\right)^{1/2} - \frac{\mu_L^0 H_x}{c} - \frac{\mu_L^E E_z}{c}\left(1-\frac{\dot{x}_0^2}{c^2}\right)^{1/2}\right],$$

$$\mu_L^0 = \frac{\pi}{2} Q^{1/2}\mu_{dw}^0, \quad \mu_L^E = \frac{\pi\gamma\Lambda_0\gamma_z^x}{4M_0\delta_0\alpha}.$$

Interestingly, the contribution of E_z to the dynamics of the line, unlike that of H_x, increases with increasing v_{dw}. A plot of $\dot{y}_0(\dot{x}_0)$ with allowance for the different values of h_x, e_z, and the damping parameters is shown in Fig. 3. We see that exchange relaxation has a substantial influence on the velocity of the line. By varying the value and direction of H_x and E_z, one can increase or decrease the velocity of the line. In the limiting case $\dot{y}_0 \to c$ (for $\dot{x}_0 = e_z = 0$) Eqs. (10) and (18) imply

$$\dot{y}_0 = c\left[1 - \left(\frac{\varepsilon_1+\varepsilon_2}{h_x}\right)^{2/3}\right]. \tag{19}$$

As in the case of the DW velocity, the saturation of the line velocity is determined in equal measure by both of the constants of exchange origin. For the case of low velocities, in contrast to Refs. 15 and 16, Eq. (10) reduces to a cubic equation with a solution of the form $\dot{y}_0 = \xi c$, but

$$p = \frac{1+\varepsilon_2^* Q^{-1}}{\varepsilon_1^* Q^{-1}}, \quad q = -\frac{lQ}{\varepsilon_1}. \tag{20}$$

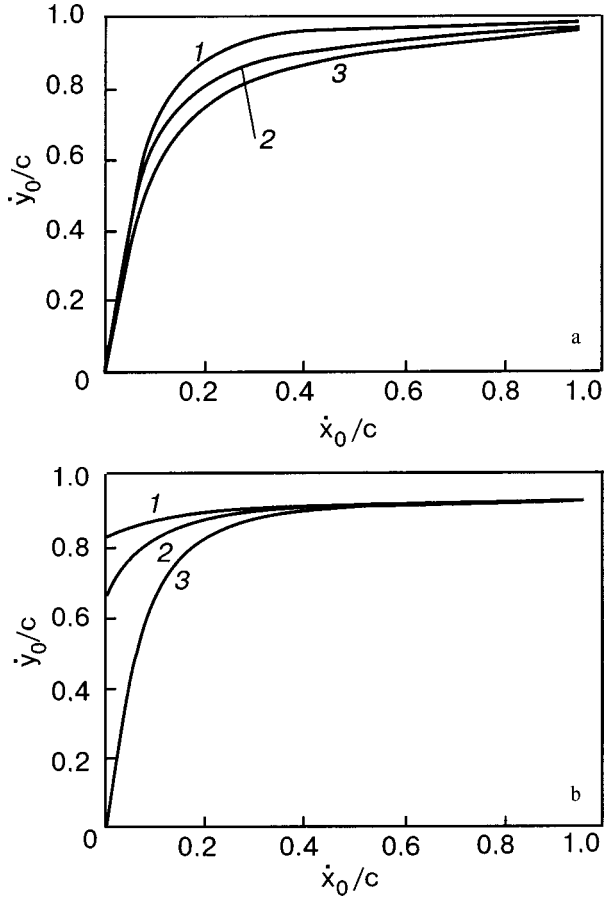

FIG. 3. Dependence of the line velocity $\dot{y}_0$ on the DW velocity $\dot{x}_0$ for $a_0 = 10$, $Q = 10$. a—$h_x = e_z = 0$: $\varepsilon_1 = 0$, $\varepsilon_2 = 0.1$ (*1*); $\varepsilon_1 = 2$, $\varepsilon_2 = 0.1$ (*2*); $\varepsilon_1 = \varepsilon_2 = 2$ (*3*); b—$\varepsilon_1 = \varepsilon_2 = 0.1$: $h_x = e_z = 1$ (*1*); $h_x = 1$, $\varepsilon_z = 0$ (*2*); $h_x = e_z = 0$ (*3*).

2.3. Limit of low DW and line velocities for $\lambda_1 = 0$ and arbitrary orientation of the fields

In this limit we can find the dependence of the DW velocity $\dot{x}_0(H_x, H_y, H_z, E_z, \lambda_2)$ and line velocity $\dot{y}_0(H_x, H_y, H_z, E_z, \lambda_2, \dot{x})$ on λ_2 and the fields for a more general orientation of the latter:

$$\dot{x}_0 = -\mu_{dw}^*\left[H_z + \frac{\pi\delta_0}{\lambda}a_0\left(H_x - \frac{\gamma_z^x H_E}{\delta_0 M_0 H d}E_z\right)\right], \tag{21}$$

$$\dot{y}_0 = -a_0^*\dot{x}_0 - \mu_L^{*E}E_z - \mu_L^* H_x, \tag{22}$$

where

$$\mu_{dw}^* = \frac{\mu_{dw}^0}{1+Q_1^{-1}(1+a_0^2)+\varepsilon_2\left(1+\dfrac{12\delta_0^2}{\Lambda_0\lambda}\right)}, \tag{23}$$

$a_0 = \pi M_0 H_y/(\gamma H_E m_L \tau^{-1})$, a_0^*, μ_L^*, and μ_L^{*E} can be obtained from the expressions for a_0, μ_L, and μ_L^E by making the substitution $\alpha \to \alpha f_1^*$ in them. We see from formulas (21)

and (23) that, although a_0 (the ratio of the gyroscopic and viscous parts of the force acting on the line) can be greater than unity,[20] by virtue of the smallness of Λ_0/λ and δ_0/λ the presence of a solitary line leads to a weak change in the velocity and mobility of the DW itself. For $H_y=E_z=0$ formulas (21) and (22) agree with the results of Ref. 16 up to the numerical coefficients of the terms containing λ_2 (because different expressions were used for the exchange relaxation terms in the equations of motion), and for $H_y=H_x=H_z=0$ they agree to the same accuracy with the results of Ref. 15.

3. DYNAMICS OF A DW WITH FINE STRUCTURE "B." LINES WITH ROTATION OF m

It is known[3] that if $K_{cb}<0$ there can be DWs with wide segments with no rotation of **m** separated by lines with rotation of **m**. Here, in analogy with the previous case, we can obtain equations of motion for the velocities of the line center, which play the role of equations (9)–(11). They now have the form

$$\frac{m_x}{\tau}\dot{x}_0+\frac{\pi M_0 H_z}{\gamma H_E}\dot{y}_0-m_c\lambda H_z=0, \tag{24}$$

$$\frac{m_y}{\tau}\dot{y}_0-\frac{\pi M_0 H_z}{\gamma H_E}\dot{x}_0+\pi E_x\gamma_x^y=0, \tag{25}$$

where

$$\delta_0=\left(\frac{A}{K_{ab}}\right)^{1/2},\quad \Lambda_0=\left(\frac{A}{|K_{cb}|}\right)^{1/2}.$$

Equations (24) and (25) are analogous to Eqs. (9) and (10), and one can therefore use the solutions of the latter after making the substitutions $H_y\to H_z$, $E_z\to E_x$, and $H_x=0$ in them. Since the parameter a_0 now depends on the external magnetic field component H_z, which leads to motion of the DW itself, by using Eqs. (21) and (22) for the case of low velocities one can obtain

$$\dot{y}_0^*=\beta\dot{x}_0^2+\mu_L^E E_x, \tag{26}$$

where $\beta=(\pi/2)(Q^{1/2}/\delta_0\gamma H_d)$.

We note that a solution of this type was first found in Ref. 22 for the case of the magnetic phase G_zF_x, $\lambda_1=\lambda_2=\mathbf{E}=0$, $\mathbf{H}\|\mathbf{m}$ within a domain. In Ref. 19 the experimentally obtained dependence of the line velocity on the DW velocity in the initial part of the curve was interpreted as quadratic, which correlates with formula (26). However, since there were not enough points on that curve at low velocities, a linear law with the origin shifted from zero is not ruled out. One notices the high selectivity of the influence of the different components of the electric and magnetic fields on the structure of the line; this, in the opinion of the author, can be used in designing new experiments.

All of the results obtained above can be carried over to the magnetic phase G_zF_x if the angle φ is measured from the a axis, θ is measured from the c axis, the substitutions $K_{cb}K_{ab}$ and $H_x\to H_z$ are made, and the components of the electric field are chosen from the tables of nonzero values of the force of electric pressure given in Ref. 15.

The author thanks M. V. Chetkin and M. A. Shamstudinov for helpful discussions of the results. This study was supported in part by the Russian Federal Target Program "Integration" (Grant B0065).

APPENDIX

The equations of motion (8) in the angle variables of the vector $\mathbf{l}=l(\cos\theta,\sin\theta\sin\varphi,\sin\theta\cos\varphi)$ can be written in the form

$$\mathbf{F}_1(\theta,\varphi)=\mathbf{f}_{11}(\theta,\varphi)+\mathbf{f}_{12}(\theta,\varphi),$$
$$\mathbf{F}_2(\theta,\varphi)=\mathbf{f}_{21}(\theta,\varphi)+\mathbf{f}_{22}(\theta,\varphi), \tag{27}$$

where the functions

$$F_1=\sin^2\theta[A(\Delta\varphi-c^{-2}\ddot{\varphi})-K_{cb}\sin\varphi\cos\varphi],$$
$$F_2=A(\Delta\theta-c^{-2}\ddot{\theta})-[K_{ab}-K_{cb}\cos^2\varphi+(\nabla\varphi)^2-c^{-2}\ddot{\varphi}]\sin\theta\cos\theta, \tag{28}$$

$$f_{11}=\gamma Ac^{-2}[H_x\sin 2\theta+2\sin^2\theta(H_y\sin\varphi+H_z\cos\varphi)]\dot{\theta}+m_cH_x\sin\theta\sin\varphi+2M_0\gamma^{-1}\dot{\varphi}\sin^2\theta-A\sin 2\theta(\nabla\varphi\nabla\theta-c^{-2}\dot{\varphi}\dot{\theta}),$$

$$f_{21}=-\gamma Ac^{-2}[H_x\sin 2\theta+2\sin^2\theta(H_y\sin\varphi+H_z\cos\varphi)]\dot{\varphi}-m_c(H_y\cos\theta\cos\varphi+H_z\sin\theta)+2M_0\gamma^{-1}\dot{\theta} \tag{29}$$

are the same as in Ref. 14, and

$$f_{12}(\theta,\varphi)=-\frac{\lambda_1\chi_\perp^2}{2(\gamma M_0)^2}\{\sin^2\theta\ddot{\varphi}+2\cos(2\theta)\dot{\theta}^2\dot{\varphi}+\sin(2\theta)(\ddot{\theta}\dot{\varphi}+2\dot{\theta}\ddot{\varphi})\}-\frac{2\lambda_2}{\gamma}\Delta(\sin^2\theta\dot{\varphi})+2E_x(\gamma_x^y\sin^2\theta\cos\varphi\theta_y'-\gamma_x^2\sin^2\theta\sin\varphi\theta_z')+2E_y\left(-\gamma_y^x\sin^2\theta\cos\varphi\theta_x'+\frac{1}{2}\gamma_y^z\sin(2\theta)\theta_z'\right)+2E_z(\gamma_z^x\sin^2\theta\sin\varphi\theta_x'-\gamma_z^y\sin\theta\cos\theta\theta_y'),$$

$$f_{22}(\theta,\varphi)=-\frac{\lambda_1\chi_\perp^2}{2(\gamma M_0)^2}\left[-\ddot{\theta}+(3\cos^2\theta-\sin^2\theta)\dot{\theta}\dot{\varphi}^2+\frac{3}{2}\sin(2\theta)\dot{\varphi}\ddot{\varphi}\right]-\frac{2\lambda_2}{\gamma}\left\{\sin\varphi\Delta\left[\sin\varphi\dot{\theta}+\frac{1}{2}\sin(2\theta)\cos\varphi\dot{\varphi}\right]-\cos\varphi\Delta\left[-\cos\varphi\dot{\theta}+\frac{1}{2}\sin(2\theta)\sin\varphi\dot{\varphi}\right]\right\}+2E_x(\gamma_x^y\sin^2\theta\cos\varphi\varphi_y'-\gamma_x^z\sin^2\theta\sin\varphi\varphi_z')+2E_y(-\gamma_y^x\sin^2\theta\sin\varphi\varphi_x'$$

$$+\gamma_y^z \sin\theta\cos\theta\varphi_z') + 2E_z(\gamma_z^x \sin^2\theta \sin\varphi\varphi_x' - \gamma_z^y \sin\theta\cos\varphi\varphi_y').$$

*E-mail: EkomasovEG@bsu.bashedu.ru

[1] M. M. Farztsdinov, *Physics of Magnetic Domains in Antiferromagnets and Ferrites with a Domain Structure* [in Russian], Nauka, Moscow (1981).
[2] V. G. Bar'yakhtar, B. A. Ivanov, and M. V. Chetkin, Usp. Fiz. Nauk **146**, 417 (1985) [Sov. Phys. Usp. **28**, 563 (1985)].
[3] M. M. Farztdinov, M. A. Shamsutdinov, and A. A. Khalfina, Fiz. Tverd. Tela (Leningrad) **21**, 1422 (1979) [Sov. Phys. Solid State **21**, 878 (1979)].
[4] A. V. Zalesskiĭ, A. M. Savvinov, IU. S. Sheludev, and A. N. Ivashchenko, Zh. Éksp. Teor. Fiz. **68**, 1449 (1975) [Sov. Phys. JETP **41**, 723 (1975)].
[5] A. K. Zvezdin and A. A. Mukhin, Zh. Éksp. Teor. Fiz. **102**, 577 (1992) [Sov. Phys. JETP **75**, 306 (1992)].
[6] V. G. Bar'yakhtar, M. V. Chetkin, B. A. Ivanov, and S. N. Gadetskii, in *Dynamics of Topological Magnetic Solitons. Experiment and Theory*, Vol. 129 of Springer Tracts in Modern Physics, Springer-Verlag, Berlin, (1994).
[7] N. Papanicolaou, Phys. Rev. B **55**, 55 (1997).
[8] M. A. Shamsutdinov and S. A. Niyazgulov, Fiz. Met. Metalloved. **85**, 23 (1998).
[9] V. S. Gerusimchuk and A. L. Sukstanskij, Phys. Rev. B **59**, 6966 (1999).
[10] V. G. Bar'yakhtar, Fiz. Nizk. Temp. **11**, 1198 (1985) [Sov. J. Low Temp. Phys. **11**, 662 (1985)].
[11] V. G. Bar'yakhtar, Zh. Éksp. Teor. Fiz. **94**, 196 (1988) [Sov. Phys. JETP **67**, 757 (1988)].
[12] V. D. Buchel'nikov, N. K. Dan'shin, L. T. Tsymbal, and V. G. Shavrov, Usp. Fiz. Nauk **169**, 1049 (1999).
[13] Yu. V. Melikhov and O. A. Perekhod, Ukr. Fiz. Zh. (Russ. Ed.) **28**, 713 (1983).
[14] M. M. Farztdinov, M. A. Shamsutdinov, and E. G. Ekomanos, Fiz. Tverd. Tela (Leningrad) **30**, 1866 (1988) [Sov. Phys. Solid State **30**, 1076 (1988)].
[15] B. B. Krotenko, Yu. V. Malikhov, and D. A. Yablonskiĭ, Fiz. Tverd. Tela (Leningrad) **27**, 3230 (1985) [Sov. Phys. Solid State **27**, 1946 (1985)].
[16] Yu. V. Melikhov, S. I. Simonenko, and V. L. Sobolev, Ukr. Fiz. Zh. (Russ. Ed.) **32**, 429 (1987).
[17] M. V. Chetkin, Yu. N. Kurbatova, and A. I. Akhutkina, J. Appl. Phys. **79**, 6132 (1996).
[18] M. V. Chetkin, Yu. N. Kurbatova, A. I. Akhutkina, and T. B. Shapaeva, Zh. Éksp. Teor. Fiz. **115**, 2160 (1999) [JETP **88**, 1179 (1999)].
[19] M. V. Chetkin and Yu. N. Kurbatova, Fiz. Tverd. Tela (St. Petersburg) **43**, 1503 (2001) [Phys. Solid State **43**, 1563 (2001)].
[20] E. G. Ekomasov and M. A. Shabalin, Fiz. Tverd. Tela (St. Petersburg) **43**, 1211 (2001) [Phys. Solid State **43**, 1257 (2001)].
[21] A. K. Zvezdin, Kratk. Soobshch. Fiz. **6**, 28 (1999).
[22] E. G. Ekomasov, M. A. Shamsutdinov, and M. M. Farztdinov, Dep. VINITI No. 4773–1389 [deposited MS, in Russian], 22 pp.

Translated by Steve Torstveit

Magnetic and transport properties of $La_{0.8}Sr_{0.2}MnO_3/La_{0.8}Ca_{0.2}MnO_3$ bilayer

V. G. Prokhorov,* G. G. Kaminsky, and V. A. Komashko

Institute of Metal Physics of the National Academy of Sciences of Ukraine, 36 Vernadsky bul'var, Kiev, 03142, Ukraine

Y. P. Lee and J. S. Park

Quantum Photonic Science Research Center and Department of Physics, Hanyang University, Seoul, 133-791 Korea

(Received January 21, 2003)
Fiz. Nizk. Temp. **29**, 885–888 (August 2003)

The effects of lattice strain on the magnetic and the transport properties of $La_{0.8}Sr_{0.2}MnO_3$ films grown on an (001) $LaAlO_3$ substrate and on a $La_{0.8}Ca_{0.2}MnO_3$ layer were studied. It was observed that the metal-insulator and the ferromagnetic transitions occur at higher temperatures for the film deposited on $La_{0.8}Ca_{0.2}MnO_3$ layer than on $LaAlO_3$. The dependence of Curie temperature on the bulk and the Jahn—Teller strains were also determined. © *2003 American Institute of Physics.* [DOI: 10.1063/1.1596796]

Doped colossal-magnetoresistance (CMR) manganite perovskites exhibit a strong correlation between their lattice structure and magneto-transport properties.[1] This phenomenon becomes apparent in thin films. The lattice strain (and stress) accumulated during epitaxial growth of a film plays an important role in the formation of the spin- and the charge-ordered states, the metal-insulator transition temperature, and the value of magnetoresistance.[2–4]

The effect of the kind of single-crystal substrate on the magnetic and the electronic properties of manganite films has been investigated well.[5,6] On the other hand, to develop hybrid devices based on multilayered CMR films detailed information on the mutual influence between constituent layers is required. It is expected that the magnetic and the transport properties of a multilayer structure can substantially differ from those of the individual films of the constituent layers. In this work we report experimental results for $La_{0.8}Sr_{0.2}MnO_3$ (LSM) and $La_{0.8}Ca_{0.2}MnO_3$ (LCM) films and for a $La_{0.8}Sr_{0.2}MnO_3/La_{0.8}Ca_{0.2}MnO_3$ bilayer (BL).

All films were prepared by rf magnetron sputtering using a so-called "soft" (or powder) target.[7] The total pressure in the chamber was 5×10^{-2} Torr with a 3:1 $Ar-O_2$ gas mixture. The substrate was a $LaAlO_3$ (001) single crystal (LAO) with an out-of-plane lattice parameter $c\simeq0.379$ nm for pseudocubic symmetry. The substrate temperature during deposition was 750 °C. Both LSM and LCM films were deposited with a thickness $d\simeq60$ nm, and the BL was deposited with the same thickness for each layer and with LSM on top. The $\theta-2\theta$ x-ray diffraction (XRD) patterns were obtained using a Rigaku diffractometer and Cu K_α radiation. The lattice parameters evaluated directly from the XRD data were plotted against $\cos^2\theta/\sin\theta$. A more precise determination of the lattice parameter was obtained extrapolating a straight line to $\cos^2\theta/\sin\theta=0$. The resistance measurements were carried out using the four-probe method in the temperature range of 4.2–300 K and a magnetic fields up to 5 T. The magnetization in a field up to 100 Oe and the susceptibility at 500 Hz were obtained with a Quantum Design SQUID magnetometer in the temperature range of 4.2–300 K.

Figure 1a presents the $\theta-2\theta$ XRD scans for LSM (curve *1*), LCM (curve *2*) and BL (curve *3*) films. The high intensities of the (00*l*) peaks show that the deposition results in highly *c*-oriented films. Figure 1b shows that the location of the (002) Bragg peak for the BL is almost coincident with that for the LCM film. In contrast, the peak for the LSM film is distinctly shifted to a smaller angle. Therefore the analysis of XRD data reveals that the out-of-plane lattice parameter for the LSM film is strongly dependent on the substrate: $c\simeq0.398$ nm on the LAO substrate and $c\simeq0.391$ nm on the $La_{0.8}Ca_{0.2}MnO_3$ film with lattice parameter $c\simeq0.3905$ nm.

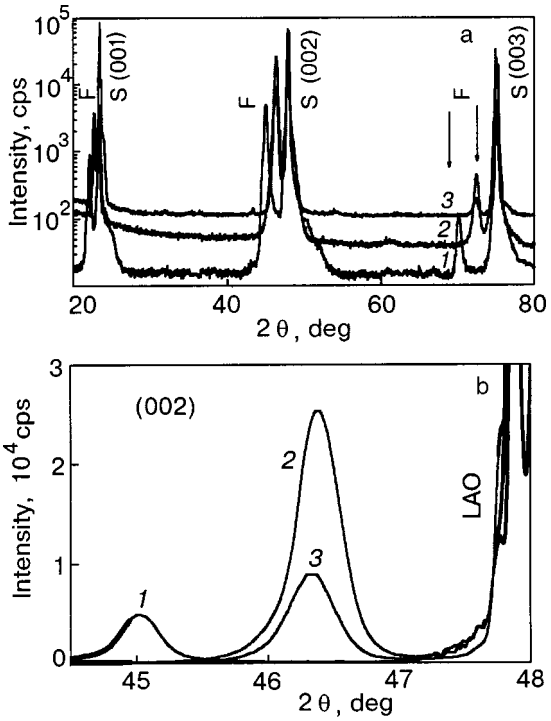

FIG. 1. $\theta-2\theta$ XRD patterns of LSM (*1*), LCM (*2*) and BL (*3*) films (a). The (002) XRD peaks (b).

Figure 2a displays the temperature dependence of the resistance R for LSM (curve *1*), LCM (curve *2*) and BL (curve *3*) films without (filled circles) and with (open circles) an applied magnetic field of 5 T. The magnetic field was directed at right angle to both the film surface and the transport current. The experimental curves show that the metal-insulator (MI) transition temperatures for both LSM and LCM films are very close, about 230 K. The BL film undergoes a MI transition at 280 K, which is higher than for the individual films. The MI transition temperatures for all samples are indicated by arrows. The inset in Fig. 2a shows that the $R(T)$ behavior of the BL film differs from that predicted by the simple two parallel-resistor model (solid line), where the first resistor corresponds to the LSM film (curve *1*) and the second one to the LCM film (curve *2*). Since the lattice parameter c changes significantly only for the LSM film deposited on the LCM layer, it is reasonable to inter that the increase in the MI transition temperature for BL is due to the improved magnetic and electronic properties of the LSM film only.

Figure 2b presents the temperature-dependent magnetoresistance, $\mathrm{MR}(\%)=[R(0)-R(H)]100/R(H)$, obtained for LSM (curve *1*), LCM (curve *2*) and BL (curve *3*) film in an applied magnetic field of 5 T. Here, $R(0)$ and $R(H)$ are the resistances without and with a magnetic field. It is seen that a slight enhancement in the MR for BL, with respect to the individual LSM and LCM films, is observed only at high temperatures. In the low-temperature range the MR of BL remains smaller than that of the LSM film and mimics the $\mathrm{MR}(T)$ behavior for the LCM film.

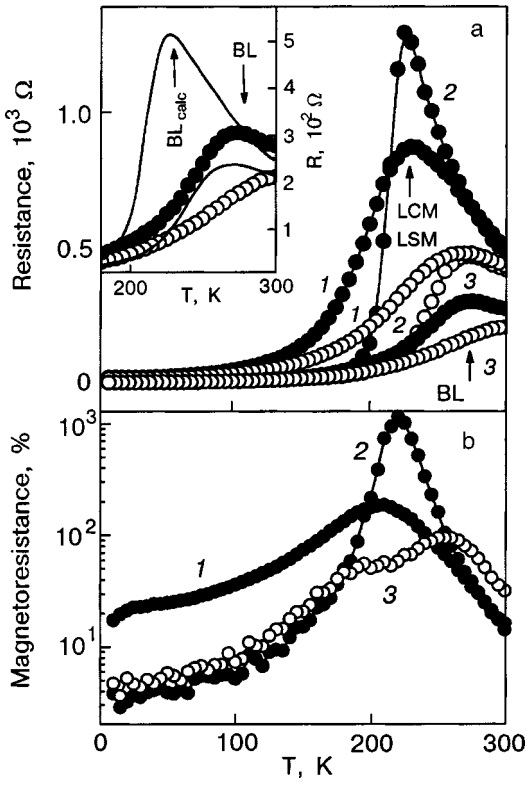

FIG. 2. Temperature dependence of the resistance for LSM (*1*), LCM (*2*) and BL (*3*) films without (filled circles) and with (open circles) an applied magnetic field of 5 T. The lines are visual aids. Inset: The experimental (circles) and computed (solid line) dependences $R(T)$ for the BL film. The arrows show the MI transition temperatures for different samples (a) Temperature dependence of the magnetoresistance for LSM (*1*), LCM (*2*) and BL (*3*) films. The lines are visual aids (b).

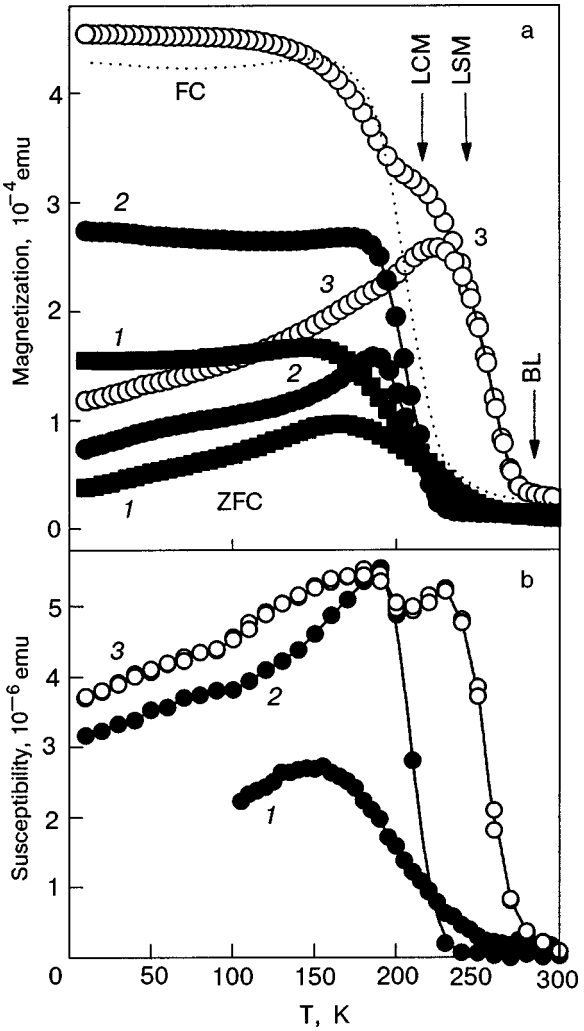

FIG. 3. Temperature dependence of the FC and the ZFC magnetization for LSM (*1*), LCM (*2*) and BL (*3*) films. The lines are visual aids. The arrows indicate the magnetic transition temperatures for different samples. The dashed line was obtained by simple addition of the FC $M(T)$ curves (*1*) and (*2*) (a) Temperature dependence of the susceptibility for LSM (*1*), LCM (*2*) and BL (*3*) films. The lines are visual aids (b).

Figure 3a shows both field-cooled (FC) and zero-field-cooled (ZFC) temperature-dependent magnetization curves for LSM (curve *1*), LCM (curve *2*) and BL (curve *3*) films. The arrows show the corresponding Curie temperatures. The LCM film manifests a sharp transition to the ferromagnetic state at $T_C=230$ K, in agreement with the published results for as-grown films.[3] In contrast, the LSM film displays a broad and smooth magnetic transition near $T_C\simeq 260$ K. Moreover, the absolute value of the saturated FC magnetization is half of that for the LCM film of similar thickness. The same behavior of $M(T)$ and a lower value of T_C with respect to the bulk value have been observed previously for a $La_{0.67}Sr_{0.33}MnO_3$ film deposited on a LAO substrate.[8,9] It was explained by the 3-dimensional strain states in the film, governed by the epitaxial mode of film growth. The temperature-dependent magnetization for BL is significantly different from that predicted by simply adding the $M(T)$ values for both individual LSM and LCM films. The dashed line in Fig. 3a shows the predicted curve: $M_{\mathrm{BL}}(T)$

$=M_{\mathrm{LCM}}(T)+M_{\mathrm{LSM}}(T)$, where $M_{\mathrm{LCM}}(T)$ and $M_{\mathrm{LSM}}(T)$ are the magnetizations for the LCM and the LSM films, respectively. Since the thicknesses of the individual films are similar to those of the corresponding layers in BL, the added curve fits the experimental data fourty well at low temperatures (in the saturation magnetization range). However, the ferromagnetic transition of the BL film occurs at a higher temperature ($T_C \simeq 280$ K) than predicted. This result confirms that a significant change occurs in the magnetic properties of the LSM film deposited on LCM with respect to that on LAO.

This conclusion is supported by the temperature dependences of susceptibility for LSM (curve *1*), LCM (curve *2*) and BL (curve *3*) films in Fig. 3b. Since the low-temperature susceptibility peak for BL (curve *3*) mimics that of the individual LCM film, it can be concluded that the second peak belongs to the LSM layer in the BL. It is evident that the magnetic transition of the LSM film deposited on LCM becomes sharper and the saturated magnetization is achieved at a higher temperature than for a bare LSM film (see curve *1*).

Let us consider the possible mechanisms of enhanced magnetic and transport properties of the LSM film on LCM with respect to that on LAO. The aforementioned analysis of x-ray data showed that the out-of-plane lattice parameter c is larger for LSM/LAO. It is well known that LSM thin films grown on LAO substrates exhibit an out-of-plane uniaxial tensile strain and, correspondingly, an in-plane biaxial compression.[9,10] Assuming that the film is strained from the ideal bulk structure and that the structure is a single perovskite, the in-plane lattice parameter of film can be estimated from the unit cell volume in the bulk. The bulk $La_{0.8}Sr_{0.2}MnO_3$ compound has a rhombohedral pseudocubic symmetry ($R3c$) with hexagonal lattice parameters of $a_h \simeq 0.5517$ nm and $c_h \simeq 1.3359$ nm (Ref. 11). They are equivalent to cubic lattice parameters of $a \simeq b \simeq c \simeq 0.3871$ nm and to unit cell volume $V \simeq 0.058\ \mathrm{nm}^3$. Therefore, the in-plane lattice parameter for our LSM/LAO is $\sqrt{V}/c \simeq a \simeq 0.3828$ nm, which is almost identical to the value obtained for an epitaxial $La_{0.67}Sr_{0.33}MnO_3$ thin film.[1] For our LSM/LCM the in-plane lattice parameter is larger and equals $a \simeq 0.3852$ nm. This difference between film and bulk lattice parameters leads to the formation of the above-mentioned in-plane biaxial compressive strain, $\varepsilon_{100}=(a_{\mathrm{film}}-a_{\mathrm{bulk}})/a_{\mathrm{bulk}}$, and the out-of-plane uniaxial tensile strain, $\varepsilon_{001}=(c_{\mathrm{film}}-c_{\mathrm{bulk}})/c_{\mathrm{bulk}}$. The calculations performed show that $\varepsilon_{100} \simeq -1.37\%$ and $\varepsilon_{001} \simeq 2.8\%$ for the LSM/LAO and -0.49% and 1%, respectively, for the LSM/LCM. For weaker strains and cubic symmetry the Curie point can be expressed as, according to Millis model,[12]

$$T_C(\varepsilon)=T_C(\varepsilon=0)\left(1-\alpha\varepsilon_B-\frac{1}{2}\Delta\varepsilon_{JT}^2\right),$$

where $\varepsilon_B=(2\varepsilon_{100}+\varepsilon_{001})$ is the bulk strain, $\varepsilon_{JT}=\sqrt{2/3}(\varepsilon_{001}-\varepsilon_{100})$ is the Jahn—Teller strain, $\alpha=(1/T_C)(dT_C/d\varepsilon_B)$, and $\Delta=(1/T_C)(d^2T_C/d\varepsilon_{JT}^2)$. For the last two quantities we are took the values from Ref. 12, i.e., $\alpha=10$ and $\Delta=1000$. Using this equation and the values obtained for ε_{100} and ε_{001} in our LSM film and layer we calculated the change in Curie temperature $T_{C_{\mathrm{LSM/LCM}}}^{\mathrm{calc}}/T_{C_{\mathrm{LSM/LAO}}}^{\mathrm{calc}} \simeq 1.07$, which is an excellent agreement with our experimental result $T_{C_{\mathrm{LSM/LCM}}}/T_{C_{\mathrm{LSM/LAO}}} \simeq 1.077$. This confirms the strong correlation between crystal lattice distortion and the electronic and magnetic states in CMR materials.

In summary, the magnetic and the transport properties of $La_{0.8}Sr_{0.2}MnO_3$ films grown on an (001) $LaAlO_3$ substrate and on a $La_{0.8}Ca_{0.2}MnO_3$ layer were studied. It was shown that the metal-insulator and the ferromagnetic transitions occur at higher temperatures for the film deposited on $La_{0.8}Ca_{0.2}MnO_3$ layer than on $LaAlO_3$. The enhanced magnetoresistance and ferromagnetic ordering in the $La_{0.8}Sr_{0.2}MnO_3/La_{0.8}Ca_{0.2}MnO_3$ bilayer can be explained by lattice strain relaxation in the $La_{0.8}Sr_{0.2}MnO_3$ film.

This work was funded by the KOSEF through the Quantum Photonic Science Research Center.

*E-mail: pvg@imp.kiev.ua

[1] F. Tsui, M. C. Smoak, T. K. Nath, and C. B. Eom, Appl. Phys. Lett. **76**, 2421 (2000).
[2] R. A. Rao, D. Lavric, T. K. Nath, C. B. Eom, L. Wu, and F. Tsui, Appl. Phys. Lett. **73**, 3294 (1998).
[3] S. Jacob, T. Roch, F. S. Razavi, G. M. Gross, and H.-U. Habermeier, J. Appl. Phys. **91**, 2232 (2002).
[4] A. Biswas, M. Rajeswari, R. C. Srivastava, T. Venkatesan, R. L. Green, Q. Lu, A. L. de Lozanne, and A. J. Millis, Phys. Rev. B **63**, 184424 (2001).
[5] O. I. Lebedev, G. Van Tendeloo, S. Amelinckx, H. L. Ju, and K. M. Krishnan, Philos. Mag. **80**, 673 (2000).
[6] J. R. Sun, C. F. Yeung, K. Zhou, L. Z. Zhou, C. H. Leung, H. K. Wong, and B. G. Shen, Appl. Phys. Lett. **76**, 1164 (2000).
[7] V. G. Prokhorov, G. G. Kaminsky, V. A. Komashko, J. S. Park, and Y. P. Lee, J. Appl. Phys. **90**, 1055 (2001).
[8] T. K. Nath, R. A. Rao, D. Lavric, C. B. Eom, L. Wu, and F. Tsui, Appl. Phys. Lett. **74**, 1615 (1999).
[9] A. M. Haghiri-Gosnet, J. Wolfman, B. Mercey, Ch. Simon, P. Lecoeur, M. Korzenski, M. Hervieu, R. Desfeux, and G. Baldinozzi, J. Appl. Phys. **88**, 4257 (2000).
[10] Y. H. Li, K. A. Thomas, P. S. I. P. N. de Silva, L. F. Cohen, A. Goyal, M. Rajeswari, N. D. Mathur, M. G. Blamire, J. E. Evetts, T. Venkatesan, and J. L. MacManus-Driscoll, J. Mater. Res. **13**, 2161 (1998).
[11] J. F. Mitchell, D. N. Argyriou, C. D. Potter, D. G. Hinks, J. D. Jorgensen, and S. D. Bader, Phys. Rev. B **54**, 6172 (1996).
[12] A. J. Millis, T. Darling, and A. Migliori, J. Appl. Phys. **83**, 1588 (1998).

This article was published in English in the original Russian journal. Reproduced here with stylistic changes by AIP.

ELECTRONIC PROPERTIES OF METALS AND ALLOYS

Spectroscopy of bosonic excitations in manganite-based heterostructures

M. A. Belogolovskiĭ, Yu. F. Revenko, A. Yu. Gerasimenko, Yu. V. Medvedev, O. I. Chernyak, and V. M. Svistunov

*A. A. Galkin Donetsk Physicotechnical Institute, ul. R. Lyuksemburg 72, 83114 Donetsk, Ukraine**

G. Plitnik

Frostburg State University, Frostburg, MD 21532, USA
(Submitted January 8, 2003)
Fiz. Nizk. Temp. **29**, 889–893 (August 2003)

The tunneling current transport is investigated in layered structures based on lanthanum manganite. The spectral function of the electron–boson interaction is reconstructed over a wide energy range. High-energy excitations localized in the barrier and near-barrier regions are revealed. The inelastic scattering of charge carriers on these states can lead to suppression of the magnetoresistance of tunnel junctions with increasing applied voltage. © *2003 American Institute of Physics.* [DOI: 10.1063/1.1596797]

The observation of giant magnetoresistance in ferromagnetic heterostructures has stimulated detailed research on the physics of the phenomenon of spin-dependent tunneling of electrons in such systems.[1] One of the most interesting effects from both the fundamental and applied standpoints is the dependence of the magnetoresistance on the voltage applied to the junction. It has been found that the magnetoresistive effect decreases monotonically with increasing voltage, and its value depends substantially on the structure of the barrier layer (see the data of Refs. 2 and 3). Attempts to explain this phenomenon by distortion of the barrier potential in the region of the tunnel junction lead to values of the magnetoresistance which are much lower than the observed.[4] An alternative explanation may be found in the fact that the scattering of the tunneling electrons on magnetic states in the barrier flip the electron spin and thereby suppress the magnetoresistance effect.[4,5] In this connection we call attention to the spectra of the inelastic scattering of tunneling electrons in $Co/Al_2O_3/Ni_{80}Fe_{20}$ contacts.[6] They clearly exhibit a sharp feature at ± 100 mV, the intensity of which increases sharply as the temperature is lowered from room temperature to 1 K. However, observation of this anomaly is still not proof that a part of the electron's energy in inelastic tunneling processes is transferred to excitation specifically in the barrier layer. The hypothesis that the voltage dependence of the magnetoresistance is related to the intensity of inelastic processes in the near-barrier region and inside the barrier rests on two facts: a) the spectrum of the high-magnetoresistance heterostructures studied does indeed contain excitations with high energies ($\sim$100 MeV and higher); b) these excitations are localized inside the barrier and/or the near-barrier region. We note that, according to Ref. 7, besides processes involving a spin flip of the electron on magnetic impurities within the junction an appreciable role in the suppression of the magnetoresistance effect with increasing voltage may also be played by scattering on phonons.

In this paper we investigate tunnel contacts based on lanthanum manganite. As we have shown previously,[8] the conductance of such structures has a high sensitivity to magnetic field even when only one of the electrodes is made of doped lanthanum manganite. The observed effect was attributed to the realization of a magnetically two-phase state in the near-contact region and to the tunneling of electrons through spin-polarized localized states in the tunnel barrier. Here the magnetoresistance of the contacts studied in Ref. 8, like that of conventional structures with two ferromagnetic electrodes, decreased as the bias voltage across the contact was increased. The goal of the present study was to measure and analyze the spectra of elementary excitations of the asymmetric structure $La_{0.7}Ca_{0.3}MnO_3$–Ag over a wide range of energies considerably higher than 100 meV with the aid of our previously developed approach to the study of tunneling spectroscopy of normal contacts of the metal–insulator–metal type,[9] which has been successfully employed to explain the results obtained for normal lead, bismuth,[10] and the magnetic metals gadolinium and chromium.[11,12] In essence it consists in the study of the fine structure of the even $\sigma_+(V)=[dI(+V)/dV+dI(-V)/dV]/2$ and odd (in voltage) $\sigma_-(V)=[dI(+V)/dV-dI(-V)/dV]/2$ contributions to the differential conductance of the contact. As was shown in Ref. 9, the value of $\sigma_-(V)$ is proportional to the real part of the self-energy correction $\Sigma(\omega)$ to the electron energy in the metallic plates and can be used to reconstruct the shape of the spectral function $g(\omega)$ of the electron–boson interaction of the normal metal:

$$g(\omega)=\frac{2\omega}{Ce\sigma(0)\pi^2}\int_0^\infty \frac{d\sigma_-(V)/dV}{V^2-(\omega/e)^2}\,dV. \qquad (1)$$

We note that the electron–phonon interaction function $g(\omega)$ for the manganite $La_{0.75}Ca_{0.25}MnO_3$, which is very close in chemical composition, has been reconstructed[13] by the method of Yanson point-contact spectroscopy.[14] However, in

that approach there is practically no barrier, and that technique therefore yields information only about the bulk properties of the material. Indeed, the function $g(\omega)$ reconstructed in Ref. 13 exhibits features whose energy positions agree well with the data obtained in other bulk experiments. We, however, are interested in the barrier region, and for that reason we used a method based on the study of tunnel structures.

The $La_{0.7}Ca_{0.3}MnO_3$ manganites were obtained by the standard solid-phase synthesis from the initial oxides La_2O_3, CaO, and MnO at a temperature $T_s = 1200-1250\,^\circ$C in an air atmosphere with repeated pulverizing, pressing, and annealing. The time of the synthesis and sintering was 12 hours. Strips of dimensions $8\times1.5\times0.4$ mm for use as the investigated electrode of the tunnel contact were prepared by pressing the crushed manganite powder on an anvil between guides made of copper or aluminum wires and then sintering for 12 hours at a temperature of $1200-1250\,^\circ$C. Saturation with oxygen occurred during natural cooling to room temperature in the laboratory furnace. It is known that the surfaces of manganites prepared in this way have a natural layer with a lower oxygen content, which serves as a potential barrier for tunneling electrons. Electrical contacts were formed by burning in a silver past at a temperature of $\sim 450\,^\circ$C. As the injector we used silver in the form of a sharpened wire which was pressed against the sample with a force that was regulated by an adjusting mechanism, or a film deposited on the ceramic to be studied. The resistance of the resulting tunnel contacts at zero bias voltage at a temperature of 77 K fluctuated from tens to hundreds of ohms. The reconstruction of the spectral function and its subsequent analysis were done for contacts having a zero resistance not over 100 Ω, in which, in our opinion, it is more likely for a ferromagnetic metallic state to be realized in the manganite under study.

The derivatives of the current–voltage characteristics of the tunnel contacts were measured by a standard modulation technique in the fixed-voltage regime. The time constant of the output circuit was 100 ms, and the main filtering of the signal was done numerically with a Gaussian weight function, which made it possible to minimize the dynamic error. The second derivative $d^2I(V)/dV^2$, which was used for extraction of the spectral information, was obtained by numerical differentiation of the experimentally measured and numerically smoothed differential conductance $dI(V)/dV$.

Figure 1a shows the derivative of the odd part of the differential conductance of a tunnel contact at a temperature of 77 K, and Fig. 1b (solid curve) shows the electron–boson interaction function $g^{\sim}(\omega)$ reconstructed from it by the method of Ref. 9. One notices the existence (unlike the data of Ref. 13) of negative values of the function $g^{\sim}(\omega)$ at energies above 100 meV. Of course, this function itself is always positive. The apparent contradiction is removed when one considers the total contribution of the self-energy and ''interference'' corrections to the elastic tunneling channel. In the lowest order in the coupling constant of the electrons with bosonic states the self-energy contribution arises as a result of the emission and absorption of excitations within the electrode, while the ''interference'' correction corresponds to the ''redressing'' of the tunneling electron in the region between the electrode and the insulator. This correction is of opposite sign to the self-energy contribution, and its fine structure is determined by the spectrum of elementary excitations in the barrier and near-barrier regions. When the many-particle effects during tunneling are taken into account completely in this manner, according to Ref. 15, the electron–boson interaction function in the bulk of the conductor under study, $g_v(\omega)$, recstructed from the odd part of the conductance, will be modulated by a factor of $1-\varphi(\omega)$. The function $\varphi(\omega)$ is the product, averaged over angles of the vectors of the tunneling electrons, of the matrix elements of the classical tunneling Hamiltonian describing elastic tunneling and a modified correction to it which takes into account the interaction of the electrons with other excitations of the junction. The appearance of this factor reflects the simple fact that a tunneling electron cannot drag behind it intact the polarization cloud that forms around it when it moves in the interior of the electrode, and it is partially ''undressed.'' [15] since low frequencies correspond to long wavelengths (for the acoustic branch of vibrations), which are alone for the entire tunnel contact, at low frequencies the ''redressing'' will not occur, and, hence, the function $\varphi(\omega)$ should increase continuously with increasing frequency. At the same time, the intrabarrier and near-surface excitations described by the function $g_s(\omega)$ manifest themselves in the odd part of the conductance only through the ''interference'' correction, which is negative in sign. The net function $g^{\sim}(\omega)$ is the algebraic sum of two contributions:

$$g^{\sim}(\omega) = g_v(\omega)[1-\varphi(\omega)] - g_s(\omega)\varphi(\omega). \qquad (2)$$

Naturally, at energies corresponding to vibrations of the

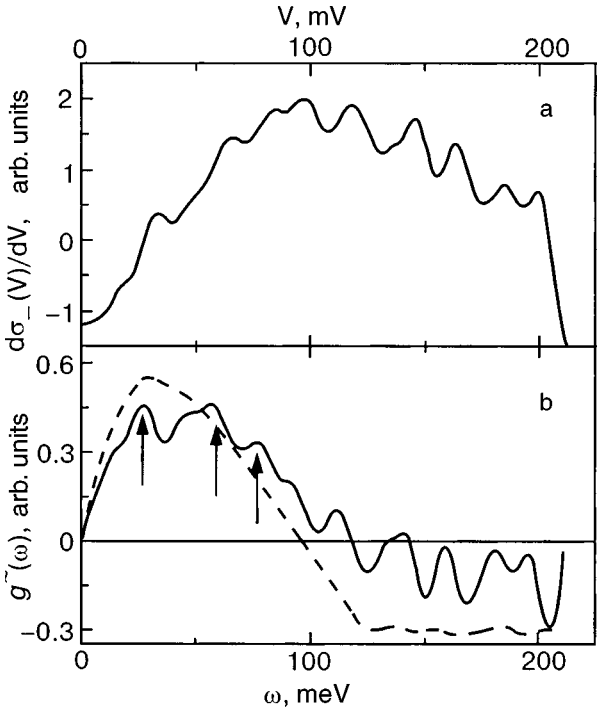

FIG. 1. Derivative of the odd part of the differential conductance of an asymmetric tunnel contact $La_{0.7}Ca_{0.3}MnO_3$–Ag (a) and the spectral function of the electron–boson interaction (the solid curve); the spectral function obtained according to expression (2) is shown by the dashed curve (b). The arrows indicate features in the Raman scattering spectrum of polycrystalline $La_{0.75}Ca_{0.25}MnO_3$ (Ref. 17).

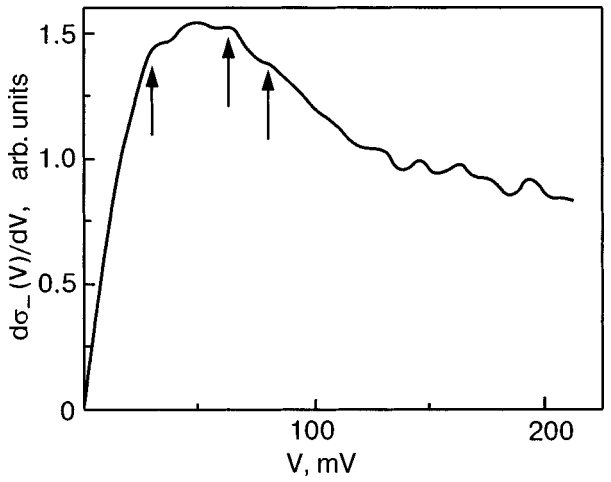

FIG. 2. Derivative with respect to voltage of the even part of the conductance of a $La_{0.7}Ca_{0.3}MnO_3$–Ag tunnel contact. The arrows indicate features in the Raman scattering spectrum of polycrystalline $La_{0.7}Ca_{0.25}MnO_3$ (Ref. 17).

manganite crystal lattice this function is positive, but where only the barrier contribution is present it is formally negative and thereby demonstrates the presence of intrabarrier states on which the tunneling electrons scatter. We note that, according to the standard theory of tunneling,[16] those states also manifest themselves in the inelastic channel, and the derivative of the even part of the conductance with respect to voltage is proportional to the density of states for all the bosonic excitations that exist in the system, including those localized within the barrier and in the near-barrier region.

Let us consider the results presented in Fig. 1 in terms of these ideas. Figure 2 shows the voltage derivative of the even part of the conductance measured at 77 K, and the arrows indicate the positions of the spectral features that are manifested in Raman scattering experiments in polycrystalline $La_{0.75}Ca_{0.25}MnO_3$ (Ref. 17). It is known from this and other experimental studies (see, e.g., Ref. 13) that the spectrum of bosonic excitations of the manganites ends at around 100 meV. The higher-energy features clearly observed in Fig. 2 must be associated with states in the barrier and in the near-barrier region. This assumption immediately accounts for the negative part in the reconstructed function $g^{\sim}(\omega)$ in Fig. 1b, since, as we have said, the interaction of the tunneling electron with such excitations leads to a negative contribution to the reconstructed electron–boson interaction function. Let us illustrate this circumstance again by assuming, as follows from formula (2), that the spectrum shown in Fig. 2 consists of two components: the spectrum $g_v(\omega)$ of the corresponding Bose states in the manganite itself (below 100 meV), and the spectrum of subsurface excitations $g_s(\omega)$ (above 100 meV). The form of the function $\varphi(\omega)$ in (2) is determined by the properties of the tunnel junction and, generally speaking, varies from sample to sample. In the present study we have used for $\varphi(\omega)$ the shape obtained for lead junctions in Ref. 15. The corresponding curve for the total $g^{\sim}(\omega)$ (the dashed curve in Fig. 1b) obtained according to formula (2), which, of course, should be regarded as a qualitative result, agrees with the behavior of the function $g^{\sim}(\omega)$ reconstructed from the odd part of the differential conductance.

We have observed experimentally the presence of a broad continuum of high-energy bosonic excitations localized in the barrier and near-barrier regions of manganite-based tunnel junctions. The energies of these features are too high for phonons and, according to an analysis, indicate that they are of a magnetic origin. The point is that the scattering of a tunneling electron on such excitations should lead to a flip of its spin and, ultimately, to suppression of the magnetoresistance. The lower limit of the energies of the states we have observed is around 100 meV, in good agreement with the data on the dependence of the magnetoresistance of manganite-based tunnel junctions on the applied voltage.[2,3,8] The data obtained provide a substantial argument in favor of the hypothesis that this behavior is of a magnetic nature.[4,5]

*E-mail: vlamis@hsts.fti.ac.donetsk.ua

[1] J. S. Moodera, J. Nassar, and G. Mathon, Annu. Rev. Mater. Sci. **29**, 381 (1999).
[2] L. P. Shelp, A. Fert, F. Fettar, P. Holody, S. F. Lee, J. L. Maurice, F. Petroff, and A. Vaures, Phys. Rev. B **56**, R5747 (1997).
[3] J. S. Moodera, L. R. Kinder, T. M. Wong, and R. Meservey, Phys. Rev. Lett. **74**, 3273 (1995).
[4] A. M. Bratkovsky, Phys. Rev. B **56**, 2344 (1997); X. Zhang, B. Z. Li, G. Sun, and F. C. Pu, Phys. Rev. B **56**, 5484 (1997).
[5] S. Zhang, P. M. Levy, A. C. Marley, and S. S. P. Parkin, Phys. Rev. Lett. **79**, 3744 (1997).
[6] J. S. Moodera, J. Nowak, and R. J. M. van de Veerdonk, Phys. Rev. Lett. **80**, 2941 (1998).
[7] A. M. Bratkovsky, Appl. Phys. Lett. **72**, 2334 (1998).
[8] V. M. Svistunov, Yu. V. Medvedev, V. Yu. Tarenkov, A. I. D'yachenko, E. Hatta, M. Mukasa, R. Aoki, H. Szymczak, S. Lewandowski, and J. Leszczynski, Zh. Éksp. Teor. Fiz. **118**, 629 (2000) [JETP **91**, 547 (2000)].
[9] V. M. Svistunov and M. A. Belogolovskiĭ, *Tunneling Spectroscopy of Quasi-Particle Excitations in Metals* [in Russian], Naukova Dumka, Kiev (1986).
[10] V. M. Svistunov, M. A. Belogolovskiĭ, O. I. Chernyak, A. I. Khachaturov, and A. P. Kvachev, Zh. Éksp. Teor. Fiz. **84**, 1781 (1983) [Sov. Phys. JETP **57**, 1038 (1983)].
[11] E. Hatta, T. Sasaki, V. Svistunov, M. Belogolovskii, O. Chernyak, A. Khachaturov, and A. Gerasimenko, J. Phys. Soc. Jpn. **70**, 1865 (2001).
[12] A. Yu. Gerasimenko, M. A. Belogolovskiĭ, Yu. F. Revenko, O. I. Chernyak, V. M. Svistunov, V. E. Shaternik, E. M. Rudenko, E. Hatta, and T. Sasaki, Fiz. Tverd. Tela (St. Petersburg) **44**, 1158 (2002) [Phys. Solid State **44**, 1208 (2002)].
[13] J. Mitra, A. K. Raychaudhuri, N. Gayathri, and Ya. M. Mukovskii, Phys. Rev. B **65**, 140406 (2002).
[14] I. K. Yanson, Zh. Éksp. Teor. Fiz. **66**, 1035 (1974); I. K. Yanson and A. V. Khotkevich, *Atlas of Microscopic Spectra of the Electron–Phonon Coupling in Metals* [in Russian], Naukova Dumka, Kiev (1986).
[15] M. A. Belogolovskiĭ, Yu. M. Ivanchenko, and Yu. V. Medvedev, JETP Lett. **21**, 332 (1985).
[16] Yu. M. Ivanchenko and Yu. V. Medvedev, Fiz. Nizk. Temp. **2**, 141 (1976) [Sov. J. Low Temp. Phys. **2**, 69 (1976)].
[17] Jian-Min Li, C. H. A. Huan, You-Wei Du, Duan Feng, and Z. X. Shen, Phys. Rev. B **63**, 024416 (2000).

Translated by Steve Torstveit

LOW-DIMENSIONAL AND DISORDERED SYSTEMS

Changes of the IR spectrum and hydrogen bond enthalpy in thin-film water cryocondensates*

A. Drobyshev,** A. Aldijarov, K. Abdykalykov, and G. Panchenko

Kazakh National University, Tole bi 96, 480012 Alma Ata, Kazakhstan
(Submitted December 19, 2002)
Fiz. Nizk. Temp. **29**, 894–899 (August 2003)

Measurements of the IR spectra are made on thin-film water cryovacuum condensates formed on a metal substrate in the temperature range 16–200 K. It is found that the frequency of molecular stretching vibrations are shifted to lower frequencies with increasing temperature; this is explained by a weakening of the hydrogen bond. A calculation of the change in H-bond enthalpy shows that this change is larger for thinner samples. A fine structure of the librational bands of intramolecular protonic transitions in the cryocondensate is revealed. It may be due to the different orientations of the molecules relative to the internal field in samples formed at different temperatures. © *2003 American Institute of Physics.* [DOI: 10.1063/1.1596798]

INTRODUCTION

The well-known structural diversity of the solid phase of water is largely due to the specific interaction between its molecules in the condensed state—the hydrogen bond,[1,2] which arises as a result proton–proton exchange between neighboring water molecules. This allows one to consider water in the condensed state as a system ordered with respect to the oxygen but with a disordered proton subsystem. Of the more than ten structural modifications of ice, only phases II and VIII are ordered with respect to the protons; ice in phase IX has a partially ordered proton subsystem.[3]

The presence of the hydrogen bond is manifested, in particular, in a decrease of the characteristic frequencies of the O—H stretching vibrations in the IR spectra. This circumstance makes IR spectroscopy one of the main methods used to study the hydrogen bond and its influence on the structural phase transformations in condensed media.

In the course of proton exchange, two types of defects are created in the structure of ice: ionic and orientational (Bjerrum defects). In the first case the hop of a proton occurs along the hydrogen bond from one molecule to another. As a result, a pair of ionic defects, H_3O^+ and OH^-, are formed, and this decreases the length of the O—H bond and decreases the frequency of stretching vibrations. In the second case the proton goes over to a neighboring bond of the same H_2O molecule. Formally such a hop can be considered to be a rotation of the water molecule by 120°. As a result, an absorption band corresponding to librational vibrations appears in the IR spectrum.

The above considerations are the underlying basis for the research reported here on the dependence of the IR spectra of thin-film cryovacuum condensates of water on the deposition temperature and on the temperature regime in which the samples have existed. Previous studies[4] had revealed substantial temperature dependence of the IR spectra of ordinary and heavy water. However, those studies were done on rather thick samples, with thicknesses of more than 3 μm. The fine structure of the characteristic absorption bands corresponding to the main intra- and intermolecular vibrations were not analyzed, although it is known[5] that processes such as cluster formation and the interaction via the hydrogen bonds can be manifested in the form of overtones against the background of the fundamental frequencies. Moreover, the presence of a static field due to the formation of hydrogen bonds in the crystal leads to a perturbation of the fundamental intramolecular and lattice vibrations. This is expressed in a shift of their frequencies and in a change in the absorption amplitude. Thus analysis of the IR spectrum of cryovacuum condensates formed at different thermodynamic parameters can yield information about the change in the character of the intermolecular interaction in the cryocrystal.

EXPERIMENTAL SETUP AND PROCEDURE

The IR spectra of H_2O cryocondensates were measured for the purpose of revealing the features of the formation of Bjerrum defects under different conditions of cryodeposition. The measurements were made on the experimental setup described in detail in previous papers.[6,7] The experimental procedure was as follows. At a fixed substrate temperature T_c (the condensation temperature) and fixed water vapor pressure $P=5\times10^6$ torr in the volume a sample for study was formed on the substrate. During the condensation a double-beam laser interferometer was used to determine the thickness of the sample and the index of refraction, and the IR reflection spectrum of the cryocrystal–substrate system was measured at the condensation temperature. As a result we obtained absorption spectra recorded after two passes of the optical signal through the film.

Then the substrate temperature was slowly increased at a rate of not more than 0.05 K/s. When a specified temperature was reached, a temperature stabilization system was turned on and the measurement of the IR spectrum was repeated.

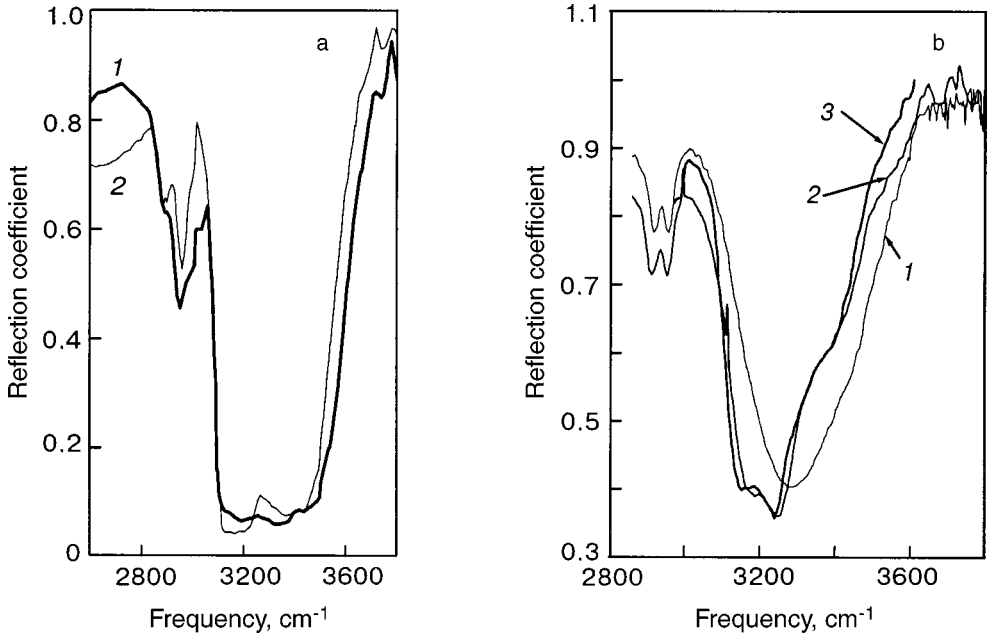

FIG. 1. IR spectrum of water cryocondensates in the frequency interval of the stretching vibrations: a—sample thickness $d=2.5$ μm, $T_c=40$ K (*1*) and 120 K (*2*); b—sample thickness $d=0.25$ μm, $T_c=16$ K (*1*), 120 K (*2*), and 140 K (*3*).

RESULTS AND DISCUSSION

Vacuum cryocondensates of H_2O

In the temperature interval from 10 to 200 K, vacuum cryocondensates of water can be found in three structural states, depending on the deposition temperature: amorphous ice ($T_c<80$ K), cubic I_c ($110\text{ K}<T_c<160$ K), and hexagonal I_h ($T_c>130-140$ K). The amorphous and cubic ices are metastable and undergo a transition to ice I_h (or to amorphous ice via I_c) as the temperature is raised.

Figure 1 shows the IR spectra of water cryovacuum condensates in the frequency range of the stretching vibrations. Samples of different thickness were obtained on a metal (Invar) substrate at condensation temperatures corresponding to the existence of the amorphous, cubic, and hexagonal phases of ice cryocrystals. We see that increasing the condensation temperature leads to a substantial narrowing of the absorption band and to a certain general transformation of the spectra, especially in the interval $2900-3000$ cm^{-1}. This change is more noticeable at the transition from the existence temperatures of the amorphous phase to those of the crystalline state. At the same time, the difference between spectra *2* and *3* in Fig. 1b (presumably states I_c and I_h) is insignificant. It is also interesting that, unlike the case of amorphous ice, the spectrum of the crystalline state displays fine structure.

One notices the presence of features near 3000 cm^{-1} in the spectrum of the films formed at $T=120$ K. The appearance of the small peak is apparently a manifestation of a Fermi resonance, which in this case arises when the first overtone of the deformation vibrations coincides in frequency with the stretching vibrations, leading to an increase in the intensity of the former against the background of the stronger stretching vibrations (this is properly called a Fermi resonance).

The above-mentioned shift of the stretching vibrations to lower frequencies was attributed by Badger and Bauer[3] to a change of the enthalpy of the hydrogen bond according to the relation $\Delta\nu_{\text{OH}}=-\Delta H/0.024$, where ΔH is the change in enthalpy of the O—H valence bond in the static field of the hydrogen bond. This relation can be used to calculate the change in enthalpy of the hydrogen bond of the films as a result of an increase in temperature for samples of different thickness (see Table I).

As expected, increasing the temperature of a water cryocondensate leads to a decrease in the energy of the hydrogen bond. However, this change is more significant for thinner films. This is most likely because of a size effect, as we have pointed out previously.[7,10]

The IR spectra of the condensate in the frequency interval $2000-2600$ cm^{-1} are shown in Fig. 2a. This is the interval of the so-called associative vibrations. It is assumed that the appearance of this band in water cryocrystals is due to an interaction of the translational and librational modes of vibrations with the deformation vibrations of the molecule. As is seen in the figure, the spectra corresponding to different condensation temperatures are significantly different. Increasing the condensation temperature leads to a decrease of both the width and intensity of the absorption band. It can be assumed with a high degree of certainty that these changes are a consequence of structural phase transformations in the ice cryocrystal on going from low condensation temperatures to higher ones. Most likely this is a transition from an amorphous to a crystalline (I_c) state of ice.

TABLE I. Change in enthalpy of the hydrogen bond in a water cryocondensate upon a change in deposition temperature.

Sample thickness, μm	Measurement temperature, K	$\Delta\nu$, cm^{-1}	ΔH, J/mole
0.25	16–120	67	−19.21
2.5	40–120	22	−6.28

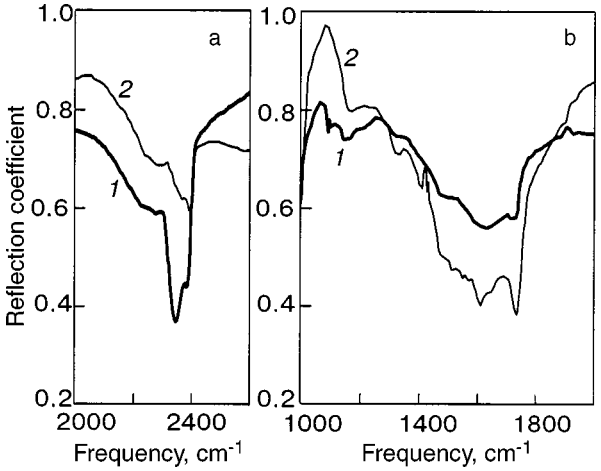

FIG. 2. IR spectrum of water cryocondensates in the frequency intervals of associative vibrations (a) and deformation vibrations (b). Sample thickness $d=2.5$ μm. Condensation temperature $T_c=40$ K (*1*) and 120 K (*2*).

Figure 2b shows the interval 1000–2000 cm^{-1}. This is the interval of deformation angular vibrations of the ice molecule along the H—O—H bonds, with a maximum of the absorption at a frequency $\nu_2=1650$ cm^{-1}. It is seen that the intensity of the absorption increases substantially with increasing condensation temperature, and the fine structure of the spectrum is manifested to a greater degree. This may be evidence that the hydrogen bonds in ice I_c are bent more than in amorphous ice.[9] Here the width and position of the band remain practically unchanged. This corresponds to the stated assumption that the deformation vibrations react weakly to the structural transformations in proton-disordered ices.

The IR spectrum of the condensate in the frequency interval 500–1000 cm^{-1} are shown in Fig. 3. This is the frequency interval of the maximum of the absorption band corresponding to librational vibrations of a water molecule (Fig. 3a) at a site of the crystal lattice. It is clear that we are not talking about physical librations of the molecules. At low temperatures these vibrations are frozen out and require an activation energy comparable to the enthalpy of fusion of the crystal. The appearance of this frequency is due to the disordered nature of the proton subsystem in vacuum cryocondensates of water vapor. The intramolecular transition of a proton to one of the unshared oxygen bonds (the formation of L–D defects) formally leads to rotation of the molecule by 120°. There are two interesting features in the shape and position of the spectral lines: the presence of fine structure, and a shift of the absorption half-width to higher frequencies as the temperature is raised.

The appearance of two pronounced absorption peaks is due, we believe, to the following circumstances. The presence of an internal field in the water cryocondensate makes for spatial anisotropy. This means that, depending on the orientation of the molecules, the intramolecular transition of protons to one unshared oxygen bond or another has a different activation energy and, hence, librational frequency. For two protons this means the presence of four combinations of tunneling, two of which are energetically equivalent. An increase in the temperature of the cryocrystal and the corresponding structural transformation lead to a change in the field of the lattice and the orientation of the molecule. In particular, the spectra shown in the figure for different condensation temperatures reliably correspond to the existence regions of the amorphous (spectrum *1*), cubic (*2*), and hexagonal (*3*) structures of ice. These circumstances may be the cause of the overall shift of the absorption bands of the librational vibrations to higher frequencies, which means an increase in the energy of formation of L–D defects.

Vacuum cryocondensates of an isotopic mixture of water

The presence of stable isotopes (D_2O and HDO) in water makes it possible to obtain more complete information in a single experiment by condensing films of isotopic mixtures. In particular, one can reveal the features of the proton–proton and proton–deuteron exchange in the cryocondensed mixture upon the formation of Bjerrum defects. In our case the objects of study wee cryocrystal films deposited from water vapor with a composition by mass of H_2O(10%)

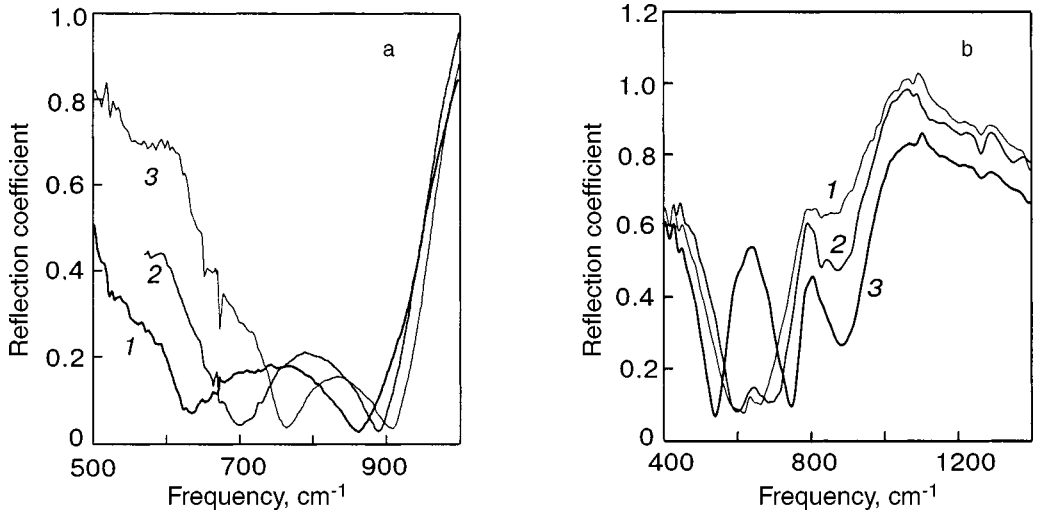

FIG. 3. IR spectrum of cryocondensates of H_2O (a) and D_2O (b) in the frequency interval of librational vibrations. Sample thickness $d=2.5$ μm. Sample temperatures: a—$T_c=16$ K (*1*), 120 K (*2*), 180 K (*3*); b—$T_c=30$ (*1*), $T=100$ K (heated from $T_c=30$ K) (*2*), $T_c=100$ (deposited at this same temperature) (*3*).

TABLE II. Change in the enthalpy of the hydrogen bond in a cryocondensate of an isotopic mixture of water upon a change in the deposition temperature.

Type of bond	Measurement temperature, K	$\Delta\nu$, cm^{-1}	ΔH, J/mole
O—H	30–100	36	−10.28
O—D	30–100	5	−1.43

$+HDO(50\%)+D_2O(40\%)$. The results obtained for the O—H and O—D stretching vibrations of the HDO and D_2O molecules and also the deformation vibrations of these molecules are in many respects similar to the data for pure water. For both the O—H and O—D valence bonds one observes a noticeable change in the absorption spectrum. The calculated changes in the enthalpy of the hydrogen bond accompanying these structural changes are given in Table II.

It is seen from the data presented that the change in enthalpy of the hydrogen bond is substantially greater for the O—H valence bond than for the O—D bond. This may be due to the fact that because of the larger mass of the D_2O molecule the transition temperature from the amorphous to the cubic state of the cryocondensate of heavy water is higher than that of light water. In this case the degree of annealing of the sample would be different for the different components.

It should be noted that the heating temperature and the condensation temperature $T=100$ K in this case are several degrees lower than the temperature of the transition from amorphous ice to the cubic modification, $T\approx 110$ K (this observation will be important for analysis of the librational vibrations). Therefore, in the temperature regimes indicated one observes not so significant a change in the width and position of the absorption bands in the frequency interval of the stretching vibrations as on heating to $T=130$ K (see Ref. 10); this may be due to a partial transition of amorphous low-temperature ice to the cubic state.

In the interval $400-1400\ cm^{-1}$ (Fig. 3b) one finds the absorption bands of the librational vibrations corresponding to the formal rotation of the molecule upon intramolecular transitions of the protons (deuterons). A common characteristic of the spectra analyzed is their substantial dependence on the condensation temperature. This means that the intramolecular vibrations under study depend on the intermolecular interaction.

Spectra *1* and *2* correspond to the temperature existence region of the amorphous phase. However, sample 2 in the course of heating was found rather close to the boundary of the existence region of the amorphous state for pure water (110 K). This had a noticeable effect on the shape of the spectrum. A general shift to higher frequencies occurred. In the frequency interval corresponding to protonic intramolecular transitions along the O—H bonds of the H_2O and HDO molecules ($800-1000\ cm^{-1}$) the amplitude of the absorption spectrum increased. In addition, a fine structure was identified, the nature of which was discussed above in the analysis of the data shown in Fig. 3a.

A more substantial change in the spectrum is observed for the sample deposited directly at the condensation temperature $T_c=100$ K (curve *3*). First, the absorption spectrum becomes considerably wider. Its structure has three pronounced absorption bands. The first lies in the frequency interval $800-1000\ cm^{-1}$ with a maximum at $\nu=890\ cm^{-1}$. This band is probably the result of a superposition of the frequencies of the protonic transition along the O—H bond of the H_2O and HDO molecules. Since one would not expect substantial structural changes when the condensation temperature is changed from 30 to 100 K (as is confirmed by analysis of the stretching vibrations), the observed effect most likely is of an orientational nature. During condensation at the higher temperature there is a greater likelihood that the orientation of the molecules will be determined by the internal field of the crystal. At the same time the orientational disorder which is observed for condensation on a substrate at the lower temperature cannot be substantially altered by a slight heating of the sample. These circumstances are fully capable of causing the formation of a single absorption band and an increase of its intensity.

The second band lies in the frequency interval from 650 to $800\ cm^{-1}$, with a maximum of the absorption at $\nu\approx 760\ cm^{-1}$. It is apparently due to intramolecular transitions of deuterons in D_2O molecules. The band lying in the frequency interval $450-600\ cm^{-1}$ with a maximum at $\nu\approx 550\ cm^{-1}$ corresponds to analogous transitions in the HDO molecule.

CONCLUSIONS

1. We have observed a shift of the stretching vibrations of water to lower frequencies, indicating a weakening of the hydrogen bond, as the sample temperature is raised. This effect is larger for thinner samples.

2. The features in the spectrum of water cryocrystals in the region $3000\ cm^{-1}$ can be explained as being a manifestation of a Fermi resonance between the first mode of the deformation vibrations and the stretching vibrations.

3. We have found that the deposition temperature of cryocrystals of an isotopic mixture of water has a substational influence on the bands of librational vibrations corresponding to intramolecular transitions of protons and deuterons. This is due to the difference in the orientational ordering of samples prepared at different temperatures.

*This report was presented at the Third International Workshop on Low-Temperature Physics in Microgravity Environment (CWS-2002)

**E-mail: drobyshev@nursat.kz

[1] G. C. Pimentel and A. L. McClelan, *The Hydrogen Bond*, Freeman, San Francisco (1960), Mir, Moscow (1964).
[2] V. V. Moskva, "The hydrogen bond in organic chemistry" [in Russian], Sorosovkiĭ Obrazovatel'nyĭ Zhurnal No. 2, 58 (1999).
[3] G. N. Zatsepina, *Physical Properties and the Structure of Water* [in Russian], Moscow University Press, Moscow (1987), p. 53.
[4] A. S. Drobyshev and D. N. Garipoglyi, Fiz. Nizk. Temp. **22**, 1064 (1996) [Low Temp. Phys. **22**, 812 (1996)].
[5] H. Ogasawara, J. Yoshinobu, and M. Kawai, J. Chem. Phys. **111**, 70038 (1999).
[6] A. S. Drobyshev and T. A. Prokhodtseva, J. Low Temp. Phys. **119**, 431 (2000).

[7] A. Aldijarov, A. S. Drobyshev, and Sh. Sh. Sarsembinov, Fiz. Nizk. Temp. **28**, 297 (2002) [Low Temp. Phys. **28**, 210 (2002)].
[8] D. Eizenber and V. Kautsman, *Structure and Properties of Water* [in Russian], Gidrometeoizdat, Leningrad (1975), p. 124.
[9] J. E Bertie and E. J. Whalley, Chem. Phys. **40**, 1646 (1964).
[10] A. Aldijarov, A. S. Drobyshev, and Sh. Sh. Sarsembinov, Fiz. Nizk. Temp. **28**, 414 (2002) [Low Temp. Phys. **28**, 290 (2002)].

Translated by Steve Torstveit

Thermodynamics of a one-dimensional generalized Wigner crystal

V. V. Slavin*

B. Verkin Institute for Low Temperature Physics and Engineering, National Academy of Sciences of Ukraine, pr. Lenina 47, 61103 Kharkov, Ukraine

(Submitted February 5, 2003; revised March 4, 2003)
Fiz. Nizk. Temp. **29**, 900–905 (August 2003)

The thermodynamic characteristics of a one-dimensional generalized Wigner crystal are investigated for arbitrary temperature, particle density, and character of the interparticle repulsive pair potential. A method is proposed which permits calculating the partition function of the system with allowance for the interaction between an arbitrary number of neighboring particles. It is shown that increasing this number leads to the appearance of increasingly fine steps in the low-temperature dependence of the particle density on the chemical potential. These steps are remnants of a dependence of the ''devil's staircase'' type that is characteristic for this sort of system at zero temperature. © *2003 American Institute of Physics.* [DOI: 10.1063/1.1596799]

1. INTRODUCTION

Narrow-band low-dimensional conductors with a long-range interparticle repulsive potential have been attracting heightened interest in recent years. This interest is largely a result of progress in the technology of fabricating multilayer structures based on metal oxides (including high-temperature superconductors) and also one- and two-dimensional artificial conducting systems—superlattices.

It has been shown[1,2] that if the bandwidth $t \lesssim U$ ($U \sim (a/R)E$ is the characteristic change in the energy of the long-range repulsive electron–electron potential upon an electron hop, a is the interatomic distance in the substrate, R is the average distance between electrons, and E is the Coulomb energy per electron), complete destruction of the Bloch states occurs, and the electrons become localized within quantum traps of atomic size. It should be noted that by virtue of of the dynamic nature of the localization, this state, which has been given the name ''frozen electron phase'' (FEP), is qualitatively different from a Wigner crystal.[1,3,4] For example, heating the FEP does not lead to delocalization of the electrons, and so, unlike a Wigner crystal, the FEP does not transform into a Fermi liquid at any temperature (for the sake of brevity we shall understand the term FEP to mean a system found in a state of frozen electron phase). The behavior of a FEP at not too small a ratio t/U is extremely complex,[5] and for this reason it is necessary to do a number of additional studies in order to construct a consistent thermodynamics and to describe the kinetics of such systems.

It is logical to begin with a study of the thermodynamics of the FEP, neglecting all dynamic effects arising because of the finite bandwidths (i.e., assuming $t=0$). The ground state of such systems, which Hubbard has called the ''generalized Wigner crystal,'' was first considered in Ref. 6. A thermodynamics of the one-dimensional generalized Wigner crystal, in a model neglecting the dynamic effects due to the finite bandwidths was constructed in Ref. 5. In that model the simplifying assumption was made that the pair interaction potential falls off so fast that one can neglect the interactions between next-nearest-neighbor particles. Nevertheless the thermodynamics constructed in the framework of even that simplified model displays a number of extremely interesting properties. For example, it was shown that the low-temperature dependence of the particle density ν on the pressure P is a set of steps corresponding to densities of the form $\nu = 1/q$, $q = 1,2,3...$. These steps are the remnants of the ''devil's staircase'' that characterizes the dependence $\nu(P)$ at zero temperature. Each step corresponds to an electron ''crystal'' with period q. At a finite temperature, defects form in the ''crystal''—pairs of particles with interparticle distances different from q. The density of defects $\rho_{\text{def}} = N'/N$ (N' is the number of pairs of particles with an interparticle distance different from q; N is the number of pairs of particles with an interparticle distance equal to q) is exponentially small near the center of the steps and is close to unity near the boundaries of the intervals, completely destroying the given electron ''crystal.''

However, there remains an open question as to the influence of the structure of the pair potential on the thermodynamic properties of the system. The goal of that article is a generalization of the treatment of Ref. 5 to the case of an arbitrary character of the mutually repulsive pair potential of the particles.

2. MODEL

The Hamiltonian of the system has the form

$$\mathcal{H} = \mathcal{H}(l_1, l_2, \ldots, l_N) = \frac{1}{2} \sum_{\substack{m,n=1 \\ m \neq n}}^{N} \varepsilon(l_m - l_n), \tag{1}$$

where the discrete independent variable l_m ($m = 1,\ldots,N$) is the coordinate of the mth electron, measured in units of a, N is the total number of electrons, and $\varepsilon(x)$ is the long-range repulsive interparticle pair potential. This potential is a convex function of the continuous argument x and falls off faster than x^{-1} but is otherwise arbitrary. To begin it is necessary to study the features of the ground state of the Hamiltonian (1). That was first done by Hubbard,[6] who proposed a rigorous procedure for constructing the configuration of the ground state of the system. As was later shown by Sinai,[7] the Hubbard algorithm can be described by the simple formula

$$l_i=\left[i\frac{1}{\nu}+\varphi\right]. \tag{2}$$

Here $\nu=N/N_0$ is the electron density (filling factor), N_0 is the total number of lattice sites (N_0 is the length L of the one-dimensional system, measured in units of a), $1/\nu$ has the meaning of the average interelectron distance, [...] denotes the integer part of a number, and φ is an arbitrary quantity (the initial phase). Below we shall study the usual thermodynamic limit (i.e., $N,N_0\to\infty$ in such a way that the density ν remains finite).

We begin by listing the most important properties of the generalized Wigner crystal.[7]

— At a given chemical potential μ only *rational* values "survive": $\nu=p/q$ (p and q are integers).

— The "crystal" is a periodic electron structure with p particles per cell and a length of the period equal to q.

— The latter fact leads to a rather specific dependence of ν on μ—the so-called "devil's staircase"—a well-developed fractal structure[6–8] in which to each rational value $\nu=p/q$ there corresponds a finite interval $\Delta\mu$ of the chemical potential μ within which ν is constant.

Following the arguments given in Ref. 8, we find

$$\Delta\mu=q\Delta\varepsilon(q), \tag{3}$$

where

$$\Delta\varepsilon(q)=\sum_{k=1}^{\infty}k(\varepsilon(qk+1)-2\varepsilon(qk)+\varepsilon(qk-1)). \tag{4}$$

The boundary conditions ($\mu_d(p/q)$ and $\mu_i(p/q)$) of the $\nu(\mu)$ intervals of the devil's staircase are the changes of the ground state energy which arise when N increases or decreases by *one particle*, respectively. The ground state and its spatial structure have a universal nature for all physically reasonable pair potentials $\varepsilon(x)>0$.

As will be seen from the discussion that follows, T and P will be more convenient thermodynamic variables for our analysis than T and μ. It has been shown[5] that the dependence of ν on P at $T=0$ is also a devil's staircase, which differs from $\nu(\mu)$ only in the width of the "steps," ΔP. The end points of this devil's staircase—$P_d(p/q)$ and $P_i(p/q)$—correspond to a change in energy of the ground state upon a decrease or increase in the length L of the system by *one step* at a fixed N (P is measured in energy units, and $P_i<P_d$):

$$\Delta P=p\Delta\mu/q=p\Delta\varepsilon(q). \tag{5}$$

Let us consider the change in energy $E(N,L)$ ($\nu=N/L=p/q$) when N and L decrease or increase by an amount equal to the number of electrons per cell p or by the period of the crystal q, respectively. Taking into account the definition of the end points of the steps of the devil's staircase, $P_i(\nu)$ and $P_d(\nu)$, we have

$$E(N,L-q)=E(N,L)+qP_d,$$
$$E(N,L+q)=E(N,L)-qP_i. \tag{6}$$

On the other hand, the energies $E(N,L\pm q)$ can be expressed in terms of the end points $\nu(\mu)$ of the devil's staircase—$\mu_i(\nu)$ and $\mu_d(\nu)$:

$$E(N,L-q)=E(N-p,L-q)+p\mu_i,$$
$$E(N,L+q)=E(N+p,L+q)-p\mu_d. \tag{7}$$

The simultaneous increase (decrease) of N by p and L by q is equivalent to the addition (removal) of one unit cell of the "crystal." Consequently,

$$E(N\pm pL\pm q)=E(N,L)\pm u(\nu), \tag{8}$$

where $u(\nu)$ is the energy per cell of the generalized Wigner crystal.

Combining Eqs. (6), (7), and (8), one can easily show that

$$(\mu_i-\mu_d)p=(P_d-P_i)q.$$

This relation is the same as formula (5), since $\Delta\mu=\mu_i-\mu_d$ and $\Delta P=P_d-P_i$.

Expressions (3) and (5) have one remarkable property that is worthy of special note: the intervals of the steps of the devil's staircase $\Delta\mu$ and ΔP are proportional to the quantity $\Delta\varepsilon$ (4), which is determined by the electron–electron interaction at distances $\gtrsim q$, *independently of the number of electrons per cell* p. Thus $\Delta\mu$ and ΔP go to zero for $q\to\infty$ as $\partial^2\varepsilon(x)/\partial x^2|_{x=q}$. Consequently, the larger the "irrational" coefficient p/q, the shorter the length of the intervals (3), (5). This suggests that at finite temperatures *all* the spatial structures of the generalized Wigner crystal of period q for which the condition $\varepsilon(q)\gg T$ is satisfied are only slightly perturbed by thermal fluctuations. If, on the contrary, q satisfies the condition $\varepsilon(q)\lesssim T$, then the corresponding structures are essentially destroyed, obliterating the intervals of the devil's staircase $\Delta P(q)$ and $\Delta\mu(q)$.[1)]

3. THERMODYNAMIC POTENTIAL

The proposed method for construction of the thermodynamics is based on the derivation of recursion relations for the partition function of the system under study. In the derivation we shall take into account the interaction between $\mathcal{K}$ nearest neighbors ($\mathcal{K}=1,2,3,\ldots$). $\mathcal{K}=1$ corresponds to the nearest-neighbor approximation, considered in Ref. 5; for $\mathcal{K}=2$ the interactions between nearest and next-nearest neighbors are taken into account, and so on. We introduce a partial partition function of the one-dimensional lattice system of N particles and L sites in which the last site is occupied by a particle. In addition, let i_1, i_2, and $i_{\mathcal{K}-1}$ be the coordinates of the last $\mathcal{K}-1$ particles. We denote this partial partition function by $S(N,i_1,i_2,i_{\mathcal{K}-1},L)$. Obviously the total partition function $Z(N,L)$ of the system is given by

$$Z(N,L)=\sum_{i_{\mathcal{K}}=N}^{L}\sum_{i_{\mathcal{K}-1}=1}^{i_{\mathcal{K}}-1}\cdots\sum_{i_1=1}^{i_2-1}S(N,i_1,i_2,i_{\mathcal{K}-1},i_{\mathcal{K}}). \tag{9}$$

Let us now consider the partition function of a system of N particles and $L+1$ sites. Obviously, if the additional site is not occupied by a particle, then $Z(N,L+1)=Z(N,L)$. If one of the particles does occupy the site $L+1$, then

$$Z(N,L+1)$$
$$=\sum_{i_{\mathcal{K}}=1}^{L}\sum_{i_{\mathcal{K}-1}=1}^{i_{\mathcal{K}}-1}\cdots\sum_{i_1=1}^{i_2-1}S(N-1,i_1,i_2,i_{\mathcal{K}-1},i_{\mathcal{K}})$$
$$\times\exp\left(-\frac{\varepsilon(L+1-i_1)}{T}\right)\cdots$$
$$\times\exp\left(-\frac{\varepsilon(L+1-i_{\mathcal{K}-1})}{T}\right)$$
$$\times\exp\left(-\frac{\varepsilon(L+1-i_{\mathcal{K}})}{T}\right). \tag{10}$$

Consequently,

$$Z(N,L+1)$$
$$=Z(N,L)+\sum_{i_{\mathcal{K}}=1}^{L}\sum_{i_{\mathcal{K}-1}=1}^{i_{\mathcal{K}}-1}\cdots\sum_{i_1=1}^{i_2-1}S(N-1,i_1,i_2,i_{\mathcal{K}-1},i_{\mathcal{K}})$$
$$\times\exp\left(-\frac{\varepsilon(L+1-i_1)}{T}\right)\cdots$$
$$\times\exp\left(-\frac{\varepsilon(L+1-i_{\mathcal{K}-1})}{T}\right)$$
$$\times\exp\left(-\frac{\varepsilon(L+1-i_{\mathcal{K}})}{T}\right). \tag{11}$$

On the other hand,

$$Z(N,L+1)-Z(N,L)$$
$$=\sum_{i_{\mathcal{K}-1}=1}^{L}\sum_{i_{\mathcal{K}-2}=1}^{i_{\mathcal{K}-1}-1}\cdots\sum_{i_1=1}^{i_2-1}S(N,i_1,i_2,i_{\mathcal{K}-1},L+1). \tag{12}$$

Combining (11) with (12), we obtain

$$S(N,i_1,i_2,i_{\mathcal{K}-1},L+1)$$
$$=\prod_{m=1}^{\mathcal{K}}\exp\left(-\frac{\varepsilon(L+1-i_m)}{T}\right)$$
$$\times\sum_{j=1}^{i_1-1}S(N-1,j,i_1,i_2,i_{\mathcal{K}-1})$$
$$\times\exp\left(-\frac{\varepsilon(L-j)}{T}\right). \tag{13}$$

This is the final recursion relation expressing the partial partition function of a system of N particles in terms of that for a system of $N-1$ particles. For our calculations we need to supplement (13) by an "initial condition"—an expression for $S(\mathcal{K}+1,i_1,i_2,\ldots,i_{\mathcal{K}})$. Obviously

$$S(\mathcal{K}+1,i_1,i_2,\ldots,i_{\mathcal{K}})$$
$$=\exp\left(-\frac{E(i_1,i_2,\ldots,i_{\mathcal{K}})}{T}\right)\sum_{j}^{i_1-1}\prod_{m=1}^{\mathcal{K}}\exp\left(-\frac{\varepsilon(i_m-j)}{T}\right). \tag{14}$$

Here $E(i_1,i_2,\ldots,i_{\mathcal{K}})$ is the sum of the pair energies of $\mathcal{K}$ particles with coordinates $i_1, i_2,\ldots,i_{\mathcal{K}}$.

Let us consider the extremely interesting cases $\mathcal{K}=1$ and $\mathcal{K}=2$. As we have already mentioned, $\mathcal{K}=1$ corresponds to taking into account the interaction only between nearest neighbors, while for $\mathcal{K}=2$ the interactions between nearest and next-nearest neighbors are taken into account.

In the first case expressions (9) and (13) take the simple form

$$Z(N,L)=\sum_{i=N}^{L}S(N,i), \tag{15}$$

$$S(N,L+1)=\sum_{i=N}^{L}S(N-1,i)\exp\left(-\frac{\varepsilon(L+1-i)}{T}\right). \tag{16}$$

Here $S(N,i)$ is the partition function of a system of N particles and i sites, in which the last (ith) site is occupied by a particle.

We do a discrete Laplace transformation in (16), introducing the parameter $\gamma=P/T$:

$$F(\gamma)=\sum_{i=1}^{\infty}f(i)\exp(-\gamma i).$$

Then

$$\sum_{L=1}^{\infty}S(N,L+1)\exp(-\gamma L)=S(N,\gamma)$$
$$=\sum_{L=1}^{\infty}\exp(-\gamma L)\sum_{i=N}^{L}S(N-1,i)$$
$$\times\exp\left(-\frac{\varepsilon(L-i)}{T}\right).$$

Using the theorem on the Laplace transformation for a convolution,[9] we obtain

$$S(N,\gamma)=S(N-1,\gamma)G(\gamma),$$

where $G(\gamma)=\Sigma_{i=1}^{\infty}\exp(-\varepsilon(i)+iP/T)$. Making the substitution $S(N,\gamma)=\exp(Nf(\gamma))$ in the thermodynamic limit, we obtain

$$\exp(Nf(\gamma))=\exp((N-1)f(\gamma))G(\gamma).$$

Hence

$$Z(N,P)=\exp\left(N\ln\left(\sum_{i=1}^{\infty}\exp\left(-\frac{\varepsilon(i)+iP}{T}\right)\right)\right),$$

and consequently

$$\Phi(N,P,T)=-T\ln(Z(N,P))$$
$$=-TN\ln\left(\sum_{i=1}^{\infty}\exp\left(-\frac{\varepsilon(i)+iP}{T}\right)\right). \tag{17}$$

As expected, Eq. (17) agrees with the expression for the thermodynamic potential obtained in Ref. 5 with only the nearest-neighbor interaction taken into account.

In the case $\mathcal{K}=2$ expression (9) takes the form

$$Z(N,L)=\sum_{i=N}^{L}\sum_{j=1}^{i-1}S(N,j,i). \tag{18}$$

Here $S(N,j,i)$ is the partition function of a system of N particles and i sites in which the last (ith) site is occupied by

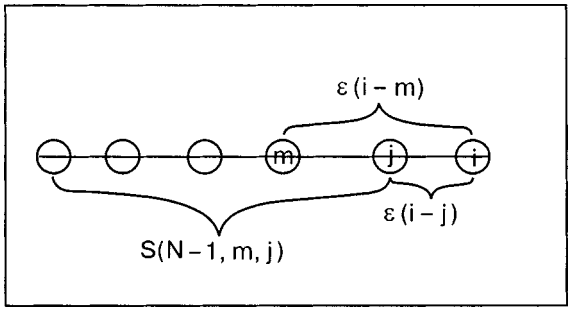

FIG. 1. Partial partition function $S(N,j,i)$ of a system of N particles and i sites in which the last (ith) site is occupied by a particle and the next-to-last particle has the coordinate j.

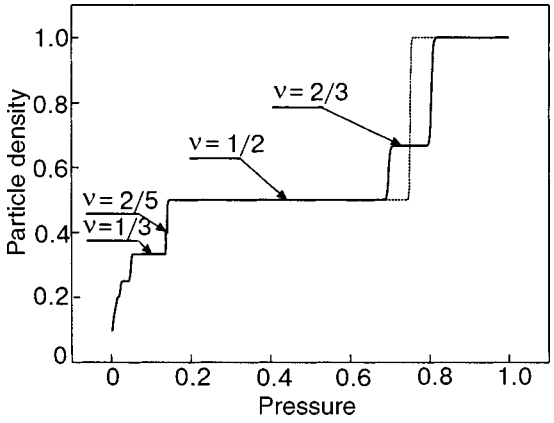

FIG. 2. The function $\nu(P)$ calculated with the use of Eqs. (19) and (20). The dotted line reflects the analogous function obtained in the nearest-neighbor approximation (17).

a particle and the next-to-last particle has the coordinate j (see Fig. 1). In this case expressions (13) and (14) take the form

$$S(N,i,L)=\exp\left(-\frac{\varepsilon(L-i)}{T}\right)\sum_{j=N-1}^{i-1}S(N-1,j,i)\times\exp\left(-\frac{\varepsilon(L-j)}{T}\right), \tag{19}$$

$$S(3,j,i)=\exp\left(-\frac{\varepsilon(i-j)}{T}\right)\times\sum_{m=1}^{j-1}\exp\left(-\frac{\varepsilon(j-m)}{T}\right)\exp\left(-\frac{\varepsilon(i-m)}{T}\right). \tag{20}$$

A computer calculation of the thermodynamic potential $F(N,L,T)$ with the use of Eqs. (9), (19), and (20) was done for $N,L\gtrsim 100$. It was found that those values of the length of the system and the number of particles are sufficient to make effects due to the finite size of the system negligibly small. The function was constructed as follows. The thermodynamic potential $F(N,L,T)$ was calculated for different values of N and L. For each pair N,L the values of $P(N/L)_- = F(N,L,T)-F(N,L+1,T)$ and $P(N/L)_+ = F(N,L-1,T)-F(N,L,T)$, which are the boundaries of the interval of the devil's staircase corresponding to the density $\nu=N/L$, were calculated. The results of the calculation of $\nu(P)$ for $\mathcal{K}=1$ and $\mathcal{K}=2$ with the use of Eqs. (17), (19), and (20) are presented in Fig. 2. We see that taking the next-nearest neighbor interaction into account leads to the appearance of new, weaker steps corresponding to particle densities of the type $2/(2i+1)$, where $i=1,2,3,\ldots$. The widths of these steps are proportional to $\varepsilon''(2i+1)$ (Ref. 7) and are consequently much less than the widths of the steps corresponding to electron crystals with densities of nearly the same values but belonging to the class $\nu=1/i$. This fact has a rather clear physical explanation. The system under study is conveniently considered as a set of pairs of neighboring electrons found at distances $l=1,2,3,\ldots$ from each other. We shall call these l-pairs. In the nearest-neighbor approximation the arrangement of the l-pairs within a unit cell containing two or more particles is degenerate. For example, the configuration with $\nu=2/7$ in the ground state corresponds to an arrangement of the l-pairs of the form 3–4–3–4–... . In the nearest-neighbor approximation this configuration is equivalent to 3–3–4–4–... . Taking the next-nearest-neighbor interaction into account lifts the degeneracy. In fact, for the configuration 3–4–3–4–... the energy of the system per cell is equal to $2(\varepsilon(3)+\varepsilon(4)+\varepsilon(7))$, whereas for the configuration 3–3–4–4–... this energy is equal to $2(\varepsilon(3)+\varepsilon(4))+\varepsilon(6)+\varepsilon(8)$. By virtue of the properties of the pair potential, which were discussed in detail above, one has $2\varepsilon(7)<\varepsilon(6)+\varepsilon(8)$. Thus the next-nearest-neighbor interaction tends to stabilize electron "crystals" with two particles per unit cell. On the other hand, the effective energy of degeneracy, $\tilde{E}\sim 2\varepsilon(7)-(\varepsilon(6)+\varepsilon(8))$, is much less than the energies corresponding to electron "crystals" containing one particle per cell and having the nearest values of the concentration (for $\nu=1/3$ and $\nu=1/4$ these are $\varepsilon(3)$ and $\varepsilon(4)$, respectively). This hierarchy of energies is also reflected in the dependence of $\nu(P)$ in the form a small segment corresponding to $\nu=2/7$ between strong segments corresponding to $\nu=1/3$ and $\nu=1/4$. Obviously, taking interactions between the next neighbors into account will lead to stabilization of the structure with three particles per cell, etc.

4. CONCLUSION

We have proposed a method by which one can calculate the thermodynamic characteristics of a one-dimensional generalized Wigner crystal for arbitrary temperature, particle density, and character of the repulsive interparticle pair potential. We have shown that at a finite temperature the main role in the formation of the thermodynamics of the system for $P/T\gg 1$ is played by electron "crystals" with $\nu=1/i$, $i=1,2,3,\ldots$. Taking the interactions between next-nearest neighbors into account leads to a weak modification of the functions $\nu(P)$ and $\nu(\mu)$ owing to the appearance of "finer" details in the function $\nu(P)$, which correspond to electron "crystals" with filling factors of the form $2/(2i+1)$, where $i=1,2,3,\ldots$.

In closing the author expresses his sincere gratitude to A. A. Slutskin for helpful discussions in the course of writing this paper.

*E-mail: slavin@ilt.kharkov.ua

[1)]Indeed, we have already pointed out in the Introduction that in the case of a pair interaction potential that falls off sufficiently rapidly the low-temperature dependence $\nu(P)$ has the form of steps corresponding to the concentrations $\nu=1/q$, $q=1,2,\ldots$ (Ref. 5).

[1] A. A. Slutskin, in *General Conference European Physical Society*, Regensburg (1993), Vol. A17, p. 1085.
[2] A. A. Slutskin and L. Yu. Gorelik, Fiz. Nizk. Temp. **19**, 1199 (1993) [Sov. J. Low Temp. Phys. **19**, 852 (1993)].
[3] E. Wigner, Phys. Rev. **46**, 1002 (1934).
[4] D. Pines, *Elementary Excitations in Solids*, New York (1963).
[5] V. V. Slavin and A. A. Slutskin, Phys. Rev. B **54**, 8095 (1996).
[6] J. Hubbard, Phys. Rev. B **17**, 494 (1978).
[7] Ya. G. Sinai and S. E. Burkov, Usp. Mat. Nauk **38**, 205 (1983).
[8] P. Bak and R. Bruinsma, Phys. Rev. Lett. **49**, 249 (1982).
[9] A. D. Sveshnikov and A. N. Tikhonov, *Theory of Functions of a Complex Variable* [in Russian], Nauka, Moscow (1970)

Translated by Steve Torstveit

Features of low-temperature exciton dynamics in *J*-aggregates with topological disorder

Yu. V. Malyukin, G. S. Katrich, S. L. Efimova, and A. V. Sorokin*

Institute for Single Crystals of the National Academy of Sciences of Ukraine, 60 Lenin Ave., Kharkov 61001, Ukraine

(Received February 7, 2003, revised March 20, 2003)
Fiz. Nizk. Temp. **29**, 906–909 (August 2003)

It is shown on the basis of an analysis of the *J*-band shape, luminescence spectra, and luminescence decay that self-trapping of excitons takes place in *J*-aggregates with strong topological disorder. A self-trapping barrier must be overcome for this to occur. A microscopic model of the self-trapped state is presented. © *2003 American Institute of Physics.*
[DOI: 10.1063/1.1596800]

1. INTRODUCTION

J-aggregates of polymethine dyes are highly ordered nanosize luminescent clusters. Because of their unusually large absorption cross section *J*-aggregates have been used for many years as photomaterial sensitizers.[1] In recent years, *J*-aggregates have been used for diagnostics of the membrane potential in living cells.[2]

Since it was first discovered by Jelly and Scheibe,[3,4] *J*-aggregate structure remains little studied. *J*-aggregates are usually considered to be one-dimensional molecular chains, which makes it possible to describe their optical and luminescent properties systematically. In most cases *J*-aggregates are characterized by a narrow resonance luminescence band, indicating the absence of relaxation of the molecular configuration of photoexcited *J*-aggregates. However, it was shown in[5] that in *J*-aggregates polaronic relaxation can take place below the bottom of an exciton band and causes the formation of a strongly-relaxed polaronic state.

In the present work the special features of 1-methyl-1′-octadecyl-2,2′-cyanineiodide (S120) *J*-aggregate exciton dynamics in a frozen dimethyl-formamide-water (DMFA-W) matrix was studied in the temperature range 1.5–80 K. S120 molecules, which are an amphiphilic analogue of PIC, allow topological disorder in S120 *J*-aggregates to be controlled.[6]

2. EXPERIMENTAL

The assembly of experimental equipment used in these investigations is described in detail in Ref. 5.

3. RESULTS AND DISCUSSION

Figure 1 shows the low-temperature absorption bands of S120 *J*-aggregates in frozen DMFA-W solutions with different amounts of water. For low water content (Fig. 1a) the low-frequency edge of the *J*-band is fit well by a Lorentzian contour, indicating substantial topological disorder in the *J*-aggregate structure.[6–8] In contrast, for high water content (Fig. 1b) the *J*-aggregate structure becomes more perfect and the low-frequency edge of the *J*-band is fit well by a Gaussian contour.[6–8] At low temperatures the latter case occurs for *J*-aggregates of PIC,[8,9] TOCBC[10] and TDBC.[11] The absorption band of S120 *J*-aggregates ($\Delta\nu_{FWHM}=380\,\mathrm{cm}^{-1}$) is much wider than that of PIC ($\Delta\nu_{FWHM}=34\,\mathrm{cm}^{-1}$),[8,9] TOCBC ($\Delta\nu_{FWHM}=65\,\mathrm{cm}^{-1}$),[10] and TDBC ($\Delta\upsilon_{FWHM}=160\,\mathrm{cm}^{-1}$).[11] This indicates greater diagonal disorder in S120 *J*-aggregates.[6–8]

At low temperatures only a narrow resonance luminescence *J*-band is observed for perfect S120 *J*-aggregates (Fig.

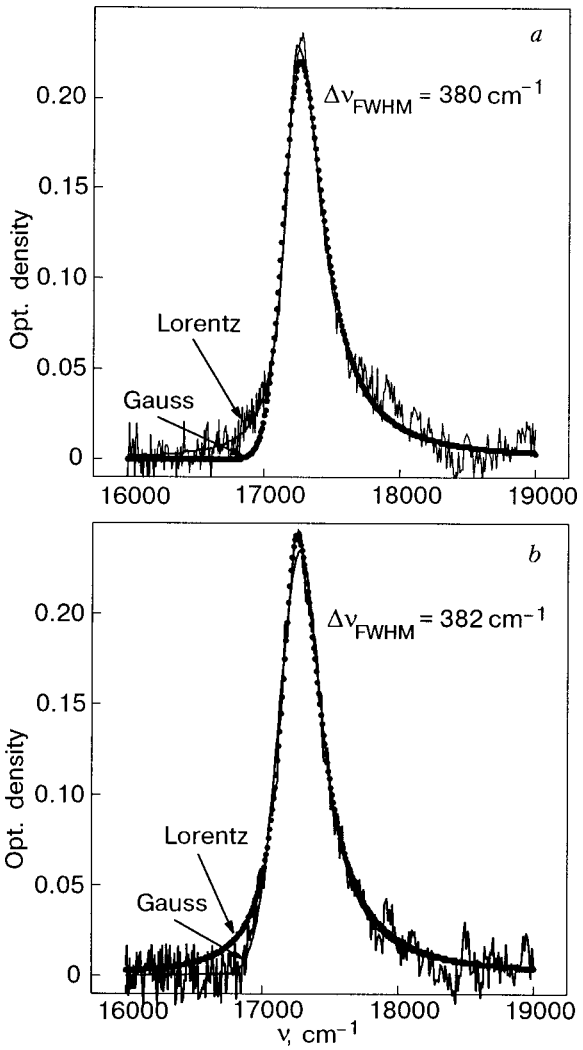

FIG. 1. The absorption band of S120 *J*-aggregates in a frozen DMFA-W matrix ($T=1.5$ K) with different water content: 50% (*a*); 75% (*b*).

2, curve *a*). The time-resolved spectra indicate[12] that the broad luminescence spectrum of the S120 *J*-aggregates with topological disorder (Fig. 2, curve *b*) consists of two bands: a narrow resonance band, which coincides with the luminescence band of perfect S120 *J*-aggregates (Fig. 2, curve *a*), and a wide long-wavelength band. Two bands are clearly visible at 80 K (Fig. 2, curve *c*). The narrow luminescence band is strongly quenched by exciton traps.[12] Luminescence decay in this band exhibits a single exponential time dependence with a temperature-dependent decay constant (1.5–80 K).[5] The luminescence characteristics of the narrow resonance luminescence band of S120 *J*-aggregates (Fig. 2, curve *a*) are similar to those of *J*-aggregates of PIC and TDBC.[8,9,11] On this basis the narrow luminescence band of the perfect and imperfect S120 *J*-aggregates can be ascribed to the emission of free excitons.[5,13]

As temperature decreases, the spectrum represented in Fig. 2, curve *c* reversibly transforms into the spectrum shown in Fig. 2, curve *b*. Within the wide band (Fig. 2, curve *b*) the luminescence decay depends on the detection point and does not exhibit a simple exponential time dependence (Fig. 3). The luminescence decay recorded at the same spectral point within the wide band depends on the water content in the frozen DMF-W matrix.[5] For more imperfect *J*-aggregates the luminescence decays faster at the specified spectral point of the wide band.[5]

The wide luminescence band (Fig. 2) may be associated with the emission of stationary exciton traps present in the *J*-aggregates for unknown reasons. Then the energy gap ($\sim$1350 cm^{-1}) between the maxima of the two bands (Fig. 2, curve *c*) is too large compared to the thermal energy kT ($\sim$56 cm^{-1}) to attribute it's origin to the thermal depopulation of traps. The exciton traps could appear in a *J*-aggregate structure with increasing temperature. In this case reversible changes of the luminescence spectrum (Fig. 2) are impossible with inverse decreasing temperature. These and other origins of the wide luminescence band are discussed in greater detail in Refs. 5 and 13.

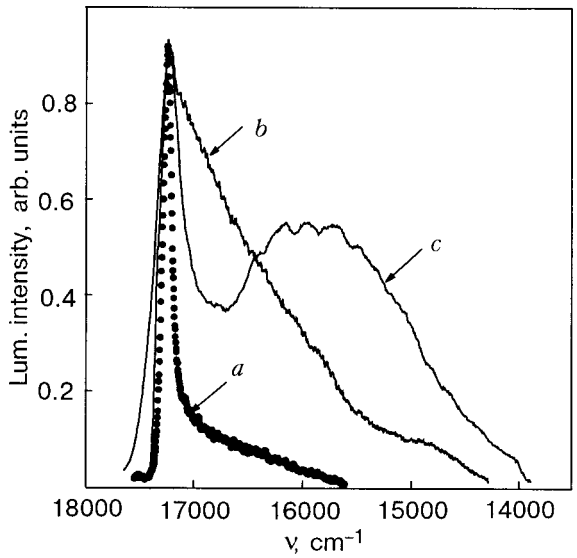

FIG. 2. The luminescence spectrum of S120 *J*-aggregates in a frozen DMFA-W matrix with different water content at different temperatures: 75%, $T=1.5$ K (*a*); 50%, $T=1.5$ K (*b*); 50%, $T=80$ K (*c*).

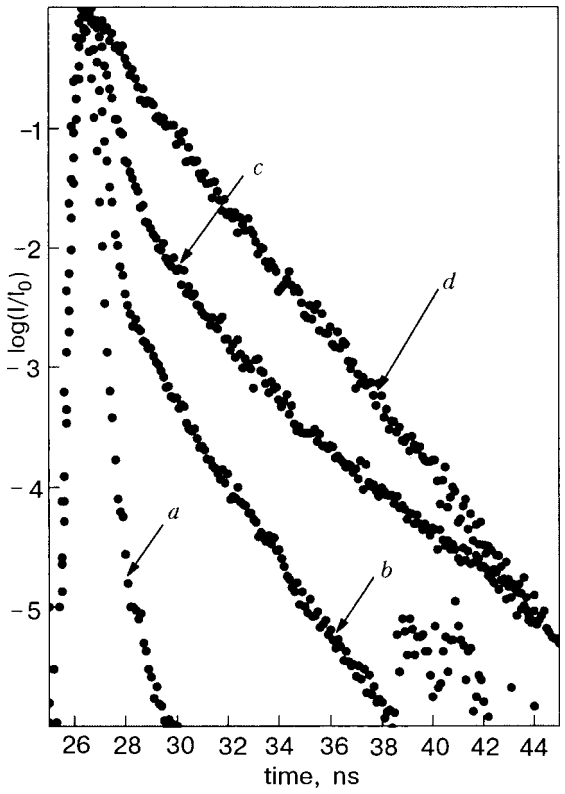

FIG. 3. The luminescence decay of S120 *J*-aggregates and S120 monomers in a frozen DMFA-W matrix with a 50% water content at $T=1.5$ K: the resonant luminescence decay of *J*-aggregates, $\lambda_{rec}=580$ nm (17241 cm^{-1}) (*a*); the wide-band luminescence decay of *J*-aggregates, $\lambda_{rec}=600$ nm (16667 cm^{-1}) (*b*); the wide-band luminescence decay of *J*-aggregates, $\lambda_{rec}=640$ nm (15625 cm^{-1}) (*c*); the luminescence decay of S120 monomers, $\lambda_{rec}=560$ nm (17857 cm^{-1}) (*d*).

The wide *J*-aggregate luminescence band with strong topological disorder should be ascribed to the emission of dynamic (relaxing) states forming below the bottom of the exciton band. These states arise only after photoexcitation of the *J*-aggregates and after the self-trapped exciton states have lost their mobility. The simultaneous presence of two bands in the luminescence spectrum (Fig. 2, curve c) indicates the coexistence of free and self-trapped excitons and the existence of a self-trapping barrier.[5,13] Nevertheless, it is known that there is no self-trapping barrier in 1D systems (which the *J*-aggregates in solutions are).[5,13,14] Such a barrier is possible if the exciton self-trapping in *J*-aggregates involves one-dimensional electronic motion and three-dimensional lattice deformation.[13]

Since $\Delta\nu_{FWHM}$ is essentially the same for the *J*-bands in the cases considered (Fig. 1), it may be inferred that the topological disorder plays a key role in the development of polaronic relaxation below the bottom of the exciton band. This is due to, first and foremost, the large initial distortions in a *J*-aggregate structure with topological disorder. Nevertheless, this is not the only reason. It was shown[13] that self-trapping occurs when the exciton delocalization length N_{del} reaches a critical value N_{del}^{cr}. N_{del} is defined by the energy disorder and is contained in the two relations:[8,9,14]

$$\delta_{ex}^2=\frac{3\delta^2}{2(N_{del}+1)}, \tag{1}$$

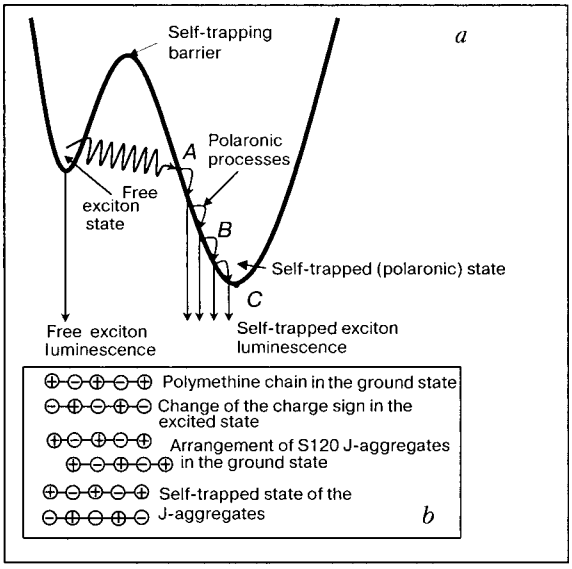

FIG. 4. The adiabatic potential describing the formation of a self-trapped exciton state in S120 *J*-aggregates (*a*); the formation of an excimer state in a *J*-aggregate molecular chain (*b*).

$$\tau_J = \frac{\pi^2 \tau_{\text{mon}}}{8 N_{\text{del}}}, \tag{2}$$

where δ and δ_{ex}^2 are the effective energy disorders ($\Delta\nu_{FWHM}$, in fact) in the monomer and exciton bands, respectively; τ_J and τ_{mon} are the luminescence decay constants of *J*-aggregates and monomers.

On the basis of $\Delta\nu_{FWHM}$ for S120, PIC and TDBS *J*-aggregates (see above), N_{del} for S120 *J*-aggregates is smallest. Using (1) and (2) and the appropriate experimental data for the S120 *J*-aggregates[5,6,13] we find that $N_{\text{del}} \sim 25$. The smaller N_{del}, the larger the change in the charge corresponds to one molecule under the photoexcitation of the *J*-aggregate is. Electric dipole transitions we implied. When $N_{\text{del}} = N_{\text{del}}^{\text{cr}}$, a substantial change in the nonequilibrium charge distribution over a molecule stimulates substantial reorganization of the equilibrium molecular arrangement in the photoexcited *J*-aggregate. For a favorable ratio of the energy gain under polaronic relaxation and the energy gain with deformation of a solid matrix, a polaronic state is formed below the exciton band bottom.[13] Such a formation can be described by a model with a double-well adiabatic potential (Fig. 4a). At 1.5 K the self-trapping rate in the *AB* region is low, and we observe emission from the relaxing states. As a result, a continuous luminescence spectrum is formed (Fig. 2, curve *b*). As temperature increases, the self-trapping accelerates and excitations are accumulated in the minimum *C* before radiative deactivation occurs. This case corresponds to the curve c in Fig. 2.

At the microscopic level a self-trapped exciton state in S120 *J*-aggregates is an excimer (Fig. 4b). It is known that reversible charge modulation occurs along a polymethine chain. The fact that the S120 *J*-aggregate absorption bands in DMFA-W solutions[5,6,13] and LB-films[6] coincide with one another suggests that a fragment of the ''brick layer'' (the arrangement of molecules in a pile with their relative displacement)[15] remains for S120 *J*-aggregates in DMFA-W solutions. Thus excimer formation becomes possible under photoexcitation of *J*-aggregates because of a cross displacement of two molecules in the *J*-aggregate chain (Fig. 4b). So, in the ground state, the adiabatic potential of *J*-aggregates has one minimum, and the probability of a radiative transition from a self-trapped state must decrease. Actually, at long times after an excitation pulse the luminescence decay is slower in the luminescence band of the self-trapped states (Fig. 3, curve c) than that in the monomer band (Fig. 3, curve *d*).

4. CONCLUSIONS

It has been shown that in *J*-aggregates with strong topological disorder polaronic states may be formed below the bottom of the exciton band. The topological disorder plays two roles. On the one hand the initial deformation of the *J*-aggregate structure promotes the appearance and relaxation of polaronic states. On the other hand the energy and topological disorders decrease N_{del}, which reaches the critical value $N_{\text{del}}^{\text{cr}}$ and then the formation of self-trapped states in the 1D system becomes energetically favorable.

*E-mail: sorokin@isc.kharkov.com

[1] W. West and P. B. Gilman, in *The Theory of The Photographic Process*, MacMillan, New York (1977), p. 251.
[2] *Handbook of Fluorescent Probes and Research Chemicals*, edited by P. Richard, Molecular probes, Haugland (1998).
[3] E. E. Jelly, Nature (London) **139**, 631 (1937).
[4] G. Scheibe, Angew. Chem. **50**, 212 (1937).
[5] Yu. V. Malyukin, V. P. Seminozenko, and O. G. Tovmachenko, Zh. Éksp. Teor. Fiz. **107**, 812 (1995) [JETP **80**, 460 (1995).
[6] Yu. V. Malyukin, G. S. Katrich, and K. Kemnitz, Mol. Cryst. Liq. Crys. **348**, 15 (2000).
[7] E. W. Knapp, Chem. Phys. **85**, 73 (1984).
[8] H. Fidder, J. Knoester, and D. A. Wiersma, J. Chem. Phys. **95**, 7880 (1991).
[9] H. Fidder, J. Terpstra, and D. A. Wiersma, J. Chem. Phys. **94**, 6895 (1991).
[10] M. Lindrum and S. Daehne, Phys. Status Solidi B **189**, 51 (1995).
[11] J. Moll, S. Daehne, J. R. Durrant, and D. A. Wiersma, J. Chem. Phys. **102**, 6362 (1995).
[12] Yu. V. Malyukin, Fiz. Nizk. Temp. **23**, 476 (1997) [Low Temp. Phys. **23**, 123 (1997)].
[13] G. S. Katrich, K. Kemnitz, Yu. V. Malyukin, and A. M. Ratner, J. Lumin. **90**, 55 (2000).
[14] L. D. Bakalis and J. Knoester, J. Lumin. **87–89**, 66 (2000).

This article was published in English in the original Russian journal. Reproduced here with stylistic changes by AIP.

Low-frequency conductivity of a two-dimensional Wigner solid coupled to surface excitations of liquid helium

Yu. P. Monarkha

B. Verkin Institute for Low Temperature Physics and Engineering of the National Academy of Sciences of Ukraine, 47 Lenin Ave., Kharkov 61103, Ukraine

(Received March 26, 2003)
Fiz. Nizk. Temp. **29**, 910–921 (August 2003)

The line-shape and broadening of coupled phonon-ripplon resonances of Wigner-solid conductivity are studied using the memory function formalism. The analytic properties of the memory function permit coordinating the approximations of the secular equation for the coupled phonon-ripplon modes and the line-broadening of these resonances. Special attention is paid to the description of the strong-coupling regime realized for surface electrons on superfluid helium. For this case it is shown that the line-broadening is much smaller than and the line-shape is different from those found previously using the weak-coupling theory. Different theoretical approaches are compared with available experimental data. © *2003 American Institute of Physics.* [DOI: 10.1063/1.1596801]

1. INTRODUCTION

A Wigner solid (WS) is usually associated with the insulator state of an electron system. In such highly correlated state the electrons are assumed to be pinned by static media defects or boundary-shape distortions. A remarkable exception is the two-dimensional (2D) WS formed on the free surface of liquid helium. In this case there are no static media defects and the edges of the electron sheet are formed by the external electric fields of the guard electrodes. In the presence of an ac driving electric field such WS can move along the helium surface, interacting with media excitations.

At typical temperatures $T \lesssim 0.5\,\mathrm{K}$, which can be associated with the WS state for areal electron densities $n_s \sim 10^8 - 10^9\,\mathrm{cm}^{-2}$, electrons interact predominantly with capillary wave quanta (ripplons). Because each electron is localized near its lattice site, the electron-ripplon interaction induces a sublattice of surface dimples:[1] a static surface displacement $\xi(\mathbf{r}) = \Sigma_{\mathbf{g}} \xi_{\mathbf{g}}^{(0)} \exp(i\mathbf{gr})$, where $\mathbf{g}$ is the reciprocal lattice vector. Thus, the electrons become self-pinned to the surface dimples, which can move and follow slow electrons. In other words, phonons of the WS formed on the surface of liquid helium are strongly coupled to the media (surface) excitations. Therefore, the low-frequency excitation spectrum of the WS interacting with ripplons differs significantly from that established for a 2D electron solid without interactions.[2]

The observation of the coupled phonon-ripplon modes with $\omega < \omega_{g_1} = \sqrt{\alpha/\rho} g_1^{3/2}$ (here α and ρ are the surface tension and mass density of liquid helium, respectively, and $\mathbf{g}_1$ is the smallest reciprocal lattice vector) and electron-ripplon resonances at higher frequencies $\omega = \omega_g$, with larger g, have served as unique proof of the ordered state of the electron system.[3] Considerable research has been performed on the theory describing these coupled modes and the positions of the electron-ripplon resonances.[4–6] At the same time, there is a lack of theoretical research on the line-broadening and line-shape of the electron-ripplon resonances in the strong-coupling regime which can be used for the analysis of the large body of data that is now available.[7–9]

Another important issue related to the electron self-pinning to the sublattice of surface dimples is a remarkable nonlinear conductivity of the WS reported for surface electrons on liquid helium.[10,11] Possible explanations of this phenomenon also involve the concept of strong coupling of the Wigner lattice to surface excitations of liquid helium. Therefore, an accurate description of the conductivity of the electron crystal interacting strongly with media excitations is very important for understanding the unusual properties of «solid» currents observed for surface electrons on liquid helium.

The real part of the conductivity of a highly correlated electron system in a nonuniform electric field $\mathbf{E_k}$ with a small excitation wave-vector $\mathbf{k}$ directed along the electric field can be quite generally written in the form[12]

$$\mathrm{Re}\,\sigma_k(\omega) = \frac{e^2 n_s}{m} \frac{\nu(\omega)}{[\omega + w(\omega) - \Omega_l^2(k)/\omega]^2 + \nu^2(\omega)}, \quad (1)$$

where m_e is the free electron mass and $\Omega_l(k) \equiv \Omega_{l,k}$ is the plasmon spectrum or the spectrum of longitudinal phonons of the WS established for the flat surface. The auxiliary functions $\nu(\omega)$ and $w(\omega)$ make up the conductivity relaxation kernel $M(\omega) = w(\omega) + i\nu(\omega)$, usually called the memory function. The imaginary part of the relaxation kernel $\nu(\omega)$ can be called the effective collision frequency because it determines the kinetic friction acting on the electron system because of the interaction with scatterers.

The real part $w(\omega)$ describes the non-dissipative force acting on electrons because of the induced media polarization cloud. This force is proportional to the average electron displacement $\mathbf{u}$ induced by an ac driving electric field. If $w(\omega)$ can be disregarded, Eq. (1) describes the power absorption because of the resonant excitation of 2D plasmons. For the WS state of the electron system realized on liquid

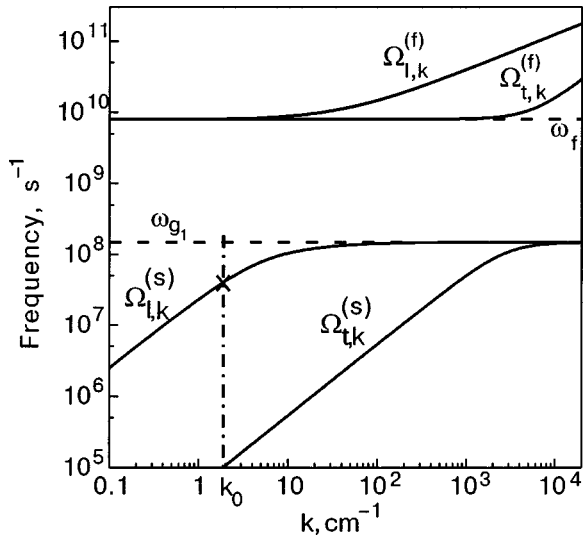

FIG. 1. View of the spectrum of the WS phonon modes coupled to media vibrations (ripplons) for $n_s = 9.5\times 10^8$ cm^{-2}.

helium, $w(\omega)$ determines the secular equation for the coupled phonon-ripplon modes:

$$\omega + w(\omega) - \Omega^2_{p,k}/\omega = 0, \tag{2}$$

where the subscript p denotes the polarization: $p=(l,t)$. At frequencies satisfying this equation with $p=l$, the power absorption proportional to $\mathrm{Re}[\sigma_k(\omega)]$ increases in a resonance manner. In the theory of the coupled phonon-ripplon modes the function $w(\omega)$ has singularities at typical ripplon frequencies $(\omega=\omega_g)$:[2,4]

$$\omega w(\omega) \propto \frac{\omega^2}{\omega_g^2-\omega^2}.$$

Therefore ω_{g_1} is the upper bound for the slow coupled phonon-ripplon modes $\Omega^{(s)}_{p,k} < \omega_{g_1}$, as shown in Fig. 1. This figure shows only a very small part of the first Brillouin zone with $k=|\mathbf{k}| \ll g$. The lowest dotted horizontal line indicates the ripplon spectrum at much larger wave-numbers $q=|\mathbf{g}_1 \pm \mathbf{k}| \simeq g_1$ represented in the first Brillouin zone. There are also coupled modes below each of the higher ripplon frequencies $\omega_g > \omega_{g_1}$ which are not shown in Fig. 1. The fast modes $\Omega^{(f)}_{p,k}$ are determined as the phonon modes affected by the field of static surface dimples: $\Omega^{(f)}_{p,k} = \sqrt{\omega_f^2+\Omega^2_{p,k}}$, where ω_f is the frequency of single electron oscillations in a dimple.

In the strong coupling regime $\omega_f \gg \omega_{g_1}$ usually realized for the surface electrons on liquid helium, the secular equation and the positions of the resonances are well described by the self-consistent approach proposed in Refs. 5, 6. The characteristic frequencies ω_{g_1} and ω_f introduce a natural separation of electron displacements $\mathbf{u_l}$ from the lattice sites into the slow and fast parts $(\mathbf{u_l}=\mathbf{u}_{s,\mathbf{l}}+\mathbf{u}_{f,\mathbf{l}})$, as follows from Fig. 1. Therefore, the equation of motion for the slow modes $\Omega^{(s)}_{p,k}$ (or equivalently the interaction Hamiltonian) can be averaged over the fast vibrations, which introduces the high-frequency Debye-Waller factor (DWF) $\exp(-q^2\langle u_f^2\rangle/4)$. Owing to the limiting frequency ω_f, the mean-square displacement of the fast mode $\langle u_f^2\rangle$ does not exhibit the logarithmic dependence on the linear dimensions of the sample that is typical for 2D solids. The quantities $\langle u_f^2\rangle$ and ω_f are found by a self-consistent procedure. Good agreement between the theory and experiment has been reported for the slow modes in the temperature range $0.2\,\mathrm{K} \leqslant T \leqslant 0.6\,\mathrm{K}$.[8]

The ultra-low temperature measurements of the high-frequency DWF conducted in Ref. 13 also agree well with the self-consistent theory in the entire temperature range. This means that the real part of the conductivity relaxation kernel $w(\omega)$ has been well established. In contrast, the imaginary part $\nu(\omega)$ has been analyzed only for the weak coupling regime[14] or high-frequency conditions $\omega \sim \omega_f \gg \omega_g$.[15] In this paper we use the memory function formulation of the electron conductivity[16] to describe the electron-ripplon resonances and the dc mobility of the WS in the regime of strong coupling with media excitations.

It should be emphasized that in the memory function approach $\nu(\omega)$ and $w(\omega)$ are not entirely independent because they are the imaginary and real parts of the memory function which possesses certain analytical properties.[16] They must obey the Kramers-Kronig relations. Both parts can be expressed in terms of the electron dynamical structure factor (DSF) $S(\mathbf{q},\omega)$. Therefore, the approximations for $S(\mathbf{q},\omega)$ and $\nu(\omega)$ must be consistent with $w(\omega)$ and with the well-established secular equation for the coupled phonon-ripplon modes. In this paper we show that some important conductivity results from the weak-coupling theory, formally extended to the strong-coupling regime, do not satisfy this consistency requirement and overestimate $\nu(\omega)$ significantly.

We have analyzed the properties of $S(\mathbf{q},\omega)$ and $\nu(\omega)$ in the strong-coupling regime and found that the discrepancy primarily originates from the fact that a significant part of the electron-ripplon interaction Hamiltonian

$$H_{\mathrm{int}} = \frac{1}{\sqrt{S_A}} \sum_{\mathbf{q}} V_q \xi_{\mathbf{q}} \sum_{\mathbf{l}} e^{i\mathbf{q}\mathbf{R_l} + i\mathbf{q}(\mathbf{u}_{s,\mathbf{l}}+\mathbf{u}_{f,\mathbf{l}})}$$

$$= \frac{1}{\sqrt{S_A}} \sum_{\mathbf{q}} V_q \xi_{\mathbf{q}} \sum_{\mathbf{l}} [1 + i\mathbf{q}\mathbf{u}_{s,\mathbf{l}} + \ldots] e^{i\mathbf{q}\mathbf{R_l} + i\mathbf{q}\mathbf{u}_{f,\mathbf{l}}} \tag{3}$$

(here $\mathbf{R_l}$ is the lattice-site vector, V_q is the electron-ripplon coupling, and S_A is the surface area) is included in the Hamiltonian of the new slow modes causing the strong renormalization of the WS phonon spectrum $\Omega^{(s)}_{p,k}$. This concerns the second term of the expansion enclosed in the square brackets [...], and even the next term $(i\mathbf{q}\mathbf{u}_{s,\mathbf{l}})^2/2$ when $\xi_{\mathbf{q}} \simeq \xi^{(0)}_{\mathbf{q}}$. These terms play an essential role in the secular equation for the slow modes.

In the weak-coupling theory the interaction proportional to $V_q \xi_{\mathbf{q}} i\mathbf{q}\mathbf{u}_{s,\mathbf{l}}$ describes scattering events involving one slow phonon $(\Omega^{(s)}_{p,k})$. Therefore, any approximation for the electron DSF in the strong-coupling regime should exclude these scattering events in order to avoid double counting the contribution due to the term $i\mathbf{q}\mathbf{u}_{s,\mathbf{l}}$. This reduces significantly the effective collision frequency $\nu(\omega)$ as compared to the result found by formal extension of the weak coupling theory, and affects the line-shape of the electron-ripplon resonances.

The discussion above is not applicable to the fast phonon modes because they represent electron oscillations in the

presence of the field due to static dimples $\xi_g^{(0)}$. Anyway, at low frequencies one-phonon processes involving $\Omega_{p,k}^{(f)}$ and ω_g are forbidden because $\omega_f \gg \omega_g$. In this paper we shall also analyze multi-phonon processes for slow and fast modes. This analysis can be used to describe the conductivity of the WS in the strong-coupling regime. The results are compared with available experimental data.

2. BASIC RELATIONS

Götze and Wölfle[16] proposed the following approximation for the conductivity relaxation kernel

$$M(\omega)=\frac{1}{m_e\omega N_e}[G^{(R)}_{F_xF_x}(0)-G^{(R)}_{F_xF_x}(\omega)], \tag{4}$$

where

$$N_e=n_sS_A$$

is the number of electrons, $\mathbf{F}=-\Sigma_e\partial H_{\rm int}/\partial\mathbf{r}_e$ is the force owing to the interaction with scatterers, $G^{(R)}_{AB}(\omega)$ is the conventional retarded Green's function for two operators A and B

$$G^{(R)}_{AB}(\omega)\equiv\langle\langle A;B\rangle\rangle_\omega=-\frac{i}{\hbar}\int_0^\infty e^{i\omega t}\langle[A(t),B(0)]\rangle dt, \tag{5}$$

and $\langle\ \rangle$ means averaging over equilibrium distributions. Even though for the main interactions Eqs. (1) and (4) reproduce the well-known results of the kinetic equation method in the entire frequency range, in general Eq. (4) is a high-frequency approximation ($\omega\gg\nu$). Therefore at low frequencies, for certain coupling potentials V_q, it may give a wrong numerical proportionality factor of the order of 2. A remarkable exception is a highly correlated electron liquid, where the electron-electron collision rate $\nu_{ee}\gg\nu$. In this case the approximation Eq. (4) is proven to be valid at all relevant frequencies.[12] The Wigner solid certainly satisfies this requirement.

The real and imaginary parts of the memory function are related with one another because of the well-known representation

$$G^{(R)}_{F_xF_x}(\omega)=\int_{-\infty}^{\infty}\langle F_x(t)F_x(0)\rangle_{\omega'}\frac{(1-e^{-\hbar\omega'/T})}{\omega-\omega'+i0}\frac{d\omega'}{2\pi\hbar}, \tag{6}$$

where $\langle\ \rangle_\omega$ is the Fourier transform of the correlation function. For the interaction Hamiltonian $H_{\rm int}$ given in Eq. (3), the above introduced force operator $\mathbf{F}$ can be written in the form

$$\mathbf{F}=-\frac{i}{\sqrt{S_A}}\sum_{\mathbf{q}}\mathbf{q}V_q\xi_{\mathbf{q}}n_{-\mathbf{q}}, \tag{7}$$

where $n_{-\mathbf{q}}=\Sigma_{\mathbf{l}}\exp(i\mathbf{q}\mathbf{r}_{\mathbf{l}})$ is the electron density fluctuation operator. Straightforward evaluation of the force-force correlation function yields

$$\langle F_x(t)F_x(0)\rangle_\omega=n_s\sum_{\mathbf{q}}q_x^2V_q^2Q_q^2[(N_q+1)S(\mathbf{q},\omega-\omega_q)+N_qS(\mathbf{q},\omega+\omega_q)], \tag{8}$$

where $Q_q=\sqrt{\hbar q/2\rho\omega_q}$, and N_q is the equilibrium ripplon distribution function. The electron DSF $S(\mathbf{q},\omega)$ is defined in the usual way

$$S(\mathbf{q},\omega)=N_e^{-1}\int_{-\infty}^{\infty}e^{i\omega t}\langle n_{\mathbf{q}}(t)n_{-\mathbf{q}}(0)\rangle dt. \tag{9}$$

Thus, Eqs. (4), (6) and (8) make it possible to express the real and imaginary parts of the conductivity relaxation kernel in terms of the electron DSF.

Under the usual experimental conditions $N_q\simeq T/\hbar\omega_q$. Therefore the effective collision frequency can be written in the very simple form

$$\nu(\omega)=\frac{(1-e^{-\hbar\omega/T})T}{8\alpha m_eS_A\hbar\omega}\sum_{\mathbf{q}}V_q^2[S(\mathbf{q},\omega-\omega_q)+S(\mathbf{q},\omega+\omega_q)]. \tag{10}$$

At the same time, the real part of the conductivity relaxation kernel $w(\omega)$ contains additional integration over the frequency argument ω' with the factor $(\omega-\omega')^{-1}$ according to Eq. (6).

Let us ignore, at first, the separation of electron displacements into slow and fast modes and consider possible approaches to evaluating the electron DSF. The conventional procedure is to rewrite Eq. (9) in the following form employing the Bloch identity and the algebra of noncommuting operators:

$$S(\mathbf{q},\omega)=\sum_{\mathbf{l}}e^{-i\mathbf{q}\mathbf{R}_{\mathbf{l}}}\int_{-\infty}^{\infty}e^{i\omega t-h_q(\mathbf{l},t)}dt, \tag{11}$$

where

$$h_q(\mathbf{l},t)=2q^2[W(0,0)-W(1,t)], \tag{12}$$

$$W(\mathbf{l},t)=\frac{\hbar}{4N_em_e}\sum_{p,\mathbf{k}}\frac{|E^{(q)}_{p,\mathbf{k}}|^2}{\Omega_{p,k}}[(n_{p,k}+1)e^{i(\mathbf{k}\mathbf{R}_{\mathbf{l}}-\Omega_{p,k}t)}+n_{p,k}e^{-i(\mathbf{k}\mathbf{R}_{\mathbf{l}}-\Omega_{p,k}t)}],$$

$n_{p,k}$ is the WS phonon distribution function and $E^{(q)}_{p,\mathbf{k}}$ is the projection of the phonon polarization vector $\mathbf{E}_{p,\mathbf{k}}$ onto the direction of $\mathbf{q}$.

At high temperatures, the exponent $h_q(\mathbf{l},t)$ is large and it is reasonable to use the short-time approximation, expanding $h_q(\mathbf{l},t)$ in powers of $\Omega_{p,k}t$ up to second-order terms near its minimum. In this limit the DSF of the electron solid coincides with the DSF of a nondegenerate electron gas. This conclusion has an analogy in the theory of neutron scattering by crystals, where the solid target can be approximated by a nuclear gas.

At low temperatures in ordinary solids the conventional approach is to expand the exponential in Eq. (11) in powers of $2q^2W(\mathbf{l},t)$. This gives zero-(elastic), one-, two- and other multi-phonon terms. This is called the phonon expansion. For example, the first two terms of this expansion can be written as

$$S^{(\rm elas)}(\mathbf{q},\omega)=2\pi e^{-2W_q}\delta(\omega)N_e\sum_{\mathbf{g}}\delta_{\mathbf{q},\mathbf{g}}, \tag{13}$$

$$S^{(1-\mathrm{ph})}=\frac{\pi\hbar q^2}{2m_e|\omega|}\left\{[n_{\mathrm{B}}(\hbar|\omega|)+1]\sum_{\mathbf{k}}\left|\mathbf{E}_{t,\mathbf{k}}\right|^2\delta(\omega-\Omega_{t,k})\right.$$
$$\left.+n_B(\hbar|\omega|)\sum_{\mathbf{k}}\left|\mathbf{E}_{t,\mathbf{k}}\right|^2\delta(\omega+\Omega_{t,k})\right\}\mathrm{e}^{-2W_q}$$
$$\times\sum_{\mathbf{g}}\delta_{\mathbf{q},\mathbf{g}+\mathbf{k}}, \tag{14}$$

where $n_B(\hbar\omega)$ is the Bose distribution function, $W_q=q^2W(0,0)$, and we have taken into account the fact that the main contribution to $S^{(1-\mathrm{ph})}$ comes from transverse phonons. In conventional systems $|\mathbf{E}_{t,\mathbf{k}}|^2=1$. We shall retain this factor in Eq. (14), so that it is applicable to the slow phonon modes of the strongly coupled system, where $|\mathbf{E}_{t,\mathbf{k}}|^2\neq 1$. The factor $\delta_{\mathbf{q},\mathbf{g}+\mathbf{k}}$ taken out of the brackets {..} indicates that in one-phonon processes a WS phonon interacts with a ripplon of the wave-vector $\mathbf{q}=\mathbf{g}\pm\mathbf{k}$. In most cases, typical phonon wave-vectors $k\ll g$ and $\delta_{\mathbf{q},\mathbf{g}\pm\mathbf{k}}$ can be replaced by $\delta_{\mathbf{q},\mathbf{g}}$.

In the elastic approximation $[S(\mathbf{q},\omega)\simeq S^{(\mathrm{elas})}(\mathbf{q},\omega)]$ the conductivity relaxation kernel can be evaluated employing Eqs. (6) and (13):

$$w(\omega)=\frac{n_s}{2\omega m_e\alpha}\sum_{\mathbf{g}}V_g^2\mathrm{e}^{-2W_g}\frac{\omega^2}{\omega_g^2-\omega^2}, \tag{15}$$

$$\nu(\omega)=\frac{\pi n_s(1-\mathrm{e}^{-\hbar\omega/T})T}{4\alpha m_e\hbar\omega}\sum_{\mathbf{g}}V_g^2\mathrm{e}^{-2W_g}\delta(\omega-\omega_g). \tag{16}$$

The real part $w(\omega)$ of Eq. (15) gives the proper secular equation for the slow coupled phonon modes, if $2W_g\to g^2\langle u_f^2\rangle/2$. It is important that the effective collision frequency of electrons forming the 2D Wigner solid has a resonance structure itself, which agrees with the hydrodynamic model.[17,18] Equations (15) and (16) with the self-consistent DWF can be also found directly by evaluating the force acting on the Wigner lattice induced by slow uniform displacements $(\mathbf{u}_s(t)\propto\mathrm{e}^{-i\omega t})$,

$$\frac{\mathbf{F}(t)}{N_e}=m_e\omega[w(\omega)+i\nu(\omega)]\mathbf{u}_s(t), \tag{17}$$

when the surface displacements $\xi_{\mathbf{q}}(t)$ are described by the usual capillary wave equations. In the latter treatment the averaging over the fast modes is an accurate procedure which results in the appearance of the self-consistent DWF $\exp(-g^2\langle u_f^2\rangle/2)$.

For 2D solids the conventional low-temperature phonon expansion is problematic because $W(0,0)=\langle u^2\rangle/4$ diverges as the linear dimension $L\to\infty$. The correct treatment has been proposed in Refs. 19, 20. It represents h_q as a logarithmic function of $R_{\mathbf{l}}$. For surface electrons on liquid helium a similar approximation was used in Refs. 14, 21:

$$h_q(\mathbf{l},t)\approx\alpha_q(T)\ln(\omega_m\sqrt{t^2+bR_{\mathbf{l}}^2/c_t^2})+q^2\langle u_0^2\rangle/2. \tag{18}$$

where

$$\alpha_q(T)=\frac{q^2T}{4\pi m_e c_t^2 n_s}, \tag{19}$$

$\langle u_0^2\rangle$ is the zero-point mean-square displacement, b is a number of the order of 1, $\omega_m=\min(T/\hbar,c_tk_m)$, and $k_m=\sqrt{4\pi n_s}$. At low temperatures $\omega_m=T/\hbar$, because the logarithmic increase of $\langle u^2\rangle$ at large wavenumbers is cut off by the Bose distribution function.

According to Refs. 14, 21 the time dependence of the approximation for $h_q(\mathbf{l},t)$ given above smears the δ-shaped spikes in the frictional force and the effective collision frequency in Eq. (16). The final results can be expressed as a long-time approximation for the effective WS dynamical structure factor

$$S(\mathbf{q},\omega)\simeq\frac{\pi\zeta_qN_e}{\omega_m^{\alpha_q}|\omega|^{1-\alpha_q}}\mathrm{e}^{-q^2\langle u_0^2\rangle/2}\sum_{\mathbf{g}}\delta_{\mathbf{q},\mathbf{g}}, \tag{20}$$

where

$$\zeta_q=\frac{2}{\pi}\sin(\pi\alpha_q/2)\Gamma(1-\alpha_q), \tag{21}$$

and $\Gamma(x)$ is the gamma function. Then the WS collision frequency can be written in the form

$$\nu(\omega)=\frac{\pi n_s}{8\alpha m_e\omega_m}\sum_{\mathbf{g}}\zeta_g|V_g|^2\mathrm{e}^{-g^2\langle u_0^2\rangle/2}$$
$$\times\left[\left|\frac{\omega_m}{\omega-\omega_g}\right|^{1-\alpha_g(T)}+\left|\frac{\omega_m}{\omega+\omega_g}\right|^{1-\alpha_g(T)}\right]. \tag{22}$$

The conductivity obtained in Ref. 14 can be found employing this expression and the general relation Eq. (1). The nonresonant term in the square brackets in Eq. (22) was previously disregarded. If $\alpha_g\ll 1$, the dimensionless factor $\zeta_g\to\alpha_g(T)\propto T$. The important points are that Eq. (22) does not transform into Eq. (16) at $T\to 0$ and the resonance structure of the effective collision frequency has unusual tails: the frictional force increases as a power law of the reciprocal detuning $|\omega-\omega_g|^{-1}$ with a temperature-dependent exponent $1-\alpha_g(T)$. The line-shape of the electron-ripplon resonances which follows from the conductivity equation given in Ref. 14 has a tail that decays much more weakly than in the usual Lorentzian form. These results have also been used to describe of the Bragg—Cherenkov scattering and the nonlinear conductivity of the WS.[21]

3. WEAK-COUPLING TREATMENT

The approximation of Eq. (18) and the result of Eq. (22) were found neglecting the changes induced in the WS phonon spectrum by the phonon-ripplon interaction. This means that strictly speaking they correspond to the weak coupling regime. The important question is why $S(\mathbf{q},\omega)$ and $\nu(\omega)$ do not transform into the result given by the elastic approximation if $T\to 0$. A related important point is that the approximation of Eq. (20) for the electron DSF is not consistent with the secular equation for the coupled phonon-ripplon modes because it cannot reproduce Eq. (15) for the real part of the conductivity relaxation kernel.

The answer can be anticipated, if we note that ν in Eq. (22) is proportional to $\alpha_g(T)$ when $\alpha_g(T)\ll 1$. It is clear that it relates somehow to the one-phonon term [Eq. (14)] of the conventional low-temperature expansion. Indeed, the main contribution to the sums $\Sigma_{\mathbf{k}}$ containing the delta-functions is due to quite large wavenumbers $k_t=\omega/c_t$ (much larger than $k_0\sim 1/L$). Then, for phonons with $k\gtrsim k_t$ only, we can sepa-

rate $W(0,0)$ and $W(\mathbf{l},t)$ in $h_q(\mathbf{l},t)$ and expand the exponential function in Eq. (11) in powers of $2q^2W(\mathbf{l},t)$, assuming that the rest of $h_q(\mathbf{l},t)$ is small at low enough temperatures. Comparing with the result given in Eq. (22) for arbitrary $\alpha_g(T)<1$ will show if the latter assumption is true. For example, if it is not true and the rest of $h_q(\mathbf{l},t)$ is important at $\alpha_g(T)\ll 1$, we will arrive at a different asymptotic behavior as $T\to 0$.

Assuming that $\Omega_{t,k}=c_tk$ is not affected by ripplons, $|\mathbf{E}_{t,\mathbf{k}}|^2=1$, and $\hbar|\omega|\ll T$ Eq. (14) can be transformed into the form

$$S^{(1\text{-ph})}(\mathbf{q},\omega)\simeq\frac{\hbar q^2S_A}{4m_ec_t^2}\mathrm{e}^{-q^2\langle u_f^2\rangle/2}\frac{T}{\hbar|\omega|}\sum_{\mathbf{g}}\ \delta_{\mathbf{q},\mathbf{g}}$$

$$=\frac{\pi\alpha_q(T)}{|\omega|}\mathrm{e}^{-q^2\langle u_f^2\rangle/2}N_e\sum_{\mathbf{g}}\ \delta_{\mathbf{q},\mathbf{g}}, \qquad (23)$$

where the factor $T/\hbar|\omega|$ originates from the phonon distribution function $n_B(\hbar|\omega|)\simeq T/\hbar|\omega|$. This factor is responsible for the unusual resonance structure of the effective collision frequency which can be evaluated employing the general relation Eq. (10)

$$\nu^{(1\text{-ph})}(\omega)=\frac{\pi n_s}{8\alpha m_e}\sum_{\mathbf{g}}\ \alpha_g(T)V_g^2\mathrm{e}^{-g^2\langle u_f^2\rangle/2}$$

$$\times\left(\frac{1}{|\omega-\omega_g|}+\frac{1}{|\omega+\omega_g|}\right). \qquad (24)$$

The resonance structure of the effective collision frequency as $\omega\to\omega_g$ is described by the first term in parentheses. Comparing Eq. (24) with the previously found result [Eq. (22)] shows that these equations are equivalent in the limiting case $\alpha_g(T)\ll 1$. The comparison also shows the effect of long-wavelength fluctuations in the 2D electron crystal on the conventional one-phonon term. The long-wavelength fluctuations just change the exponent of the resonant term ($|\omega-\omega_g|^{-1}\to|\omega-\omega_g|^{-1+\alpha_g}$) and restrict the proportionality factor $\alpha_g(T)$ when it becomes of the order of 1. Both these effects just reduce the result of the conventional one-phonon term [Eq. (24)]. Therefore, we see that in the limiting case $\alpha_g(T)\ll 1$ Eq. (22) transforms into the one-phonon term of the conventional phonon expansion rather then into the elastic term.

Thus the approximations for $S(\mathbf{q},\omega)$ and $\nu(\omega)$ given in Eqs. (20) and (22) at low temperatures should not be treated as substitutes for the zero-temperature forms of Eqs. (13) and (16), but rather as the forms that should be added to them. This can be verified in terms of the approximation given in Eq. (18) by expanding formally the proper time integral in powers of the small parameter α_q. In order to guarantee the convergence of the time integral we can introduce an additional infinitesimal parameter and set it to zero in the final result. This gives the following transformation of the conventional δ-spikes:

$$\delta(\omega)\to\delta(\omega)+\frac{\alpha_q(T)}{2|\omega|}, \qquad (25)$$

if $\alpha_q\ll 1$. This agrees with the elastic and one-phonon terms in the conventional phonon expansion. The important point is that in this case we regain the proper form for the real part of the memory function and the secular equation for the coupled modes, at least for $\alpha_q\ll 1$.

Comparing Eqs. (22) and (24) one can conclude that the long-wavelength fluctuations can be disregarded when $\alpha_g(T)\ll 1$. For the first reciprocal lattice vector, at the WS melting temperature the parameter $\alpha_g(T_m)=1/3$. It increases rapidly with g because $\alpha_g(T)\propto g^2$. This affects electron-ripplon resonances with higher frequencies ω_g. For steady motion of the WS with a constant velocity $\mathbf{v}$ we can formally make the substitution $\omega\to\mathbf{gv}$. Then both terms in parentheses contribute equally in Eq. (24), because one can set $\mathbf{g}\to-\mathbf{g}$ in the second term. This increases the resonant term of $\nu(\mathbf{v})$ for Bragg—Cherenkov scattering by a factor of 2 as compared to the ac resonant term, and it agrees accurately with the result found for the nonlinear conductivity[21] when $\alpha_g(T)\ll 1$. The one-phonon origin of the result given by Eq. (22) is very important for the strong-coupling treatment.

4. STRONG-COUPLING REGIME

The WS DSF $S(\mathbf{q},t)$ can be formally evaluated in terms of the new coupled phonon-ripplon modes. In the regime $\omega_f\gg\omega_{g_1}$ the fast modes $\Omega_{p,k}^{(f)}$ represent electron oscillations in the field of steady dimples and $|\mathbf{E}_{p,k}^{(f)}|^2\simeq|\mathbf{E}_{p,k}|^2=1$ (here $\mathbf{E}_{p,k}^{(f)}$ is the polarization vector of the fast modes).[22] Because the spectrum of the fast mode $\Omega_{t,k}^{(f)}$ has a quite high limiting frequency ω_f, one can use the conventional phonon expansion to evaluate the contribution of this mode. This procedure was performed in Ref. 15 for high signal frequencies $\omega\sim\omega_f$. The important point is that at low frequencies $\omega\sim\omega_g$ under the strong-coupling-condition $\omega_f\gg\omega_{g_1}$ there are no one-phonon terms involving fast phonons because of the energy conserving delta function, and the slow modes must be taken into account in order to find the contribution due to one-phonon processes.

For slow modes the spectrum of the transverse phonons can be found in an analytical form[2]

$$\Omega_{t,k}^{(s)}\simeq\frac{\omega_{g_1}c_tk}{\sqrt{\omega_f^2+c_t^2k^2}} \qquad (26)$$

which is valid near the melting point, where coupling with ripplons of $q\simeq g_1$ dominates. At lower temperatures this equation can be used as a simple analytical interpolation. In this approximation the fact that the polarization vector $\mathbf{E}_{t,k}^{(s)}$ of the slow mode decreases rapidly when $k>\omega_f/c_t$ and this mode transforms into the pure ripplon mode with $\mathbf{q}=\mathbf{g}_1\pm\mathbf{k}$ must be taken into account:[22]

$$\mathbf{E}_{t,k}^{(s)}\simeq\frac{\omega_{g_1}^2-(\Omega_{t,k}^{(s)})^2}{\omega_f\omega_{g_1}}\mathbf{E}_{t,k}\equiv M_{t,k}^{(s)}\mathbf{E}_{t,k}, \qquad (27)$$

where $\mathbf{E}_{t,k}$ is defined for a flat surface. Combining Eqs. (26) and (27) one can see that $M_{t,k}^{(s)}\propto k^{-2}$ for $k\gg\omega_f/c_t$. For small $k\ll\omega_f/c_t$ the quantity $M_{t,k}^{(s)}\simeq\omega_{g_1}/\omega_f\ll 1$ reflects the mass increase due to surface dimples.

Substituting Eqs. (26) and (27) into the expression for $S^{(1\text{-ph})}(\mathbf{q},\omega)$ given in Eq. (14) we note that in one-phonon processes the phonon wavenumber

$$k=k_t^*\equiv\frac{\omega_f\omega}{c_t\sqrt{\omega_{g_1}^2-\omega^2}} \tag{28}$$

is even larger than that of the weak-coupling approach, where $k=k_t\equiv\omega/c_t$. Remarkably, the increase of the wavenumber k and $1/|\partial\Omega_{t,k}^{(s)}/\partial k|$ is exactly compensated by a decrease in $|\mathbf{E}_{p,k}^{(f)}|^2=(M_{t,k}^{(s)})^2$. Therefore for $\mathbf{g}=\mathbf{g}_1$ we reproduce the one-phonon contribution to the electron DSF found in the weak-coupling treatment [Eq. (23)], except that energy conservation $\omega\pm\Omega_{t,k}^{(s)}=0$ restricts the possible values of the frequency argument because $\Omega_{t,k}^{(s)}<\omega_{g_1}$:

$$S^{(1-\mathrm{ph})}(\mathbf{q},\omega)\simeq\frac{\pi\alpha_q}{|\omega|}\mathrm{e}^{-q^2\langle u_f^2\rangle/2}\theta(\omega_{g_1}-|\omega|)N_e\sum_{|\mathbf{g}|=g_1}\delta_{\mathbf{q},\mathbf{g}}, \tag{29}$$

where the reciprocal lattice vectors involved have the smallest absolute value g_1. An important consequence of the restriction $|\omega|<\omega_{g_1}$ is that the ripplon-absorption term of the effective collision frequency, containing $|\omega+\omega_g|^{-1}$, is zero in the strong-coupling treatment.

To understand the behavior of the electron DSF in the strong-coupling regime for $\alpha_q(T)\sim 1$, consider the contribution of the slow modes only $h_q^{(s)}(\mathbf{l},t)$. Using the actual forms for the slow phonon spectrum $\Omega_{t,k}^{(s)}$ and the polarization factor $M_{t,k}^{(s)}$ given above we obtain

$$h_q^{(s)}(\mathbf{l},t)\simeq\alpha_q(T)\int_0^{2\pi}\frac{d\varphi}{2\pi}\int_0^{\infty}\frac{dx}{x}\frac{\omega_f^2}{\omega_f^2+x^2}\times\left[1-\cos\left(\frac{xR_{\mathbf{l}}}{c_t}\cos\varphi-\frac{x\omega_{g_1}t}{\sqrt{\omega_f^2+x^2}}\right)\right]. \tag{30}$$

As compared to the weak-coupling theory, here the upper bound for the logarithmically large term is ω_f instead of ω_m. Therefore, the strong-coupling theory approximation for $h_q^{(s)}(\mathbf{l},t)$, similar to Eq. (18), can be written as

$$h_q^{(s)}(\mathbf{l},t)\approx\alpha_q(T)\ln(\omega_{g_1}\sqrt{t^2+bR_{\mathbf{l}}^2/(c_t^*)^2}). \tag{31}$$

The complete function $h_q(\mathbf{l},t)$ also includes the contribution due to the fast modes $h_q^{(f)}(\mathbf{l},t)$. At low temperatures the latter can be approximated as $h_q^{(f)}(\mathbf{l},t)\simeq q^2\langle u_f^2\rangle/2$. Thus, employing the approximation Eq. (18), in the strong-coupling regime we must make the substitutions $\omega_m\to\omega_{g_1}$ and $c_t\to c_t^*=c_t\omega_{g_1}/\omega_f$.

The analysis given above indicates that strong phonon-ripplon coupling does not change much the electron DSF for small values of the frequency argument $|\omega|<\omega_{g_1}$, if $\alpha_q(T)\ll 1$. As a result, the one-phonon term in the effective collision frequency responsible for the unusual resonance shape of $\nu(\omega)$ at $\omega\sim\omega_{g_1}$ appears to be the same as in the weak-coupling theory. The important question is whether this form of the DSF can be used in Eqs. (4) and (8) for the conductivity relaxation kernel $M(\omega)$. The electron DSF appearing in these equations originates from the total interaction Hamiltonian given in Eq. (3). In the strong-coupling theory the interaction term proportional to $\xi_{\mathbf{q}}i\mathbf{q}\mathbf{u}_{s,\mathbf{l}}$ is included in the Hamiltonian of the slow phonon modes (see Refs. 2, 22) which is then transformed to the canonical form of independent oscillators by a linear transformation of the normal coordinates. Therefore, if we consider scattering events in terms of the new (reconstructed) phonon modes, the term $\xi_{\mathbf{q}}i\mathbf{q}\mathbf{u}_{s,\mathbf{l}}$ should be excluded from the scattering Hamiltonian.

It is clear that the rest of the interaction Hamiltonian in Eq. (3) cannot result in one-phonon scattering events involving slow phonons. Therefore, in the strong coupling regime it is reasonable to exclude the one-phonon terms $S^{(1\text{-ph})}(\mathbf{q},\omega)$ and $\nu^{(1\text{-ph})}(\omega)$ from the conductivity relaxation kernel. This concerns Eq. (22) also, if we agree that it represents the conventional one-phonon term affected by long-wave-length fluctuations with $k<k_t$. The rest of the interaction Hamiltonian can result only in multi-phonon terms of the electron DSF which we are going to discuss below.

The electron-ripplon coupling V_q entering the effective collision frequency is an increasing function of q or a constant proportional to the holding electric field $E_\perp$ ($V_q\simeq eE_\perp$). This means that the main contribution to the sum $\Sigma_{\mathbf{q}}$ of Eq. (10) is due to large wavenumbers q. In this case, the multi-phonon terms can be taken into account by a short-time approximation expanding h_q in powers of t near the minimum ($t=0$). This approximation for $h_q(\mathbf{l},t)$ and $S(\mathbf{q},\omega)$ favors the contribution due to the fast modes $\Omega_{p,k}^{(f)}$ and $\mathbf{l}=0$, which can be written in the following form well-known in the theory of thermal neutron scattering by crystals:

$$S(q,\omega)=\hbar\sqrt{\frac{\pi}{\varepsilon_q K_e}}\exp\left[-\frac{(\varepsilon_q-\hbar\omega)^2}{4\varepsilon_q K_e}\right], \tag{32}$$

where K_e is the mean kinetic energy per electron

$$K_e=(2N_e)^{-1}\sum_{p,\mathbf{k}}\hbar\Omega_{p,k}(n_{p,k}+1/2). \tag{33}$$

It is clear that at low temperatures the main contribution to K_e is due to large wavenumbers.

In the Debye approximation

$$K_e=T\left(\frac{2T}{\hbar c_t k_m}\right)^2\int_0^{\hbar c_t k_m/2T}x^2\coth(x)dx+2T\left(\frac{2T}{\hbar\Omega_{l,k_m}}\right)^4\int_0^{\hbar\Omega_{l,k_m}/2T}x^4\coth(x)dx,$$

where $k_m=\sqrt{4\pi n_s}$. For $T\gg\hbar c_t k_m$ this equation yields $K_e\to T$, but for lower T the mean kinetic energy of electrons in the WS state is larger than T because of the zero-point term. For a nondegenerate electron gas the typical wavenumbers $q\sim\sqrt{8m_eT}/\hbar$, which make the main contribution to the effective collision frequency, decrease strongly with cooling. If the characteristic wavenumbers q behaved in this manner in the WS state, the approximation Eq. (32) would fail rapidly as the temperature decreases. The important point is that for the WS $q_e=\sqrt{8m_eK_e}/\hbar$ remains large because of the zero-point vibrations as shown in Fig. 2 [at $T>0.1$ K it is substantially smaller than the wavenumbers of thermal ripplons $q_T\sim(T/\hbar)^{2/3}(\rho/\alpha)^{1/3}$]. This makes Eq. (32) a reasonable approximation even at quite low temperatures.

The electron-ripplon coupling V_q consists of the polarization term and the holding field term $eE_\perp$ (Ref. 12). There-

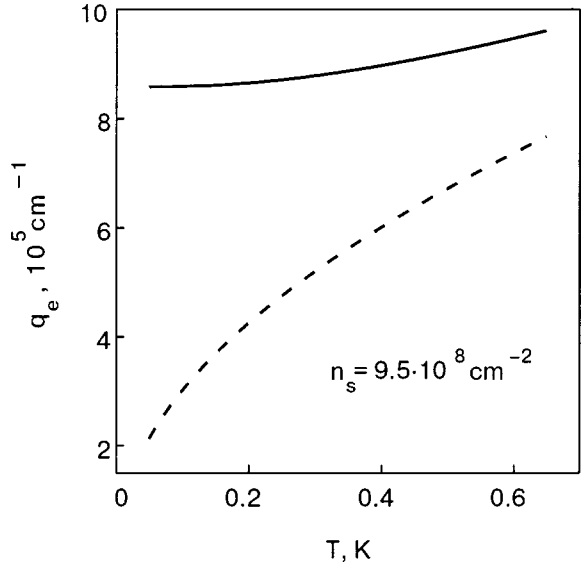

FIG. 2. Temperature dependence of the characteristic wavenumber q_e of the electron dynamical structure factor for the WS (solid line) and gas (dashed line) states.

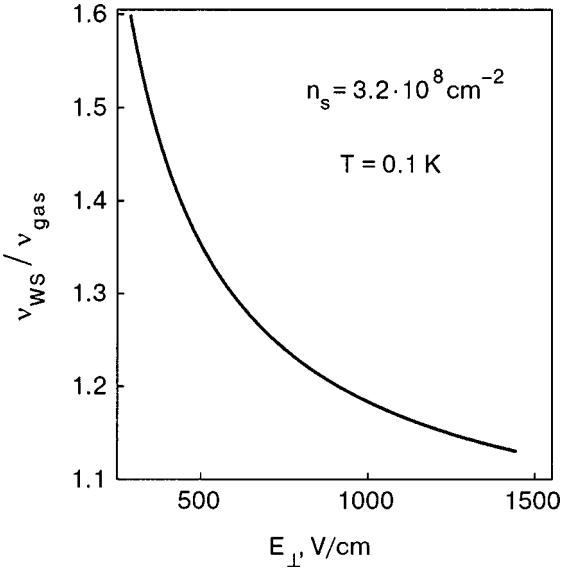

FIG. 3. The holding field dependence of the effective collision frequency of the WS normalized to the collision frequency of a nondegenerate electron gas.

fore the effective collision frequency, which follows from the short-time approximation of Eq. (32), can be written as

$$\nu_{WS}=\frac{(eE_\perp)^2}{4\alpha\hbar}\frac{2}{\sqrt{\pi}}\int_0^\infty U^2(x)\mathrm{e}^{-x^2}dx, \tag{34}$$

where

$$U(x)=1+\frac{\Lambda q_e^2}{2eE_\perp}x^2P\left(\frac{q_e^2x^2}{4\gamma^2}\right),$$
$$\Lambda=\frac{\mathrm{e}^2(\epsilon-1)}{4(\epsilon+1)}, \tag{35}$$

$q_e=\sqrt{8m_eK_e}/\hbar$, ϵ is the dielectric constant of liquid helium, and $P(y)$ is the electron-ripplon coupling function for the polarization term [at low temperatures $P(y)\simeq 0.5\ln(4/y)-1$]. In the limit of strong holding fields $V_q\simeq eE_\perp$ ($U\simeq 1$) the effective collision frequency ν_{WS} is, remarkably, independent of K_e and is identical to that found for a nondegenerate electron gas with $\nu_{ee}\gg\nu$. The high values of q_e found in the WS state affect only the polarization term of Eq. (35). In particular, this increases the part of ν_{WS} that is linear in $E_\perp$. The ratio of ν_{WS} to the result found for the gas state ν_{gas} is shown in Fig. 3 as a function of the holding electric field $E_\perp$. This indicates that the effective collision frequency of the WS given in Eq. (34) is relatively larger than ν_{gas} for weaker holding fields $E_\perp$.

The magnitude of the multi-phonon terms can be determined by analyzing the two-phonon terms in the phonon expansion of the WS DSF. Consider, first, the contribution due to the fast modes whose frequencies are restricted by the condition $\Omega_{p,k}^{(f)}>\omega_f\gg\omega_g$. Then energy conservation restricts the analysis to phonon scattering processes only, where the WS phonon frequencies enter the δ-functions with opposite signs. In the temperature range $T>\hbar\omega_f$ direct evaluation yields

$$S^{(2\text{-ph})}(\mathbf{q},\omega)\simeq\frac{\pi\alpha_q^2(T)}{2\omega_f}\mathrm{e}^{-q^2\langle u_f^2\rangle/2}N_e\sum_{\mathbf{g}}\delta_{\mathbf{q},\mathbf{g}}. \tag{36}$$

The respective contribution to the electron collision frequency can be written in the form

$$\nu^{(2\text{-ph})}=\frac{\pi n_s}{8\alpha m_e\omega_f}\sum_{\mathbf{g}}\alpha_g^2(T)V_g^2\mathrm{e}^{-g^2\langle u_f^2\rangle/2}. \tag{37}$$

The temperature dependence of this term is determined by the interplay of two parameters: $\alpha_g(T)\propto T$ and $\langle u_f^2(T)\rangle$. As $\langle u_f^2(T)\rangle\to\langle u_f^2(0)\rangle$ we obviously have $\nu^{(2\text{-ph})}\propto T^2$.

For slow modes $[\Omega_{p,k}^{(s)}<\omega_{g_1}]$ the situation is more difficult. Formal evaluation taking into account the polarization factors $M_{t,k}^{(s)}$ gives

$$S_{\mathrm{slow}}^{(2\text{-ph})}(\mathbf{q},\omega)\simeq\frac{\pi\alpha_q^2}{2|\omega|}\mathrm{e}^{-q^2\langle u_f^2\rangle/2}J(\omega)N_e\sum_{|\mathbf{g}|=g_1}\delta_{\mathbf{q},\mathbf{g}}, \tag{38}$$

where

$$J(\omega)=\int_{y_0}^{y_m}\frac{dy}{y}\frac{|\omega|\,\theta(\omega_{g_1}-|\omega|)}{(1+y^2)(|\omega|+\omega_{g_1}y/\sqrt{1+y^2})}, \tag{39}$$

$y_m=\omega/\sqrt{\omega_{g_1}^2-\omega^2}$, the lower limit $y_0=ck_0/\omega_f$, and k_0 is the smallest wavenumber of the finite electron system ($k_0\propto 1/L$). The integral $J(\omega)$ depends on the linear size L of the system logarithmically as $J(\omega)\approx\ln(y_m/y_0)$, which indicates that the conventional phonon expansion of the WS DSF for the slow modes is asymptotic and the high-order terms cannot be used carelessly, especially if the parameter α_g is not small enough. Generally, Eq. (38) is similar to the result found for the fast modes [Eq. (36)]. The important point is that in the sum $\Sigma_{\mathbf{g}}$ the reciprocal lattice vectors are now restricted to $|\mathbf{g}|=g_1$ because the phonon frequencies are limited by ω_{g_1}. This also indicates that the ripplon emission term in the effective collision frequency is zero because the argument $\omega+\omega_g$ of the DSF does not satisfy the requirement of Eq. (39).

There are also multi-ripplon scattering processes in which the ripplon wavenumbers q are less restricted by the electron wavenumbers. For $q \gg 1/\sqrt{\langle u_f^2 \rangle}$ their contribution can be estimated by the geometrical optics approximation. The interaction changes the energy and velocity of ripplons in the electron localization area. The respective correction to the effective collision frequency of electrons is found as[23]

$$\Delta\nu \approx \frac{\hbar^3 \gamma^4 \rho T^2}{4\pi\alpha^3 m^3 (\langle u_f^2 \rangle)^{3/2}}. \tag{40}$$

This correction has a relatively weaker dependence on the holding electric field ($\Delta\nu \propto \gamma^4 \propto E_\perp^{4/3}$). Usually, it is much smaller than the result given by the short-time approximation Eq. (34).

5. RESULTS AND DISCUSSION

An important consequence of the weak-coupling result[14] given by Eqs. (20) and (22) is that the appearance of the electron-ripplon resonances generally does not coincide with the WS phase transition. Let us define the characteristic temperatures T_n^* (here $n=1,2,3,...$) as the solutions of the equation $\alpha_{g_n}(T_n^*)=1$. Recalling the melting temperature of the 2D electron crystal $T_m = n_s a^2 m_e c_t^2/4\pi$ given by the dislocation-melting theory[24] and the definition of $\alpha_g(T)$, we can see that for the triangular electron lattice the series T_n^* is $T_1^* = 3T_m$, $T_2^* = T_m$, and $T_3^* = 3T_m/4 < T_m$. Therefore, near the WS phase transition the only resonance at $\omega \simeq \omega_{g_1}$ can exist in the presence of long-wavelength fluctuations. Still, at this resonant frequency there are no electron-ripplon resonances under the usual experimental conditions (they are shifted into the range $\omega < \omega_{g_1}$). The other two resonances $\omega \simeq \omega_{g_2}$ and $\omega = \omega_{g_3}$ cannot exist at $T \simeq T_m$ in the weak-coupling theory because the exponent $1-\alpha_g(T)$ appearing in the resonant conductivity term $\sigma \propto 1/|\omega - \omega_g|^{1-\alpha_g}$ is zero or negative.

According to the relation between T_3^* and T_m written above, as temperature decreases the weak-coupling theory gives a 25% delay in the appearance of the electron resonances with $\omega \simeq \omega_{g_3}$ as compared to the resonance with $\omega \simeq \omega_{g_2}$ and the WS phase transition. For example, the resonance Z of the experiment of Grimes and Adams[3] should not be observed before $T = (3/4)0.45\,\mathrm{K} \simeq 0.345\,\mathrm{K}$. Still, it is clearly seen already at a substantially higher temperature $T = 0.42\,\mathrm{K}$. A similar conclusion follows from a detailed study of the electron-ripplon resonances reported by Deville.[7] He observed the high-order resonances up to $\omega = \omega_{g_{13}}$. The high-order resonances indeed appear successively at progressively lower temperatures below T_m. It was reported that at $T \simeq T_m/5$ modes up to $n=13$ can be detected for typical density $n \simeq 2\times 10^8\,\mathrm{cm}^{-2}$. The characteristic temperature T_n^*, below which the resonance can be observed according to the weak-coupling theory under these conditions, is substantially lower than $T: T_{13} = 3T_m/28 \simeq 0.1T_m$. Thus both experiments show that the weak-coupling treatment of thermal fluctuations of the 2D WS overestimates the role of long-wavelength vibrations.

The discussion above pertains not only to the resonance structure of the effective collision rate $\nu(\omega)$. It is clear that the model DSF Eq. (20) cannot give the proper resonance structure of the real part of the conductivity relaxation kernel $w(\omega) = \mathrm{Re}\, M(\omega) \propto \omega/(\omega_g^2 - \omega^2)$ which is responsible for the high-order coupled phonon-ripplon modes. Therefore the observation of the high-order resonances for $1-\alpha_g(T) \leqslant 0$ indicates that long-wavelength fluctuations of the 2D WS which are strongly coupled to media vibrations are less important for the conductivity relaxation kernel. An explanation of this surprising conclusion was given in the preceding section. It is based on the fact that the most important part of the electron-ripplon interaction proportional to $\xi_{\mathbf{q}} i\mathbf{q}\mathbf{u}_{s,\mathbf{l}}$ is included in the Hamiltonian of the slow coupled phonon-ripplon modes. As a result, it cannot lead to any scattering of excitations of the slow modes. The long-wave fluctuations represent the excitations of slow coupled phonon-ripplon modes and therefore in the strong-coupling theory they affect the conductivity relaxation kernel to a much lesser extent. Then the appearance of the slow plasmon-ripplon resonance with $\omega < \omega_{g_1}$ obviously coincides with the WS phase transition, and the high-order resonances ($g_n > g_1$) are not restricted by the condition $1-\alpha_g(T) > 0$; this is important for experimental determination of the liquid-solid phase diagram.

For small wavenumbers q the WS DSF $S(\mathbf{q},\omega)$ which should be employed in the conductivity relaxation kernel of the strong-coupling theory has well-defined peaks $S(\mathbf{q},\omega) \propto \delta(\omega)\Sigma_{\mathbf{g}}\delta_{\mathbf{q},\mathbf{g}}$. This results in the characteristic form $w(\omega) \propto \omega/(\omega_g^2 - \omega^2)$, which is important for the secular equation describing the slow coupled modes [Eq. (2)]. At low frequencies the main contribution to $w(\omega)$ is due to the smallest g, even if the DWF $\exp(-g^2\langle u_f^2\rangle/2)$ is not small, because the corresponding terms of the sum over $\mathbf{g}$ are proportional to $1/\omega_g^2 \propto 1/g^3$. At the same time the main contribution to the effective collision frequency $\nu(\omega)$ defined by Eq. (10) sometimes is due to large q, where the WS DSF can be described by the short-time approximation [Eq. (32)]. This follows from the general structure of Eqs. (10) and (32).

Another important result of the weak-coupling theory is the unusual line-shape with the non-Lorentzian tails: $\sigma \propto 1/|\omega - \omega_g|^{1-\alpha_g}$. In contrast, the strong-coupling theory considered here results in the usual Lorentzian shape of the electron-ripplon resonances which is described by Eq. (1). Even if the sharp resonance structure of $\nu(\omega)$ becomes important, the line-shape of the resonance excitation of the slow plasmon-ripplon mode $\Omega_l^{(s)}(k_0)$, which is shifted substantially in the range $\omega < \omega_{g_1}$, is obviously close to a Lorentzian function. The presence of the nonresonance terms in the effective collision frequency $\nu(\omega)$ means that the tails of the high-order resonances ($g_n > g_1$) are the usual Lorentzian functions determined by Eq. (1) as well.

Besides qualitative distinctions stated above, it is interesting to give a numerical comparison of the weak- and strong-coupling approaches for typical experimental conditions. Consider the effective collision frequency ν of the WS and the corresponding mobility $\mu = e/(m_e\nu)$ which is related to the conductivity form of Eq. (1) at the resonance $\omega = \omega_R$. The results of different theoretical approximations and the experimental data of Ref. 9 are shown in Fig. 4. The weak-coupling theory result Eq. (22) (dash-dotted line) was calculated considering terms with $g < g_4$ only, because for

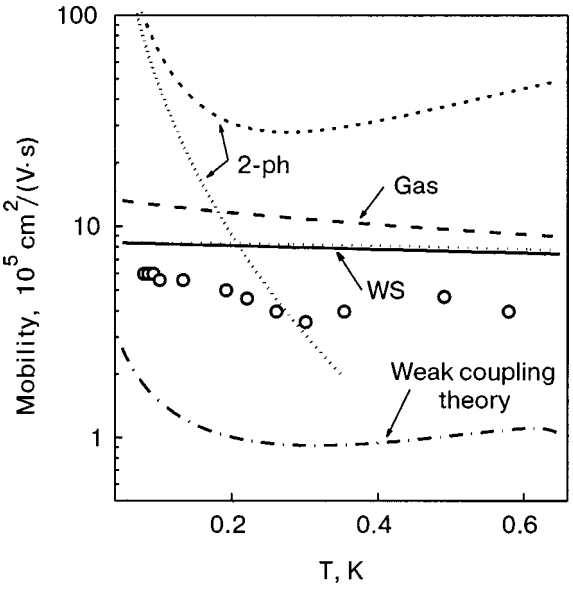

FIG. 4. Temperature dependence of the mobility of highly correlated electrons for different models of electron transport: the weak-coupling theory for the WS (dash-dotted line), mobility of a nondegenerate electron gas (dashed line), the WS mobility in the short-time approximation (dotted and solid lines; the latter includes the two-ripplon correction), the two-phonon term (short dashed and short dotted lines, as discussed in the text). The experimental data are taken from Ref. 9.

$g \geqslant g_4$ the parameter α_g becomes larger than 1 and the approximation fails. Numerically it is approximately 6 times lower than the experimental data, which means that electron scattering by ripplons is overestimated in this approach. This would give a much broader resonance line-shape for the excitation of the slow plasmon-ripplon modes. The short time approximation for the WS DSF gives a substantially higher mobility (dotted line labeled «WS»). It is lower than the mobility evaluated for the gas state of the electron system (dashed line labeled «Gas»). Under the conditions considered the two-ripplon processes [Eq. (40)] have only a weak effect on the WS mobility (solid line).

The short-time approximation Eq. (34) describes the contribution of multi-phonon scattering events when the Debye—Waller function $2q^2W(0,0)$ is large. The accuracy of this approximation can be estimated considering the contribution of two-phonon scattering events for two models of the WS DWF $\exp(-g^2\langle u^2\rangle/2)$. If only zero-point vibrations are taken into account ($\langle u^2\rangle = \langle u_0^2\rangle$) in Eq. (37) found for the fast modes, then the respective collision frequency increases rapidly with temperature and the WS mobility decreases as indicated by short-dot line labeled «2-ph». When thermal fluctuations are included ($\langle u^2\rangle = \langle u_f^2\rangle$) the mobility curve (short-dash line labeled «2-ph») deviate strongly at $T > 0.2\,\mathrm{K}$ and the effective collision frequency induced by two-phonon processes is drastically decreased. This means that in this temperature range $2q^2W(0,0)$ is large and the short-time approximations Eqs. (32) and (34) are reasonable for the description of the WS conductivity.

The experimental data shown in Fig. 4 do not contradict the short-time approximation for the DSF. Still they indicate lower mobility values than that shown by the solid curve. The numerical difference may be due to the Debye approximation used to evaluate K_e and $\langle u_0^2\rangle$. The influence of other mechanisms of momentum relaxation, which were disregarded in this work, cannot be ruled out. For example, it is well known that for the usual driving voltages the WS conductivity shows a remarkable nonlinear behavior,[10,11] which is not entirely understood.

In conclusion, we found that the quantum transport framework based on the memory function formalism is very fruitful for analyzing the WS conductivity in the low-frequency range, where it exhibits the resonance anomalies due to the interaction with media vibrations. The analytical properties of the memory function and its relationship with the electron dynamical structure factor makes it possible to coordinate the approximations used to describe the real part of the relaxation kernel, determining the positions of the resonance frequencies, and the effective collision frequency responsible for the broadening and line-shape of the resonances. For example, the model used to describe the secular equation for the coupled WS phonon-ripplon modes imposes strict consistency requirements on the approximations that can be used to obtain the effective collision frequency. The conductivity analysis given here for the strong-coupling regime eliminates the discrepancies between experiment and the weak-coupling approximation which concerns the line-shape and broadening of the conductivity resonances.

[1] Yu. P. Monarkha and V. B. Shikin, Zh. Éksp. Teor. Fiz. **68**, 1423 (1975) [Sov. Phys. JETP **68**, 710 (1975)].
[2] D. S. Fisher, B. I. Halperin, and P. M. Platzman, Phys. Rev. Lett. **42**, 798 (1979).
[3] C. C. Grimes and G. Adams, Phys. Rev. Lett. **42**, 795 (1979).
[4] A. G. Eguiluz, A. A. Maradudin, and R. J. Elliott, Phys. Rev. B **24**, 197 (1981).
[5] H. Namaizawa, Solid State Commun. **34**, 607 (1980).
[6] Yu. P. Monarkha and V. B. Shikin, Fiz. Nizk. Temp. **9**, 913 (1983) [Sov. J. Low Temp. Phys. **9**, 471 (1983)].
[7] G. Deville, J. Low Temp. Phys. **72**, 135 (1988).
[8] V. E. Sivokon', V. V. Dotsenko, Yu. Z. Kovdrya, and V. N. Grigor'ev, Fiz. Nizk. Temp. **22**, 1107 (1996) [Low Temp. Phys. **22**, 845 (1996)].
[9] V. V. Dotsenko, V. E. Sivokon, Yu. Z. Kovdrya, and V. N. Grigor'ev, Physica B **249**, 648 (1998).
[10] K. Shirahama and K. Kono, Phys. Rev. Lett. **74**, 781 (1995).
[11] A. Kristensen, K. Djerfi, P. Fozooni, M. J. Lea, P. J. Richardson, A. Santrich-Badal, A. Blackburn, and R. W. van der Heijden, Phys. Rev. Lett. **77**, 1350 (1996).
[12] Yu. P. Monarkha, E. Teske, and P. Wyder, Phys. Rep. **370**, Issue 1 (2002).
[13] O. Kirichek, M. Saitoh, K. Kono, and F. I. B. Williams, Phys. Rev. Lett. **86**, 4064 (2001).
[14] M. I. Dykman, Fiz. Nizk. Temp. **10**, 453 (1984) [Sov. J. Low Temp. Phys. **10**, 233 (1984)].
[15] Yu. P. Monarkha and K. Kono, J. Phys. Soc. Jpn. **70**, 1617 (2001).
[16] W. Götze and P. Wölfle, Phys. Rev. B **6**, 1226 (1972).
[17] Yu. P. Monarkha, Fiz. Nizk. Temp. **6**, 685 (1980) [Sov. J. Low Temp. Phys. **6**, 331 (1980)].
[18] Yu. P. Monarkha, Fiz. Nizk. Temp. **7**, 692 (1981) [Sov. J. Low Temp. Phys. **7**, 338 (1981)].
[19] B. Jancovici, Phys. Rev. Lett. **19**, 20 (1967).
[20] Y. Imry and L. Gunther, Phys. Rev. B **3**, 3939 (1971).
[21] M. I. Dykman and Yu. G. Rubo, Phys. Rev. Lett. **78**, 4813 (1997).
[22] Yu. P. Monarkha and S. S. Sokolov, Fiz. Nizk. Temp. **8**, 350 (1982) [Sov. J. Low Temp. Phys. **8**, 173 (1982)].
[23] Yu. P. Monarkha, Fiz. Nizk. Temp. **19**, 235 (1993) [Sov. J. Low Temp. Phys. **19**, 163 (1993)].
[24] D. J. Thouless, J. Phys. C **11**, L189 (1978).

This article was published in English in the original Russian journal. Reproduced here with stylistic changes by AIP.

QUANTUM EFFECTS IN SEMICONDUCTORS AND DIELECTRICS

Excitonic absorption spectra and phase transitions in thin films of the ferroelastics Cs_2CdI_4 and Rb_2CdI_4

O. N. Yunakova and V. K. Miloslavsky*

V. N. Karazin Kharkov National University, pl. Svobody 4, 61077 Kharkov, Ukraine

E. N. Kovalenko

Scientific Center of Physical Technologies of the Ministry of Education and National Academy of Sciences of Ukraine, ul. Novgorodskaya 1, 61145 Kharkov, Ukraine

(Submitted January 16, 2003; revised March 18, 2003)
Fiz. Nizk. Temp. **29**, 922–929 (August 2003)

The absorption spectrum of thin films of the ferroelastics M_2CdI_4 (M=Cs, Rb) with a structure of the β-K_2SO_4 type is investigated in the energy range 3–6 eV and temperature range 90–420 K. It is found that both compounds are direct-gap insulators, and the low-frequency electronic and excitonic excitations are localized in the CdI_4^{2-} structural elements of their crystal lattice. From the temperature dependence of the spectral absorption and the half-widths of the low-frequency excitonic bands in Rb_2CdI_4 it is found that there is a phase transition at 380 K (paraphase→incommensurate), a first-order phase transition at 320 K (incommensurate →first ferroelastic phase), and a second-order phase transition at 210 K (first→second ferroelastic phase). Similar, but less pronounced phase transitions are found in Cs_2CdI_4 at lower temperatures. In the ferroelastic phases of these compounds an additional broadening of the bands appears, apparently due to the scattering of excitons on strain fluctuations in the domain-wall regions. © *2003 American Institute of Physics.* [DOI: 10.1063/1.1596802]

INTRODUCTION

The compounds M_2CdI_r (M=Cs, Rb) are of interest in connection with the ferroelectric and ferroelastic properties manifested in them at low temperatures. The results of a thermodynamic analysis of the systems $MI–CdI_2$ indicate the formation of compounds with melting temperatures of 210 °C (Cs_2CdI_4) and 216 °C (Rb_2CdI_4).[1] The crystal structure has been studied most in Cs_2CdI_4. When Cs_2CdI_4 crystals are grown from the melt, they have an orthorhombic lattice of the β-K_2SO_4 type at room temperature, with parameters $a=10.74$, $b=8.458$, and $c=14.85$ Å (space group P_{nma}, $Z=4$).[2,3] However, when grown from an aqueous solution, Cs_2CdI_4 forms into a monoclinic lattice of the Sr_2GeS_4 type, with parameters[4] $a=7.827$, $b=8.397$, and $c=11.05$ Å ($P12_1/m$; $Z=2$). On heating above 120 °C, crystals of the second type undergo a transition to the orthorhombic phase. According to the data of Ref. 2, with decreasing temperature Cs_2CdI_4 in the orthorhombic modification undergoes a number of phase transitions to a ferroelastic state: at 332 K from a commensurate to an incommensurate phase, at 260 K to a monoclinic phase, and at 180 K to a triclinic ferroelastic phase. Analogous phase transitions do not occur for crystals of the second type. The phase transitions are manifested in the temperature dependence of the specific heat,[5] dielectric constant,[6,7] and birefringence.[2,7]

The compound Rb_2CdI_4 has been studied less, and the data on its crystal structure are incomplete. According to Ref. 8 the Rb_2CdI_4 crystal has a monoclinic structure of the Sr_2GeS_4 type, with parameters $a=8.004$, $b=8.323$, and $c=10.16$ Å, and $\beta=108.36°$, but the manner of growth of the crystals was not mentioned in that paper. In Ref. 9, in crystals grown from the melt, two phase transitions were inferred from the temperature dependence of the dielectric constant: at 150 and 210 K. The authors of Ref. 9, following the data of Ref. 8, ascribed the phase transitions of Rb_2CdI_4 to a structure of the Sr_2GeS_4 type, even though the analogous temperatures have not been observed in Cs_2CdI_4 crystals with that structure. At the same time, the temperature dependence of the intensity of the luminescence bands of Mn^{2+} impurity ions in Rb_2CdI_4, which are sensitive probes, reveals the presence of more high-temperature phase transitions at $T_{c1}=384$ K, $T_{c2}=325$ K, in addition to the transition at $T_{c3}=216$ K.[10] The authors of Ref. 10, by analogy with Cs_2CdI_4, assign to Rb_2CdI_4 the following sequence of phases: at $T>T_{c1}$—paraphase, in the interval $T_{c1}-T_{c2}$—incommensurate phase, and below T_{c2}—ferroelastic phases. It is assumed that in crystals grown from the melt, Rb_2CdI_4 forms into a structure of the β-K_2SO_4 type, although structural studies were not done in Ref. 10. It should also be noted that, to our knowledge, the fundamental absorption spectra of M_2CdI_4 compounds have not been studied. At the same time, it is of interest to study excitonic states in such compounds and the influence of phase transitions on the parameters of the excitonic bands.

In this paper we present the results of a study of the absorption spectra of thin films of M_2CdI_4 in the spectral region 2–6 eV and in the temperature range 90–420 K, which includes possible temperature-induced phase transitions. An electron-diffraction analysis of the films is also carried out.

TABLE I. Parameters of the excitonic bands of the compounds.

Compound	E_{A0}, eV	E_{A1}, eV	E_{C1}, eV	E_{C2}, eV	E_g, eV
Cs_2CdI_4	4.65	4.89	5.25	5.6	4.96
Rb_2CdI_4	4.608	4.87	5.35	5.6	4.89
CsI	5.8				
RbI	5.7				6.37 (Ref. 19)
CdI_2	4.03(X_1)	4.60(X_2)			3.473 (Ref. 13)

EXPERIMENTAL TECHNIQUES

Thin films of M_2CdI_4 (M=Cs, Rb) were grown by vacuum evaporation of a mixture of pure MI and CdI_2 powders of specified stoichiometric composition onto quartz substrates heated to 80 °C. The powder mixture was melted beforehand beneath a shield placed between the evaporator and substrate. The mass thickness of the films was determined by KIT. The geometric thickness was measured directly by the Tolansky method. Films around 100 nm thick were used for the spectral measurements. The absorption spectra of the films were determined from the transmission of the films relative to the clean substrate. The temperature of the sample was measured by a copper–Constantan thermocouple. The spectra were investigated in the interval 90–293 K in a vacuum cryostat and at higher temperatures in an ordinary cryostat. In the measurements of the spectra in the energy interval 4–5 eV the specified temperature of the sample was maintained to within ±2 K. The majority of the measurements were made on slow heating of the samples.

The phase composition of the films was monitored beforehand from the absorption spectra. This can be done because of the substantial differences in the positions of the long-wavelength excitonic bands in the spectrum of MI, M_2CdI_4 and CdI_2 (see Table I). It was found that in the evaporation of the mixture from the melt the absorption spectrum of thin films of Cs_2CdI_4 contained, in addition to the intense and frequency-stable A_0 and C bands, a weak long-wavelength A band, the position and intensity of which was different in different samples obtained under identical evaporation conditions.[11] The A band vanishes when the sample is heated above 120 °C, while the A_0 band becomes sharper, from which we concluded that the A band belongs to the monoclinic modification of Cs_2CdI_4. Thin films of the orthorhombic phase are also obtained directly during evaporation; if the first portions of the liquid melt are evaporated onto the shield, then the crystalline residue left on the bottom of the boat evaporates onto the substrate at a higher temperature. Apparently the monoclinic phase is formed at a lower average kinetic energy of the molecular beam, so that the two modifications can be separated during the evaporation process. Thin films of Rb_2CdI_4 were obtained in an analogous way.

The phase composition of the films was also monitored by electron diffraction. At room temperature the Cs_2CdI_4 films are single-phase and have an orthorhombic structure with lattice parameters $a=10.4\pm0.1$ Å, $b=8.2\pm0.1$ Å, and $c=14.7\pm0.1$ Å, in agreement with the data of Refs. 1 and 2. The corresponding diffraction rings of a slightly smaller diameter are also observed on the electron diffraction patterns of Rb_2CdI_4. Some of them are slightly split. The character of the splitting indicates a monoclinic distortion of the lattice. Additional reflections appear. Analysis of the extinction rules for the reflections indicates a possible pace group $P2_1/n$. The lattice parameters of Rb_2CdI_4 are $a=10.6\pm0.1$ Å, $b=8.4\pm0.1$ Å, and $c=14.9\pm0.1$ A; the angles are 90° within the error limits. As will be shown below, at $T\sim320$ K Rb_2CdI_4 undergoes a first-order phase transition and, as in the similar compound Cs_2CdI_4 (Refs. 1 and 2), has a monoclinic lattice, which arises as a slight distortion of the orthorhombic lattice, in the ferroelastic phase (at room temperature).

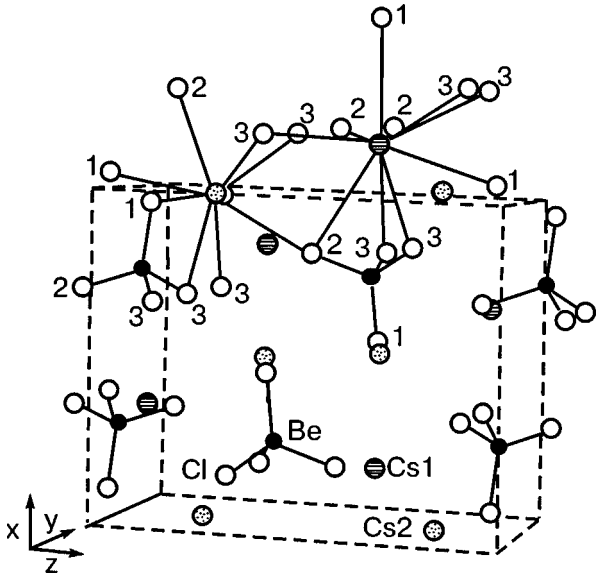

FIG. 1. Crystal lattice of the structural type β-K_2SO_4 (Cs_2BeCl_4; Ref. 12).

The position of the atoms in the unit cell of crystals of the β-K_2SO_4 type is shown in Fig. 1 (the compound Cs_2BeCl_4; Ref. 12). It is seen that the divalent ions are found at the center of tetrahedra of negative halide ions. The monovalent alkali metal ions form a hendecagon in the second coordination sphere with respect to the divalent ion.[2,3] One can also see the almost layered arrangement of the tetrahedra, the layers lying perpendicular to the **a** axis. A similar arrangement of ions is observed in the unit cell of M_2CdI_4 crystals of the β-K_2SO_4 type. In Cs_2CdI_4 the distance $d_{Cs-I}=3.825-4.499$ Å and is considerably larger than $d_{Cd-I}=2.76-2.91$ Å.[3]

EXCITONIC SPECTRUM IN M_2CdI_4 COMPOUNDS

The absorption spectra of thin films of Cs_2CdI_4 and Rb_2CdI_4 (Fig. 2) are similar both in the structure of the spectrum and in the position of the main bands, confirming the isostructural nature of these compounds. There is a slight difference only in the intensity of the C bands, which are more intense in Rb_2CdI_4.

The absorption spectrum of thin films of M_2CdI_4 has intense A_0 and A_1 bands at the long-wavelength edge of the fundamental absorption band and C_1 and C_2 bands in the shorter-wavelength part of the spectrum. The positions of the main absorption bands are given in Table I.

With increasing temperature the A bands shift to longer wavelengths and are broadened and attenuated on account of the exciton–phonon coupling, which attests to their excitonic

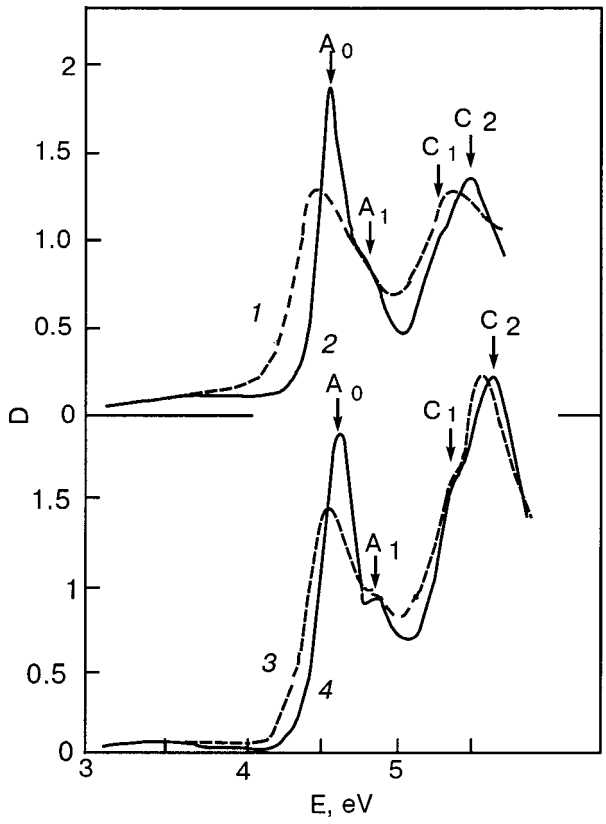

FIG. 2. Absorption spectra of thin films in units of the optical density D: Cs_2CdI_4, $T=290$ K (*1*), Cs_2CdI_4, $T=90$ K (*2*), Rb_2CdI_4, $T=290$ K (*3*), Rb_2CdI_4, $T=90$ K (*4*), orthorhombic phase.

origin. The C bands are less sensitive to temperature and are apparently due to the superposition of excitonic bands on the interband absorption edge.

To interpret the observed spectra, we compare them with the spectra of the initial components—CdI_2, RbI, and CsI. In CdI_2 the absorption edge is formed by indirect transitions across a band gap of width $E_g=3.437$ eV. The long-wavelength X_1 and X_2 bands correspond to direct transitions between the valence band, formed by the $5p$ states of I and the $4s$ conduction band of Cd.[13,14] The interval $E_{X1}-E_{X2}=0.59$ eV is determined by the spin–orbit splitting of the $5p$ valence band of CdI_2.

The long-wavelength A band lies at 5.8 eV in CsI and at 5.7 eV in RbI, $T=90$ K (see Table I).[11] The higher intensity of the C bands in the spectrum of Rb_2CdI_4 in comparison with Cs_2CdI_4 is probably due to the contribution to the C bands from excitonic absorption in the RbI sublattice.

In terms of its spectral position the A_0 band in M_2CdI_4 lies closer to the X_1 band in CdI_2 than to the A bands in MI; this suggests that the excitonic excitations are localized in the CdI_4^{2-} tetrahedra, which are a structural element of the lattice of the compounds (in M_2CdI_4 the CdI_4^{2-} tetrahedra are surrounded by 11 Cs atoms[2,3]). Also attesting to localization of the excitonic and electronic excitations in CdI_4^{2-} is the closeness of the positions of the fundamental absorption bands in the spectra of Cs_2CdI_4 and Rb_2CdI_4 (see Table I).

The tetrahedral environment of the Cd promotes the appearance of covalency in the Cd–I interatomic bond and leads to a decrease in the distance d_{Cd-I} in the compounds ($d_{Cd-I}=2.76-2.91$ Å in the orthorhombic modification of Cs_2CdI_4 (Ref. 3) and $d_{Cd-I}=2.739-2.794$ Å in the monoclinic[4]) in comparison with CdI_2 ($d_{Cd-I}=2.99$ Å), in which the Cd^{2+} ions are surrounded by an octahedron of I^- ions.

It is known that in copper halides the tetrahedral bonding leads to mixing of the d states of the Cu^+ ion and the p states of I^- in the upper valence band.[15,16] It is possible that in M_2CdI_4 the tetrahedral bonding in CdI_4^{2-} also promotes mixing of the $4d$ states of Cd^{2+} with the $5p$ states of I^-, in contrast to pure CdI_2, in which the $5p$ upper valence band of I is separated from the $4d$ band of Cd by a band gap.[17,18] The lower conduction band in M_2CdI_4, as in CdI_2, is formed by the $5s$ electronic states of Cd.

The sharp long-wavelength edge of the A_0 bands in M_2CdI_4 and their high intensity (Fig. 2) indicate that these compounds are direct-gap insulators, i.e., the interband absorption edge corresponds to direct allowed transitions. The shift of the long-wavelength excitonic bands in M_2CdI_4 to shorter wavelengths in comparison with CdI_2 attests to growth of the band gap, which was estimated from the inflection point of the absorption edge after separation of the A_0 and A_1 bands. The numerical values obtained, $E_1=5.2$ and 5.15 eV for Cs_2CdI_4 and Rb_2CdI_4, respectively, correspond to an optical transition from the lower valence subband to the conduction band. To determine the band gap one must take into account the distance between the subbands $\Delta E=E_{A1}-E_{A0}$ and $E_g=E_1-\Delta E=4.96$ and 4.89 eV for Cs_2CdI_4 and Rb_2CdI_4. The exciton binding energy $R_{ex}=E_g-E_{A0}=0.31$ eV in Cs_2CdI_4 and 0.28 eV in Rb_2CdI_4.

The presence of two valence subbands in M_2CdI_4 is most likely due, as in CdI_2, to the splitting off of the top of the valence band by the spin–orbit interaction. The lower value of the spin–orbit splitting Δ_{SO} in M_2CdI_4 ($\Delta_{SO}=E_{A1}-E_{A0}=0.24$ eV in Cs_2CdI_4 and 0.26 eV in Rb_2CdI_4) in comparison with CdI_2 ($\Delta_{SO}=0.59$ eV) is due, in our opinion, to an impurity of d states of Cd in the upper valence band. For Cd the splitting has the value $\Delta_{SO}=0.15$ eV.[19] When the $4d$ states of Cd and the $5p$ states of iodine are mixed, Δ_{SO} decreases, just as in the compounds CuI and AgI. The quantity $\Delta_{SO}=A[(1-\gamma)\Delta_I+\gamma\Delta_{Cd})]$, where γ is the fraction of the $4d$ states in the valence band of the compounds. An estimate of γ is difficult, however, because of the undetermined coefficient A.

The splitting of the C bands is probably also due to the spin–orbit coupling. The splitting of the C bands has the values $\Delta E=E_{C2}-E_{C1}=0.35$ eV in Cs_2CdI_4 and 0.25 eV in Rb_2CdI_4, which agree within the accuracy of determination with the corresponding values of $\Delta E=E_{A1}-E_{A0}$.

TEMPERATURE DEPENDENCE OF THE PARAMETERS OF THE EXCITONIC BANDS AND PHASE TRANSITIONS IN M_2CdI_4

In the 3.6–5.1 eV region the absorption spectrum of thin films of M_2CdI_4 was measured in the temperature range 90–420 K, which includes the temperatures of the possible phase transitions. The parameters of the long-wavelength A_0 and A_1 excitonic bands (the position E_m, the half-width Γ, and the oscillator strength f) were studied by the method of Ref. 20. The A_0 and A_1 bands were approximated by a two-oscillator symmetric mixed contour—a linear combination of

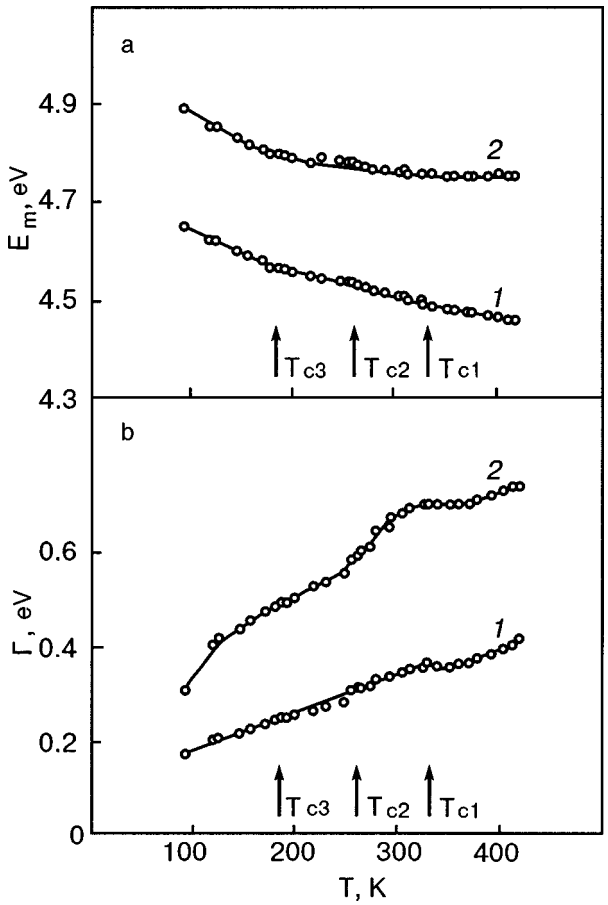

FIG. 3. Temperature dependence of the spectral position $E_m(T)$ (a) and half-width $\Gamma(T)$ (b) of the A_0 (*1*) and A_2 (*2*) excitonic bands in Cs_2CdI_4.

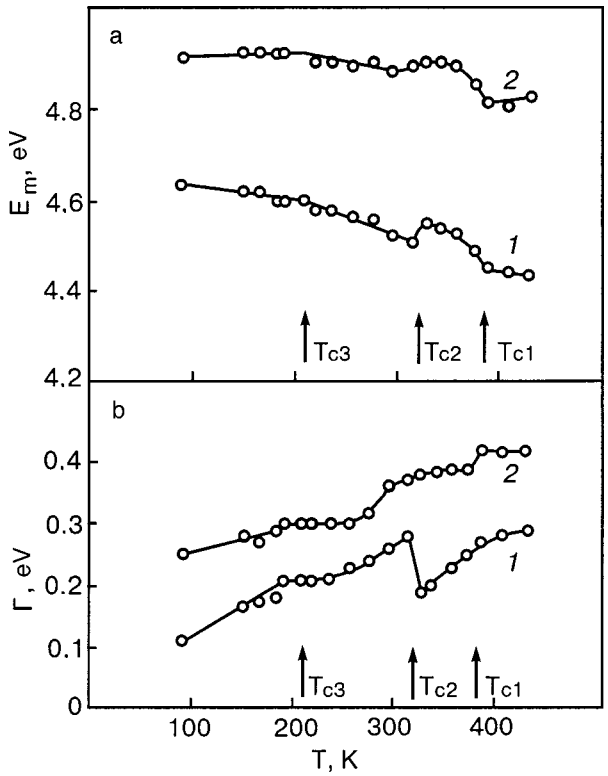

FIG. 4. Temperature dependence of the spectral position $E_m(T)$ (a) and half-width $\Gamma(T)$ (b) of the A_0 (*1*) and A_1 (*2*) excitonic bands in Rb_2CdI_4.

a Lorentzian and a Gaussian contour. The parameters of the excitonic bands (E_m, Γ, and ε_{2m}) were chosen so as, first, to give a best fit of the experimental and calculated contours on the long-wavelength declivity of the A_0 band, and second, to minimize the difference between the calculated and measured contours in the interval 4.5–5.2 eV. The Gaussian fraction in the mixed contour for the films studied increases with increasing temperature, from 0.2 (90 K) to 1 ($T>290$ K).

In the temperature interval 90–183 K the A_0 and A_1 bands in Cs_2CdI_4 are shifted to longer wavelengths at a rate $dE_m/dT=-9.1\times10^{-4}$ eV/K and -10×10^{-4} eV/K (Fig. 3a). At the transition to the second ferroelastic phase (183–260 K) the value of dE_m/dT decreases to -4.6×10^{-4} eV/K for the A_0 band and to -2.1×10^{-4} eV/K for A_1. The transition to the incommensurate phase (260–322 K) is not accompanied by a change in dE_m/dT within the error limits, and in the paraelastic phase (332–420 K) one has $dE_m/dT=-2.3\times10^{-4}$ eV/K for the A_0 band and -1.9×10^{-5} eV/K for A_1. The value of the derivative dE_m/dT is of a typical order of magnitude for many similar compounds and is mainly determined by the exciton–phonon coupling. The large value of dE_m/dT in the interval 90–183 is apparently due to appreciable thermal expansion of the lattice in this temperature interval, involving growth of the parameter c (Ref. 2). The phase transitions are manifested as kinks in the temperature dependence of $E_m(T)$ (Fig. 3a). At $T=260$ K, however, no features are observed on $E_m(T)$, even though, according to the data of Refs. 2 and 3, a first-order phase transition from the incommensurate to the ferroelastic phase occurs occurs at that temperature.

The phase transitions are more clearly expressed in the temperature dependence of $E_m(T)$ in Rb_2CdI_4 (Fig. 4a). In the temperature interval 90–210 K the A_0 band is shifted to longer wavelengths at a rate $dE_m/dT=-3.9\times10^{-4}$ eV/K, while the position of the A_1 band remains practically unchanged in this temperature interval. At $T\sim210$ K a kink is observed on the $E_m(T)$ curves, and in the interval 210–320 K one has $dE_m/dT=-8.03\times10^{-4}$ eV/K for the A_0 band and -1.485×10^{-4} eV/K for A_1. In a narrow temperature interval 315–327 K both bands have a jumplike shift to shorter wavelengths: the A_0 band by 35 meV and the A_1 band by 10 meV; the temperature coefficients of the shift in the region 330–360 K are $dE_m/dT=-4.96\times10^{-4}$ eV/K for the A_0 band and -3.25×10^{-4} eV/K for A_1. Then in the temperature interval 360–390 K both bands shift abruptly to longer wavelengths, and in the region 390–430 K one has $dE_m/dT=-3.7\times10^{-4}$ eV/K for the A_0 band, while the position of the A_1 band remains practically unchanged.

Thus it follows from the $E_m(T)$ curve for Rb_2CdI_4 (Fig. 4) that, as in Cs_2CdI_4, three phase transitions are observed in this compound: in the region 360–390 there is a phase transition which is diffuse in temperature (presumably from the paraphase to an incommensurate phase, in analogy with Cs_2CdI_4); at $T_{c2}\approx320$ K there is a transition accompanied by a jump in $E_m(T)$, as is characteristic of a first-order phase transition; this transition can apparently be identified as a transition from the incommensurate phase to ferroelastic phase I; at $T_{c1}\approx210$ K there is a transition corresponding to a second-order phase transition between two ferroelastic phases (I→II).

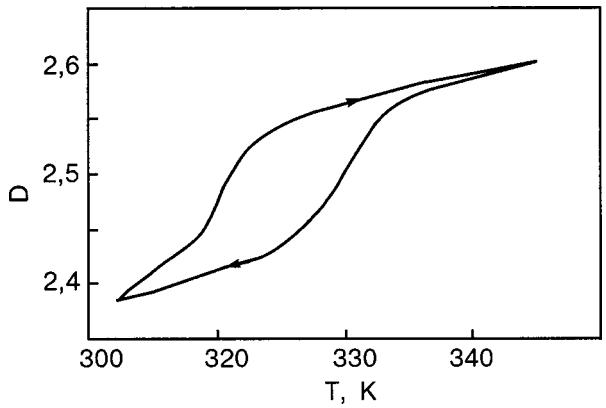

FIG. 5. Temperature dependence of the optical density at $E=4.37$ eV on heating and cooling of a thin film of Rb_2CdI_4.

The jumplike change in the position of the excitonic bands at $T\approx 320$ K is indicative of a first-order phase transition, which is accompanied by a change in volume. The presence of a first-order phase transition also is attested to by the hysteresis in the temperature dependence of the transmission at $E=4.37$ eV (on the long-wavelength declivity of the A_0 band) on heating and cooling of an Rb_2CdI_4 film at a rate of 0.3 deg/min (Fig. 5).

At the same time, jumps in $E_m(T)$ are not observed at $T\sim 210$ K, even though according to the data of Ref. 9 this is a first-order phase transition.

The exciton–phonon coupling leads to growth of the half-width Γ of the excitonic bands in Cs_2CdI_4. For the A_0 band $\Gamma(T)$ increases from 0.18 eV (90 K) to 0.4 eV (420 K), while for the A_1 band it increases from 0.35 eV (90 K) to 0.74 eV (420 K) (Fig. 3b). The average value of $d\Gamma/dT$ over the entire temperature interval is equal to 0.605×10^{-3} eV/K for the A_0 band and 1.06×10^{-3} eV/K for A_1. The larger value of Γ for the A_1 band is obviously due to additional broadening on account of autoionization of the A_1 exciton as a result of the superposition of the A_1 band on the interband absorption edge. The practically linear character of the overall trend of the temperature dependence of the half-width of the excitonic band indicates that the excitons in Cs_2CdI_4 are low-dimensional.[21] According to Ref. 21, $\Gamma(T)\sim T^2$, T, and $T^{2/3}$ for three-dimensional, two-dimensional, and one-dimensional excitons, respectively. The low dimensionality of the excitons in Cs_2CdI_4 is consistent with the assumption of their localization in the CdI_4^{2-} tetrahedra, the spatial distribution of which exhibits layering (Fig. 1).

The monotonic character of $\Gamma(T)$ is disrupted somewhat at the phase transition temperatures: at T_{c3} and T_{c2} one observes a small bump (Fig. 3b), and in the region of the transition to the paraphase (T_{c1}) the half-width of the excitonic bands decreases slightly and then grows for $T>T_{c1}$ because of the exciton–phonon coupling.

The temperature dependence of $\Gamma(T)$ in Rb_2CdI_4 (Fig. 4b), as that of $E_m(T)$, has three distinct intervals within which the temperature dependence of the half-width of the excitonic line varies in accordance with different laws: I—90–210 K, II—210–315 K, III—320–370 K. In interval I the half-width $\Gamma(T)$ increases linearly at a rate of $\Gamma/dT=9.6\times 10^{-4}$ eV/K for the A_0 band and 4.4×10^{-4} eV/K for A_1; in interval II the half-width $\Gamma(T)\approx$const on the 210–230 K part and increases linearly at a rate $d\Gamma/dT=10\times 10^{-4}$ eV/K (A_0 band) for $T\geqslant 230$ K; then in a narrow interval 315–327 K the half-width of the A_0 band jumps downward from 0.38 to 0.29 eV; this, like the behavior of $E_m(T)$, is indicative of a first-order phase transition at the transition from the ferroelastic to the incommensurate phase. Interval III is again characterized by a linear trend, with $d\Gamma/dT=1.1\times 10^{-4}$ eV/K, and at $T>380$ K the temperature dependence of the half-width of the A_0 band goes to saturation. A slight growth of $d\Gamma/dT$ at the transition from the first interval to the third attests to the manifestation of a partial three-dimensional character of the exciton distribution in Rb_2CdI_4.

One notices a decrease of Γ at the transition from the ferroelastic phase to the paraphase both in Cs_2CdI_4 (Fig. 3b) and especially in the A_0 band, in Rb_2CdI_4 (Fig. 4b), in spite of its growth for $T>T_{c2}$. The jump in $\Gamma(T)$ is evidently due to the vanishing of the domain structure and twinning inherent in the ferroelastic phase. In the monoclinic phase there is scattering of excitons on domain walls and, possibly, on strain fluctuations near them. At the transition from the monoclinic phase to the orthorhombic paraphase the domain structure and strain fluctuations are not observed, and that removes an additional mechanism of broadening of the excitonic bands at $T>T_{c2}$. No such jump is detected in the A_1 band, although signs of a lowering of $\Gamma(T)$ are manifested in a decrease of $d\Gamma/dT$ on the segment 315–340 K. A possible reason for the differences in $\Gamma(T)$ for the A_0 and A_1 bands is that the maxima of these bands draw closer together (by 0.02 eV) for $T>T_{c2}$. This makes the interaction of the A_1 band with the interband absorption edge more efficient, and its additional broadening due to autoionization compensates the lowering of Γ for $T>T_{c2}$. A similar, flatter trend of $\Gamma(T)$ is observed at the second-order phase transition from the triclinic to the monoclinic phase for $T>T_{c3}=210$ K, which is apparently due to a slight decrease in the number of domain walls at the transition to the more symmetric phase.

The unusual behavior of the temperature dependence of the spectral position and half-width in interval III can be ascribed to the existence of an incommensurate phase. When the temperature is raised from 320 to 380 K the maximum of the excitonic band is shifted to lower frequencies, the greatest shift ($dE_m/dT=-6\times 10^{-3}$ eV/K, A_0 band) being reached at $T_{c1}=380$ K. An analogous shift with a somewhat smaller value of $|dE_m/dT|$ occurs for the A_1 band (Fig. 4a). At $T>T_{c1}$ the $E_m(T)$ curve becomes flatter and is similar to the temperature dependence for $T<T_{c2}$. The half-width on this same segment increases nonmonotonically with increasing T, reaching saturation at $T\geqslant T_{c1}$. These results agree with the data of Ref. 10, according to which the transition from the incommensurate to the commensurate phase is accompanied by a substantial redistribution of the intensities of the two luminescence bands of the Mn^{2+} ions at $T_{c1}=384$ K. The temperature dependence of $E_m(T)$ and the kink in $\Gamma(T)$ at the transition to the commensurate phase suggest that the transition from the incommensurate to the commensurate phase is a first-order transition. It is possibly a phase transition of the order–disorder type wherein the tetrahedra of iodine ions acquires an arbitrary orientation with

respect to the crystallographic axes in the commensurate phase (Fig. 1). It will be possible to draw more-detailed conclusions from the experimental results in temperature interval III after studying the temperature dependence of the lattice modulation period and hysteresis effects in the incommensurate phase.

CONCLUSION

We have developed a method of growing thin films of the compounds M_2CdI_4 (M=Cs, Rb) with an orthorhombic lattice of the β-K_2SO_4 type in the paraphase, making it possible for the first time to study the excitonic spectrum of these compounds. Analysis of the absorption spectra permits the conclusion that the low-frequency electronic and excitonic excitations are localized in the CdI_4^{2-} structural elements of the crystal lattice and that the formation of electronic bands adjacent to the band interval occurs. A study of the temperature dependence of the spectral position and halfwidth of the excitonic bands in Rb_2CdI_4 revealed phase transitions at $T_{c1}=380$ K, $T_{c2}=320$ K, and $T_{c3}=210$ K. The temperature dependence of the parameters of the bands at T_{c2} is indicative of a second-order phase transition. Similar phase transitions are observed in Cs_2CdI_4 at lower temperatures, but the parameters of the excitonic bands in the transition regions do not change as much as in Rb_2CdI_4. By analogy with the better-studied ferroelastic Cs_2CdI_4 it is conjectured that Rb_2CdI_4 is in an incommensurate phase in the region $T_{c1}>T>T_{c2}$, a monoclinic ferroelastic phase in the interval $T_{c2}>T>T_{c3}$, and a ferroelastic triclinic phase for $T<T_{c3}$.

*E-mail: Vladimir.K.Miloslavsky@univer.kharkov.ua

[1] I. N. Belyaev, E. A. Shurginov, and N. S. Kudryashov, Zh. Neorg. Khim. **17**, 2812 (1972).
[2] K. S. Aleksandrov, S. V. Melnikova, I. N. Flerov, A. D. Vasilev, A. I. Kruglik, and I. T. Kokov, Phys. Status Solidi A **105**, 441 (1988).
[3] V. Touchard, V. Louer, J. P. Auffredic, and D. Louer, Rev. Chem. Miner. **24**, 414 (1987).
[4] B. R. Sjovall, Acta Crystallogr., Sect. C: Cryst. Struct. Commun. **45**, 667 (1989).
[5] I. N. Flerov, M. V. Gorev, L. A. Kot, and V. A. Grankina, Fiz. Tverd. Tela (Leningrad) **30**, 1948 (1988) [Sov. Phys. Solid State **30**, 1125 (1988)].
[6] F. Shimizu, T. Kurihama, T. Yamaguchi, and M. Takashige, Ferroelectrics **230**, 133 (1999).
[7] K. S. Aleksandrov, S. V. Mel'nikova, and I. T. Kokov, Fiz. Tverd. Tela (Leningrad) **29**, 2487 (1987) [Sov. Phys. Solid State **29**, 1431 (1987)].
[8] H. W. Zandbergen, G. C. Verschoor, and D. I. W. Ijdo, Acta Crystallogr., Sect. B: Struct. Crystallogr. Cryst. Chem. **35**, 1425 (1979).
[9] F. Shimizu and M. Takashige, J. Phys. Soc. Jpn. **67**, 2555 (1998).
[10] I. M. Bolesta and Yu. M. Furgala, Ukr. Fiz. Zh. **36**, 1654 (1991).
[11] O. N. Yunakova, V. K. Miloslavskiĭ, and E. N. Kovalenko, Fiz. Tverd. Tela (St. Petersburg) **45**, 887 (2003) [Phys. Solid State **45**, 932 (2003)].
[12] H. Gaebell and B. Mejer, Z. Anorg. Allg. Chem. **515**, 133 (1984).
[13] M. K. Tubbs, J. Phys. Chem. Solids **29**, 1191 (1968).
[14] I. Pollini, J. Tomas, R. Coehoorn, and C. Haas, Phys. Rev. B **33**, 5747 (1986).
[15] A. Blacha, S. Ves, and M. Cardona, Phys. Rev. B **27**, 6346 (1983).
[16] A. Goldmann, Phys. Status Solidi B **81**, 9 (1977).
[17] Ya. O. Dovgiĭ and I. V. Kityk, Ukr. Fiz. Zh. **29**, 886 (1984).
[18] I. Robertson, J. Phys. C **12**, 4753 (1979).
[19] M. Cardona, *Modulation Spectroscopy*, Academic Press, New York (1969), Mir, Moscow (1972).
[20] V. K. Miloslavskii, O. N. Yunakova, and Sun Tsya-Lin, Opt. Spektrosk. **78**, 436 (1995) [Opt. Spectrosc. **78**, 391 (1995)].
[21] V. Schreiber and Y. Toyozawa, J. Phys. Soc. Jpn. **51**, 1528 (1982).

Translated by Steve Torstveit

SHORT NOTES

Collective vibrations of a lattice of screw dislocations as an example of the dynamics of an acoustic superlattice

A. M. Kosevich*

B. Verkin Institute for Low Temperature Physics and Engineering, National Academy of Sciences of Ukraine, pr. Lenina 47, 61103 Kharkov, Ukraine

(Submitted March 17, 2003)
Fiz. Nizk. Temp. **29**, 930–933 (August 2003)

Equations for small oscillations of a dislocation lattice are formulated in a simple one-component model. The lattice is formed by a periodic system of parallel rectilinear screw dislocations. Long-wavelength collective vibrations are described, among which are found vibrations similar to plasma oscillations in a system of electric charges. The possibility of a gap appearing in the frequency spectrum near the analog of the plasma frequency is pointed out. © *2003 American Institute of Physics.* [DOI: 10.1063/1.1602351]

Many papers devoted to the dynamics of vortex lattices have appeared in recent years, particularly in the theory of superconductivity (the Abrikosov vortex lattice; see, e.g., the reviews[1,2]). Screw dislocations in a crystal are analogous to vortices, but the dynamics and interaction of the dislocations differ from those for vortices. Rectilinear screw dislocations interact like rectilinear electric charges, and it is expected that plasma oscillations will arise in the dynamics of the dislocation lattice.[3,4] Unfortunately, the authors of Ref. 5 failed to discuss plasma oscillations in a system of rectilinear dislocations.

In the present paper we consider a lattice of parallel screw dislocations on the basis of a simple model. A one-component *scalar model* of vibrations of the crystal is used in which it is assumed that all of the atoms are displaced only in one direction.[6] Such a model gives a correct description of the elastic field created in an isotropic medium by parallel screw dislocations. The solution of such a problem in a real vector displacement scheme can in principle be found analytically, but it permits obtaining the dispersion relation of the dislocation lattice only in implicit form. In the present problem of oscillations of the plasma type such a treatment does not yield qualitatively new results in comparison with those obtained in the scalar model.

By dislocation lattice we mean a system of parallel screw dislocations orientated along the z axis and intersecting the xy plane at discrete periodically arranged points, forming a 2D lattice, the unit cell of which has area S_0: $S = NS_0$, where S is the cross-sectional area of the sample in the xy plane and N is the number of dislocations. The coordinates of those points in the equilibrium lattice are

$$\mathbf{x}(\mathbf{n}) = \mathbf{R}_\mathbf{n} \equiv \sum_\alpha \mathbf{a}_\alpha n_\alpha, \quad \mathbf{n} = (n_1, n_2, 0), \tag{1}$$

where $\mathbf{a}_\alpha$ ($\alpha = 1,2$) are the basic translation vectors of the lattice ($a_\alpha \sim a$ is the distance between neighboring dislocations).

If there are rectilinear screw dislocations directed along the z axis, then the elastic field is more conveniently described not by the displacement w along the z axis as a function of the coordinate and time but by the distortion and the velocity of the displacements. For describing the shear field of screw dislocations it is sufficient to introduce a distortion vector $\mathbf{h}$ and a velocity v:

$$\mathbf{h} = \text{grad}\ w \quad \left(\mathbf{h}_i = \nabla_i w = \frac{\partial w}{\partial x_i} \right), \quad i = 1,2,3;$$

$$v = \frac{\partial w}{\partial t}. \tag{2}$$

The stress will be characterized by a vector $\boldsymbol{\sigma}$, with $\sigma_i = G h_i$, where G is the shear modulus.

Then the wave equation for the elastic field (1) takes the form

$$\text{div}\, \mathbf{h} - \frac{1}{c^2} \frac{\partial v}{\partial t} = 0, \tag{3}$$

where $c^2 = G/\rho$, and ρ is the density (mass per unit volume) of the substance.

The presence of dislocations gives rise to a new equation

$$\text{curl}\ \ \mathbf{h} = -\boldsymbol{\eta}, \tag{4}$$

where $\boldsymbol{\eta}$, the density of dislocations, which in the case of an individual dislocation intersecting the plane $z = \text{const}$ at the point $\mathbf{x}_0 = (x_0, y_0)$ is equal to

$$\boldsymbol{\eta} = \tau b\, \delta(\mathbf{x} - \mathbf{x}_0) = \boldsymbol{\tau} b\, \delta(x - x_0)\, \delta(y - y_0);$$

here b is the modulus of the Burgers vector, and $\boldsymbol{\tau}$ is the tangent vector to the dislocation; for a static dislocation it is conveniently chosen as $\tau(0,0,-1)$. The density of dislocations in the lattice is

$$\boldsymbol{\eta} = \tau b \sum_\mathbf{n} \delta(\mathbf{x} - \mathbf{R}_\mathbf{n}). \tag{5}$$

If the dislocations move (vibrate), then Eqs. (3) and (4) do not change, but a new dynamical variable of the dislocation structure appears: the displacement vector of a dislocation line in the xy plane: $\mathbf{u}=(u_x,u_y,0)$ (of course, $\mathbf{u}=\mathbf{u}(\mathbf{n},t)$ for the $\mathbf{n}$th dislocation), which determines the instantaneous coordinate of an element of the dislocation:

$$\mathbf{x_n}=\mathbf{R}(\mathbf{n})+\mathbf{u}(\mathbf{n},t).$$

The time dependence of the displacement vector $\mathbf{u}$ gives the velocity $\mathbf{V}$ of an element of the dislocation: $V_\alpha=\partial u_\alpha/\partial t$.

The presence of the dislocation velocity field generates a new dynamical characteristic of the system of dislocations—the *dislocation flux density* $\mathbf{j}$. The introduction of a dislocation flux density is a key development in the construction of the dynamic elastic field of moving dislocations. The vector $\mathbf{j}$ arises in the frequency dynamical equation:[3,6]

$$\frac{\partial \mathbf{h}}{\partial t}=\text{grad}\ \ v+\mathbf{j}. \tag{6}$$

A comparison of (6) and (4) yields the condition

$$\frac{\partial \boldsymbol{\eta}}{\partial t}+\text{curl}\ \ \mathbf{j}=0. \tag{7}$$

The flux density created by an individual dislocation in a linear approximation in $\mathbf{u}$ and $\mathbf{V}$ is given by the formula

$$j_\alpha=b\varepsilon_{\alpha\beta}V_\beta(\mathbf{n})\,\delta(\mathbf{x}-\mathbf{R}(\mathbf{n})), \tag{8}$$

where the matrix $\varepsilon_{\alpha\beta}$ is equal to

$$\varepsilon_{\alpha\beta}=\begin{pmatrix}0 & 1\\ -1 & 0\end{pmatrix},\quad \alpha=1,2. \tag{9}$$

The dislocation flux density in the lattice is the sum of the quantities (8) over the whole lattice:

$$j_\alpha=b\varepsilon_{\alpha\beta}\sum_{\mathbf{n}}\ V_\beta(\mathbf{n})\,\delta(\mathbf{x}-\mathbf{R}(\mathbf{n})). \tag{10}$$

Collecting together Eqs. (3), (4), and (6), we obtain the total system of equations describing the elastic field in the sample if the distribution of dislocations and their fluxes are known. To close this system it is necessary to write equations of motion for the dislocations under the influence of the elastic fields. The simplest form of such an equation is[3]

$$m\frac{\partial V_\alpha}{\partial t}=f_\alpha+S_\alpha, \tag{11}$$

where m is the effective mass of a unit length of the dislocation:

$$m=\frac{\rho b^2}{4\pi}\log\left(\frac{R_0}{r_0}\right), \tag{12}$$

where R_0 is either the length of the dislocation line or the distance between dislocations a (in our case); r_0 is the interatomic distance, and $\mathbf{f}$ is the elastic coupling force with the other dislocations, which is equal to

$$f_\alpha=b\varepsilon_{\alpha,\beta}\sigma_\beta=bG\varepsilon_{\alpha,\beta}h_\beta. \tag{13}$$

In the case of a curved dislocation line expression (13) will include the self-force from different elements of the same dislocation, which is proportional to the curvature of the dislocation line at the given point. In the analysis of the vibrations under consideration here the curvature of the dislocations is not taken into account, and the force (13) includes only the stresses created by the other dislocations.

$\mathbf{S}$ is the force due to the discreteness of the lattice, including dissipative forces. As we are interested in the dispersion relation for small vibrations, we neglect the latter and take the force $\mathbf{S}$ in the form

$$\mathbf{S}=-m\omega_0^2\mathbf{u}, \tag{14}$$

where ω_0 is the frequency of vibrations of the dislocation string in a valley of the Peierls relief.

Let us investigate the long-wavelength vibrations of the dislocation lattice, assuming the wavelength of the vibrations is much larger than the lattice period a ($ak\ll 1$). In this approximation the distribution of the dislocations can be assumed continuous, characterized by a density $n(\mathbf{x},t)$. In equilibrium $n=n_0$, where $n_0=1/S_0=\text{const}$. The dynamics of the lattice is governed mainly by the average dislocation flux density $\mathbf{j}$, which in the linear approximation has the nonzero components

$$j_\alpha(\mathbf{x},t)=bn_0\varepsilon_{\alpha\beta}V_\beta(\mathbf{x},t),\quad \alpha=1,2, \tag{15}$$

where $\mathbf{V}$ is the average velocity of the dislocations. The velocity $\mathbf{V}$ must be determined by the equation of motion of the dislocations (11). We write the equation of motion (11) with the use of (13) and (14):

$$\frac{\partial V_\alpha}{\partial t}+\omega_0^2u_\alpha=\frac{bG}{m}\varepsilon_{\alpha\beta}h_\beta. \tag{16}$$

We differentiate (16) with respect to time and use Eqs. (6) and (15). After elementary calculations we get

$$\frac{\partial^2 V_\alpha}{\partial t^2}+(\omega_0^2+\omega_{pl}^2)V_\alpha=\frac{bG}{m}\varepsilon_{\alpha\beta}\frac{\partial v}{\partial x_\beta}, \tag{17}$$

where

$$\omega_{pl}^2=\frac{b^2Gn_0}{m}. \tag{18}$$

The frequency ω_{pl} is the analog of the plasma frequency.

We now differentiate Eq. (3) with respect to time and again use relation (6):

$$\left(\Delta-\frac{1}{c^2}\frac{\partial^2}{\partial t^2}\right)v=-bn_0\varepsilon_{\alpha\beta}\nabla_\alpha V_\beta. \tag{19}$$

(Here Δ is the Laplacian operator.)

The pair of equations (17) and (19) describe the collective dynamics of the dislocation lattice and the elastic field. It is easy to see that the equation for the ''longitudinal'' vibrations of the lattice separates. Indeed, for the variable $P=\text{div}\,\mathbf{V}=\nabla_\alpha V_\alpha$ it follows from Eq. (17) that

$$\frac{\partial^2 P}{\partial t^2}+\omega_l^2P=0,\quad \omega_l^2=\omega_0^2+\omega_{pl}^2, \tag{20}$$

where ω_l plays the role of the frequency of the longitudinal vibrations of the lattice.

The longitudinal component of the average velocity of the dislocations is derivable from a potential: $V_\alpha^{(l)}=\nabla_\alpha Q$, $\alpha=1,2$. Taking that into account, we see that the ''longitudinal'' vibrations of the elastic field $v=v(z)$ do not depend on

the lattice vibrations. Thus one branch of collective oscillations (we call it the branch of ''longitudinal'' vibrations) corresponds to independent oscillations of the elastic field $v=v(z,t)$ with the dispersion relation $\omega=ck_z$ and to compression–rarefaction oscillations of the dislocation lattice $P=P(z,t)$ with a plasma dispersion relation $\omega=\omega_l$.

To describe to ''transverse'' vibrations we introduce the variable

$$M=bn_0(\text{curl }\mathbf{V})_z\equiv bn_0\varepsilon_{\alpha\beta}\nabla_\alpha V_\beta. \tag{21}$$

The equation for this variable follows from (17):

$$\frac{\partial^2 M}{\partial t^2}+\omega_l^2 M=-\omega_{pl}^2\frac{\partial^2 v}{\partial x_\alpha^2}. \tag{22}$$

The ''transverse'' collective vibrations are described by Eq. (22) and the following equation obtained from (19) for the function $v(x,y,t)$:

$$\left(\frac{1}{c^2}\frac{\partial^2}{\partial t^2}-\frac{\partial^2}{\partial x_\alpha^2}\right)v=M. \tag{23}$$

The compatibility conditions for (22) and (23) give the dispersion relation relation for a wave with wave vector $\mathbf{k}$ $(k_x,k_y,0)$:

$$\omega^4-(\omega_l^2+c^2k^2)\omega^2-\omega_0^2c^2k^2=0. \tag{24}$$

Equation (24) has two roots for ω^2, which correspond to low-frequency and high-frequency oscillations. Without writing the trivial expressions for these solutions in quadratures, we note the following:

Low-frequency branch. For $ck\ll\omega_0$ the dispersion relation has the form

$$\omega=\left(\frac{\omega_0}{\omega_l}\right)ck. \tag{25}$$

The vibrations are characterized by a transverse sound velocity, the value of which is less than the sound velocity c in the medium without the dislocations.

High-frequency branch. For $ck\gg\omega_l$ the inertial dislocation lattice is not entrained in the motion, and one observes only vibrations of the elastic field with the usual sound dispersion relation $\omega=ck$. Finally, in the long-wavelength limit $(ck\ll\omega_0)$ we obtain

$$\omega^2=\omega_l^2+\left(\frac{\omega_{pl}}{\omega_l}\right)^2c^2(k_x^2+k_y^2). \tag{26}$$

In comparing the graphs of the two branches of the dispersion relation, one must be particularly careful in rendering the low-frequency branch. The point is that dispersion relation (24) is valid for $\lambda\gg\alpha$ (or $ak\ll1$). At large k the dispersion relation of the lattice manifests a periodic dependence on the quasi-wave vector, with the reciprocal lattice period $\mathbf{G}$: $\omega(\mathbf{k})=\omega((\mathbf{k}+\mathbf{G})$. Therefore the dispersion relation obtained is actually valid in all small neighborhoods of any reciprocal lattice vector $\mathbf{g}$, i.e., for $a|\mathbf{k}-\mathbf{g}|\ll1$. Consequently, we are justified in drawning only the part of the graphs shown by the heavy solid lines *1* and *2* in Fig. 1 for a certain ''good'' direction in the reciprocal lattice. The continuation of the graphs of the lower branch at $k\sim\pi/a$ and also the indicated crossing of the graphs of the upper branch at $k=(p+1/2)\pi/a$, $p=1,2,3,\ldots$ can be described only on the basis of a study of the dynamics of the discrete dislocation lattice. That is a subject for a separate study. We can only state that the graphs of the lower branch is closed by the curves illustrated schematically by the dotted lines *3* in Fig. 1. Whether or not there is a band of forbidden frequencies between the upper and lower branches (gap in the spectrum) one cannot say on the basis of a long-wavelength treatment. However, one can say that the frequency spectrum has a limiting frequency ω_l that marks the edge of the upper branch of vibrations, which can certainly be manifested in the acoustic resonance properties of a crystal with a dislocation lattice. An important feature of this frequency is the dependence of its position on the density of dislocations in the lattice (on the value of the lattice period). The experimental detection of this resonance behavior of the limiting frequency would be direct confirmation of the existence of plasmalike collective oscillations in the dislocation lattice.

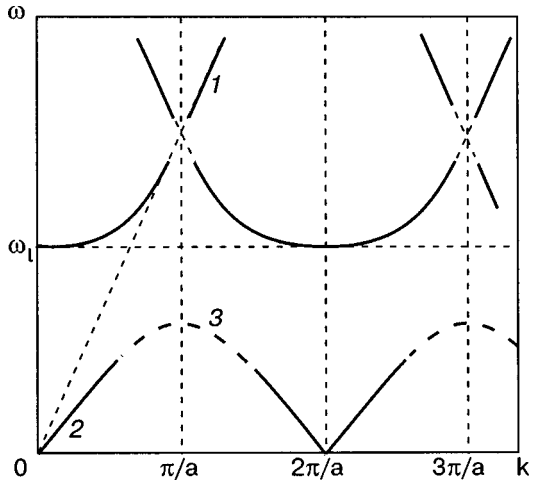

FIG. 1. Diagram of the dispersion relation: *1*—$\omega=ck$, *2*—plot of Eq. (26), *3*—expected form of the graph in the short-wavelength region.

The author is grateful to O. V. Charkina for assistance in organizing this paper, to Ali Najafi and Ramin Golestanian, the reading of whose manuscript called his attention to this problem, and to V. D. Natsik for helpful comments.

*E-mail: kosevich@ilt.kharkov.ua

[1] G. Blatter, M. V. Feigel'man, V. B. Geshkenbein, A. I. Larkin, and V. M. Vinokur, Rev. Mod. Phys. **66**, 1125 (1994).
[2] E. H. Brandt, Rep. Prog. Phys. **58**, 1465 (1995).
[3] A. M. Kosevich, *Dislocations in the Theory of Elasticity* [in Russian], Naukova Dumka, Kiev (1978); A. M. Kosevich, ''Crystal dislocations and the theory of elasticity,'' in *Dislocations in Solids*, F. R. N. Nabarro (ed.), Vol. 1, North-Holland, Amsterdam, (1979), p. 31.
[4] A. M. Kosevich and M. L. Polyakov, Fiz. Tverd. Tela (Leningrad) **21**, 2941 (1979) [Sov. Phys. Solid State **21**, 1694 (1979)].
[5] V. V. Nikoalaev, A. N. Orlov, and G. G. Taluts, Fiz. Met. Metalloved. **23**, 424 (1967).
[6] A. M. Kosevich, *Theory of the Crystal Lattice (Physical Mechanics of Solids)* [in Russian], Vishcha Shkola, Kharkov (1988); A. M. Kossevich, *The Crystal Lattice. Phonons, Solitons, Dislocations*, Wiley-VCH, Berlin (1999).

Translated by Steve Torstveit